Universidad Politécnica de Valencia
Institute of Energetic Engineering
Department of Nuclear and Chemical Engineering

EXPERIMENTAL CHARACTERIZATION OF AEROSOL RETENTION IN THE BREAK STAGE OF A DRY STEAM GENERATOR IN SGTR SEQUENCES

Ph. D. Thesis

Presented by:
Francisco Javier Sánchez Velasco

Supervisors:
Dr. Luis Enrique Herranz Puebla
Dr. José Luis Muñoz-Cobo González

EXPERIMENTAL CHARACTERIZATION OF AEROSOL RETENTION IN THE BREAK STAGE OF A DRY STEAM GENERATOR IN SGTR SEQUENCES

by

Francisco Javier Sánchez Velasco

B.S. Ind. Eng., Polytechnic University of Cartagena, 2003

Submitted to the Department of Nuclear and Chemical Engineering in Partial Fulfillment of the Requirements for the Degree of

DOCTOR of PHILOSOPHY

at the

Polytechnic University of Valencia

September 2008

Certified by Dr. Luis Enrique Herranz Puebla. Thesis Supervisor

Certified by Dr. José Luis Muñoz-Cobo. Thesis Supervisor

Accepted by …
Accepted by …
Accepted by …
Accepted by …
Accepted by …

Abstract

Severe accident Steam Generator Tube Rupture (SGTR) sequences are identified as major contributors to risk of Pressurized Water Reactors (PWR). Their relevance lies in the potential radioactive release, in form of aerosol, from reactor coolant system to the environment. However, radioactive particles could be partially retained in the secondary side of the steam generator, even in the absence of water. Lack of knowledge on the source term attenuation capability of the steam generator has avoided its consideration in probabilistic safety studies and severe accident management guidelines. As a consequence, the steam generator filtering capability is not usually taken into account either in the probabilistic risk assessment of nuclear safety or in the severe accident management guidelines.

This thesis describes the main activities and results of a bench-scale experimental program focused on getting insights into the aerosol retention in the break stage of the secondary side of a dry steam generator. The thesis is framed in the CIEMAT contribution to the ARTIST project (2003-2008) which was supported by te Spanish Nuclear Regulatory Commission (CSN). The general objective of the work was to generate a comprehensive database on fission product retention in the break stage of a dry steam generator during a severe accident SGTR sequence. The specific objectives were to assess the influence of aerodynamic flow field as well as the influence of particle nature on aerosol deposition in the tube bundle. To do so, a scaled-down mock-up with representative dimensions of a real SG was built. The aerodynamic characterization of the flow field within the break stage of the bundle was done via 2D PIV (particle image velocimetry) technique. The particle nature influence on retention was characterized through aerosol retention experiments in the tube bundle mock-up. The major variables investigated were the type of breach (guillotine vs fish-mouth), the inlet gas mass flow rate (75-250 kg/h) and the particle type (polidispersed TiO_2 agglomerates vs. solid, monodisperse SiO_2 spheres).

The aerodynamic campaign permitted to characterize the flow field close to the breach for both type of breaches and to asses their similarities. Results showed that the jet flows within the tube bundle following a generic quasi-parabolic trajectory evolving from an oblique cross flow configuration to an axial one. Mean flow field near the breach is substantially affected by the entrainment of initially stagnant gas into the jet. This effect is fostered by the presence of tubes and their tight packing. Jet penetration and turbulence intensity are considerably enhanced when increasing inlet gas mass flow rate.

The results of the aerosol campaign showed that particle nature substantially affects retention in the tube bundle: mass retention was low for TiO_2 agglomerates (less than 30%) whereas it was much higher for SiO_2 particles (around 85%). Collection efficiency is also affected by gas mass flow rate: its sensitivity was found to follow a lognormal behaviour. This evolution resulted to be similar for both type of compounds. Particle size also influences retention efficiency: the bigger the TiO_2 agglomerates the lower retention efficiency (no data were available for SiO_2). Among

all these variables, particle nature was noted to have a prime importance for in-bundle retention, whereas gas mass flow rate and particle aerodynamic size, although also affect retention efficiency, did not play such a key role.

These data will enhance the overall understanding of aerosol behavior in the secondary side of a faulted SG during SGTR sequences and will serve as a database against which compare model predictions.

Resumen

En reactores de agua a presión, las secuencias de accidente severo con rotura de tubos del generador de vapor (conocidas por sus siglas en inglés SGTR, Steam Generator Tube Rupture) son dominantes del riesgo, a pesar de ser sucesos de muy baja probabilidad. Su importancia reside en la potencial liberación de radiactividad, en forma de aerosol, que supondrían desde el circuito primario al medio ambiente, sin intervención de la contención. Sin embargo, las partículas radioactivas podrían retenerse parcialmente en el secundario del generador de vapor aun cuando no quedara agua en el mismo. La ausencia de información sobre la capacidad del generador de vapor para atenuar el Término Fuente en condiciones secas, ha impedido su consideración en los estudios probabilistas de seguridad y en las guías de gestión de accidentes severos.

Este trabajo describe las principales actividades y resultados de un programa experimental centrado en el estudio de la retención de aerosoles que se produce en la etapa de rotura del secundario de un generador de vapor seco. El trabajo está enmarcado en la contribución del CIEMAT al proyecto ARTIST (2003-2008) que ha sido financiada por el Consejo de Seguridad Nuclear. El objetivo general del trabajo fue desarrollar una base de datos de retención de productos de fisión en la etapa de rotura del secundario de un generador de vapor seco durante una secuencia SGTR de accidente severo. Los objetivos específicos del programa eran estimar tanto la influencia del campo de velocidades del gas, como la influencia de la naturaleza de las partículas en la retención de aerosoles en el haz de tubos. Para ello, se construyó una maqueta de tamaño intermedio con dimensiones y geometría representativas de una etapa un generador de vapor real. La caracterización aerodinámica del flujo en la etapa de rotura se realizó utilizando la técnica de velocimetría por imágenes de partículas (conocida por sus siglas en inglés PIV). La influencia de la naturaleza de la partícula en la retención se caracterizó a través de experimentos de retención del aerosol en el haz de tubos de la maqueta. Las variables más importantes investigadas fueron el tipo de rotura (guillotina vs boca de pez), el flujo másico de entrada a través de la rotura (75-250 kg/h) y el tipo de partícula (aglomerados de TiO_2 de tamaño polidisperso vs perlas sólidas de SiO_2 de tamaño monodisperso).

La campaña aerodinámica permitió caracterizar el campo de velocidades del flujo cerca de la rotura para ambos tipos de rotura y analizar sus similitudes. Los resultados mostraron que el chorro generado en la rotura se expande en el haz de tubos siguiendo una trayectoria cuasi-parabólica desarrollándose a partir de una configuración inicial en flujo cruzado perpendicular a los tubos hacia una configuración de flujo axial paralelo a los mismos. El campo de velocidades medio cerca de la rotura se ve afectado de manera importante por la ingestión del chorro de gas que estaba inicialmente en reposo. Este efecto está potenciado por la presencia de tubos y su compacta configuración en el haz. La penetración y la intensidad turbulenta del chorro son especialmente potenciadas cuando se aumenta el flujo másico de entrada.

Los resultados de la campaña de retención de aerosoles muestran que la naturaleza de la partícula afecta substancialmente a la retención en el haz de tubos: la masa retenida es baja para aglomerados de TiO_2 (menos de un 30%) mientras que es mucho más alta en el caso de partículas de SiO_2 (en torno al 85%). La eficiencia de retención también se ve afectada por el flujo másico de entrada y su sensibilidad sigue un comportamiento log-normal. Esta evolución es similar para ambos tipos de compuestos. El tamaño de partícula también influye en la eficiencia de retención: cuanto mayor es el aglomerado de TiO_2 menor es la eficiencia de retención (no hay datos disponibles para SiO_2). Entre todas estas variables, la naturaleza de la partícula es la que tiene la mayor influencia en la retención del haz de tubos, mientras que el flujo másico de entrada y el tamaño aerodinámico de las partículas, aunque también afectan a la eficiencia de retención, no juegan el mismo papel.

Estos datos contribuirán a mejorar el conocimiento del comportamiento del Termino Fuente en el secundario del generador de vapor accidentado durante una secuencia SGTR de accidente severo y servirán como base de datos con la que validar modelos predictivos.

Resum

En reactors d'aigua a pressió, les seqüències d'accident sever amb ruptura de tubs del generador de vapor (conegudes per les seves sigles en anglès SGTR, Steam Generator Tube Rupture) son dominants del risc, malgrat ser successos de molt baixa probabilitat. La seva importància resideix en el potencial alliberament de radioactivitat, en forma d'aerosols, que suposarien des del circuit primari al medi ambient, sense la intervenció de la contenció. No obstant això, les partícules radioactives es podrien retenir parcialment en el secundari del generador de vapor fins i tot quan no quedés aigua en el mateix. La manca d'informació sobre la capacitat del generador de vapor per atenuar el Terme Font en condicions seques, ha impedit la seva consideració en els estudis probabilistes de seguretat i en les guies de gestió d'accidents severs.

Aquest treball descriu les principals activitats i resultats d'un programa experimental centrat en l'estudi de la retenció d'aerosols que es produeix en l'etapa de ruptura del secundari d'un generador de vapor sec. El treball està emmarcat en la contribució del CIEMAT al projecte ARTIST (2003-2008) que ha estat finançat pel Consejo de Seguridad Nuclear. L'objectiu general del treball fou desenvolupar una base de dades de retenció de productes de fissió en l'etapa de ruptura del secundari d'un generador de vapor sec durant una seqüència SGTR d'accident sever. Els objectius específics del programa eren estimar tant la influència del camp de velocitats del gas, com la influència de la naturalesa de les partícules en la retenció d'aerosols en el feix de tubs. Per aquest motiu, es va construir una maqueta a escala intermèdia amb dimensions i geometria representatives d'una etapa d'un generador de vapor real. La caracterització aerodinàmica del flux de l'etapa de ruptura es va realitzar utilitzant la tècnica de la velocimetria per imatges de partícules (coneguda per les sigles en anglès PIV). La influència de la naturalesa de la partícula en la retenció es va caracteritzar mitjançant experiments de retenció de l'aerosol en el feix de tubs de la maqueta. Les variables mes importants investigades van ser el tipus de ruptura (guillotina vs boca de peix), el flux màssic d'entrada a través de la ruptura (75-250 kg/h) i el tipus de partícula (aglomerats de TiO_2 de grandària polidispersa vs perles sòlides de SiO_2 de grandària monodispersa).

La campanya aerodinàmica va permetre caracteritzar el camp de velocitats del flux prop de la ruptura per ambdós tipus de ruptura i analitzar les seves similituds. Els resultats mostraren que el raig generat en la ruptura s'expandeix en el feix de tubs seguint una trajectòria quasi-parabòlica desenvolupant-se a partir d'una configuració inicial en flux creuat perpendicular als tubs cap a una configuració de flux axial paral·lel als mateixos. El camp de velocitats mitjà prop de la ruptura es veu afectat d'una manera important per la ingestió del raig de gas que estava inicialment en repòs. Aquest efecte està potenciat per la presencia de tubs y la seva configuració compacta en el feix. La penetració i la intensitat turbulenta en el raig són especialment potenciades quan s'aumenta el flux màssic d'entrada.

Els resultats de la campanya de retenció d'aerosols mostra que la naturalesa de la partícula afecta substancialment a la retenció en el feix de tubs: la massa retinguda és baixa per a aglomerats de TiO_2 (menys del 30%) mentre que és molt més alta en el cas de partícules de SiO_2 (al voltant del 85%). La eficiència de retenció també es veu afectada pel flux màssic d'entrada i la seva sensibilitat segueix un comportament log-normal. Aquesta evolució és similar per ambdós tipus de compostos. La mida de la partícula també influeix en l'eficiència de retenció: quant més gran és l'aglomerat de TiO_2 més petita és l'eficiència de retenció (no hi ha dades disponibles pel SiO_2). Entre totes aquestes variables, la naturalesa de la partícula és la que té major influència en la retenció del feix de tubs, mentre que el flux màssic d'entrada i la mida de la partícula, encara que també afecten a l'eficiència de retenció, no juguen el mateix paper.

Aquestes dades contribuiran a millorar el coneixement del comportament del Terme Font en el secundari del generador de vapor accidentat durant una seqüència SGTR d'accident sever i serviran com a base de dades amb la qual validar models predictius.

Acknowledgements

Firstly, I would like to say thank you my wife, Belén, who has assist me during these five years of work. She has always support me to reach this goal. Her comprehension has guided me through especially in the bad moments. To her is dedicated this work. I would also like to thank F. Javier Sánchez Navarro for his the moments shared finishing this work beside him. Thank you also to my family for giving me the chance of reaching this moment.

I would also like to express my gratitude to my codirectors Jose Luis and very specially to Luis Enrique, for giving me the chance of working in this project at CIEMAT, for giving me the opportunity of using the resources of this center of excellence and expertise, and more importantly, for giving me the chance of working with them and learning from them. I am especially indebted to Luis Enrique for his assistance during these four years and especially for his assistance in the last six months. He has been not only a mentor for me but also a professional reference. He has shown me the intrinsic value of doing things well.

I would also like to thank the team of the Unit for Nuclear Safety Research at CIEMAT. I would especially like to say thanks to Claudia and Joan for their assistance in this work but also for the good moments shared.

Finally, the author also wish to acknowledge the Spanish Nuclear Safety Council for the financial support of this research and other partners of the international ARTIST project for the fruitful technical discussions, specially to the PSI scientists of ARTIST project by their contribution to this work.

Index

List of Tables

List of Figures

Chapter 1

Introduction

1.1. Severe accident SGTR sequences background

1.1.1. The steam generators of a PWR nuclear power plant

Pressurized water reactors (PWR) nuclear power plants, rely on indirect cycles to generate electricity. The thermal energy generated in the nuclear reactor is transferred to a steam power cycle through steam generators (SGs). The SGs of PWRs are large shell-and-tube heat exchangers that use the heat from the primary reactor coolant to produce steam in the secondary side to drive turbine generators. A typical western plant (Westinghouse, Framatome, Siemens designs) have from two to four SGs per plant, depending on plant capacity. Fig. 1 and 2 show a cut-away view and a side view of a typical recirculating SG. The steam generator (SG) is a complex structure housing various components and around 4000 U-inverted tubes each of them welded to a thick plate with hole for each tube end (called tube sheets) located near the bottom of the SG vessel. The reactor coolant enters the hemispherical bottom head through an inlet nozzle, flows through the U-tubes and exits the lower plenum through an outlet nozzle. The tubes are supported with plates at a number of fixed axial locations along the tube bundle. The region defined by two consecutive support plates is usually called “stage”. Above the heat exchanger, there is an integral moisture separation equipment to dry the steam. Primary coolant enters the SG at around 315 to 330ºC on the hot leg side and leaves it at about 288ºC on the cold leg side. About 25% of the secondary coolant is converted into steam on each pass through the generator. The remaining is recirculated. The SGs are generally designed to produce, at rated steam flow, saturated with less than 0.25% moisture by weight.

Since primary reactor coolant is at a higher pressure than the secondary coolant, any leakage from defects in the tubes is from the primary to secondary-side, and rupture of the tubing can result in release of radioactivity to the environment outside the reactor containment through the pressure relief valves in the secondary system. The thin-walled SG tubes are, therefore, an important part of the reactor boundary. To act as an effective barrier, this tubing must be essentially free of cracks, perforations, and general deterioration.

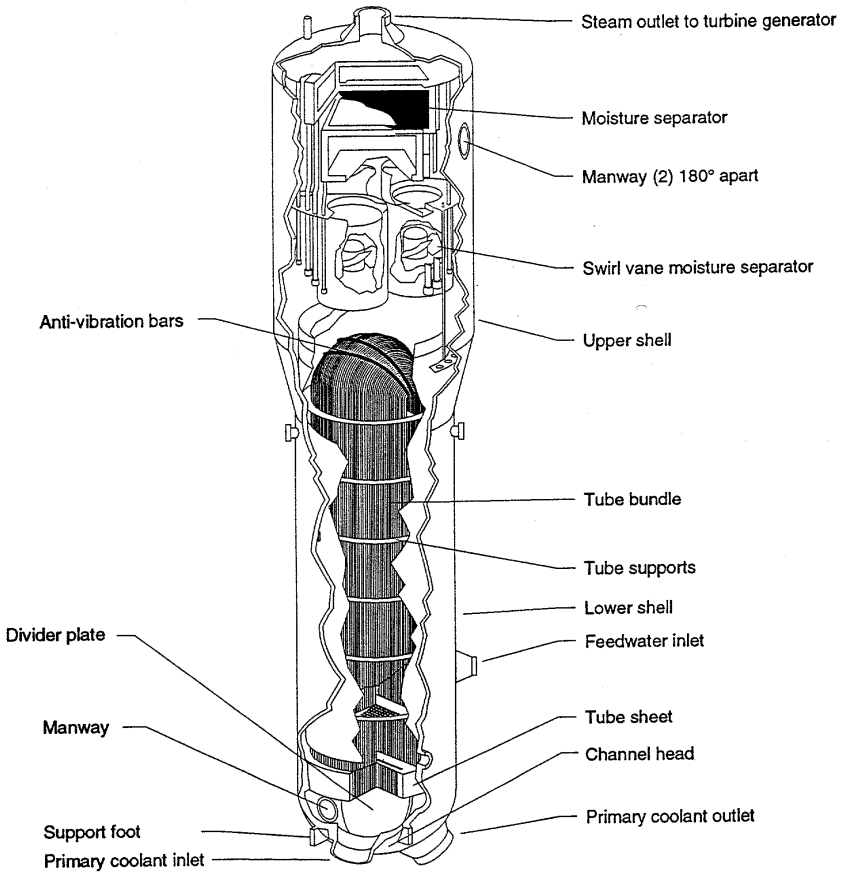

Fig. 1. Cut-away view of a PWR SG.

However, widespread degradation of the SG tubes has occurred at a number of plants. As a result, about one-half of the PWR nuclear power plants in the world have been removing from service (plugging) or repairing (sleeving) SG tubes in any given year. Up to 1996, the total number of SG tubes plugged per year ranged about 10000. Also about 48000 tubes have been sleeved per year (US NRC, 1996). This means that a large fraction of PWR plants are operating with tubing defects near of beyond the safety limits at any given time.

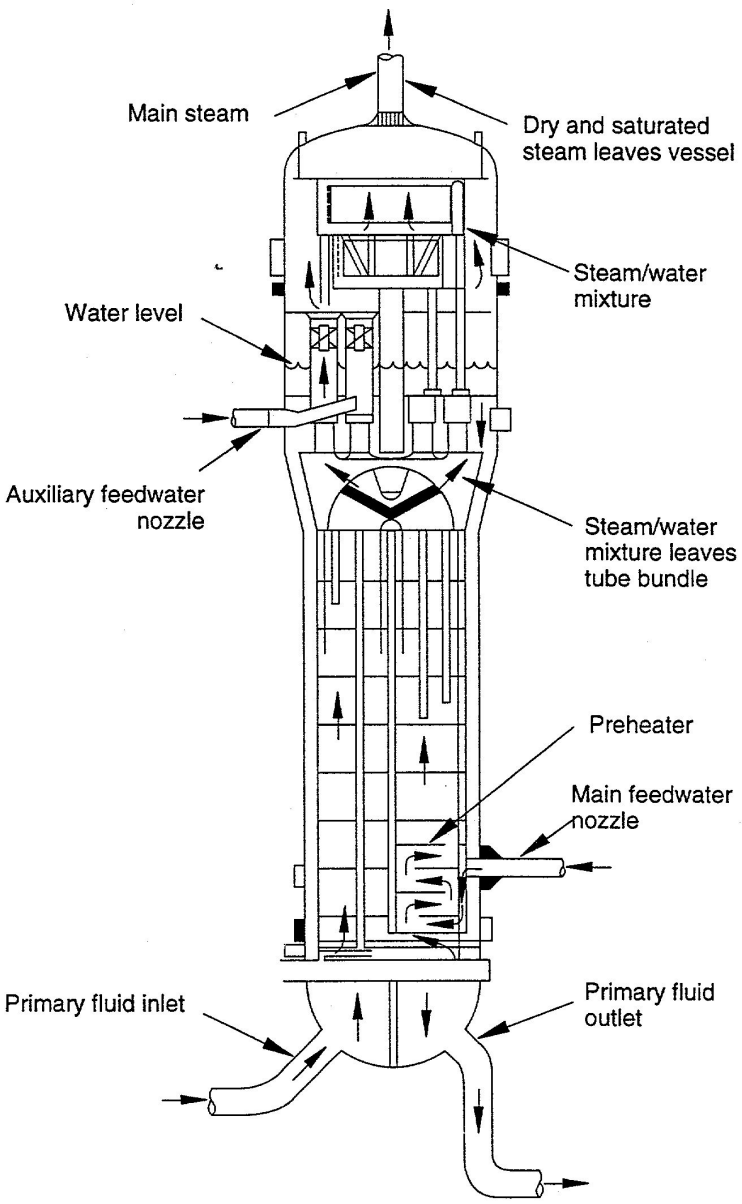

Fig. 2. Side view of a PWR SG.

1.1.2. Severe accident steam generator tube rupture sequences

Ten spontaneous steam generator tube ruptures (SGTR) have occurred over the last 20 years just in USA nuclear power plants (US NRC, 1996). A spontaneous tube rupture is a rupture of one or more SG tubes that is not caused by another event or an upset in normal expected operational parameters. These ruptures have been caused by a variety of tubing degradation mechanisms including stress corrosion of the surface of the tubing, high-cycle fatigue and wastage (uniform corrosion) (Hwang et al., 2008). Statistically, break locations have been distributed between bend region (50%) and in the hot leg near the tube sheet (50%). The ruptures resulted in leak rates ranging from 425 l/min to 2900 l/min (i.e. 0.007-0.048m^3/s) and complex plant transients which have not always been easy for the operators to control. In some cases, it took a relatively long time to realize that a SGTR had occurred and, therefore, there was a slow answer to start reducing power and isolate the defective SG. Also, at some plants, the reactor coolant system pressures were held above the defective SG secondary side pressures for relatively long periods of time and the defective SG were overfilled (US NRC, 1996). All in all, these events were always successfully countered as no other major malfunctions occurred at same time.

SGTR are handled within design basis accidents (DBA) of western PWR. Plants are designed to cope with such accidents and no major consequences should be expected. However, certain nuclear power plant DBA, such as a sudden break in the steam line, can lead to rapid depressurization of the secondary coolant system. The pressure difference across the tubing walls generated during these accidents may result in simultaneous leakage or rupture of a number of SG tubes when an active degradation mechanism has severely damaged a large number of tubes generating an induced SGTR (Da Silva et al., 2007). Simultaneous leakage or rupture of several tubes can lead to a plant transient which is even more difficult to control than a spontaneous tube rupture transient, and radioactivity levels released to the environment which may exceed site limits. The sudden rupture of several SG tubes also results in a rapid depressurization of the primary coolant system and possibly may uncover the core and cause core melting.

In addition, if during a SGTR event other malfunctions happen the sequence can lead to severe accidents. If the safety relief valve of the failed SG is damaged due to water ingression and stays stuck open it would result in a loss of coolant that, eventually, would lead to core degradation and meltdown. Under these conditions, fission products and aerosols released from the reactor would bypass the containment. These accident scenarios are very unlikely but, given the potential consequences of a direct path for fission products from the primary coolant system to the environment, they were

estimated to be important risk contributors (US NRC, 1990). Actually, spontaneous tube rupture contribution to total core damage frequency varies from 10^{-8} to 10^{-5} per reactor year. However, a review of 20 U.S. PWR individual plant examinations has shown that the risk associated with SGTR at most PWR plants is above 10% and at many plants is as high as 75% to 99% of the total risk (US NRC, 1996). These numbers are based on the past history of spontaneous tube ruptures, but do not consider the possibility of induced tube ruptures (i.e. progression of other accidents to induced SGTR) in badly degraded SGs. Current power plants operate with detectable flaws in tubes, which are controlled during revisions by a criteria of limiting the flaw size. Under accident conditions, heat transfer from the reactor core to the primary circuit boundary weakens the structure and might break at vulnerable locations, such as the hot leg nozzle, the surge line to the pressurizer or the SG tubes. As a reference for this case, NUREG-1150 showed that all three PWR plants analyzed could suffer induced SGTR.

The potential retention within the secondary side of a failed steam generator during a SGTR severe accident sequence was seen as one of the largest uncertainties in the analyses reported in NUREG-1150 (US NRC, 1990). An expert elicitation panel (US NRC, 1990) considered that little retention of radionuclides would occur both in the reactor coolant piping and the failed steam generator. They estimated the overall transmission factor from the reactor to the environment to be higher than 75% for all radionuclides considered, and agreed to attribute such a small attenuation to retention in the primary coolant piping. Consistently, and given present absence of a comprehensive database or specific model for the retention in the secondary side of the failed steam generator, Probabilistic Risk Assessments (PRA's) usually give no credit to any potential decontamination within the secondary side of a steam generator. Regulatory conservatism is based on the fact that aerosol interactions in the SG are too complex to quantify retention with good accuracy.

On the other hand, worldwide tendency is oriented towards reducing maximum dose limits. Consequently, plants have to protect public accordingly. So, for SGTR, quantifying decontamination factor ($DF=m_{in}/m_{out}$) of the dry SG is of great practical importance. Theoretical and laboratory-scale experiments showed evidences of high potential for aerosol removal in dry SG due to inertial impaction and turbulent deposition on secondary tube bundle. Based on 10μm particles studies, industry analysis suggests very high decontamination factor for dry SG (DF~10000, Güntay, 2007) which is far away of the regulators view.

In the hypothetical case of a reactor core melting, SGTR could result in a direct release of radioactive particles to the environment. However, given the large surface area available, radioactive aerosol could be partially retained in the secondary side of the steam generator. The extent of aerosol trapping is

heavily dependent on the conditions in the secondary side during the accident. Under normal working conditions the secondary side is flooded with water to generate steam. Under accident conditions, however, the tube breach could be over the water level and particles would enter a "dry" secondary side carried by a high-velocity gas flow. This scenario is especially critical since no attenuation will occur due to pool scrubbing. The particle-laden gas, however, could still be filtered as it passes through the multiple structures within the secondary side (i.e., tube bundle, separators, dryers, etc.). Under these conditions, it is expected that the tube surfaces in the region between the tube breach and the upper support plate (hereafter called "break stage"), play a key role in the retention process. Lack of a reliable and complete database of such a retention capability has prevent safety regulators to take into account the SG filtering capability either in the probabilistic risk assessment of nuclear safety or in the severe accident management guidelines.

1.2. State of art on aerosol retention in the secondary side of a vertical steam generator during SGTR sequences

The EU-SGTR project of the 5th Framework Program of EURATOM (Auvinen et al. 2005) was the only program aimed to investigate source term retention during SGTR sequences. CIEMAT results of the project were analyzed and deeply discussed as starting point of this thesis from were several specifics were obtained (Herranz et al., 2006).

The first objective of the EU-SGTR project was to generate a comprehensive database on fission product retention in a steam generator. The second objective was to verify and develop predictive models to support accident management interventions in steam generator tube rupture sequences, which either directly lead to severe accident conditions or are induced by other sequences leading to severe accidents. The models developed for fission product retention were to be included in severe accident codes. In addition, it was shown that existing models for turbulent deposition, which is the dominating deposition mechanism in dry conditions and at high flow rates, contain large uncertainties.

Regarding vertical steam generators four tests were conducted in the ARTIST facility (Güntay et al., 2004). These tests address aerosol deposition phenomena on two different scales: stages close to the break, where the gas velocities are sonic, and stages far away from the break, where the flow velocities are three orders of magnitude lower. With a bundle flooded just above the break and a steam/non-condensable mixture, the DF was between 45 and 112 for an inlet gas mass flow rate of 650 kg/h and 482 for an inlet gas mass flow rate of 110 kg/h. This implied again that the far-field stages

are more efficient at trapping aerosols than the break stage. When steam was present in the carrier gas under flooded secondary, condensation inside the tube caused aerosol deposition and produced blockage near the break, with subsequent increase in the primary pressure. This has implications for real plant conditions, as aerosol deposits inside the broken tube will cause more flow to be diverted to the intact tubes, with corresponding reduction in the source term to the secondary. With a dry bundle and the 360kg/h inlet gas mass flow rate representing conditions of the stages close to the break, the overall DF was found to be between 2.5 and 3. With a dry bundle and a small flow reproducing the far-field velocities, the overall bundle DF is of the order of 5, implying a DF of about 1.9 per stage. Extrapolating these results, it turns out that for steam generators with nine or more stages, it is expected that substantial DF's could be achieved when the break is located near the tube sheet region.

Research activities on SGTR sequences were carried out at CIEMAT in the frame of the EU-SGTR program between 2000 and 2002 to investigate the retention capability of the break stage of a SG. EU-SGTR program was the initial part of a long term program designed by CIEMAT to characterize the influence of flow and aerosol conditions in retention efficiency of the break stage of the secondary side of the SG during a SGTR sequence. The overall approach of the research program (not fully addressed in EU-SGTR project) was structured in three working lines (Fig. 3): test performance, 3D aerodynamic simulations and model development.

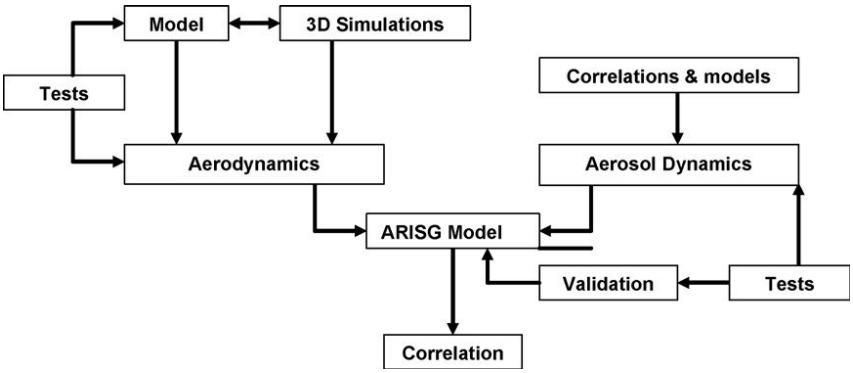

Fig. 3. Scheme of the research program approach.

The experimental phase consisted of 12 tests performed at CIEMAT's PECA-SGTR facility (Fig. 4). The instrumentation included pressure (P) and flow rate (Q) control devices, and impactors, filters and optical particle counters to characterize aerosols at the entrance and the outlet of the rig.

The break stage of the secondary side of a steam generator was reproduced by a tube bundle arranged in a square assembly of 11x11 tubes, one of which

was the broken one. Tube diameter (19 mm) and tube spacing (8 mm) were identical to those of a PWR SG. The height of the bundle was around 1.5 m.

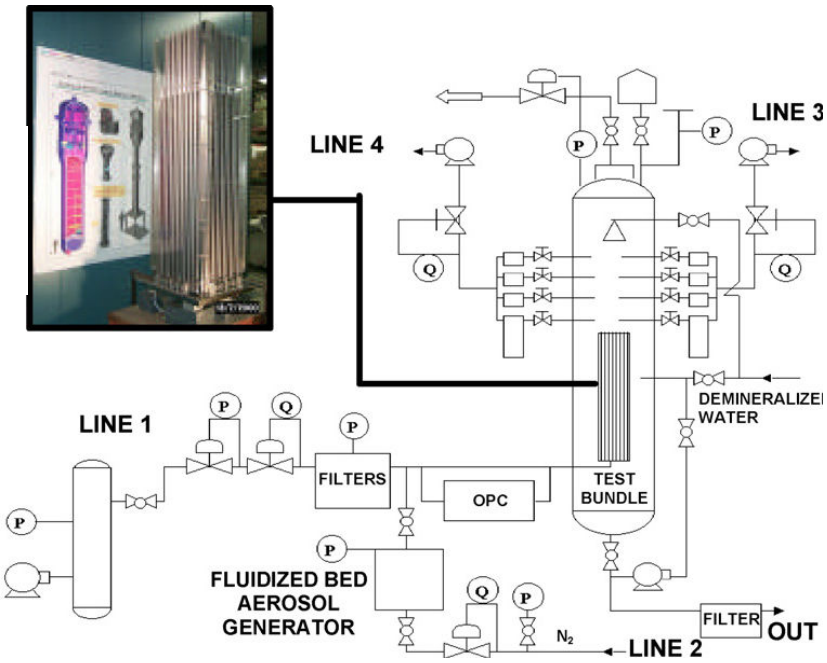

Fig. 4. Experimental schedule of the PECA-SGTR facility.

The main objective of the experimental campaign was to assess the influence of the inlet gas mass flow rate and the break configuration on particle retention. To do so, the inlet mass flow rate was varied from 75 kg/h to 250 kg/h and two break types were investigated "guillotine" and "fish mouth" at different locations and orientations (Table I). The remaining boundary conditions were imposed according to previous analysis performed with MELCOR and SCDAP/RELAP codes (Bakker, 2001; Güntay et al., 2002). TiO_2 was used as aerosol compound. The particle d_{ae} at the inlet of the rig ranged approximately from 5 to 7 μm.

Table I. Test matrix for EU-SGTR.

	Break type		Break location		Break orientation		Gas flow rate (kg/h)			
Test	Fish	Guillotine	Central	Periphery	Facing tube	Facing diagonal	75	100	150	250
1	X[1]			X	X					X
2	X[2]			X	X			X		
3	X[2]			X	X				X	
4	X[3]			X	X					X
5[3]	X[2]			X	X			X		
6	X[3]			X	X		X			
7	X[3]			X		X	X			
8	X[3]			X		X			X	
9	X[3]			X		X				X
10		X	X		X		X			
11		X	X		X				X	
12		X	X		X					X

Table II summarizes the major results of the experiments in terms of two variables: retention efficiency and decontamination factor.

Table II. Experimental results for EU-SGTR

Test Number	1	2	3	4	5	6	7	8	9	10	11	12
Φ (kg/h)	249.71	100.42	149.30	251.20	103.13	78.64	71.79	156.95	245.18	72.13	150.26	243.83
$\delta\Phi$ (kg/h)	18.72	8.74	20.24	15.16	11.59	15.41	13.62	22.01	22.16	10.22	8.04	20.59
Inlet d_{ae} (μm)	7.42	n. a.	6.72	6.69	n. a.	n. a.	3.37	6.95	7.13	5.16	6.7	4.87
Inlet GSD (μm)	1.80	n. a.	1.67	1.66	n. a.	n. a.	1.49	1.78	1.78	1.56	1.67	1.51
m_{in} (g)	96.61	108.55	113.47	133.53	74.87	65.12	56.60	182.73	186.35	49.52	120.36	133.52
m_{out} (g)	92.78	90.89	103.60	128.21	60.57	59.27	48.05	170.31	178.72	46.31	111.63	130.31
η (%)	3.96	16.09	8.65	3.98	18.84	8.93	14.98	6.77	4.08	6.45	7.24	2.40
$\delta\eta$ (%)	0.97	5.03	0.77	0.96	2.86	2.94	3.10	1.59	0.57	1.49	2.16	0.63
DF	1.04	1.19	1.09	1.04	1.23	1.10	1.18	1.07	1.04	1.07	1.08	1.02

The main results obtained may be summarized as follows (Herranz et al., 2006):

[1] 0.5 D Fish mouth
[2] 1.0 D Fish mouth
[3] Reproducibility test: repetition of test 2.

- The aerosol mass retained was always lower than a 20% of the total injected mass. The deposits distribution on the tube surfaces was not uniform. Their surface density decreased with radial distance from the breach (i.e., thicker deposits were observed at the closest tubes).
- At gas mass flow rates over 100 kg/h, the higher the inlet gas flow rate (Φ), the lower the mass fraction retained (η) regardless the breach type (Fig. 5). This trend has been correlated by:

$$\eta(\%) = \frac{\zeta}{\Phi^2} \quad \text{con} \quad \zeta = (1.81 \pm 0.7) \cdot 10^5 \left[\frac{\text{kg}}{\text{h}}\right]^2 \qquad (1)$$

From a quantitative point of view, the influence of the breach type, its orientation and location within the bundle had a secondary importance with respect to the flow rate one (this trend did not hold below 100 kg/h). Nevertheless, the mass distribution on the tubes surface was highly dependent on the breach type.

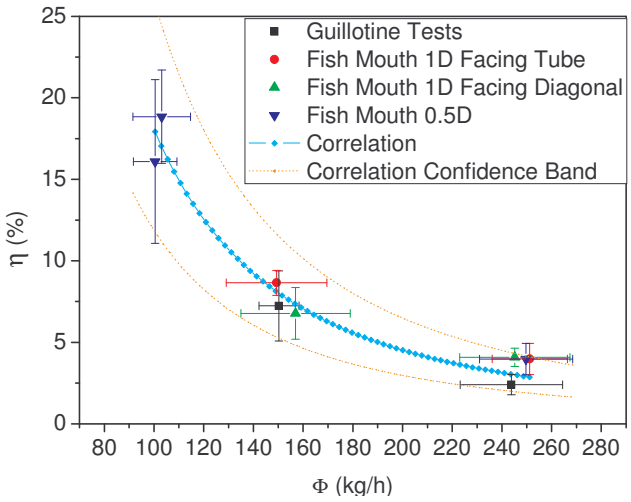

Fig. 5. Mass retention efficiency as a function of the inlet flow rate EU-SGTR.

In addition, most of the experiments showed that a fraction of particles leaving the bundle had smaller size than at the inlet (Fig. 6). This observation has a potential outstanding importance since deposition mechanisms are highly dependent on particle size. A possible explanation would be the particle fragmentation. TiO_2 particles could undergo high shearing stresses

created by particle-gas relative velocity. However, this phenomenon should be confirmed using an aerosol where cohesion forces between primary particles were more intense than those of TiO_2, as expected in accident conditions (Arreghini et al., 2000).

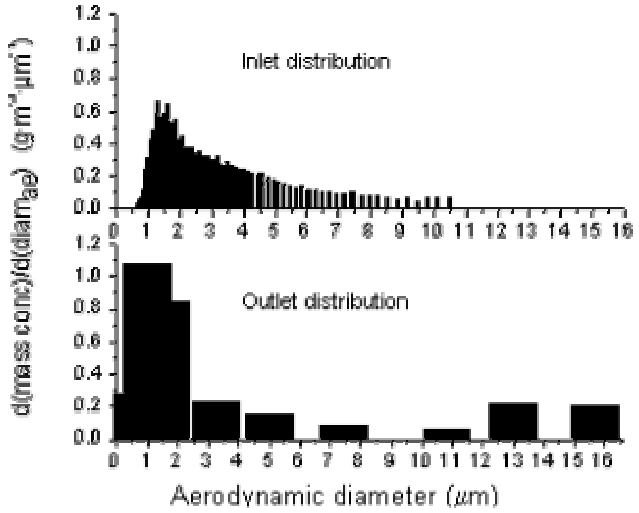

Fig. 6. Inlet Outlet mass concentration/aerosol distribution for Test 6.

The natural extension of the EU-SGTR project is the ARTIST project (Aerosol Trapping In a Steam Generator). ARTIST is a seven-phase international project (2003–2007) which investigates aerosol and droplet retention in a model steam generator under dry, wet and accident management conditions, respectively. This project seek fulfill the database and model development by applying the lessons learnt in the EU-SGTR project.

1.3. Thesis setting out: motivation, objectives and scope

1.3.1. Motivation

The motivation of present investigation rose from the EU-SGTR project results that showed that the secondary side of the SG had a potential retention capability of source term during a severe accident SGTR sequence. However, this retention capability had to be properly assessed. The break stage under dry conditions appeared as the most unfavourable scenario from the safety point of view (due to the absence of pool scrubbing) with the most potential retention capability (since the break stage is the region were flow velocity reached the highest values in the SG). In addition, the lack of specific

experimental data on the aerodynamic flow field in the break stage and the un-fulfilled characterization of the particle nature and inlet gas mass flow rate influence on aerosol retention in the scenario promoted the launch of this research.

The present research seek to get insights into the actual retention/decontamination capability of the dry SG during severe accident SGTR sequences by performing experimental separate effect studies in a mock-up of the break stage of the SG using aerosol particles with sizes close to the prototypical ones (i.e. around 1 μm, Arregini et al., 2000).

1.3.2. Objectives

The general objective of this research is to built up a consistent experimental database on aerosol retention in the break stage of the secondary side of a steam generator during severe accident SGTR sequences as well as understand the physics behind the depletion process to assist its modelling.

The EU-SGTR project showed that, under dry conditions, a tube breach would result in an aerosol flow stream emerging from the primary circuit into the secondary one. Particles carried by the gas would deposit on the tubes near the breach by different depletion mechanisms. These mechanisms are extremely dependent on the flow field across the tube bundle and on the "particle nature" (i.e. particle physical properties). Therefore, the aerodynamic characterization of the flow field in the scenario and the effect of particle nature on retention are of major importance for a thorough understanding and modeling of these mechanisms. Thus, the specific objectives of the PhD thesis are to get insights into the:

- Aerodynamic field influence in the aerosol retention in the tube bundle.
- Aerosol nature influence in the aerosol retention in the tube bundle.

The experimental database on aerodynamics will assist the validations of CFD codes in the scenario whereas the aerosol data will help the development of predictive aerosol retention models that might be introduced into current nuclear safety codes.

1.3.3. Scope

The scope of the PhD thesis is to study the break stage of the SG under dry conditions.
The research is focused in the lapse of the severe accident SGTR sequence when the fission products in form of aerosol reach the secondary side of the dry SG. In a generic sequence of the type of a SGTR with a consequentially stuck open safety relief valve, it would happen between 49 and 53 hours after

the start of the SGTR event (Auvinen et al., 2005). At this time the primary pressure in the SG is reduced from the nominal pressure (around 150bars) to 8 bars, and the secondary size is around 1.1 bars. Primary and secondary side temperatures are around 450K. In this research it was investigated the lower-bound flow rate conditions of the sequence: inlet gas mass flow rate through the breach was limited from 75-260 kg/h (i.e. primary to secondary pressure differences <3.5 bars).

Two types of prototypic breaches will be investigated in this thesis: a 360º axil-symmetric type breach, hereafter called guillotine type breach and an axial breach, hereafter called fish-mouth type breach.

Two types of particles of different nature will be used: TiO_2 fractal like agglomerates and SiO_2 solid spheres. These aerosol particles are not considered prototypical of the scenario, however their size is close to the one expected during a severe accident (Arreghini et al., 2000). Since the main objective of the research is to understand the aerosol retention mechanisms in the scenario, the particles were chosen to be easy to handle. Previous working experience with this materials and its insoluble nature were supposed to simplify both the measurements and the results analysis.

1.3.4. PhD approach

The PhD thesis is arranged in two phases according to nature of the test performed in each phase:

- Phase I, called CAHT (Ciemat Artist Hydrodynamic Tests), seeks the aerodynamic characterization of the breach jet expansion across the tube bundle.
- Phase II, called CAAT (Ciemat Artist Aerosol Tests) is aimed to get insights into the influence of particle nature on break stage aerosol retention efficiency.

The aerodynamic characterization of the flow field within the break stage of the bundle will be done via 2D PIV (particle image velocimetry) technique. Therefore, it is assumed that insights into the jet expansion across the tube bundle can be obtained from a bidimentional analysis. These tests will be faced in different series taking into account the different parameters presented before. The specific objectives of these tests are to:

- Map the whole aerodynamic field within the break stage.
- Link the near breach and far field flow pattern within the break stage.
- Identify the boundary conditions that affect the aerosol behavior.
- Provide a sound and reliable database to validate CFD numerical simulations.

The CAHT experiments require the design and manufacture of a new experimental set-up.

The aerosol retention will be investigated by a set of experiments (Ciemat Artist Aerosol Tests, CAATs). The main objective is to analyze the influence of two key variables for the aerosol retention processes at the break stage: the gas mass flow rate and the particle nature. The specific objectives of these phases are:

- To support and extend the aerosol retention data base generated by CIEMAT in the SGTR project.
- To provide specific insights into the effect of key variables, such as the particle nature and/ or the gas mass flow rate on the aerosol retention within the break stage.

Regarding aerosols test, aerosols used are assumed to be size-prototypical of severe accident SGTR sequences in order to assess conclusions useful for probabilistic safety assessments (PSA).

Chapter 2

Ciemat Artist Hydrodynamic Tests

2.1. Introduction

This chapter describes the main results of the CAHT program. The objective of experimental campaign was to characterize the aerodynamic flow field within the break stage of a steam generator during SGTR sequences under dry conditions. In order to do so, 2-Dimensional Particle Image Velocimetry (2D PIV) was used to measure the velocity field in an "ad-hoc" built-up facility called CAHT. Two types of breaches were investigated experimentally: a guillotine type breach and a fish-mouth type breach.

In the chapter, it is firstly presented the state of art of the aerodynamic problem investigated. Then, it is briefly introduced the fundamentals of the PIV measurement technique. After that, it is described the CAHT facility. The next two sections present the guillotine and fish-mouth experiments and their results. The following one discusses the PIV measurement technique in light of the results. Finally the last section presents the uncertainty analysis of the measurements.

2.2. State of art on the aerodynamics of jets from a tube breach across a tube bundle.

The aerodynamic scenario outlined above is complex and specific. No previous investigations were found in the open literature. However, investigations carried out by other authors on scenarios with some similarities were reviewed to support the present research. In particular, a survey has been conducted on: turbulent radial free jets (Abramovich, 1963; Schwarz, 1963; Heskestad, 1966; Rajaratman, 1976; Witze & Dwyer, 1976), jets from elliptical or rectangular orifices with high aspect ratio (Rajaratman 1976; Quinn 1989; Hussain et al., 1989; New et al. 2003, 2004; Lee et al. 1994, 2000), plane jets in cross-flow (Girshovich, 1966; Choi & Wood, 1966), impinging jets on cylinders (Schuh & Pearson, 1964; Sparrow & Lovell, 1980; Cornaro et al, 1999), cross-flow streams in a tube bundle (Simoin & Barcouda, 1988; Meyer, 1994; Balabani & Yianneskis, 1996; Paul et al, 2007) and axial flow streams in a tube bundle (Seale, 1980; Hooper, 1980; Rowe et al, 1974).

The basics of turbulent jets were compiled and reviewed by Abramovich (1963), defining an entry region (where the flow exiting the nozzle interacts with the medium generating the transition of the initial profile into a final or developed one) and a fully developed region (where the initial conditions do not affect any more and jet evolves in the medium without any external influence keeping self-similarity in the profiles). In radial free jets, Schwarz (1963) and Rajaratman (1976) agree on stating that the maximum velocity in the fully developed region is inversely proportional to the distance from the inlet point. The spreading rate, however, is directly proportional (Schwarz, 1963). Regarding radial jets generated from the impingement of two opposing round jets, Witze and Dwyer (1976) found that a constrained radial jet ($Re_H \sim 2 \cdot 10^3$ and H/D=0.005–0.06) spreads at the same rate as does the plane jet, while

the free impinged radial jet (Re_H~$2 \cdot 10^5$ and H/D=20–42) spreads at a rate more than three times as fast.

In elliptical and rectangular jets, central velocity evolves from a decay similar to plane jets to the one shown by asi-symmetric round jets. Lee et al (2000) indicated that the azimuthal curvature variations of the elliptical vertical structures generated by this type of jets enhances jet mixing and increase the gas entrainment. Close to the nozzle the jet spreading rate along the minor axis plane is much greater than that of the major axis plane producing the "axis-switching" of orientation downstream.

Cross-flow plane jets for incompressible fluids where studied by Choi and Wood (1966). They found that for different initial jet angles (9º, 17º, 25º and 45º), the growth rate of the jets on either side of the jet axis resulted to be unequal and the growth of the total width with respect to the jet axis coordinate was not linear. For initial jet angles smaller than 25º the trajectories of the jet axis were well correlated by the system $x^*/(\alpha^2\delta_o)$ vs $y^*/(\alpha^2\delta_o)$, where α is the jet to free stream velocity ratio varied from 2.6 to 9.0 and do is the thickness of the jet at the nozzle.

Regarding free jets impinging on cylinders, Schuh and Persson (1964) found that for a specific ratio of jet-to-cylinder diameter and distance to the nozzle, transport phenomena were considerably enhanced with respect to parallel flow over the cylinder surface at $Re_D=2–6 \cdot 10^4$. This result is explained by the ability of thin jets to adhere to curved surfaces (Coanda effect) and the high intensity of turbulence in the jet.

Finally the aerodynamics of a flow stream across a tube bundle have been widely studied for flow stream perpendicular to the tubes axis specially for heat transfer applications and for fully developed flow stream in axial direction for nuclear reactors applications.

Regarding the first problem, it worth to remark the work of Paul et al. (2007). They measured mean velocities, turbulence intensities and Reynolds stresses in a cross-flow staggered tube bundle using PIV at different Re_D (4800–14400). They found that the flow becomes Reynolds number non-dependent and spatially periodic in the streamwise direction after a developing region. They also pointed high shear rates in the wake region with peaks over 100% in turbulence fluctuations. In this region, the pressure gradient terms in the RANS equations resulted to be balanced by the Reynolds stress terms whereas outside it they are balanced by the convective terms.

Regarding the second problem, Seale (1982) investigated fully developed flow in the subchannels formed by a rod bundle with a p/D=1.2 ($Re_D=8.3–34.7 \cdot 10^4$). Detailed measurements of axial velocities, secondary velocities and Reynolds stresses were made using a rotated hot wire technique. He found friction factors based on the equivalent hydraulic diameter to be 2% lower that for pipe flow. The distribution of axial velocity near the walls (normalized with the local friction velocity) could be expressed by a inner law of the wall for $y_+ \leq 1500$. The maximum secondary velocities were about 1.5% of the bulk axial velocity. Reynolds stresses and the mean turbulence

kinetic energy were similar to those observed in pipe and twodimensional channel flows and was correlated using the axial-velocity fluctuations normalized with the local friction velocity.

Insights into the turbulence behaviour through the subchannels of a rod bundle were obtained by Hooper (1980), Rowe et al. (1974). They found that turbulence structures for axial fully developed flow through the subchannels depend on the pitch-to-diameter ratio p/D. For fairly open ducts p/D≥1.2 the distributions of the three components of the normalized turbulence intensity normal to a wall are similar to those measured in circular ducts or between plane surfaces. For more closely spaced arrays the turbulence structure, especially in the rod-gap region, departs markedly from the pipe-flow distributions. This behaviour is generally attributed to the increasing strength of secondary flows as the rod-gap spacing is reduced. In the gap region high values of axial intensity were observed, which became more energetic as the rod gap was decreased.

2.3. Fundamentals of the PIV measurement technique

PIV is probably one of the most powerful experimental measurement techniques used in fluid dynamics nowadays. It is based on recording the position of images produced by small tracers suspended in the fluid at successive time instants. The results provide the instantaneous and non-intrusive visualization of the two-dimensional streamline pattern in unsteady flows as well as the quantification of the velocity field over the entire plane. The procedure of the PIV measurement technique will be described as follows:

First a selected plane or surface within the flow field is generated (Fig. 7). The orientation of this plane is such that it contains the dominant flow direction (if one exists). The plane itself is created by embedding it with small tracers and illuminating them with a beam of intense pulsed light.

The beam is shaped as a thin sheet by an optical setup and the light scattered by the tracer particles in the illuminated plane provides the moving pattern. The size of the particles is approximately 1 to 10 μm. This size is small enough so that particles do not significantly interfere with the flow, but they are large enough to scatter the laser light. The concentration of tracers for PIV lies between 10^{10} and 10^{11} particles per cubic meter, so that the images consist of individual particle images.

A camera, placed perpendicular to the plane, records the intensity distributions scattered by the particles. This recording is done by acquiring two instantaneous images in two separate frames. The time interval, Δt, is chosen so that displacement between images can be determined with sufficient resolution and, at the same time, it is short enough to avoid particles with an out-of-plane velocity component leaving the light sheet between subsequent illuminations (Raffel et al., 1998). The tracer displacement should be large enough to resolve their motion, but less than the smallest

fluid macro-scale. The underlying assumption is, as stated before, that the tracers closely follow the fluid motion with minimal lag.

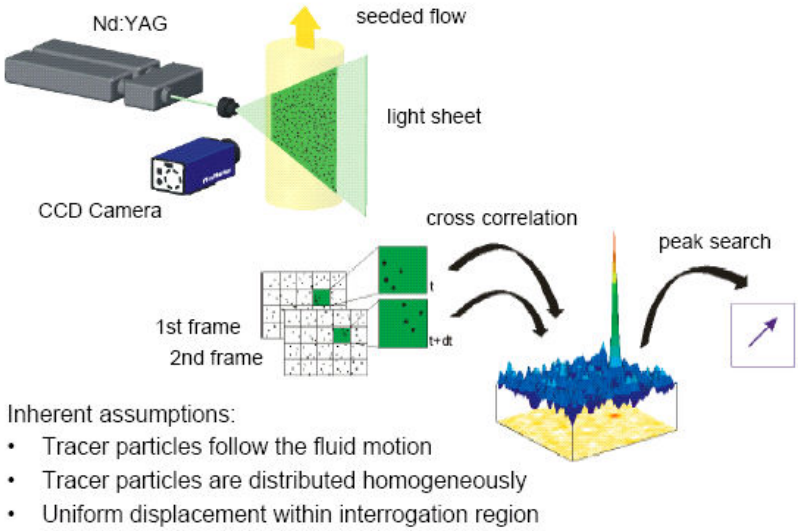

Fig. 7. PIV description.

The "local" measured fluid velocity forms an average over many tracers contained in a measurement volume or window (Fig. 7). These windows are usually regularly spaced and their size determines the spatial resolution.

After the images are obtained, the light intensity distributions inside analog windows of consecutive images are correlated to find the displacement between them (Fig. 7) using a cross-correlation algorithm.

A simplistic explanation of the correlation operation is given by Moens (1995): suppose that the pictures are transparent and that the particles are just black dots. When placing the superposed pictures in front of a light source and looking through them, doublets (pairs) appear. If one picture is shifted to the other so as to make most of the particle images coincide on top of each other, the amount of black dots that are visible will be minimized. When this happens, the linear shift that was imposed on the first picture is equivalent to the displacement of the tracers of one image to the other. Plotting the amount of overlap for each possible shift results in the correlation-map (Fig. 7).

The correlation-peak is sought since it gives information concerning the necessary shift, i.e. $\Delta x'$, to let a maximum overlap of the windows. This displacement is the volume averaged.

Assuming the time-step Δt is small enough, the velocity is calculated by using finite differences, e.g. the first order Euler approximation,

$$V = \frac{\Delta x'}{\Delta t} \tag{2}$$

2.4. CAHT facility

2.4.1. Motivation

The use of the PECA vessel CAHT experiments suffered from some drawbacks concerning the optical access of the PIV system that prevented its effective use. To overcome them, a new experimental rig was designed to carry out the experiments out of the PECA vessel and map the aerodynamic field in the break stage.

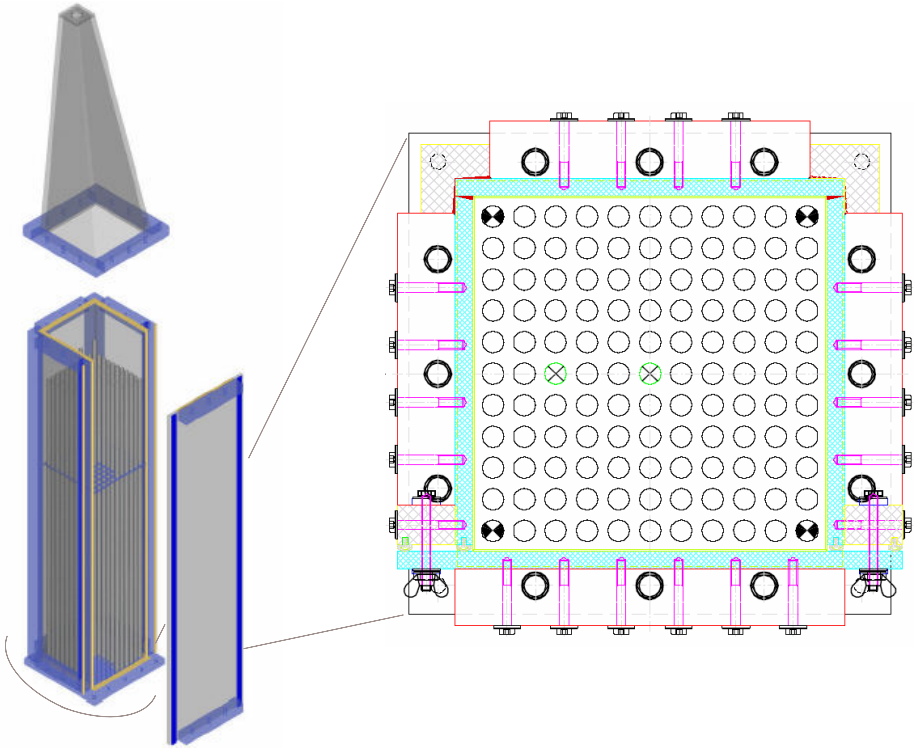

Fig. 8. 3D Side view of the new facility and plan view of the central body.

2.4.2. Technical design criteria

The facility was designed following two main guidelines:

- To enhance PIV measurements quality.
- To reduce the external distortion of the flow field in the break stage due to the facility arrangement.

On one hand, the facility was made of transparent materials to maximize the optical access of the PIV laser-camera system to the test section and improve the configuration possibilities during the measurements. Previous experiments showed that the high reflection of the laser in the steel reduces the quality of the PIV results especially near the tube surface. In the CAHT facility the transparent walls and tubes permited the laser sheet to penetrate and reduce the reflection and the general light scattering on their surface.

On the other hand, the geometry design of the CAHT facility tried to minimize any possible turbulence enhancement generated externally after the break stage that could eventually affect the measurement volume upstream.

2.4.3. Facility description

Two main parts form the facility (Fig. 8): a central body that contains the bundle and the upper nozzle that collects the aerosol stream at the exit of the bundle. Both are entirely made of methacrylate.

2.4.3.1. Central Body

The central body is basically a rectangular prism 1.7 meters high built on a $0.34 \times 0.34 m^2$ base (Fig. 8). The support structure (colored in blue in Fig. 8) connects three vertical walls of 15mm thickness (colored in grey in Fig. 8) that forms a unique body in U shape, where the door (the fourth wall) is screwed using stainless steel billets (colored in dark blue in Fig. 8) to reinforce the joints.

The whole prism is screwed on the base where the bundle is set. This base is also made of methacrylate, starting from a one-piece 60mm thick sheet, mechanizing it to its final dimensions (Fig. 8).

One meter over the tube base, there is a support plate that delimits the break stage. It is a 5mm plate filled with trefoil holes to support the tubes (Fig. 9). In the CAHT design the support plate is made from a 5mm polycarbonate sheet. Polycarbonate is slightly less transparent than the methacrylate but it is a material much more easily to mechanize in the workshop and reduces the toughness during the trefoil holes generation.

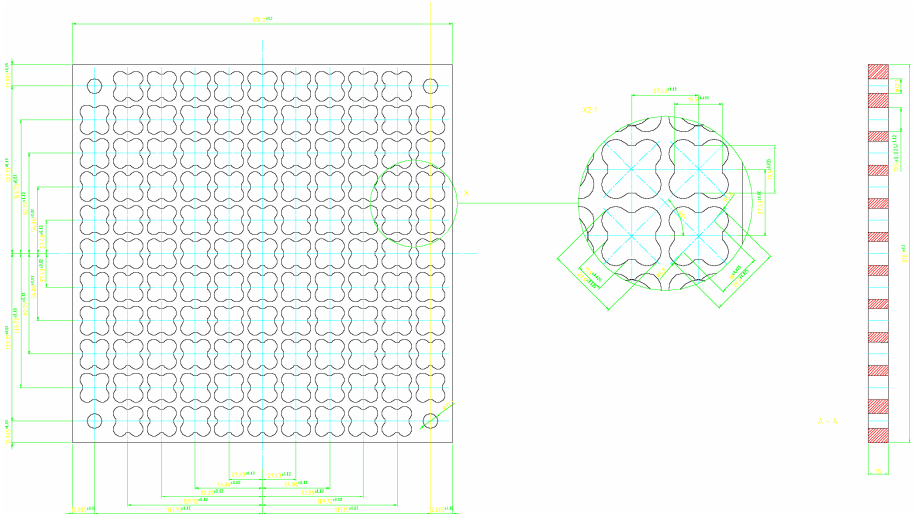

Fig. 9. Sketch of the middle support plate.

The facility permits the substitution of some of bundle steel tubes for others made of methacrylate (Fig. 10). These tubes were used to study the flow behavior near its surface since their transparency reduces the laser reflection on their surface and improves considerably the PIV imaging quality.

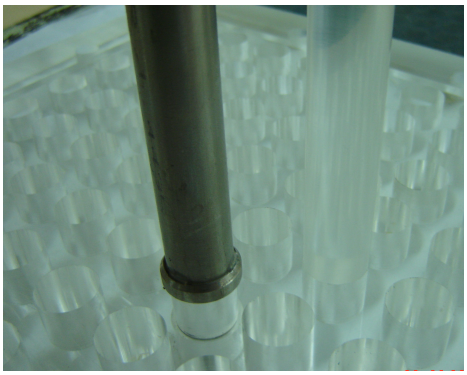

Fig. 10. Transparent tubes.

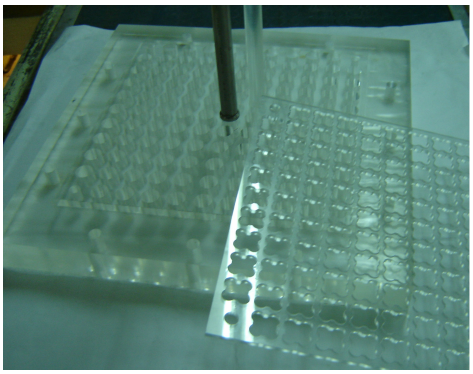

Fig. 11. Methacrylate base and support plate

Fig. 11 shows a picture of the tube base and support plate made of transparent materials. They permitted the laser sheet to be generated axially in vertical planes.

Finally, all screwed joints in the facility structure and walls (i.e. central body-base joint, door, upper nozzle-central body joint,) are hermetically sealed with rubber strip (colored in yellow in Fig. 8) to avoid losses during operating conditions.

2.4.3.2. Upper Nozzle

The upper nozzle consists on a squared pyramid of 1.08m high with a vertical wall (Figs. 12 and 13). It is totally made of methacrylate and it is screwed to the central body though its square base. It also contains a door to permit the tube bundle mounting and extraction. The vertical wall in the nozzle permits the optical access to the central tube of the bundle from a zenithal position for whether the CCD camera or the laser sheet without the interference of the air-extraction duct, which is placed laterally.

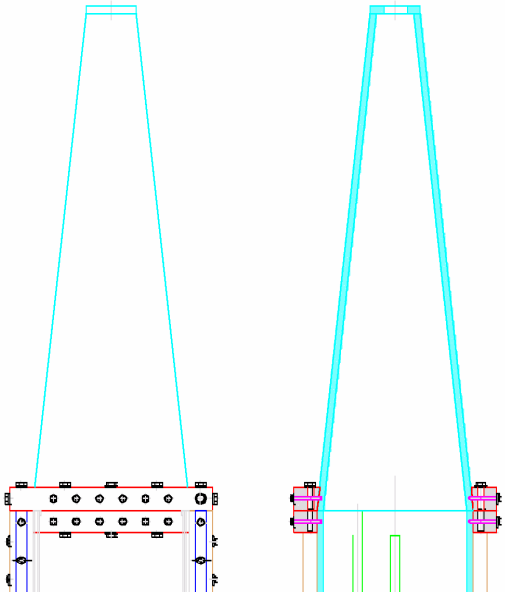

Fig. 12. Front and cross section view of the nozzle.

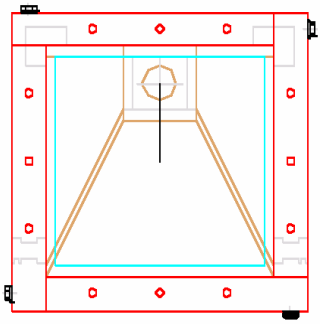

Fig. 13. Plan view of nozzle.

The air-extraction duct connected to the end of the nozzle has an inner diameter of 51mm. The velocity level estimated in that tube for the maximum mass flow rate conditions in the CAHT tests (i.e. 250 kg/h) is lower than Ma<0.3. So, nor blockage neither compressibility effects are expected in the extraction.

The facility accounts for the substitution of some of the bundle steel tubes for others made of methacrylate (Fig. 10). These transparent tubes could eventually permit the laser to penetrate through the tubes and reach different places in alternative configurations, keeping intact, at the same time, the geometry of the bundle and not modifying the aerodynamic field inside it.

Finally, Fig. 14 shows the 2D sketches of the CAHT-ARTIST facility. The detail planes of the facility can be found in the Appendix I.

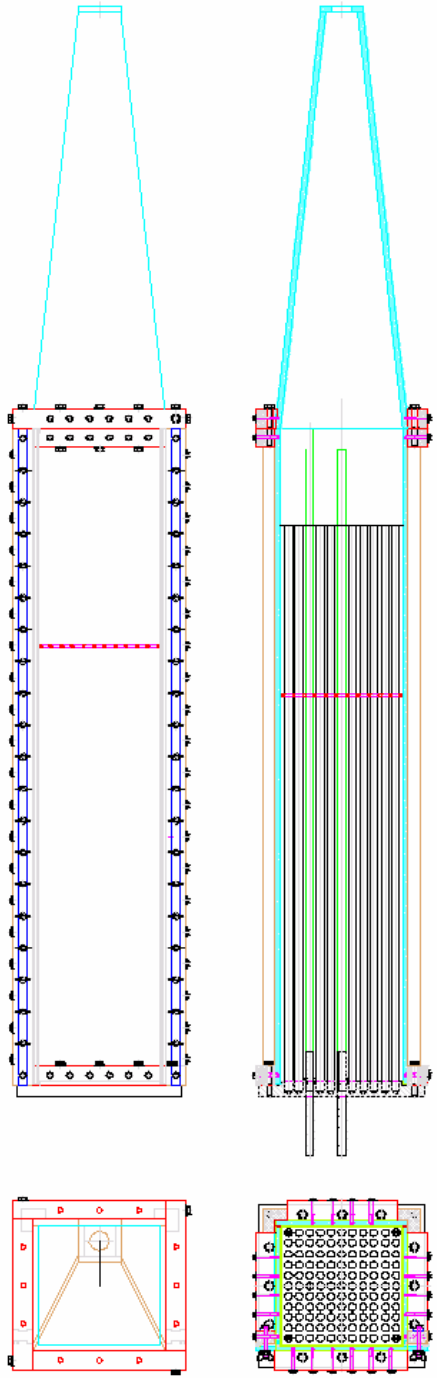

Fig. 14. 2D sketches of the new CAHT-ARTIST facility.

2.5. Guillotine experiments

This section summarizes the major insights gained from 2D PIV measurements into the aerodynamics of a radial jet entering the secondary side of the steam generator from a guillotine tube breach. In particular, the effect of the presence of tubes and the influence of the gas mass flow rate on the jet behavior were explored. Given the importance of tubes around the breach in aerosol retention, specific attention was paid to the jet behavior in the space between the broken tube and the first neighbor tubes. Free jets (i.e., those emerging from the broken tube in a "tube-free" space) was used as a reference to which compare "in-bundle" measurements.

2.5.1. Experimental set-up and measurement procedure

2.5.1.1. Facilities set-up

The experimental campaign was carried out in two phases. The first one was devoted to study aerodynamics of a free radial jet from a broken tube, whereas the second one was focused on investigating the jet behavior through a tube bundle. They were conducted in the PECA (Fig. 15) and the CAHT (Figs. 16) facilities, respectively. Both set-ups shared the main experimental systems: steam generator mock-up, air supply system, PIV hardware, aerosol generator, and data acquisition system.

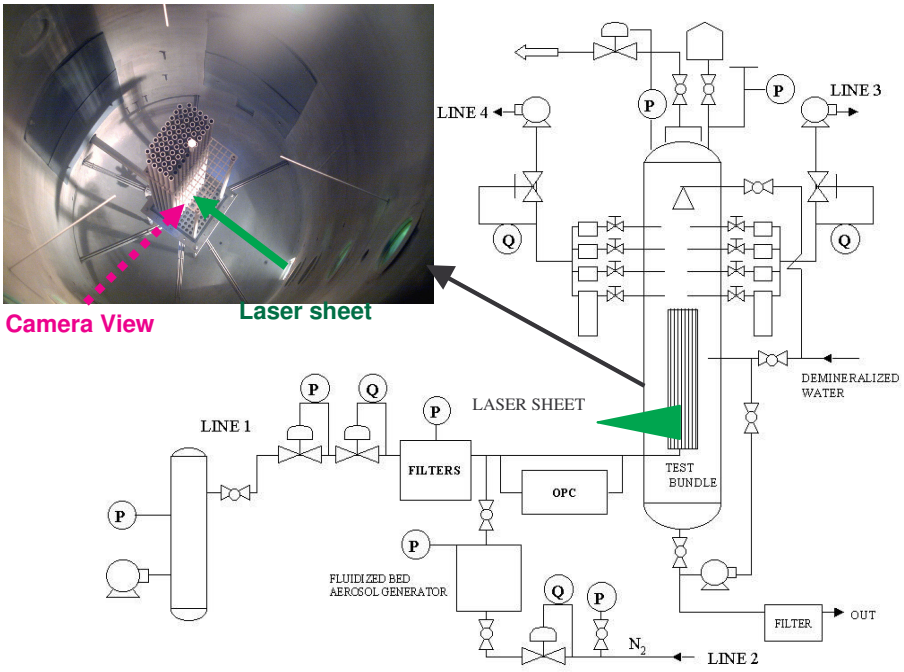

Fig. 15. Scheme of the PECA facility and bundle configuration in the vessel.

The mock-up is a scaled-down assembly simulating the break stage of the secondary side of the SG. It consists of a square array of 11x11 tubes (330 x 330 x 1000 mm), supported by an upper and a lower plate. This limited size was backed by CFD analyses (Herranz el al., 2005), where it was shown that the jet hardly reaches the 4^{th} neighbor tube. The dimensions of the tubes and the support plate are identical to those used in a stage of a real SG of a nuclear power plant (Güntay et al, 2004). The tubes are 19.05 mm in diameter with a pitch-to-diameter ratio in the bundle of p/D=0.4. The breach is of a guillotine type (axis-symmetric type), with an open area equivalent to the circular section of one tube. The breach height (Fig. 17) is $H=0.24 \cdot D$ and it is placed in the central tube at 0.24 m from the base. The flow is injected into the broken tube through the base. Since the top end of the tube is closed, the flow is forced to exit through the breach and to expand across the bundle.

The PECA configuration made it feasible to avoid any bounding constraint, whereas the CAHT one improved considerably the optical access. Some tubes were substituted for transparent ones to reduce the laser sheet reflection on their surface and to improve the imaging closer to it. Figs. 16 and 17 indicate the laser–camera arrangement in each set-up. As shown, the laser sheet was generated from a side of the PECA vessel whereas it entered the CAHT frame from the bottom and extended upwards. Both of them contained the axis of the broken tube.

An 18.5 kW compressor keeps an air supply tank at 6 bars. This tank feeds the injection line where the air is filtered and controlled through pressure and flow rate valves to achieve the desired conditions. A Bourdon manometer and a Pt-100 temperature sensor measure the inlet tube conditions upstream the breach. An additional blower placed downstream the bundle control the pressure to ensure atmospheric conditions in the bundle. These devices and variables are controlled and logged every 700 ms through the PLC of the laboratory.

An Nd: Yag, 44mJ pulse laser of 532 nm wavelength was used to illuminate the flow field at 15 Hz. Three different lenses (28 mm, 135 mm and 300 mm F2.8) were used with a cross-correlation CCD camera of 1660x1200 pixels. The Insight3G TSI software was used for processing the PIV images with a 32x32 pixels final interrogation window, 50% overlap, iterative deformation processing and Gaussian subpixel interpolation. The mean flow and turbulence statistics were computed using an own-developed post-processing script.

Titanium dioxide (TiO_2) was used as seeding material. The aerosol generator is based on fluidized bed technology and permits the injection of 10 kg/h N_2-seed-flow at high manometric pressure (up to 1.5 bars). It supplies micronic particles from nanosized powder.

Fig. 16. CAHT configuration.

Fig. 17. Guillotine break used in the CAHT experiments.

2.5.1.2. Experimental test matrix and test procedure

The specific objective of the experiments was to assess the effect of the presence of tubes and the influence of the gas mass flow rate on the jet behavior near the breach.

Table III shows the main variables and non-dimensional numbers characterizing the SGTR sequences along with those prevailing in the PECA and CAHT experiments. The magnitude of gas velocities and other SGTR features were determined by simulating SGTR severe accident sequences with nuclear safety codes (Bakker et al., 2001; Güntay et al., 2002). It is worth to note that velocities resulted in gas mass flow rates ranging from 75 to 250 kg/h. No thermal and steam concentration gradients were predicted, so that air was used as the working fluid.

Table III. Variables and non-dimensional numbers characterizing SGTR scenarios.

	d_p (μm)	D (m)	Vtheo (m/s)	Re_D	Stk	Ma	Re_p^2/Stk
SGTR[4]	1 – 10	10^{-2}	10 – 400	$10^4 – 10^6$	$10^{-2} – 10$	0.03–1.5	$10^2 – 10^3$
CAHT-PECA	1 – 10	10^{-2}	10 – 300	$10^4 – 10^5$	$10^{-2} – 10$	0.03 – 0.9	$10^2 – 10^3$

Table IV and V presents the test matrix set-up and the experimental pressure conditions used respectively. A total of 67 experimental runs were conducted in 8 test series. A good number of tests were used to confirm test reproducibility. As said above, two types of experiments were carried out: “free” and “in-bundle”. The gas mass flow rate interval was explored by setting 8 different values. PIV measurements were performed in the first, second and third gaps between tubes, right at the vertical plane containing the axes of the broken tube and the closest neighbor one. In the axial direction, data were taken at the height of the breach (0 mm) and at three additional locations to follow jet development.

Fig. 18A shows a bundle top view with the measurement areas investigated with the PIV technique. The green line represents the laser sheet generated axially upwards from the base plate. The red arrows represent accessible zones for the PIV camera from outside the bundle. Each zone corresponds to a possible PIV camera view.

[4] Low inlet gas mass flow range from 75- 350 kg/h.

Table IV. Experimental matrix for guillotine experiments.

Test serie	Jet type		PIV location				Inlet gas mass flow rate [kg/h]							
	Free	In-bundle	Radial			Axial [mm over breach]	75	100	107	139	150	180	203	254
			1st gap	2nd gap	3rd gap									
1	x		x	x	x	0			x	x			x	xx
2		x	x			0	x	x	x	x	x	x	x	x
3		x	x			0	xx	x	x	xx				
4		x			x	0	x	x	x	x	x	xx	x	xx
5		x	x			0	xx	xx	x	x	x	x	xx	x
6		x			x	30	x	x	x	x	x	x	x	xx
7		x	x			515	x	x	x	x	x	x	x	x
8		x		x		15	x	x	x	x	x			

Table V. Pressure conditions for CAHT.

Absolute Pressure	Jet type		Inlet gas mass flow rate [kg/h]							
[bar]	Free	In-bundle	75	100	107	139	150	180	203	254
P_{in}	x					1.2	1.4			2.1
P_b	x					1.1	1.1			1.4
P_{in}		x	1.2	1.3	1.3	1.5	1.6	1.9	2	2.2
P_b		x	1	1.1	1.1	1.1	1.1	1.2	1.2	1.2

Fig. 18B shows a side view of the bundle where the PIV mappings zones are indicated. A red rectangle locates the break in the bundle. The green line represents qualitatively the jet central line trajectory. The red frames place the PIV camera views for the investigation.

A total of 620 images (310 pairs) were recorded during each run. This was estimated from the study of Lourenço (1982) to be enough to achieve statistically convergence of mean flow field data. Tests were performed once control variables reached steady state. Tests were carried out at room temperature.

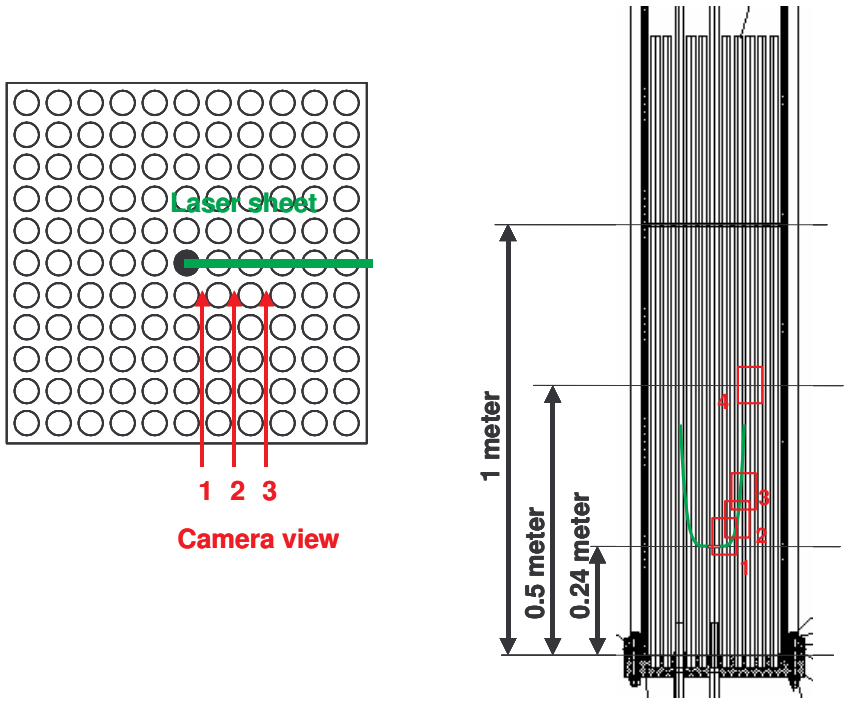

Fig. 18. Broken tube locations and accessible PIV mapping zones.

2.5.1.3. Post-processing script.

The post-processing script called PUA (Post-processing and Uncertainty Analysis) is a tool designed to analyze the data generated from the PIV measurements. PUA was designed to run under Matlab and is structured in two main modules: TIC and PUA.

The first one called TIC (Turbulence Intensity Calculus) open, read and store on variables the data from the `*.vec` files (around 310 per test) generated as a result of the processing of the PIV images with INSIGHT 3G program. From velocity data obtained (*u, v*), TIC computes their main statistical moments that permits to characterize turbulence in the measured area. These moments are: mean velocity field, standard deviation velocity field, skewness velocity field (i.e. statistical moment of third order), flatness velocity field (i.e. statistical moment of fourth order), turbulence intensity field and the 2D Reynolds stress field (i.e. $-\overline{u' \cdot v'}$).

The second module, PUA reads the variables computed by TIC as well as the two statistical data files generated by INSIGHT 3G (`*.std` files) that contain an averaged of the `*.vec` files. One of them was obtained taking into account the special calibration performed before the measurements (i.e. velocity is expressed in m/s units) and the other was obtained without taking into account the special calibration (i.e.

velocity is expressed in pixel/s units). These two fields are needed to compute the uncertainty velocity field. After reading the files, PUA computes the uncertainty velocity field (following ISO (1995) procedure), and other variables derived from velocity such as: velocity vector angle field, uncertainty field of the velocity vector angle, Ma field, Re_D field, velocity divergence field, vorticity field and residence time field.

After that PUA filters the data according to physical criteria imposed by the user basically on velocity and signal-to-noise ratio variables. This filtering is needed since eventually INSIGHT 3G software gives non-physical values associated to particles attached to surfaces, limitations in the cross-correlation PIV algorithm, and/or other factors. After the filtering, the program plots and stores the variables. In Appendix II are detailed the definitions of the main variables computed in the post-processing scripts.

2.5.2. Results and discussion

The main kinematic variables derived from the PIV measurements were: mean velocity field, turbulence quantities, jet center line trajectory and jet spreading rate. Results will be discussed on the basics of a cylindrical coordinate system (r, z, θ) centered on the broken tube axis in the middle of the breach height.

2.5.2.1. The radial free guillotine jet

The radial free jet near the breach was characterized by using the PECA configuration (Fig. 15). Velocity measurements were obtained in a vertical plane extended radially from the broken tube axis (60x70 mm). Fig. 19 illustrates the particular case of 107 kg/h. The jet was observed to enter the domain with an initial deflection angle that grows with the distance from the breach. Such an upward trend is due to three main effects: the initial vertical component of the jet at the breach exit, the lost of radial momentum as the jet penetrates and the drift caused by the gas exit location at the top of the vessel. The resulting pseudo-parabolic jet gives rise to a non-symmetric gas entrainment around it, where suction is more intense at the concave side. As a consequence, a recirculation vortex is set up at inner side of the parabola at (2.5·D, 2·D, 0) in cylindrical coordinates. This location is nearly invariable with gas flow rate.

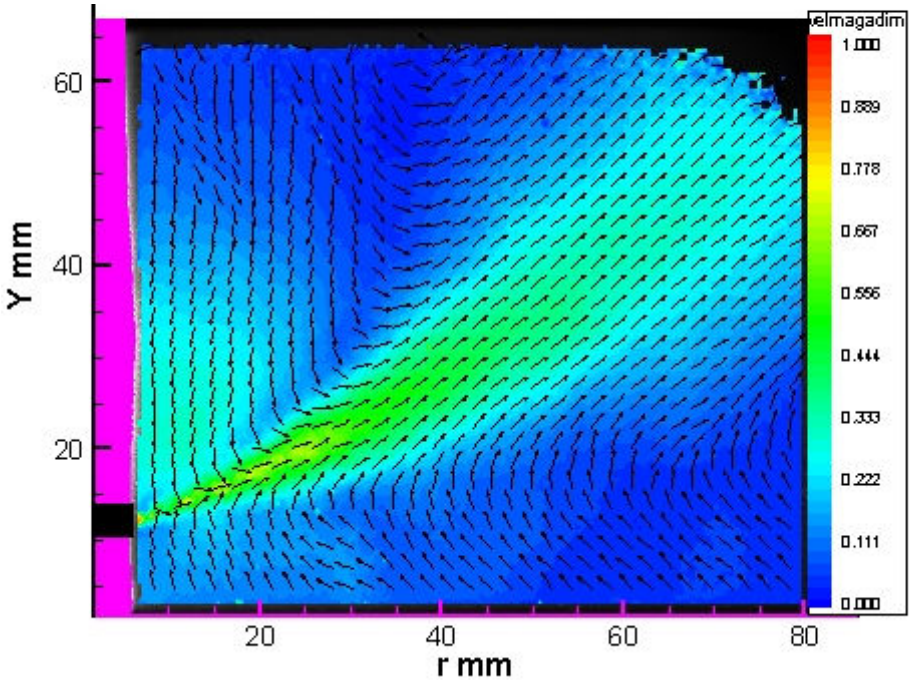

Fig. 19. Normalized mean velocity field for 107 kg/h free radial jet.

The jet trajectory was defined through the locations where the jet achieves the maximum velocity. In the region explored, the initial angle and jet trajectory remain nearly invariable for the range of gas mass flow rate investigated. Trajectories follow a parabolic curve as shown in Fig. 20, which can be correlated in a dimensionless way by the expression:

$$\frac{z}{H} = 0.0129 \cdot \left(\frac{r}{H}\right)^2 + 0.255 \cdot \left(\frac{r}{H}\right) - 1.3558 \tag{3}$$

Fig. 21 shows the jet dimensionless velocity profiles over the normal direction to the jet axis at several radial distances for the 107 kg/h case. All over the trajectory, the "jet core" (i.e. region where $\zeta/b<1$) shows a Gaussian distribution. This distribution agrees with the ones found in the literature for other jet topologies, like non-deflected radial jets (Witze and Dwyer, 1976) and oblique cross flowing jets (Choi and Wood, 1966). However, regarding the "jet rim" ($\zeta/b>1$), profiles are asymmetric and, depending on the radial distance, two regions can be differentiated as in Fig. 19: the "entry region" and the "fully-developed region". In the former, velocity profiles are still under development and gas entrainment from the upper region affects them noticeably. In the latter, the gas suction effect is negligible and the dimensionless velocity profiles become self-similar. Therefore, differences vanish at a certain distance from the entry point.

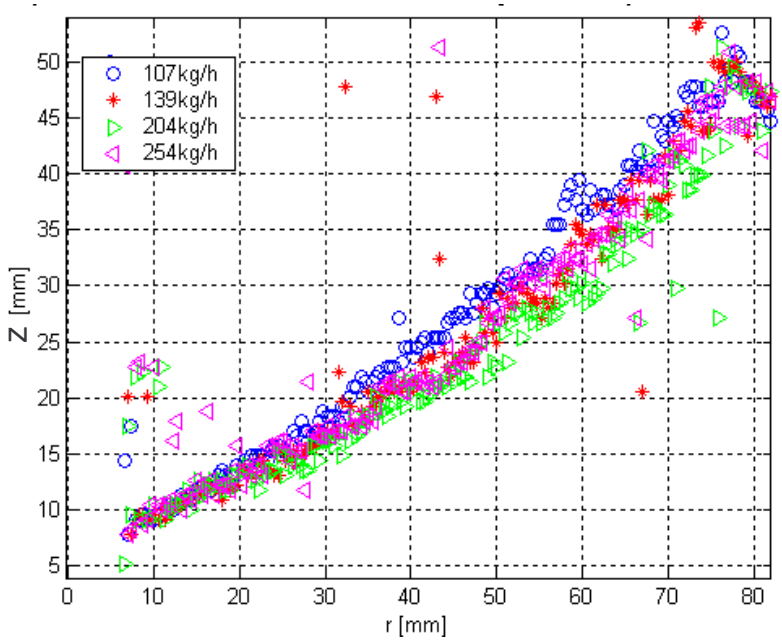

Fig. 20. Jet trajectory with the radial distance to the breach.

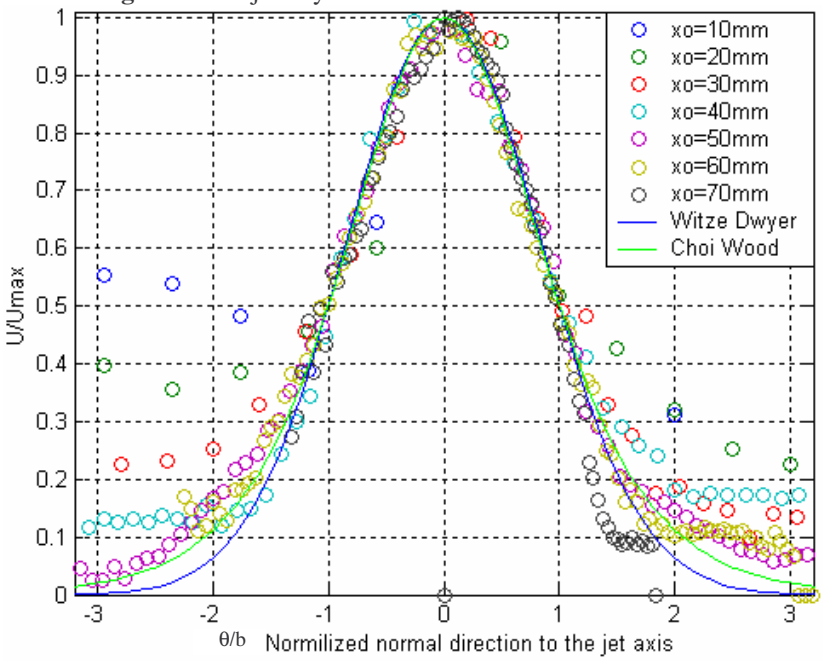

Fig. 21. Velocity profiles along the jet center line for different radial distances (107 kg/h).

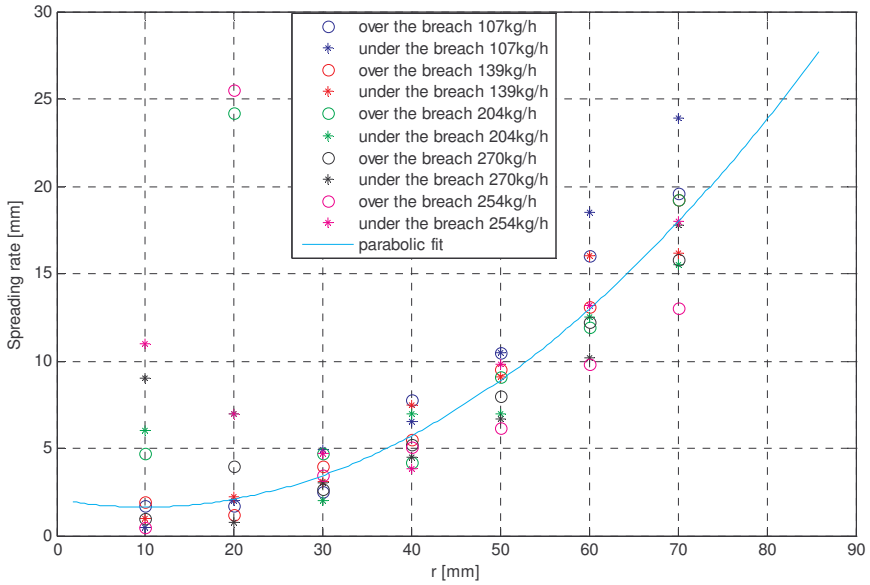

Fig. 22. Spreading rate vs radial distance.

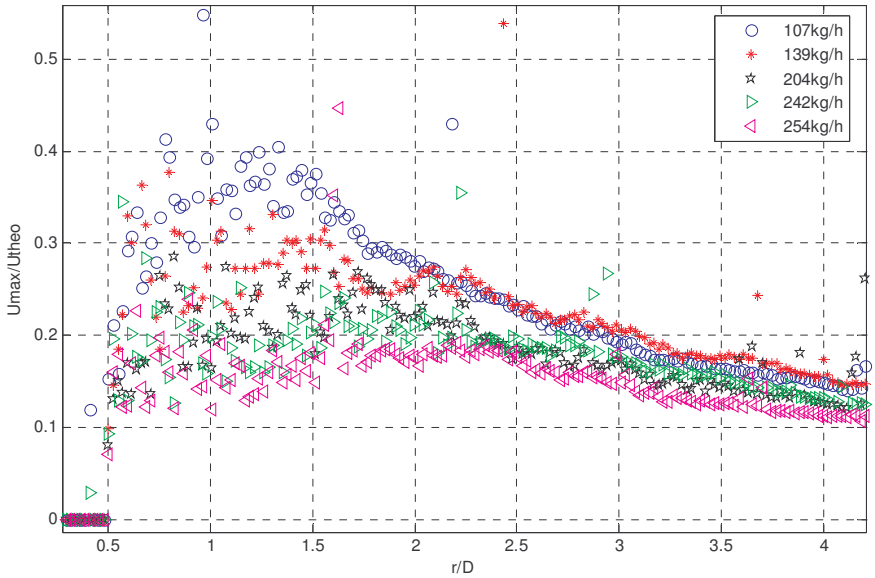

Fig. 23. Maximum velocity evolution along the radial distance to the origin.

Asymmetry of the "entry region" is promoted as gas mass flow rate increases, whereas the "fully-developed region" hardly changes. This observation is further illustrated through the spreading rate and maximum velocity evolutions (Figs. 22 and 23, respectively).

The higher the flow rates, the more noticeable the discrepancies between spreading rates at both sides of the jet core (upper and lower) in the "entry region". In the "fully-developed" region (from r=1.5·D on), however, spreading rates collapse within the data uncertainty band; namely, they become independent of the inlet gas mass flow rate. The evolution describes a parabolic curve as shown in Fig. 22:

$$\frac{SR}{H} = 0.0207 \cdot \left(\frac{r}{H}\right)^2 - 0.1316 \cdot \frac{r}{H} + 0.564 \qquad (4)$$

The maximum jet velocity accelerates until reaching its maximum value downstream the breach, in the "entry region". Then, in the "fully-developed region" it decreases smoothly along the jet center line. The radial location of the maximum moves away from the breach as the inlet gas mass flow rate increases. This is a consequence of the flow expansion generated by the pressure drop at the breach that is directly proportional to the mass flow rate.

The normalized velocity increases as the mass flow rate decreases which suggests that the dissipation of mechanical energy at the breach is reduced, in relative terms, when the mass flow rate increases. Therefore, the effect of the breach is to "homogenize" the jet, since it reduces the initial velocity differences at the outlet affecting more the jet at high mass flow rates than at low mass flow rates.

2.5.2.2. The guillotine "in-bundle" jet

Jet expanding in a tube bundle was investigated using the CAHT configuration (Fig. 16). The results are presented in two sections: one related to the insights gained into the global flow behavior across the tube bundle and another presenting the detailed analysis performed of the jet behavior close to the breach.

2.5.2.2.1. Global jet behavior

Insights into the jet evolution across the tube bundle can be extracted from the qualitative analysis of the seeding deposits at the tube bundle and from the overall discussion of the areas measured in the 1st, 2nd and 3rd gap.

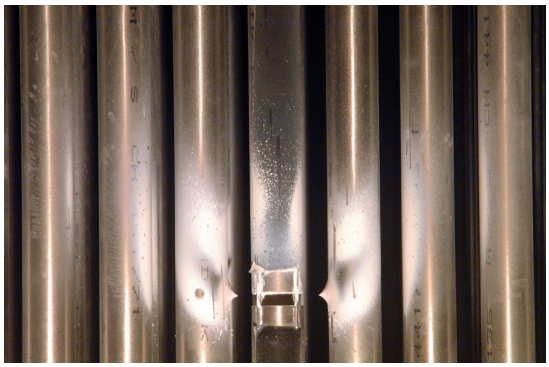

Fig. 24. Particle deposits after a experiment.

Fig. 24 shows the aerosol deposits found in the surroundings of the breach after a experiment. The deposition pattern indicates that the jet follows a pseudo-parabolic trajectory across the tube bundle similar to the free jet one. Deposits on the broken tube over the breach were only observed in the "in-bundle" jet, so that they might be related to gas recirculation and/or particle rebound.

PIV results show that when inlet gas mass flow rate increases the radial jet penetration also increases. Nonetheless, a detailed analysis of the experiments shows that the tubes decrease drastically the jet penetration with respect to the free jet. As the jet impinges on the surface, a fraction of the gas moves upwards whereas the rest flows around the tube. The Coanda effect enhances adhesion of the gas to tube surface, so that the vertical component of gas trajectory is reinforced (Schuh and Person, 1964). Sears, 1948 and Wild, 1949 found this phenomenon studying boundary layers at yawing cylinders. They reported the difference between the streamlines of the boundary layer (outer flow) and the limiting streamlines (wall shear stress streamlines) of the surface. This effect can also be deduced from the deposits pattern of Fig. 24. By taking into account the aerosol surface density shown in the picture it can be inferred the outer/bulk flow jet trajectory. However, deposits in the wake of the first tube over this trajectory would be related to the limiting streamlines that tend to adhere to the surface. As a consequence, the boundary layer flow is diverted to the back end. The separation line, which is also sketched and noticed in the deposits, is the envelope of all the limiting streamlines. This surface-jet interaction phenomenon causes a sharp reduction of jet radial momentum.

The analysis of the PIV velocity field in the 1st gap (Fig. 25) and its comparison with the results in the 2nd and 3rd gaps allow describing the global behavior of the flow field in the scenario:

- At low inlet mass flow rates (75 kg/h) the jet penetration is low; it hardly reaches the 2nd tube. Most of the jet flows upwards through the first gap. At middle height of the bundle (i.e. 500mm over the breach) velocities shows uniform top-hat profiles. Under these conditions, the jet stream generates a

low suction effect on the 2nd gap where the flow shows a uniform radial component oriented towards the 1st gap.

- At middle mass flow rates (139 kg/h), the jet penetration reaches the 2nd gap and most of the jet flows axially upwards through this gap. In the 1st gap, a recirculation region is settled over the breach (Fig. 25), as a result of the jet suction effect that is further enhanced by the presence of tubes.

- At high mass flow rates (250 kg/h) the jet penetrates reaching the 3rd gap. The recirculation region previously placed at the 1st gap seems to penetrate deeper into the bundle as the flow stream over the breach (1st gap) is reoriented towards the breach (increasing the gas entrainment into the jet (Fig. 25). This behavior influences the flow at the middle height of the bundle (i.e. 500mm over the breach), where the velocity is low and reoriented downwards towards the breach.

A priori, the applicability of the PIV technique to the 2nd and 3rd gap areas is limited due to the enhanced 3D nature of the jet by the boundary layer separation. However, the PIV results showed a dominant enough two-dimensional component for the PIV processing algorithm to obtain a satisfactory SNR level. This permitted to extract basic information such as velocity order of magnitude or flow orientation from the measurements.

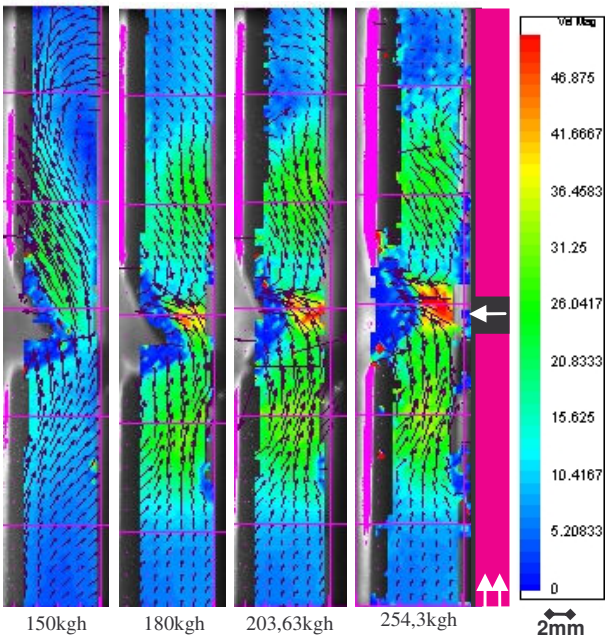

Fig. 25. Mean velocity field near the breach for the jet in tube bundle.

2.5.2.2.2. Jet behavior close to the breach

Given the importance of tubes around the breach in aerosol retention, further attention was paid to the jet behavior in the space between the broken tube and the first neighbor (Fig. 25). As shown in the figure, the jet enters the tube bundle with an initial deflection angle and starts expanding close to the breach. This expansion is soon limited by the presence of the tubes where it impinges restraining its initial momentum and deflecting its trajectory being forced to wrap over the tubes surface. Due to jet impingement, seeding particles accumulated at the neighbor facing tubes limiting the PIV application close to the deposits. The main observations are summarized below:

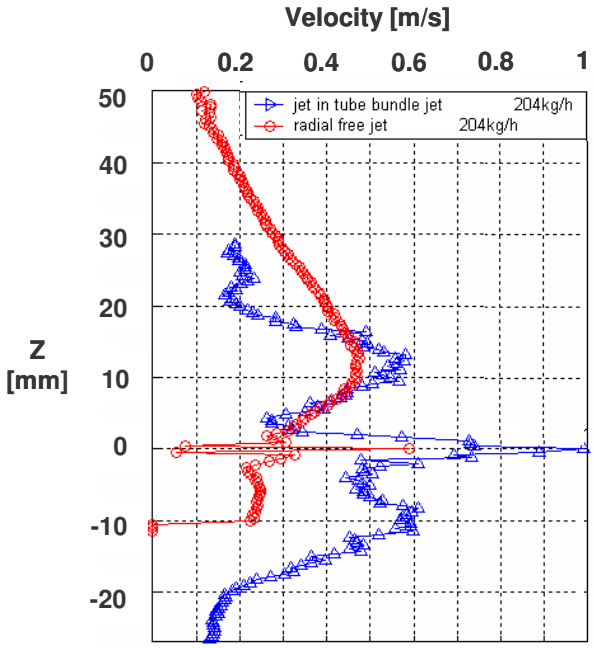

Fig. 26. Vertical velocity profiles for "free" and "In bundle" jets (r=16mm).

The jet shape and velocity are drastically distorted with respect to the free jet case. Both the presence of tubes and the high tube packing configuration in the bundle enhance the gas entrainment over and below the breach inducing secondary flows oriented towards jet core. This effect is especially important below the breach, where the velocity field increases in magnitude considerably (by a factor around 2). As a result, "in-bundle jet" profiles show a quasi-symmetric shape with two relative maxima at the jet rim, whereas "free jet" profiles show a non-symmetric shape (Fig. 26). The jet velocity is also increased with respect to the free jet one (by a factor between 1.6 and 3.5). The tube bank reduces the cross section area, so that for the

same inlet mass flow rate a higher velocity is reached (i.e. compressible effects are negligible).

Fig. 27 shows "in-bundle" vertical profiles of the radial and axial velocity components, for different inlet mass flow rates. A qualitative change is found between low and high mass flow rate profiles. This change can be explained by the jet suction effect and the initial deflection of the jet: as the flow rate increases, higher velocities appear at the breach generating the suction of the surrounding gas. At the same time, the initial jet deflection decreases so that most of the velocity becomes radial. These reduce the axial jet spreading and promote the entrainment towards the breach. As a result, profiles are considerably modified.

Regarding the radial component profiles, Fig. 27A shows that the maximum radial velocities are reached at the center of the jet and profiles are symmetric with respect to the velocity maximum. At the jet rim, the flow is reversed towards the breach. At low mass flow rates, this reverse trend is located far from the jet center line, whereas at high mass flow rates, the jet spreading rate is reduced and the reverse flow area is moved closer to the jet center line.

Fig. 27B shows that the qualitative change in the velocity-modulus profiles is mainly due to the axial component. At low mass flow rates this component is higher than the radial one in magnitude and the flow is oriented mainly upwards. However, at high mass flow rates, the suction effect becomes significant, the flow over the breach is reoriented towards it, and the axial profiles are modified becoming anti-symmetric with respect to the jet center line. The axial velocity maxima are reached where the more intense negative radial velocities are found. Under these conditions, the radial component becomes the dominant one at the jet core, and the jet penetrates deeper.

When inlet mass flow rate is increased, the radial velocity profile reduces the jet spreading, and increases the maximum velocity at the jet core. Thus, higher negative velocities are reached closer to the breach. At the same time, two relative maxima of positive radial velocities appear at the jet rim dividing the areas of back flow placed at both sides of the breach, being the one over the breach more intense than the one below it. This might be seen as if an inlet mass flow rate increase caused shrinkage of the radial jet velocity profile.

A potential explanation of the relative maxima in the radial velocity profiles can be obtained by a detailed analysis of Fig. 25. As the mass flow rate increases, the initial recirculation placed over the breach seems to penetrate deeper into the bundle. At 250 kg/h it appears that two vortexes are set over the breach in the first gap. An intense one close to the breach (center at around 0.75·D) and a weaker one (center around 1.5·D) over it. Close to the broken tube, both vortexes interact and it appears a weak flow stream diverging from the tube over the breach, generating a relative maximum in the radial velocity.

In addition, it was also observed that velocity profiles evolved with radial distance more noticeably at low mass flow rates than at high mass flow rates. In other words, at high mass flow rates (as approaching chocked conditions), velocity field tends to uniformize radially.

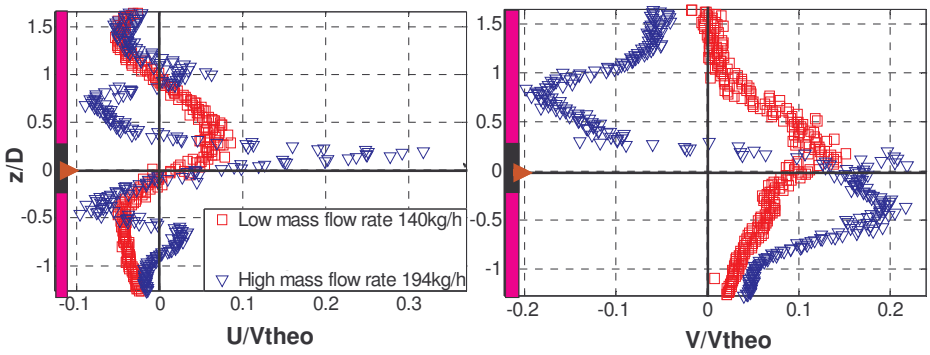

Fig. 27. Vertical profiles of non-dimensional radial (A) and axial (B) velocity components for high and low inlet gas mass flow rates.

In-bundle and free jets showed meaningful differences regarding spreading performance. In the in-bundle jet, the spreading was found to decrease when the mass flow rate increases whereas in the free jet, the spreading was found to be non-dependent. This suggests that an effect of the tubes is to induce the mass flow rate influence on the spreading through the promotion of axial gas entrainment over and below the breach, that reduces the jet core spreading.

Jet Trajectory

The in-bundle jet trajectories as well as their non-dimensional velocities are presented in Figs. 28 and 29, respectively, for different inlet gas mass flow rate in the 1st gap. The jet trajectory was defined by the positions where the maximum velocity was measured. The jet enters the bundle with an initial deflection angle with respect to the radial coordinate. Even though slightly, it decreases with the inlet mass flow rate so that the radial component of velocity is enhanced. The jet trajectory also seems to move axially downwards when the inlet mass flow rate is increased. A potential explanation to this fact might come from the configuration used to generate the radial jet through the breach. Since the top end of the broken tube is closed, the flow is forced to bend and exit through the breach. When inlet gas mass flow rate increases, the pressure of the stagnant gas located over the breach inside the broken tube, might increase, reducing the effective area of the “vena contracta”, and moving downwards the jet center line. This explanation is backed by CFD results obtained when modeling the sequence (López del Prá et al, 2007).

Fig. 29 shows the velocity evolution along jet trajectory. At low mass flow rates, the jet expands with nearly no influence of the closest tubes. However, at high mass flow rate, the influence of the tubes is considerably higher, the jet-surface interaction is

stronger and the maximum velocity is reached closer to the breach. Therefore, the effect of the presence of tubes is enhanced at high mass flow rates.

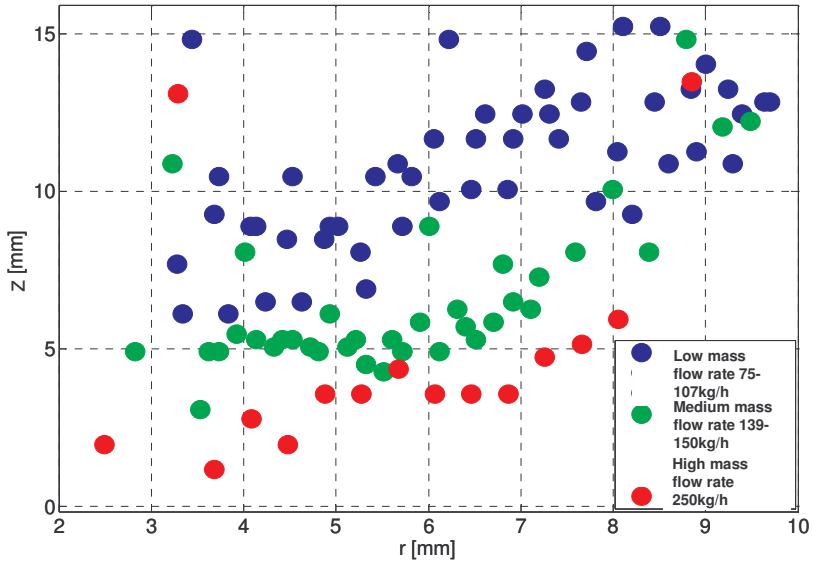

Fig. 28. Jet trajectory for "In Bundle" Jet.

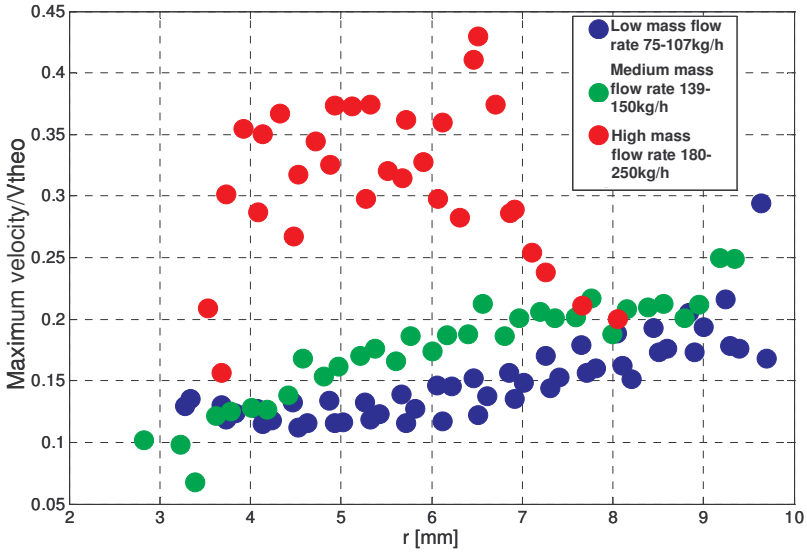

Fig. 29. Velocity evolution along jet trajectory.

Turbulence analysis

Fig. 30 shows profiles of the radial and axial components of the turbulence intensity TI (U_{RMS}/Vtheo). In general, the distributions of the radial and axial turbulence intensities are qualitatively similar in shape to the corresponding mean velocity profiles (Fig. 27). At low mass flow rates, both U_{RMS} and V_{RMS}, distributions rise from about 0.02·Vtheo below the breach to a maximum of 0.15·Vtheo at the jet core following a Gaussian shape with a high flatness factor (χ_{Vrms}). Over the breach, the scatter of the data increases distorting the distribution shape. This scattering shows that higher fluctuations of velocity are taking place in the area over the breach, where the highest velocity gradients appear as a consequence of the recirculation zone. This is due to the jet curvature, which increases the shear stress at the upper side and decreases it at the lower side (Sherif and Pletcher, 1989; Shayesteh et al, 1985).

When increasing the inlet mass flow rate, the TI distributions become symmetric with respect to the jet center line. High mass flow rate distributions show a "3-peak" shape reaching the maximum values at the jet core and two relative maxima at the jet rim. This shape indicates two regions of intense velocity fluctuations: the shear layers surrounding the jet and the jet core itself. Again, these maxima coincide with those where the highest mean velocity gradients occur.

Although the RMS values of the radial and axial components are of the same order, at low mass flow rates the ratio U_{RMS}/V_{RMS} seems to be slightly lower than 1 over the breach at the jet rim, whereas at high mass flow rates this tendency tends to dissipate and the ratio comes closer to 1 all along the jet core and rim. A similar tendency was reported by Barata et al (1992) for round impinging jets in crossflow. This trend also holds in bidimensional flow across a tube bundle, where the streamwise turbulence intensity is lower than the transverse turbulence intensity (Paul et al., 2007). This might suggest that an increase of the inlet mass flow rate results in an enhancement of turbulence uniformly both radially and axially.

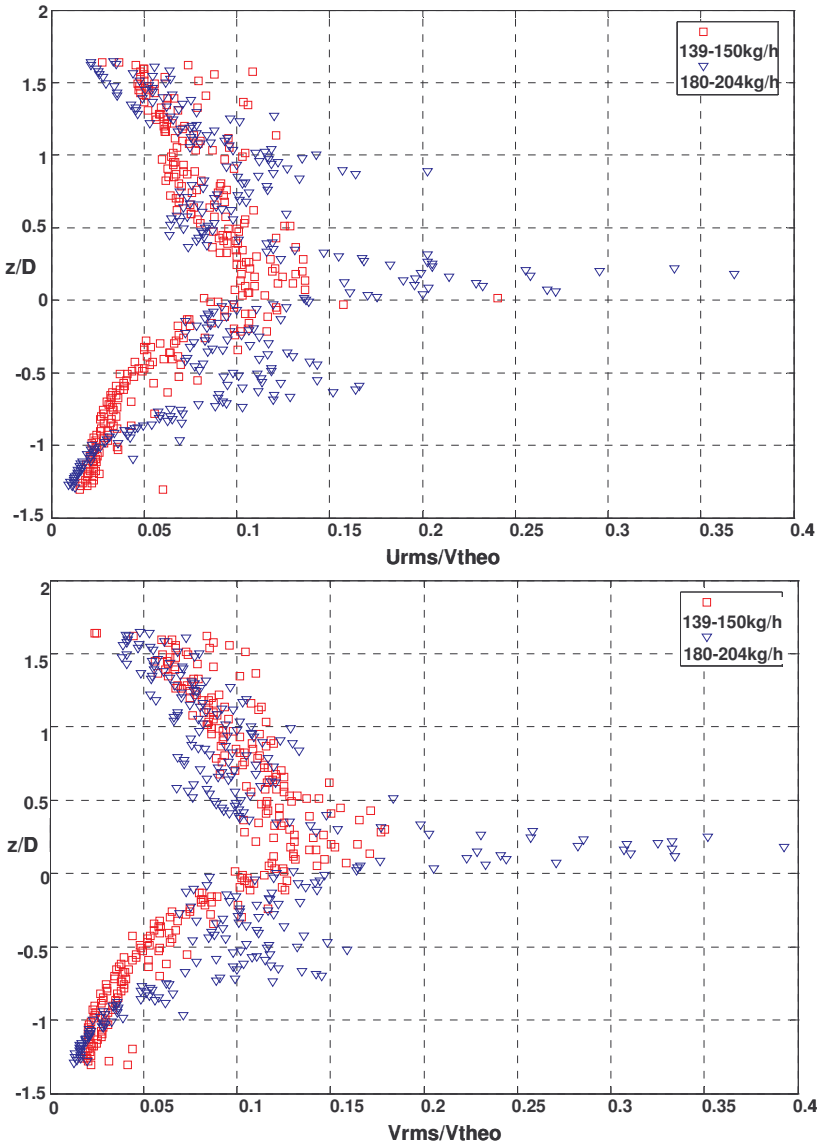

Fig. 30. Turbulence intensity radial (A) and axial (B) profiles for 250 kg/h.

A PDF analysis of turbulence behavior in the 1st gap is presented in Fig. 31 in terms of turbulence intensity based on local velocity (TU). The data obtained from all the tests carried out at the same inlet mass flow rate were used to obtain the PDFs figure. The purpose for expressing turbulence in these terms is to quantify the turbulence levels that particles are submitted to.

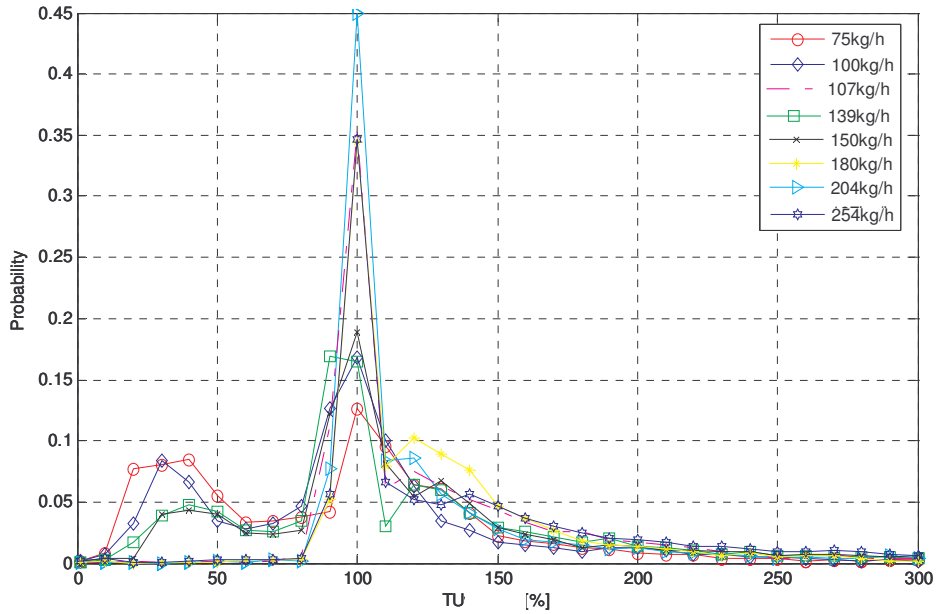

Fig. 31. TU PDFs for different mass flow rates.

"In-bundle" jets follow a bi-modal log-normal distribution where a main mode and a secondary one are observed at around 100% and 40%, respectively. The effect of increasing mass flow rate is to eliminate the secondary mode and to reduce dispersion around the major mode (i.e. change from a bi-modal to a unimodal distribution), reaching the lowest dispersion at 204 kg/h. That is, when increasing the inlet mass flow rate turbulence in the first gap increases in mean intensity and decreases its range of dispersion. Figs. 32 and 33 confirm this result by showing the evolution of the mean and GSD of the TU PDF distribution respectively. The mean of the TU clearly increases with the inlet gas mass flow rate. The GSD of TU seems to decrease until reaching nearly constant value. This analysis permits to quantify the increase of the mean TU with the inlet mass flow rate with the following correlation:

$$\overline{TU}[\%] = 25.69 \cdot 10^{-2} \cdot \Phi[kg/h] + 91.28 \qquad R^2=0.80 \qquad (5)$$

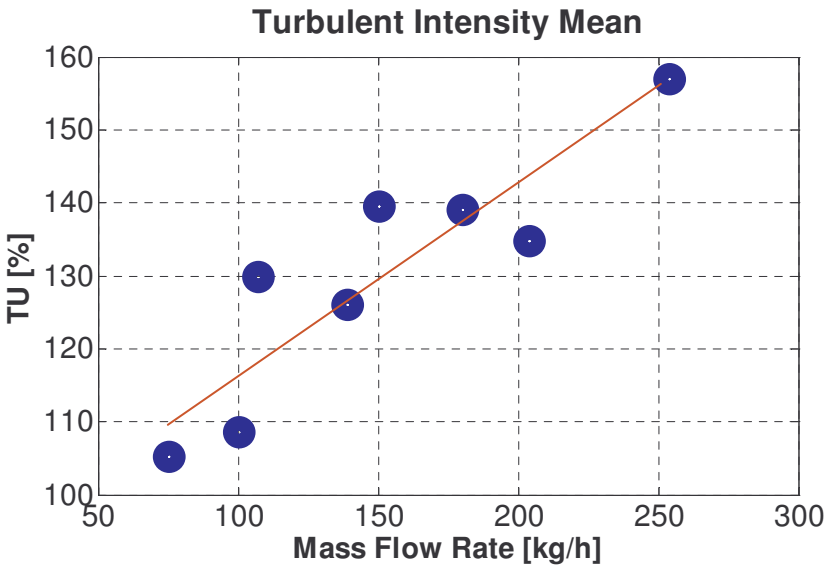

Fig. 32. Mean of the TU PDFs distribution as a function inlet gas mass flow rate.

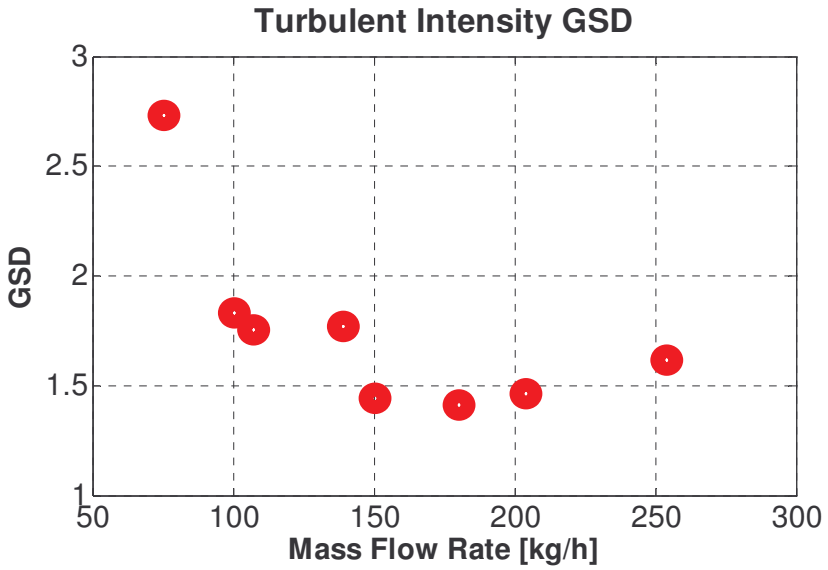

Fig. 33. GSD of the TU PDFs distribution as a function of inlet gas mass flow rate.

When comparing free and "in-bundle" jets PDFs, the effect of the tubes in the turbulence can be quantified in terms of mean and GSD of the TU (Table VI). For the free jet case, TU is determined by the inlet mass flow rate. However, two factors

influence the “in-bundle” TU: mass flow rate and jet-tube interaction. Data show that the presence of tubes increases the mean turbulence intensity between 20 and 60%. This suggests that jet-tube interaction is the one that fosters turbulence (i.e. the tubes acts as turbulence enhancers) since as inlet mass flow rate increases, the mean of the TU increases, remaining constant for the free jet case.

TableVI. Mean and GSD of TU for free and in-bundle.

	Free	In-bundle	Inlet gas mass flow rate [kg/h]			
			107	139	203	254
Mean [%]	X		98	95	99	95
GSD	X		1.8	1.7	1.3	1.2
Mean[5] [%]		X	119	127	143	157
GSD		X	1.8	1.8	1.5	1.6

Reynolds-Averaged Navier-Stokes equations

The Reynolds-Averaged Navier-Stokes (RANS) equations provide insight into the momentum transport. RANS equations terms were computed from the available PIV data in the 1st gap. For steady and incompressible flow, the two-dimensional RANS equations in the radial and axial direction may, respectively, be written in the following form:

$$\left(U\frac{\partial U}{\partial r}+V\frac{\partial V}{\partial z}\right)-\left(\nu\left(\frac{\partial}{\partial r}\left(2\frac{\partial U}{\partial r}\right)+\frac{\partial}{\partial z}\left(\frac{\partial U}{\partial z}+\frac{\partial V}{\partial r}\right)+\frac{2}{r}\left(\frac{\partial U}{\partial r}-\frac{U}{r}\right)\right)\right)+\left(\frac{2}{r}\frac{\partial}{\partial r}\left(\overline{u'^2}\right)+\frac{\partial}{\partial z}\left(\overline{u'v'}\right)\right)=\left(-\frac{1}{\rho}\frac{\partial P}{\partial r}\right) \quad (6)$$

C_r V_r T_r P_r

$$\left(U\frac{\partial U}{\partial r}+V\frac{\partial V}{\partial z}\right)-\left(\nu\left(\frac{\partial}{\partial z}\left(2\frac{\partial V}{\partial z}\right)+\frac{1}{r}\frac{\partial}{\partial r}\left(r\left(\frac{\partial U}{\partial z}+\frac{\partial V}{\partial r}\right)\right)\right)\right)+\left(\frac{2}{r}\frac{\partial}{\partial r}\left(\overline{u'v'}\right)+\frac{\partial}{\partial z}\left(\overline{v'^2}\right)\right)=\left(-\frac{1}{\rho}\frac{\partial P}{\partial z}\right) \quad (7)$$

C_z V_z T_z P_z

where:
C_r, C_z = convective term in the r and z direction respectively;
V_r, V_z = viscous term in the r and z direction respectively;
T_r, T_z = turbulent term in the r and z direction respectively;
P_r, P_z = pressure term in the r and z direction respectively;

[5] Estimated from Eq. (5)

By transforming (6) and (7) into dimensionless equations by using D and Vtheo as reference magnitudes,

$$r^* = \frac{r}{D}; \quad z^* = \frac{z}{D}; \quad U^* = \frac{U}{Vtheo}; \quad V^* = \frac{V}{Vtheo}; \quad \overline{u'^2}^* = \frac{\overline{u'^2}}{Vtheo^2}; \quad \overline{u'v'}^* = \frac{\overline{u'v'}}{Vtheo^2};$$
$$\overline{v'^2}^* = \frac{\overline{v'^2}}{Vtheo^2}$$

The vertical profiles of the dimensionless terms C_r^*, C_z^* to P_r^*, P_z^* are presented in vertical profiles in Figs. 34 and 35 The convective, viscous and Re stresses terms in Eqs. (5) and (6) were estimated directly from the measured data. The pressure gradient terms were obtained from the equation P=C-V+R. The derivatives were estimated using an adaptative Gaussian window-finite difference (AGW-FD) method with a central differencing scheme Fouras et al. (1998).

Figs. 34 and 35 reveal that the viscous terms in both the radial and axial RANS equations are negligibly small compared to the overall convective and Re stress terms. In general, the contribution terms presented in the RANS equations follow a “3-peak” profile similar to the distributions presented for the RMS velocity magnitude. The terms show a maximum at the jet core region and two relative maxima in the jet rim region, indicating that the regions where the transport phenomena are enhanced correspond to the shear layers surrounding the jet and the jet core itself.

The figures also illustrate that, the transport terms in the axial RANS equation are generally of the same order of magnitude than the corresponding terms in the radial equation. This again might suggest that transport phenomena in the region analyzed is uniform in any direction of the plane measured.

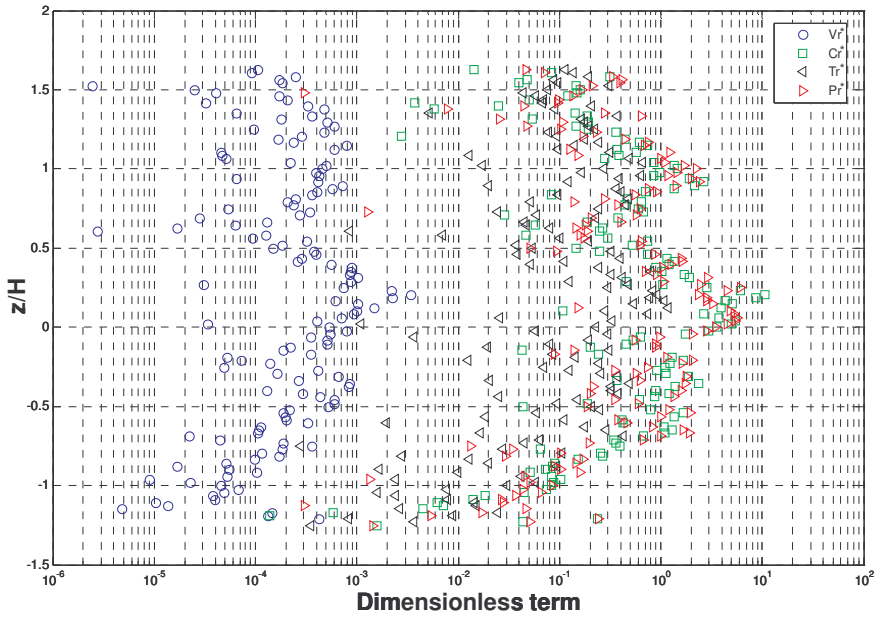

Fig. 34. Radial RANS terms profiles for 250 kg/h.

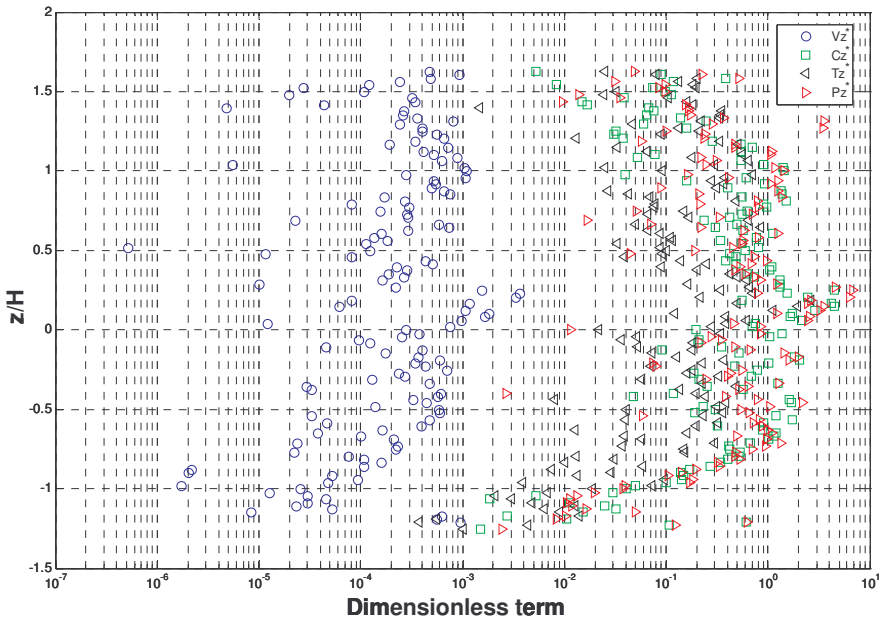

Fig. 35. Axial RANS terms profiles for 250 kg/h.

2.6. Fish-mouth experiments

Tube crack shape affects heavily aerosol deposition pattern in the break stage (Herranz et al. 2006), so that the previous aerodynamic study was extended to crack shapes other than guillotine: fish-mouth breaches. By comparing with guillotine breach results, the effect of the breach type in the flow field is assessed.

2.6.1. Experimental set-up and measurement procedure

The experimental campaign was conducted within the CAHT facility (Fig. 36). The instrumentation used and the facility configuration is the same that was used for the guillotine test, except for the location of the broken tube in the bundle and the breach geometry.

The breach height (Fig. 36) and width are respectively H=2.5·D and W=0.3·D. The breach is placed 0.24 m over the tube base in a peripheral tube (3rd row from the bundle edge mid-plane) oriented towards the center of the bundle.

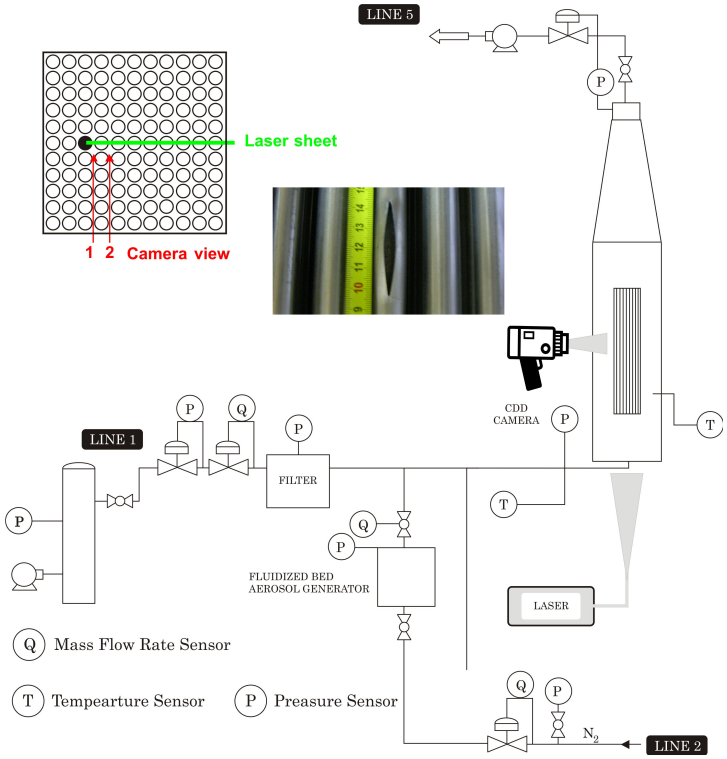

Fig. 36. Scheme of the CAHT facility, PIV configuration and fish-mouth breach detail.

2.6.1.1. Test matrix

Table VII shows the experimental test matrix used. A total of 28 experimental runs were conducted in 5 series. Some of them were used to confirm test reproducibility. The mass flow rate interval (75-250 kg/h) was explored at 8 different values. PIV measurements were performed in the first and second gaps between tubes, right at the vertical plane containing the axes of the broken tube and the closest neighbor one. In the axial direction, data were taken at the breach exit ($z<\pm 23$ mm) and at three additional locations to follow jet development. A total of 620 images were recorded during each run. Some tests extended the number of samples up to 6000 images in order to analyze turbulence quantities.

Table VII. Experimental test matrix for fish-mouth experiments

		PIV LOCATION		Inlet gas mass flow rate [kg/h]							
		1^{st} gap	2^{nd} gap	75	100	107	139	150	180	203	254
Test Serie	1	x		xx			x	x			
	2		x	x	x	x	x	x	x		
	3	x									XX
	4	x		x	x	x	x	x	x	x	xx
	5	x		x	x	x	x	x	x	x	
Pressure [bar abs]	P_{in}			1.2	1.3	1.3	1.5	1.6	1.9	2	2.2
	P_b			1	1.1	1.1	1.1	1.1	1.2	1.2	1.2

x=310 samples (i.e. 620 images) X=2700 samples (i.e. 5400 images)

2.6.2. Results and discussion

The main kinematic variables derived from the PIV measurements were mean velocity and turbulence-related magnitudes. As in the previous section, results will be discussed on the basics of a cylindrical coordinate system centered on the broken tube axis in the middle of the breach height.

The applicability of the PIV technique to this scenario suffered from several shortcomings due to scattering of the laser sheet onto tube surfaces. This scattering increases the background intensity on the images and reduces drastically the quality of the cross correlation close to the tubes. By using transparent material for the tubes, the laser sheet partially goes through the surface and the light scattering noise of data recorded at the immediate vicinity the tubes surfaces was reduced.

2.6.2.1. The fish-mouth “in-bundle” jet

Insights into the jet evolution across the tube bundle can be got from PIV velocity field and the particle deposits on tubes. A fish-mouth breach generates a “pseudo-

elliptic" jet (i.e. generated from a "pseudo-elliptic" nozzle) of large aspect ratio. Fig. 37 illustrates the normalized velocity vector field obtained for the particular case of 75 kg/h. Jet mean velocity profiles show "quasi-top hat" shape with slightly higher magnitudes of velocities in the lower part of the breach. Deposits on the facing neighbor tubes adopt an elongated shape along z (Fig. 38A), which suggests that the jet impinges the surface in a slot-like way.

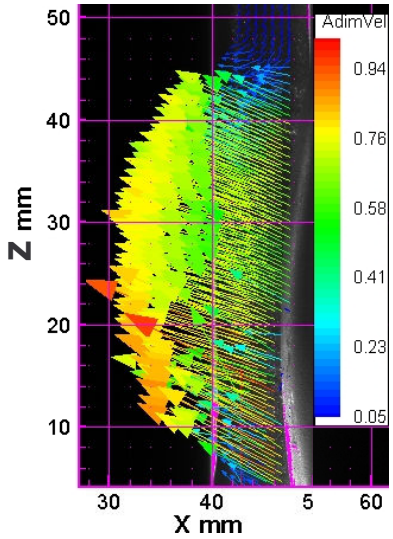

Fig. 37. Normalized mean velocity field (75 kg/h).

A) B)

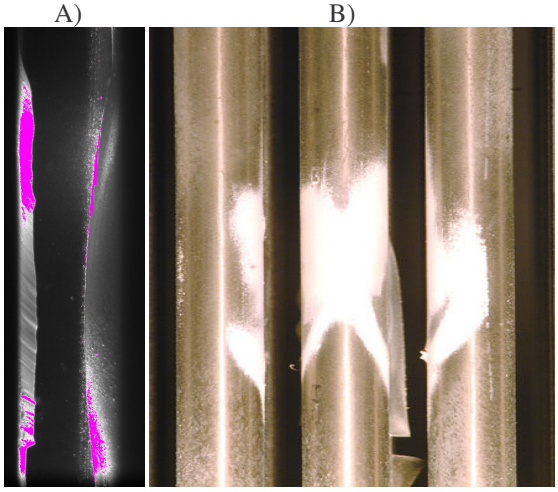

Fig. 38. Particle deposits found in the impinging and wake regions of the neighbor tubes after a PIV experiment.

The jet expands across the bundle evolving from an oblique crossflow configuration to an axial one resulting in a quasi-parabolic trajectory. This trajectory results from a combination of three factors: the initial deflection of the jet, the presence of the tubes and the location of gas exit at the top of the vessel, which drags the jet vertically.

Concerning inlet mass flow rate influence, similar observations to those from a guillotine breach were noted:

- Jet maximum velocity magnitude increases linearly with the inlet gas mass flow rate.

- As in the guillotine case, when the mass flow rate increases the jet penetration also increases. The presence of tubes decreases drastically the jet penetration with respect to the free jet. The impingement of the jet on the tube surface splits the jet that flows around and upwards over the tube surface enhancing the jet adhesion to the surface and the axial folding of the jet trajectory (Coanda effect). This effect, reported by several authors (Sears 1948, Wild 1949, Schuh and Pearson 1964), is consistent with the particle deposits found after PIV experiments (Fig. 38B).

- The increase of the radial velocity with mass flow rate promotes the axial gas entrainment into the jet as a consequence of the local suction effect. As a result, the initial deflection angle of the jet with respect to the horizontal plane (30º for 75 kg/h, Fig. 37) tends to reduce when the mass flow rate increases promoting the symmetric gas entrainment over and below the breach.

Fig. 39 shows axial profiles for the normalized mean velocity and RMS (i.e. a measure of the velocity fluctuation) velocity components at Λ=0.5 for high and low mass flow rates. As expected, radial velocity components and their associated RMS are considerably higher than axial ones.

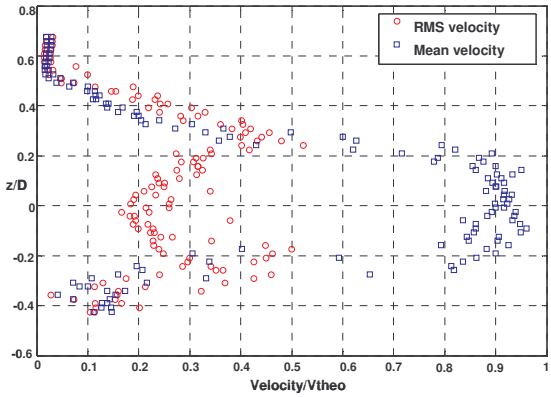

A) Umean and U_{RMS} for 75 kg/h

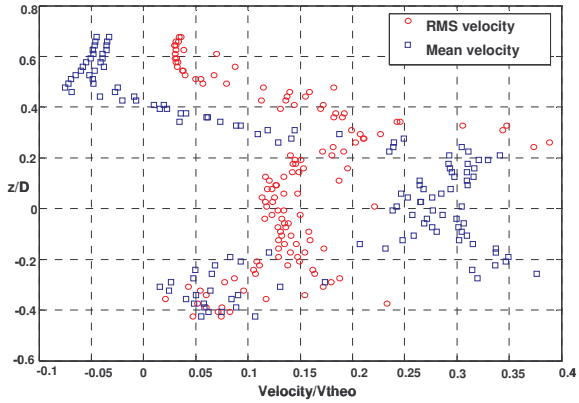

B) Vmean and V_{RMS} for 75 kg/h

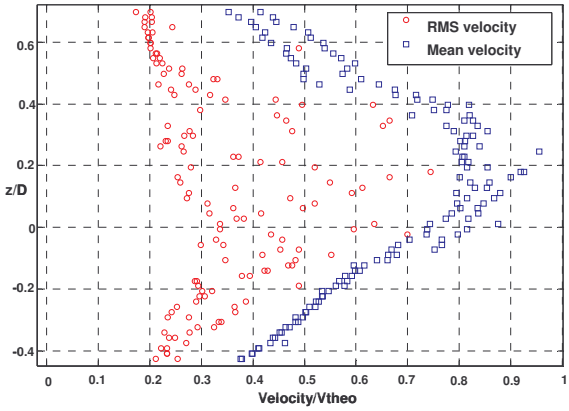

C) Umean and U_{RMS} for 250 kg/h

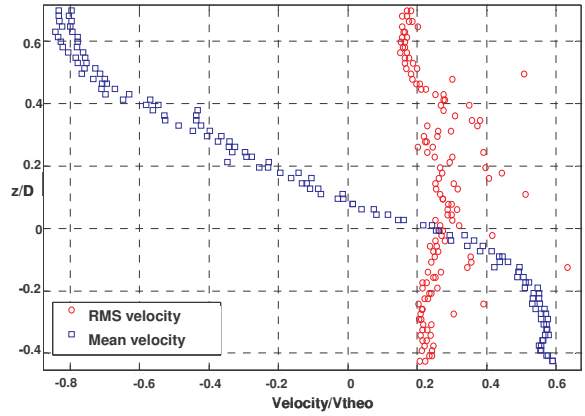

D) Vmean and V_{RMS} for 250 kg/h

Fig. 39. Radial and axial mean velocity and RMS profiles at Λ=0.5

At low mass flow rates, radial and axial components show almost symmetric profiles. Mean velocity components show top-hat profiles with maximum values at the jet core whereas RMS profiles show a saddle shape with a minimum plateau at the jet core and two maxima located at the jet shear layers. However, radial and axial components also show important differences. Axial RMS profile shows an asymmetric shape with a maximum in the shear layer over the breach. This maximum is the result of the positive axial velocities at the jet core that generates an asymmetric gas entrainment over and below the breach.

At high mass flow rates, shape similarity between radial and axial profiles is lost. The radial mean velocity profile is similar to the one found at low mass flow rates, although it becomes wider indicating that jet spreading increases. However, axial mean velocity profile changes totally reaching higher values at the jet rim and becoming anti-symmetric with respect to the jet axis. This indicates the clear effect of the gas entrainment in the axial velocities:

- Axial component of the mean velocity becomes dominant at the jet rim, whereas at the jet core the major contribution comes from the radial component.
- Entrainment extends axial velocity over a broader range. It also uniformizes axially the RMS component indicating that the transport phenomena are considerably fostered in the area.

Thus the inlet gas mass flow rate effect is:

- In the radial component it promotes a smoother decay of the velocity as well as a slight axial displacement of the top-hat plateau. It also generates a clear lost of the structure of the shear layers (RMS).
- In the axial component it enhances the entrainment that stretches the mean velocity range, causing an inversion in the flow direction, from positive values below the breach to very negative ones over it. This monotony in the tendency generates a uniform axial RMS distribution.

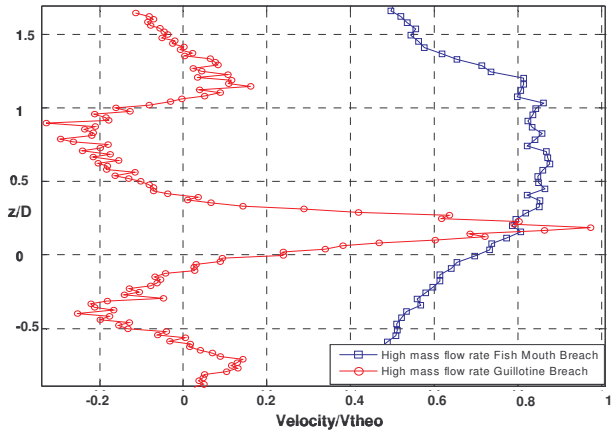

A) U mean component. Axial normaliz. with D

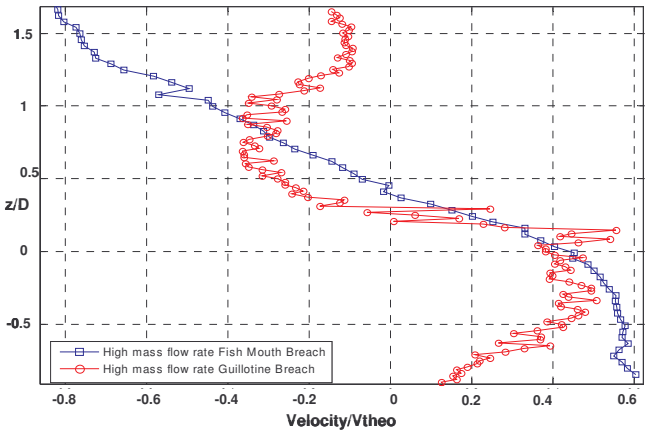

B) V mean component. Axial normaliz. with D

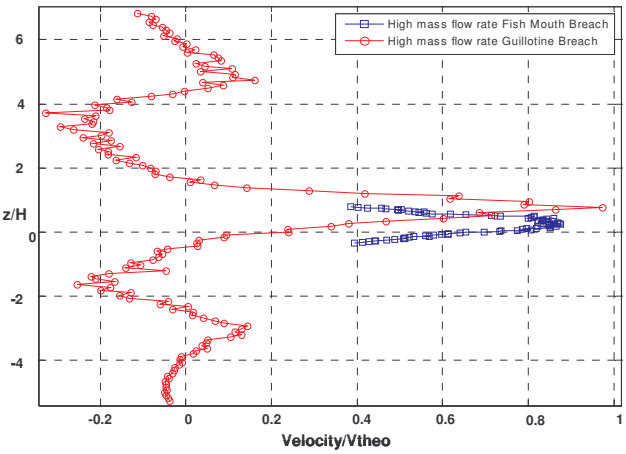

C) U mean component. Axial normaliz. with H

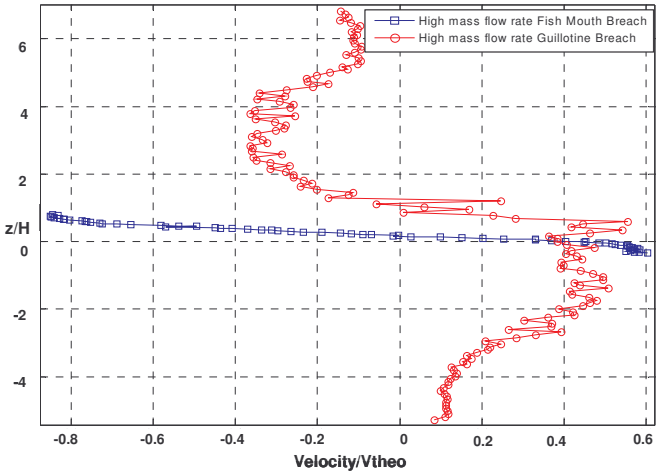

D) V mean component. Axial normaliz. with H

Fig. 40. Fish-mouth vs guillotine type breach axial velocity profile (250 kg/h).

2.6.2.2.Comparison to guillotine "in-bundle" jet

Insights into the breach effect can be got from the comparison of "fish-mouth" and "guillotine" jets. Even though, fish-mouth breach was designed to have half of the cross-section area of the guillotine breach, this comparison permits a comprehensive understanding of jet expansion phenomena.

The jet expansion across the bundle changes with the type of breach. A fish-mouth type breach generates a conical jet expansion across the bundle whereas a guillotine breach generates an axis-symmetric tulip-like jet expansion (Lopez del Prá et al, 2007). This difference in the expansion pattern entails different local pressure fields close to the breach and different momentum exchange surface areas between the jet and the in-bundle gas. As a result, fish-mouth jet shows different velocity distributions and milder velocity decays than the guillotine jet.

Distributions of radial and axial velocity components are shown in Fig. 40 for the 250 kg/h case. Velocities are normalized with respect to the maximum modulus of velocity for each breach type. Two types of normalization of the axial component were performed. On one side, the tube diameter, D, was used to take into account the size and profiles of the aerosol deposits. On the other, it was also used the breach height, H, to estimate aerodynamic self-similarity between breaches.

As observed, fish-mouth type breaches generate top-hat profiles whereas the guillotine type breaches displays pseudo-Gaussian profiles at the jet core with two relative minima at the jet rim. These minima are related to regions where the flow is reversed towards the breach. As a result of the different behavior, deposits on the neighbor facing tube adopt a slot shape for the fish-mouth breaches (Fig. 38A) and a round peak for the guillotine ones (Fig. 41).

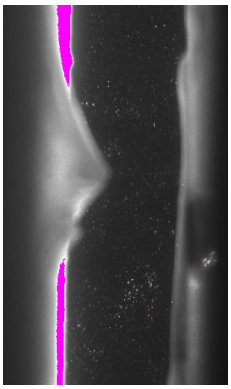

Fig. 41. Particle deposits found after a guillotine type PIV experiment.

Axial velocity component profiles also show different distributions. Fish-mouth breaches extend axial velocity component in a wider range than guillotine breaches. Guillotine breaches generate anti-symmetric profiles with two relative maxima over and below the breach. Fish-mouth breaches also generate quasi-anti-symmetric profiles although the asymptotic trend is not so clear over the breach where the velocities tend to keep decreasing out of the measurement area (note that breach height is 10 times larger in the fish-mouth configuration). Therefore, fish-mouth profiles of Fig. 40 correspond to the core of the jet, whereas guillotine also includes the jet rim region. Thus, even higher axial velocity component might be expected for the fish-mouth jet over and below the breach, out of the measurement region and a similar profile shape might be found.

Figs. 40C and 40D suggest that, when restricting to the domain shared by both types of breaches in the measurement plane ($z/H<\pm1$), velocity profiles become self-similar when removing axial dimension of the breach. This result might be expected since the axial boundary conditions that the jet "feels" close to the breach remain the same for both cases. However, from the particle behavior point of view, the aerodynamic flow field results different in the space between tubes close to the breach, where the main deposition takes place.

As a result of the different expansion pattern, the gas entrainment into the jet core also changes:

In the guillotine case, the axis-symmetry of the jet divides the flow field in two regions with no continuity between them and the gas entrainment is contained within the symmetry plane over and below the breach. However, in the fish-mouth case, the suction effects generate additional lateral/out-of-plane gas entrainment around the broken tube resulting in a non-symmetric flow field in the azimuthal dimension. Hence, similarities found between breaches are reduced to a small region of the first gap in measurement plane (Fig. 40C and 40D) and it is out of the measurement plane where the main differences might be found.

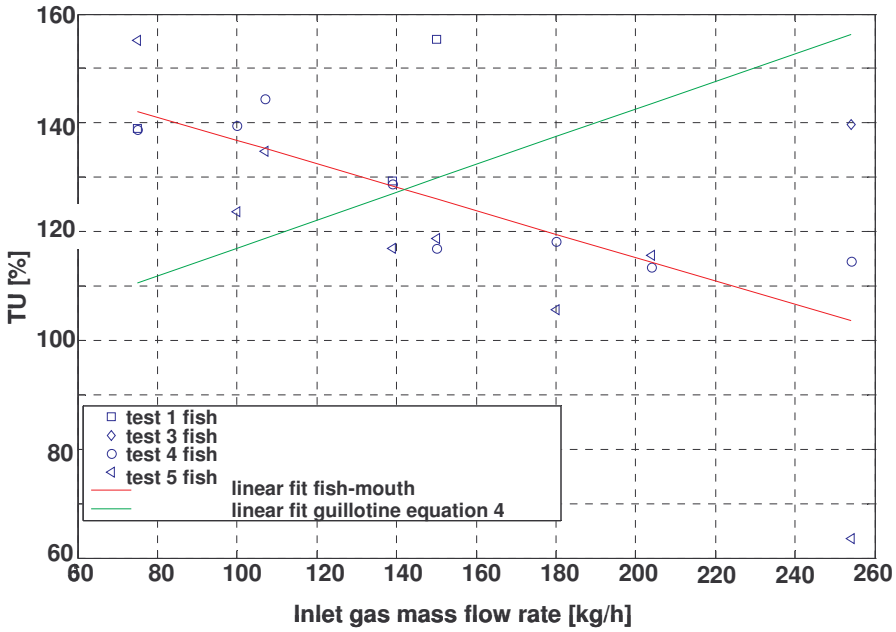

Fig. 42. Mean TU% evolution with mass flow rate for fish and guillotine jets in the 1st gap.

Regarding turbulence, a comparative analysis can be obtained by collapsing the TU data of the area measured in the 1st gap into a probability density function (PDF). Turbulence differences are quantified in terms of mean value and geometric standard deviation (GSD) of the PDF distributions. Fig. 42 shows a comparison of the mean TU% for "fish-mouth" and "guillotine" jets as a function of the inlet gas mass flow rate.

Guillotine trend were obtained accounting for the jet core and jet rim regions and illustrate that the mean turbulence intensity increases with mass flow rate. Whereas fish-mouth trend were obtained for the jet core region and shows a decrease of the mean turbulence intensity with mass flow rate. Turbulence intensity increases due to the enhancement of velocity fluctuations in the jet shear layers (Barata et al. 1992). In the jet core region, however, this tendency is reversed and the jet core experiences a lower level of turbulence as the mass flow rate grows (Schuh & Person, 1964). Anyhow, both types of breaches show a similar level of mean turbulence intensity.

2.7. PIV measurement technique discussion

Comparison of PIV measurements with CFD simulations of the break stage highlighted meaningful differences in the jet core between the measured velocities and the predicted ones. Fig. 43 shows a comparison of axial velocity profiles at Λ=0.31 obtained by PIV in different campaigns and the equivalent CFD predictions. As shown, measurements and simulations agree on velocity magnitude at the rim region of the jet, but they become drastically different at the jet core, where simulations were notably closer to the isentropic expansion estimates. Neither data uncertainties nor code approximations could be responsible for the noticeable differences found.

In order to assess PIV measurements reliability in the jet core region, Pitot tube measurements were performed and compared to the PIV ones. Fig. 45 show the jet core maximum velocity evolution with mass flow rate measured with PIV and Pitot for the free radial jet configuration. Pitot velocities are close to the ones estimated theoretically from an isentropic expansion (i.e. Vtheo), and they come much closer to CFD estimates. Then, Pitot measurements of velocity magnitude in the jet core region were given credit.

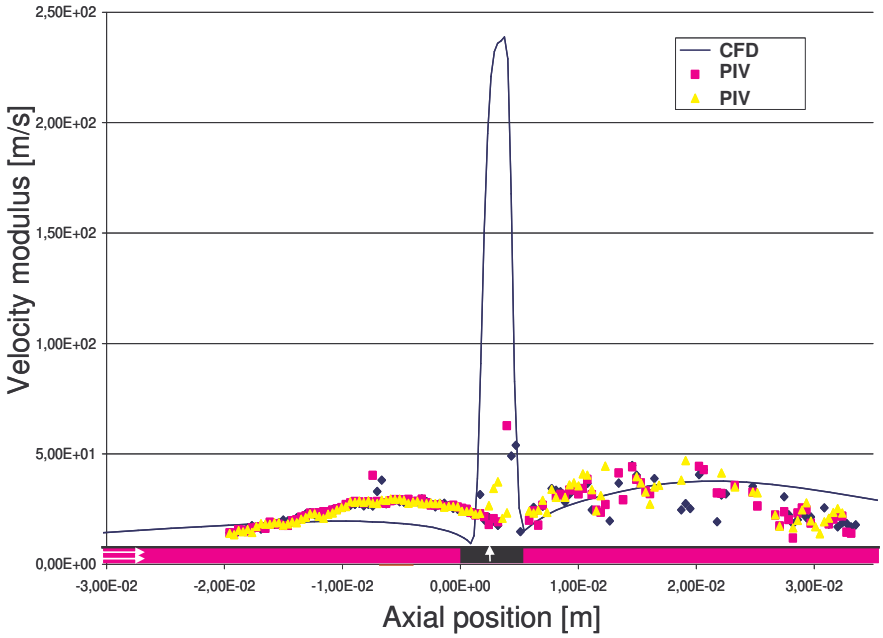

Fig. 43. Comparison PIV mesuerements and CFD predictions.

It was proven that the systematic error in PIV measurements was not dependent on the number of samples, breach geometry, the presence or absence of tubes in the bundle or the TiO_2 seeding manufacturer. In all cases, number of tracked particles (i.e. the

number velocity vectors used to compute the mean flow field) was two orders of magnitude lower than the one at the jet rim. Data-predictions difference was shown to increase inlet mass flow rate was increased.

There are different phenomena that may contribute to explain the PIV limitation. Analysis of the images and data suggests that the major ones might be:

- Three-dimensionality of the flow at the jet core. The breach exit is an area of extremely high local turbulence due mainly to the Re_D range studied, but also to the curvature of the flow and the "vena contracta" at the breach. This turbulence means that the 3D nature of particle motion would be noticeably enhanced in the jet core, decreasing likelihood of establishing meaningful cross-correlations.

- Particle inertia. Big particles might not be able to follow the gas flow streamlines at the breach exit. This would yield to a scarce particle population at the measurement volume analyzed. The particle "cut" diameter of the breach (i.e. diameter of the particle of maximum size that could pass through the breach under ideal conditions) could be written as a function of the dimensionless Stokes number as (Hinds, 1982):

$$\left(d_{ae}\right)_{50\%} = \frac{9\mu \cdot D \cdot Stk_{50\%}}{\rho_p \cdot Vtheo} \tag{8}$$

  Under the studied conditions, $(d_{ae})_{50\%}$ ranges between 3.5 and 1.8 μm (for 200 and 1000 kg/m^3 particles density estimation, respectively). Thus, particles over these "cut" values have low probability of exiting the breach. An initial campaign permitted the characterization of the seeding particles in terms of mean diameter and size distribution by introducing iso-kinetic samples into the injection line upstream the breach and using different instruments (OPC, cascade impactors and SEM) (Herranz et al, 2006). Results showed that although primary particles are nano size ones (d_p~210nm), due to agglomeration in the generation and injection line, they grow up to a measured d_{ae} between 3.5 and 6 μm (depending of the TiO_2 manufacturer). Hence, seeding aerosol seems to be affected by the flow curvature at the breach. However, since aerosol injected was measured to be polydispersed (GSD~1.9), particles with smaller diameter than the "cut" one may exit the breach and seed the flow.

- Segregation of particles due to eddies. Presence of eddies in the gas flow fosters particle segregation; that is, uniformity of particle concentration breaks down possibly due to the acceleration induced by the eddies. This effect, experimentally shown by Fung and Vassilicos (2003), results in a systematic reduction of the number of velocity vector detected at the jet core

since the expected "seeded" images transform into regions of uniform low/high intensity.

- Particle entrainment. Data showed that particles carried by the entrained gas from the jet rim into the jet core are eventually detected and quantified in the velocity field. Since these particles have relatively lower velocities than the one expected for the flow at the jet core, they might be the main contributors to the measured mean velocity field in this area. This is consistent with the order of magnitude of velocity measured in this region.

The quantitative contribution of each of the phenomenon discussed above cannot be estimated. However, it seems that all of them might have a significant contribution to the final systematic difference.

Therefore, PIV measurements proved to be reliable in the area of influence of the jet at the breach exit, except for the narrow region of the jet core. Pitot measurements in the radial free jet configuration and CFD simulations in the "in-bundle" one confirmed this conclusion and allowed qualitative discussion of velocity profiles.

2.7.1. Pitot tube measurements

2.7.1.1. Pitot tube principle

A Pitot tube is a metal probe with several small holes drilled around the outside of the tube and a central hole drilled down the axis of the tube (Fig. 44). The outside holes are connected to one side of a pressure transducer. The center hole in the tube is kept separate from the outside holes and is connected to the other side of the transducer, which measures the pressure difference between both sides. Since the outside holes are perpendicular to the flow direction, these tubes are pressurized by the local random component air velocity, i.e. the static pressure (p_s). The center tube, however, is pointed in the flow direction and is pressurized by both the random and the stream air velocity, i.e. the total pressure (p_t). Hence, the pressure transducer measures the difference in total and static pressure i.e. the dynamic pressure $\Delta p=p_t-p_s$:

Fig. 44. Pitot tube schedule.

$$\Delta p = \frac{1}{2}\rho v^2 \rightarrow v = \sqrt{\frac{2\cdot\Delta p}{\rho}} \qquad (9)$$

An Hg barometer and a thermocouple were also used to compute air density.

2.7.1.1. Pitot tube results

Fig. 45 shows the maximum velocity measured as a function of the inlet gas mass flow rate for Pitot tube measurements in free jet configuration. PIV maximum velocities for free configuration were also included for comparison. Proposed experimental correlations permit to show that, as expected, the actual evolution of the maximum potential jet core velocity with the inlet gas mass flow rate follows a linear law for the free jet.

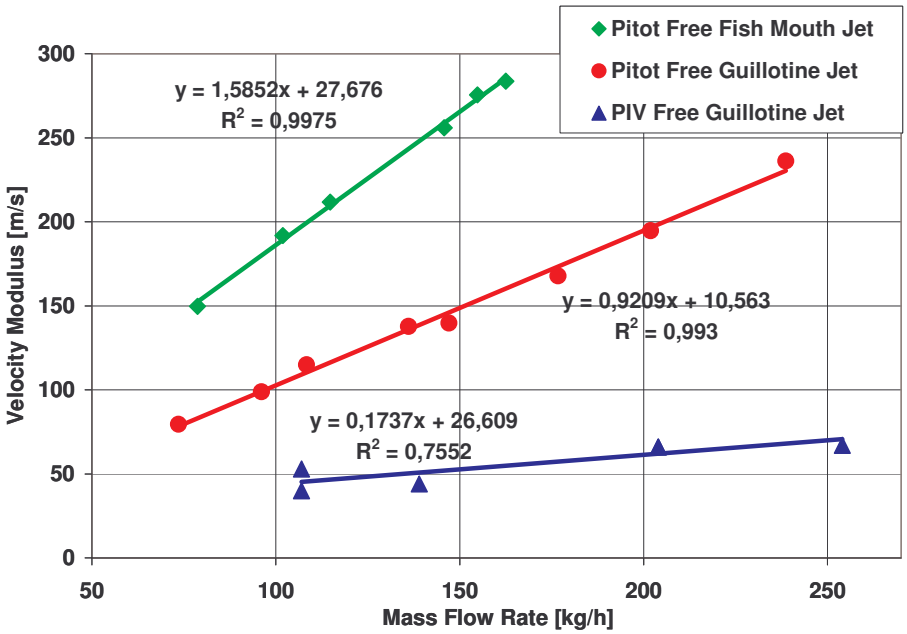

Fig. 45. Jet maximum velocity as a function of inlet mass flow rate.

As said above, Pitot measurements of jet core velocities are close to the ones estimated theoretically from an isentropic expansion (i.e. Vtheo), and they come much closer to CFD estimates. Therefore Pitot tube data can be considered a reliable characterization of jet core. Figs. 46 and 47 show the jet vertical velocity profiles as a function of the inlet gas mass flow rate at Λ=0.3 for guillotine and fish-mouth breaches, respectively.

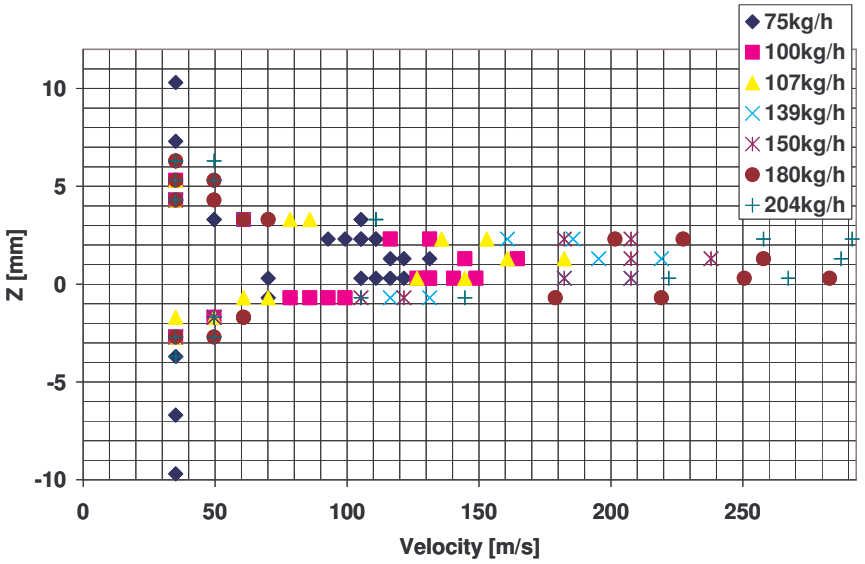

Fig. 46. Jet velocity profiles for guillotine breach at different inlet mass flow rates.

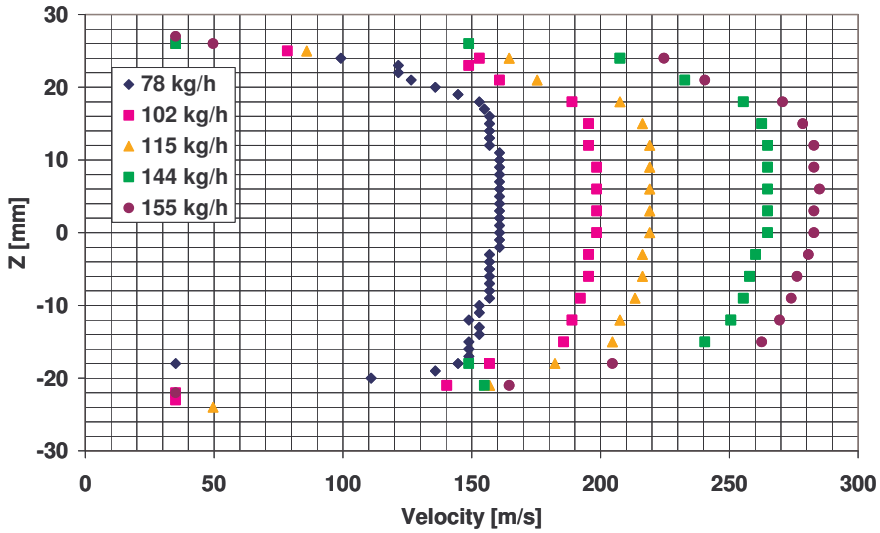

Fig. 47. Jet velocity profiles for fish-mouth breach at different inlet mass flow rates.

2.8. Experimental measurements uncertainty analysis

2.8.1. PIV Uncertainty analysis

A complete uncertainty analysis involves identifying both the bias error and accuracy in each part of the measurement chain.

In PIV techniques, the accuracy of velocity measurement is limited by the accuracy of the sub-pixel interpolation of the displacement correlation peak. Other sources of measurement uncertainties include particle response to fluid motion, light sheet positioning, light pulse timing and size of PIV processing interrogation window.

In the presented study, the tubes were set with an accuracy of ±0.5mm of their relative position between them. However, due to the jet momentum, during the tests the first neighbor tubes and the broken one separate from each other up to 1.25·p. The inaccuracy in the vertical alignment of the tubes axis in the setup has been estimated in ±0.3º. The light sheet positioning of the laser with respect to the middle bundle plane (pitch plane) has an estimated uncertainty of ±1.5mm. Considering the flow investigated axis-symmetric at the breach exit, these sources of error are critical since a misalignment of the laser sheet and the pitch plane could generate that particles scattering the light in the first pulse does not flow along the laser sheet (Fig. 48).

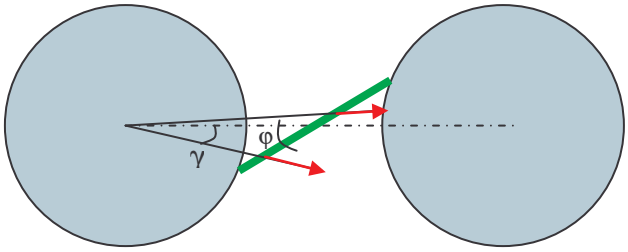

Fig. 48. Misalignment uncertainty estimation.

For the in-bundle measurements, this uncertainty has been bounded by a theoretical analysis presented below:

$$\varepsilon_{laser\_mis}(\%) = \frac{\sqrt{(V_{real} - V_{laser})^2}}{V_{real}} 100 = \sqrt{1 - \cos^2(\varphi - \gamma)} = \sin(\varphi - \gamma) \tag{10}$$

Errors result in a non-uniform uncertainty field. The maximum error in the laser sheet positioning results in a 35% of uncertainty. For the free jet measurements, γ is considerable lower since the laser is positioned outside the PECA vessel. In this case, the uncertainty due to the misalignment is reduced to less than 6%.

However, in any case, this source of error would imply a meaningful failure of the cross-correlation algorithm in the velocity vector calculation and could be noticed in the SNR. This magnitude shows a value higher than 3 in the measurement plane and validates the results presented.

A total of 310 pairs of images were acquired during each test. According to Lourenço (1982) this sampling should yield, a priori, an uncertainty associated to the turbulence nature of the flow of around ε_{turb}=5% with a 95% confidence.

Regarding post-processing, a Matlab script to estimate PIV results uncertainty has been developed based on ISO Norm (1995). By using error propagation theory the uncertainty on the mean velocity field can be calculated as:

$$\delta V_{proc} = \sqrt{\left(\frac{1}{M\cdot\Delta t}\delta\Delta x'\right)^2 + \left(-\frac{\Delta x'}{M^2\Delta t}\delta M\right)^2 + \left(-\frac{\Delta x'}{M\Delta t^2}\delta\Delta t\right)^2} \tag{11}$$

where

$$\Delta x' = M\cdot\Delta x \tag{12}$$

$$V = \frac{\Delta x'}{M\cdot\Delta t} \tag{13}$$

being M the magnification factor relating the real physical space (Δx) and the camera domain (Δx'). Table VIII shows the order of magnitude of the different uncertainty sources of variables in Eq. 11.

Table VIII. Uncertainty source terms estimations.

Source term	Estimation	Comments
Pulse separation	$\delta\Delta t = 0.1\mu s$	Obtained from hardware settings from TSI (1997)
Magnification factor M	$\delta M = 0.1 pixels/mm$	Calculated from the calibration process
Pixel displacement	$\delta\Delta x' = 0.1 pixels$	Depends on the processing algorithm. Order of magnitude estimated from Scarano and Riethmuller (2000).

The estimation of the magnification uncertainty (i.e. the quality of the spatial calibration) rose as the main factor affecting the velocity processing uncertainty. The uncertainty in the PIV processing has been estimated to be less than 6% within 95% of confidence level. As a result, the global uncertainty can be calculated as:

$$\delta V = \sqrt{(\delta V_{proc})^2 + (\varepsilon_{laser\_mis})^2 + (\varepsilon_{turb})^2} \tag{14}$$

From all the above considerations, uncertainty in the PIV measurements of the mean velocity field has been estimated to be less than 35% for the in-bundle measurements and less than 11% for the free jet case. Both uncertainties estimated within a 95% of confidence level.

2.8.2. Pitot tube uncertainty analysis

The uncertainty in the velocity measurements done with Pitot tube probe can be obtained from:

$$v = \sqrt{\frac{2Press}{\rho}} \rightarrow \delta v = \sqrt{\left(-\frac{1}{2}\left(\frac{2Press}{\rho}\right)^{-\frac{3}{2}}\right)^2 \delta Press^2 + \left(-\frac{1}{2}\left(\frac{2Press}{\rho}\right)^{-\frac{3}{2}}\left(-\frac{2Press}{\rho^2}\right)\right)^2 \delta\rho^2}$$

(15)

Being Press the dynamic pressure measured by the pressure transducer. ΔPress will be determined by the device resolution and the standard deviation of the dynamic pressure signal measured.

Density ρ is obtained assuming ideal gas, from ambient pressure measured with an Hg barometer and flow temperature measured with a thermocouple close to the breach. The uncertainty can be defined by:

$$\rho = \frac{p}{R_g T} \rightarrow \delta\rho = \sqrt{\left(\frac{1}{R_g T}\right)^2 \delta p^2 + \left(-\frac{p}{R_g}\frac{1}{T^2}\right)^2 \delta T^2} \tag{16}$$

where δp and δT is the uncertainty of the ambient pressure and temperature given by the resolution of the laboratory barometer and the thermocouple, respectively.

All in all, Pitot tube velocity measurements uncertainty of the reported data was estimated to be lower than 10% within 95% confidence interval.

Chapter 3

Ciemat Artist Aerosol Tests

3.1. Introduction

This chapter describes the main results of the CAAT campaign oriented to get insights into the influence of particle nature on aerosol retention of a particle laden jet expanding from a tube breach across the bundle of tubes of a SG. As detailed in the scope of this work, inlet mass flow rate influence on aerosol retention was investigated in the range studied (i.e. 75-250 kg/h). The observations gathered provided relevant qualitative and quantitative insights into the filtering capability of a tube bundle and it highlighted key aspects on which further research should be focused on. Whenever feasible, comparisons to results from similar experimental programs (EU-SGTR, ARTIST partners) have been set.

3.2. State of art on aerosol retention across a tube bundle

No previous experimental studies oriented to assess the effect of particle nature on aerosol retention in a bundle of tubes have been found in the open literature. However, there exist several contributions related to the investigation of aerosol retention in tubes that will be briefly reviewed here in order to support the present research.

There is a lack of data regarding deposition in geometries similar to the one studied here. Most of the existing deposition correlations are referred to internal flows. There are some experimental studies on particle retention on single tubes (Douglas & Illias (1988), Wessel et al. (1988), Wong et al (1953), Ranz et al. (1952), Zhu et al.(2000)) as well as on dynamic adhesion of particles impacting on single tubes (Wang & John (1988), Pau (1982), Aylor et al. (1985)).

Douglas & Ilias (1988) obtained some experimental data for $Re_D<7200$ by exposing a tube inside a wind tunnel to an aerosol stream and collecting the mass retained on it afterwards. Despite scarcity and spreading of data he showed that retention efficiency roughly correlates with Stk number for $Stk\leq0.1$. Ranz et al. (1952) and Wong et al. (1953) performed similar experimental studies for $Re_D<450$ and $Stk>0.1$. Their results constitute a more consistent database of around 135 experimental data. Their data showed that, under the conditions studied, retention efficiency increases with Stk number.

Pau (1982) and Aylor et al. (1985) showed that particle rebound when colliding against a tube surface is a function of its kinetic energy. The sticking probability was measured to be near unity for kinetic energies below 10^{-12} J and dropped to <1% when kinetic energy was raised by one order of magnitude.

There are few investigations dealing with the particle retention across a bundle of tubes. In the bundle configuration, the retention of a tube differs to the one obtained in the single tube configuration since the “proximity effects” of adjacent tubes might influence deposition (Konstandopoulos et al. (1993)). In this case, the presence of neighbour tubes, modifies the flow field in the tube analyzed resulting in a different

aerosol retention efficiency and thus in a non-uniform deposition across the tubes of the bundle. Tsiang et al. (1982), McLaughlin et al. (1986) and Ingham et al. (1989) dealt with arrays of fibers in cross-flow for low Re numbers (which is out of the range of interest of the present research).

As previously described in the introduction chapter, the only available experimental research on particle retention efficiency of the tube bundle in the scenario under study is the EU-SGTR program. Herranz et al. (2006) showed that, for particles ranging an inlet d_{ae} between 4-7μm, the mass fraction retained in the tube bundle of the break stage (η) was inversely proportional to the square of the inlet gas mass flow rate (Φ) between 75-250 kg/h: They also showed that the influence of the breach type (i.e. guillotine or fish-mouth), its orientation and location within the bundle had a secondary importance with respect to the mass flow rate one.

3.3. Experimental facility and measurement procedure

3.3.1. Facility Description

The experimental campaign was carried out in the PECA-CAAT rig of the Ciemat Laboratory for Analysis of Safety Systems (LASS). Basically, the rig consists of a gas supply system, an aerosol generation device, a tube bundle and a measurement system (i.e., sampling and instrumentation). Fig. 49 shows a sketch of the facility and a top view of the tube bundle within the 8.3 m^3 vessel where it stands.

The bundle (330x300mm) is a mock-up of the break stage of the secondary side of a steam generator which was previously used in the CAHT campaign. In the CAAT campaign, it was used the guillotine type breach (axi-symmetric type) which has an open area equivalent to the circular section of one tube (Fig. 17). As detailed in chapter 2, materials and dimensions of tubes (except for tube height) and support plates are identical to those used in a real SG (Güntay et al., 2004). The whole structure is housed in a methacrylate frame and ends up with an upper plate simulating the separation between the break stage and the rest of the SG and was placed inside the PECA vessel (Fig. 49).

The instrumentation used and the facility configuration is similar to the one used in the CAHT free jet tests. Basically, a compressor feeds the injection line where the air is filtered and controlled through pressure and flow rate valves to achieve the desired conditions. Pressure and temperature sensors measure the final inlet tube conditions upstream the breach as well as the conditions at the bundle downstream the breach, at the bundle exit. A blower controls the pressure to ensure atmospheric conditions at the PECA vessel. During the test, room temperature was kept in the injected flow as well as in the PECA vessel. As in the CAHT experiments, the variables were controlled and logged every 700ms through the PLC of the laboratory.

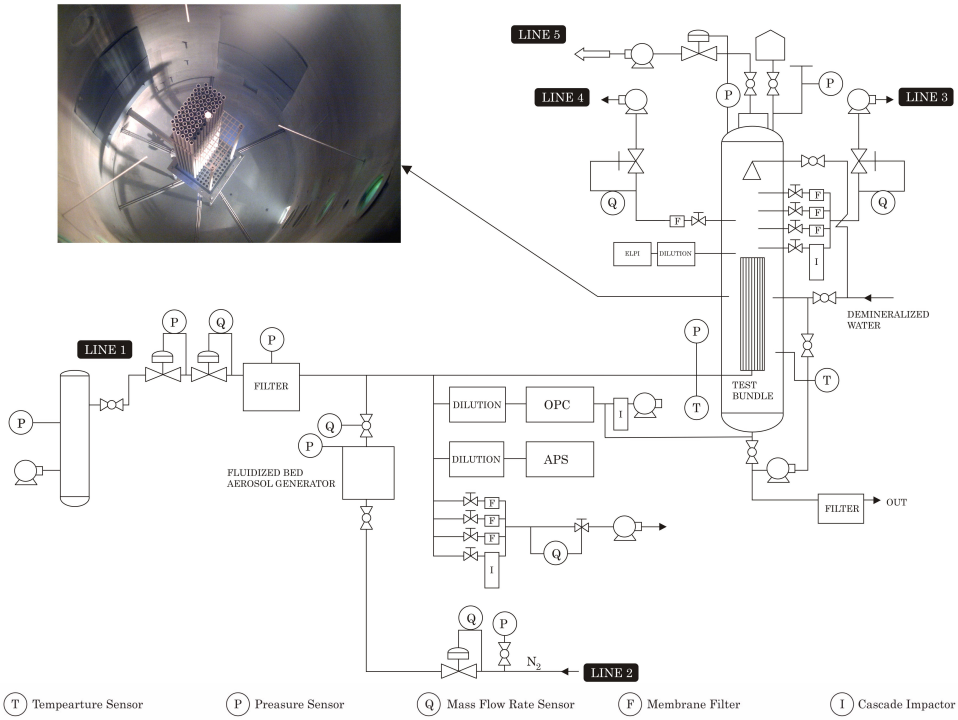

Fig. 49. Scheme of the PECA facility for CAAT.

The fluidized bed generator (FBG) used in the CAHT campaign was rearranged to produce the aerosol for the CAAT experiments. It was modified to permit the injection of up to 25kg/h N_2-seed-flow at high pressure (up to 1.5 relative bars). A Venturi cone placed at the exit of the FBG partially de-agglomerates the particles reducing the injected aerosol d_{ae}. The Venturi also permits to dilute the aerosol stream with clean air from a by-pass line. After the Venturi system, the diluted aerosol is injected into the main line. The main line is submitted to a contraction and converged into the final diameter used in the broken tube.

3.3.2. Instrumentation and sampling

During the experimental campaign it was used different general thermal-hydraulic instrumentation as well as specific aerosol instrumentation. Tables IX through XII describes briefly their main characteristics. Some of this instrumentation was not directly used in the CAAT experiments but in the calibration campaign that will be detailed in the following section.

Table IX. General instrumentation for PECA vessel and lines

Quantity measured	Device Method	Nº	Range	Accuracy
Pressure in PECA vessel and pipes	Pressure difference sensors	6	(-100)-200 mbar (-0.5)-0.5 bar, 0-5 bar, 0-7 bar, 0-10 bar	<1%
	Bourdon manometers	6	(-1)-3 bar, 0-1 bar, 0-2.5 bar, 0-4 bar, 0-7 bar, 0-10 bar	1%
Temperature vessel atmosphere fluid, walls	Thermocouples	2	0-180 ºC	0.3 K
	PT-100	2	0-100 ºC	0.2 K
Relative humidity sensor	Capacity sensor	2	0-100%	2%
Air supply system loop	Air compressor	1	19kW 0-240 kg/h < 4bar	5% flow <1% pres
Synthetic gas supply system loops	N_2, O_2, H_2, N_2+O_2	10 bottles rack	<3bar 0-750 Nl/min	<1% flow <1% pres
Exhaust depressurization loop	Radial turbine blower	1	4.4kW	<1% pres

Table X. Flow monitoring

Quantity measured	Device, Method	Nº	Range	Accuracy
Mass flow meters	Hot film sensors	3	0-30 Nl/min	<1%
	Thermal resistive sensors	4	0-50 Nl/min, 0-100 Nl/min 0-250 Nl/min, 0-750 Nl/min	<1%
	Rotameters	5	0-25 cc/min, 0-4 l/h 0-4.18 l/h, 0-15 m^3/h, 0-280 kg/h	2%
Flow meters	Orifice pressure difference sensor	1	0-250 kg/h	5%
	Pressure difference	2	0-350 cc/s, 0-3250 cc/s	3%

Table XI. Aerosol generation systems

Device Method	Specifications	Nº	Range
Fluidized Bed Generator	Solid aerosols	1	P size 1-10 μm 1-6.6 Nl/s
Monodisperse Aerosol Generator TSI Model 3475	Liquid aerosols Evaporation condensation method	1	P size 1-5 μm 0-250 l/h

Table XII. Aerosol size characterization instrumentation and sampling

Quantity measured	Device, Method	Nº	Range	
Concentration and particle size distribution.	Aerodynamic Particle Sizer (APS). On line measurements	1	d_p 0.5-20 μm 6±0.2 lpm	<1000 P/cm^3 <1.5 bar
	Electrical low pressure impactor (ELPI). On line measurements.	1	d_p 0.03-10 μm 10 lpm	<60ºC <2700 P/cm^3
Particle size distribution	Low pressure cascade impactor	3	d_p 0.41-12 μm 0.1-0.75 acfm d_p 0.25-15 μm 0.035-0.35 acfm d_p 0.028-9.88 μm 10 lpm	< 5 g/m^3
Concentration measurements	Absolute mass filters	6	<30 l/min	
Aerosol Diluter for sampling	APS diluter	1	dilution ratio 100:1	
	High temperature jet diluters	3	dilution ratio 8:1	

Characterization of particles incoming and outgoing the bundle is done by online measurements devices based on different fundamentals: OPC, APS®, ELPI® as well as by integral gravimetric systems: cascade impactors, membrane filters (Fig. 50). This instrumentation characterizes the aerosol size distribution and concentration upstream the broken tube and at the bundle exit.

Fig. 50. Instrumentation used for aerosol characterization and generation.

The position of the different instruments was decided based on the working limitations of each device (Table XIII):

Table XIII. Instruments working limitations summary

	ELPI DEKATI	OPC	APS TSI 3321	DEKATI Diluter
ΔP upper/lower stages	100 mbar ± 5			
Required Aerosol inlet pressure	1 bar	≤6 bar	1 bar	2 bar
Inlet Temperature	< 60ºC	<40º near lamp (adapted refresh)		0 - 450º
Maximal Concentration (5% error)		$0,3x10^5$ particules/cm^3	10% coincidence level	
Maximum measured current	$4*10^5$ fA ± 25			
Maximal count		65280 pulses/channel		

3.3.2.1. Aerosol measurement device fundamentals

3.3.2.1.1. Optical particle counter (OPC)

The OPC Polytec HC-15 is a particle size analyser. It measures the light scattered by single particles through a small, optically defined measuring volume located within the particle stream. The light scattered by the particles is collected by a photomultiplier and transformed into electrical pulses. Based on a calibration curve obtained for latex particles, the instrument relates voltage with particle size.

This measuring principle requires the measurement of single aerosol particle. The instruments impose limitations on the maximum particle size that should be smaller than 1/5 of the side of the measurement volume (150 μm^3), but also on the maximum aerosol concentration. This maximum concentration ($0.296.10^5$ particles/cm^3) is assigned to be the one that have a 5% probability that two or more particles are inside the measurement volume at the same time.

As a result, OPC provides optical diameter count distribution of a sampled aerosol. OPC provides the aerosol distribution that results from detecting (i.e. counting) particles during 60 seconds. After the sampling time, data are stored and the process can restart. This limits the device measurement capacity to 1 measurement every 4 minutes.

3.3.2.1.2. Aerodynamic particle sizer (APS)

The APS TSI 3321 is a time-of-flight spectrometer that measures time of flight of particles in an accelerating air flow through a nozzle. From a calibration curve, time of flight is converted into aerodynamic diameter.

In the instrument, particles are confined to the centerline of an accelerating flow by sheath air. They then pass through two parallel laser beams scattering light. Side-scattered light is collected onto photo-detector, which converts the light pulses to electrical pulses. By electronically timing between the peaks of the pulses (typically about 0.8-4.1μs), the velocity can be calculated for each individual particle. Velocity information is stored in a 1024 time-of-flight bins. Using a calibration curve based on latex particles, the APS converts each time-of-flight measurement to aerodynamic particle diameter. As a result APS provides on-line aerosol aerodynamic count distribution.

3.3.2.1.3. Electrical Low Pressure Impactor (ELPI)

ELPI is a particle sizer based on 3 elements: a charger, a low pressure cascade impactor and a charge detector. Fig. 51 shows a schedule of the structure and parts of the ELPI. During a measurement, particles are charged when passing through a high voltage electrical field in a Corona charger. Then, the aerosol flow passes through the jet nozzles of the successive 13 stages of the low pressure impactor. Particle larger than the cut size of the plate are collected and make an electrical current to be detected by the charger detectors connected to each impactor stage. A correlation curved converts charge into number of particles for each stage. As a result ELPI provides the on-line aerosol aerodynamic count distribution.

3.3.2.1.4. Mass cascade impactors and membrane filters

Mass cascade impactors use inertial impaction to differentiate particles by size when passing at high flow velocity through the nozzles of their successive stages. By pre-test and post-test weight of the stages the collected aerosol mass is determined and the mass aerodynamic size distribution of the aerosol is obtained.

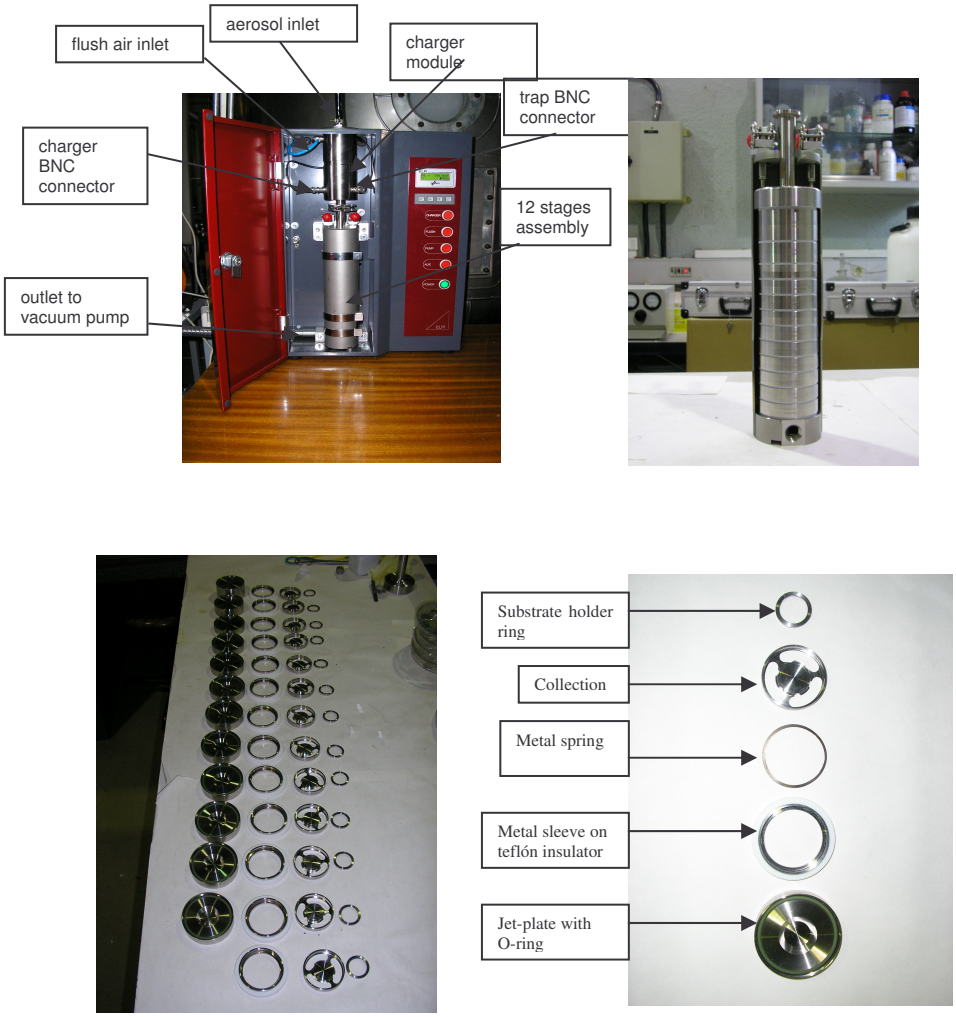

Fig. 51. ELPI structure and parts.

Mark III impactor (Fig. 50) classifies particles into 8 stages, from 0.69 μm to 15.7 μm. Andersen cascade impactor (Fig. 52) uses radial type nozzles and classifies the particles into 10 stages from 0.017 μm to 13.192 μm. Dekati impactor classifies particles into 13 stages from 0.028 μm to 9.88 μm.

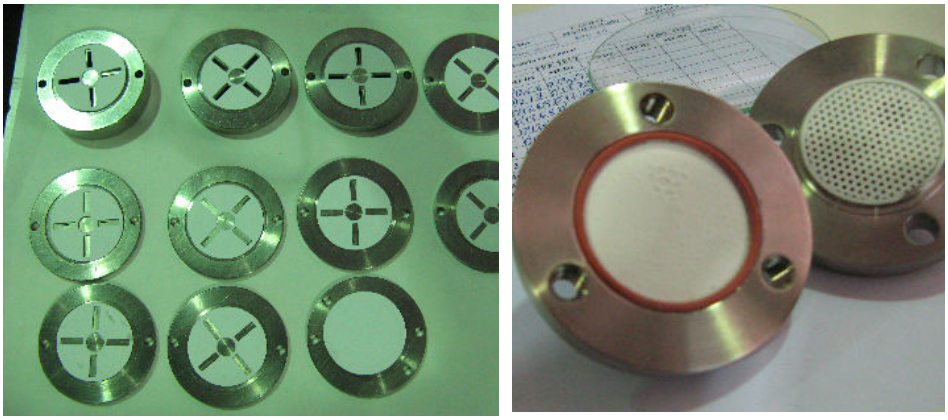

Fig. 52. Andersen impactor stages and membrane filter.

Membrane filters measure aerosol mass concentration $C_{in}(g/Nm^3)$ by sampling the aerosol using a vacuum pump during a certain time $\Delta t(s)$ at a controlled flow rate $G(Nm^3/s)$ and weighting the collected aerosol mass afterwards $m_{filt}(g)$:

$$C_{in}(g/Nm^3) = \frac{m_{filt}(g)}{\Delta t(s) \cdot G(Nm^3/s)} \quad (17)$$

3.3.2.2. Sampling and instruments layout

After the main line contraction to the final diameter of the broken tube and immediately before the entrance of the line in the PECA vessel, the inlet aerosol is characterized via three iso-kinetic samples (Fig. 53):

- One isokinetic sample is connected to a dilution battery consisting of an ejector type diluter and an APS type diluter reducing the pressure to ambient one and reaching a dilution of up to 1:800. After the dilution battery, the APS is connected.

- Another sample is connected to an ejector diluter resulting in a dilution of 1:8. After the ejector the OPC and a Dekati cascade impactor (hereafter Dek impactor) are connected in series. This configuration permits to compare the OPC light scattering measurements with the Dek impactor mass distribution measurements. However, it also limits the sampling time of the Dek impactor to the measurement time of the OPC (i.e. duty-cycle of 20% of the experiment time). Between OPC measurements, a by-pass loop allows sweeping the lens of the OPC to avoid particle deposition on them.

- The last isokinetic sample is divided in three branches where the membrane filters and Mark III cascade impactors are connected. From them, inlet concentration and integral aerosol mass distribution are estimated.

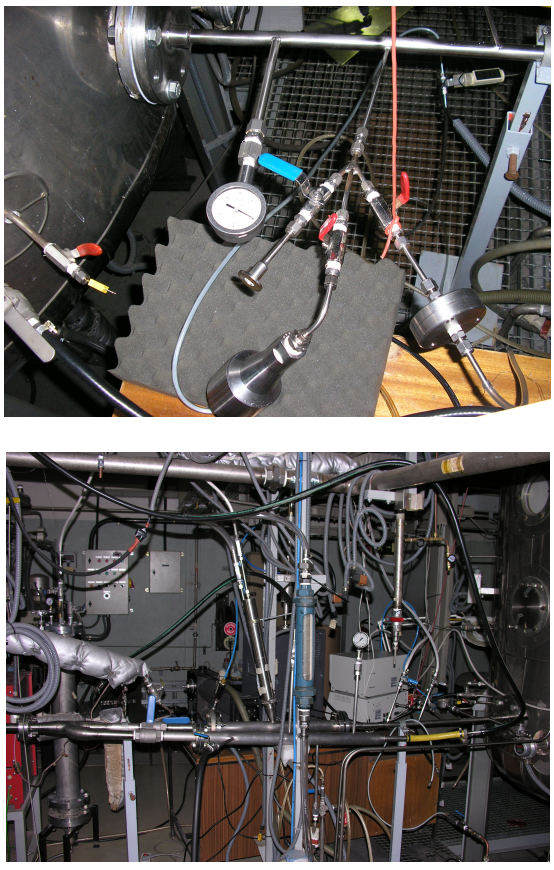

Fig. 53. Inlet isokinetic samples and inlet main line bypass.

At the exit of the bundle a collector permits the characterization of the outlet aerosol distribution via four atmospheric samples:

- One sampling is connected in series to an ejector diluter and the ELPI. This configuration permits the online characterization of the aerosol particle count distribution.

- Regarding the rest of isokinetic samples, two of them are connected to membrane filters and an additional one is connected to an Andersen cascade impactor to obtain aerosol concentration and aerosol mass distribution at the outlet of the bundle.

The aerosol deposits on tubes surfaces are also collected and weighted to characterize the deposition pattern in each tube of the bundle. The collection is performed by means of U-rings set around the base of each tube before the test and wet paper (i.e. after the U-ring collection, the tubes are swept with previously weight wet paper to collect the remaining deposits). A total of 18 U-rings are used and 23 wet paper samples are performed. Fig. 54 shows a picture of the U-rings and a layout of the tubes selected to collect the deposits with U-ring and wet paper techniques. Note that due to symmetry reasons, the configuration permits to map, nearly completely, the bundle deposition pattern.

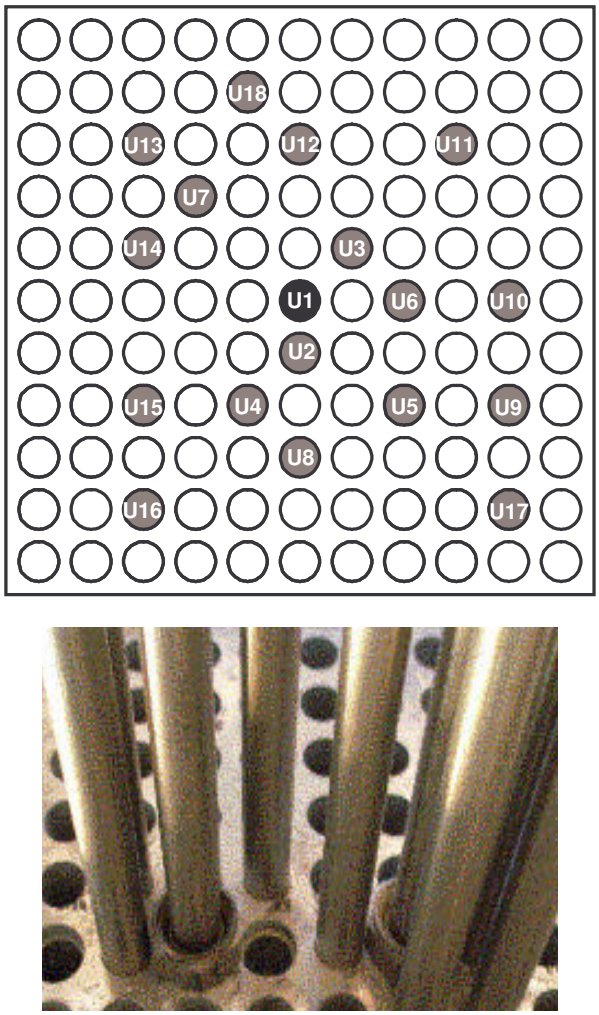

Fig. 54. Tubes selected for aerosol deposits collection and U-rings picture.

3.3.3. Test matrix and test protocol

The specific objectives of the experiments were to confirm and better quantify EU-SGTR observations, to assess the influence of the type of particles used in the aerosol on the retention efficiency of the tube bundle in the inlet gas mass flow rate range studied and finally to picture the deposition pattern across the tube bundle.

The design of the experimental matrix was based on the analysis of prototypical boundary conditions for the SGTR sequence and the LASS capabilities and limitations. The main aerodynamic-related variables and non-dimensional numbers prevailing in the CAAT experiments are similar to the ones of CAHT experiments and are shown in Table III. As can be realized, most of the CAAT variables are within the range of values anticipated in the SGTR scenario. The magnitude of gas velocities and other SGTR features were determined by simulating SGTR severe accident sequences with nuclear safety codes (Allison et al. 1995, Güntay et al. 2002). According to simulations, thermal and steam concentration gradients were not anticipated to play any role in the aerosol deposition. This made it feasible to focus attention on achieving aerodynamic scenarios as close as possible to the SGTR scenarios and to use air as the carrier gas.

A total of thirteen different tests were performed. Table XIV shows the experimental matrix set-up. The pressure conditions used in the experiments are the ones used in the CAHT experiments (Table V). The matrix is focused on two main variables: the type of particle used and inlet gas mass flow rate (from 75 to 250 kg/h).

Table XIV. CAAT test matrix

TEST	Inlet gas mass flow rate [kg/h]					PARTICLE NATURE		
	75	100	150	200	250	TiO_2 (Deg)	TiO_2 (Nph)	SiO_2
CAAT-01		X				X		
CAAT-02					X	X		
CAAT-03		X					X	
CAAT-04				X			X	
CAAT-05			X				X	
CAAT-06		X						X
CAAT-07			X					X
CAAT-08				X				X
CAAT-09		X						X
CAAT-10			X					X
CAAT-11					X			X
CAAT-12			X			X		
CAAT-13	X							X

TiO_2 and SiO_2 were chosen as aerosol compounds. Previous working experience with these materials and its insoluble nature were supposed to simplify both measurements and results analysis. Three different type of aerosols were used in the tests: TiO_2(Deg) from Degussa Inc. (Degussa, 2005), TiO_2(Nph) from Nanophase Inc. (Nanophase, 2002) and SiO_2 from Nagase Inc. (Nagase, 2006). TiO_2 aerosols are generated from nano-seeds agglomeration in the FBG, producing a polydispersed aerosol size distribution. SiO_2 aerosol is generated from 1-micron solid spheres producing a theoretical monodisperse aerosol size distribution.

The d_{ae} of the aerosol produced by the FBG ranged from 0.7 to 3 μm for TiO_2 particles whereas it was estimated to be around 1.4 μm for the SiO_2 particles. Fig. 55 shows SEM views of TiO_2 (Deg) and TiO_2 (Nph) and SiO_2 particles. As expected, TiO_2 particles are porous, fractal-like agglomerates. Thus, uncertainties related to the aerosol shape and density affected the characterization of this kind of particles. SEM analysis indicates that, even though the compound used is TiO_2 in both Deg and Nph powders, agglomerates show significant microscopic differences. Deg agglomerates show a smaller pore characteristic length than the one of Nph agglomerates and they also seem to have different grade of packing than the Nph ones. These differences may rise from the fact that the manufacturers used different generation processes to obtain the primary TiO_2 seeds.

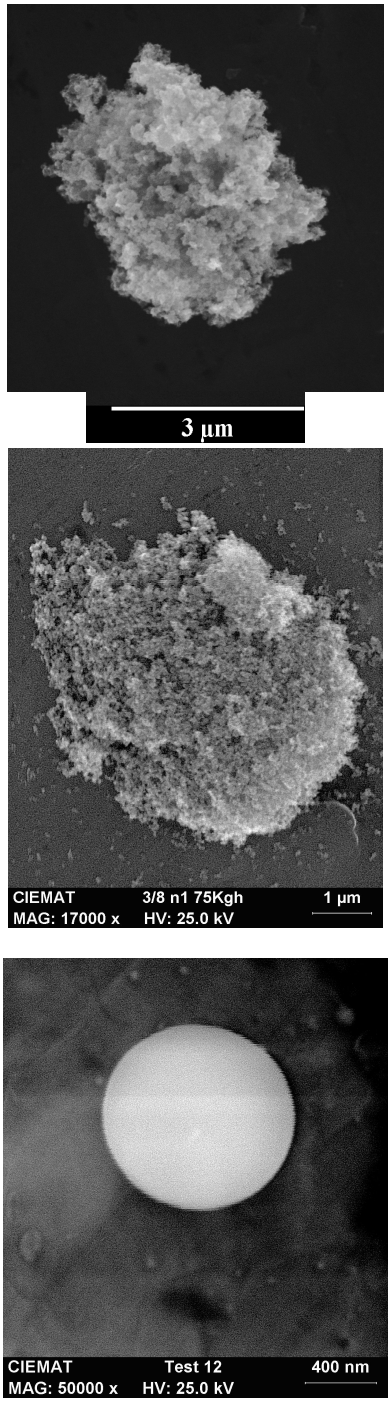

Fig. 55. SEM image of TiO_2 (Nph), (Deg) agglomerates and a SiO_2 particle.

The tests lasted between 45 and 60 minutes. This is a compromise value between the time needed for characterizing inlet and outlet size distributions with the integral measurements devices (i.e. impactors and filters) and the time that might saturate the ELPI stages. Once the desired thermal-hydrodynamic conditions are reached and stabilized, the aerosol injection and the inlet and outlet on-line measurements are started. Fig. 56 shows the schedule of the devices operation for CAAT-09. OPC and APS characterize the aerosol inlet size distribution, whereas ELPI measures the one at the exit of the bundle. Then, the integral gravimetric measurements are started in a synchronized way at the inlet and at the outlet of the bundle so that instantaneous DF values could be obtained. A total of 8 membrane filters and 2 cascade impactors are used in each test. The measurements are performed in five series. Usually, membrane filters sample last around 5 minutes and impactor sample last from 10 to 20 minutes depending on the aerosol compound. Once the gravimetric measurements are finished, the aerosol injection is finished and a resuspension phase is initiated. In this phase, the thermal-aerodynamic conditions are kept steady for 10 additional minutes and the on-line devices are kept measuring to estimate potential resuspension of previously deposited particles.

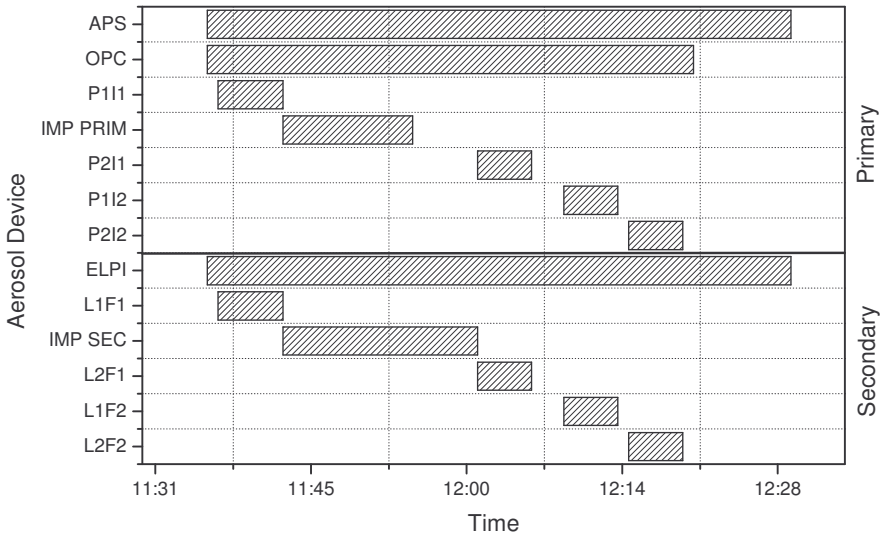

Fig. 56. Aerosol measurement schedule of CAAT-09.

After the tests, the bundle shroud is dismounted and the U-rings are slide along each tube without dismounting it. This way the mass retained is collected avoiding the fall of the deposits. After that, the tubes are washed with wet paper to collect any additional aerosol deposit that remains in the tube.

The mass retention efficiency of the tube bundle was estimated by Eq. 18 where $m_{in} = m_{ret} + m_{out}$.

$$\eta = \frac{m_{ret}}{m_{in}} 100 = \frac{m_{ret}}{m_{ret} + m_{out}} 100 \qquad (18)$$

In order to estimate the total aerosol mass deposited in the tubes (m_{ret}) an extrapolation was needed from the sampled tubes. Taking into account the symmetry of the deposition profile, samples presented in Fig. 52 can be arranged and grouped (Fig. 57). Based on that, the extrapolation method is simply given by the following expression:

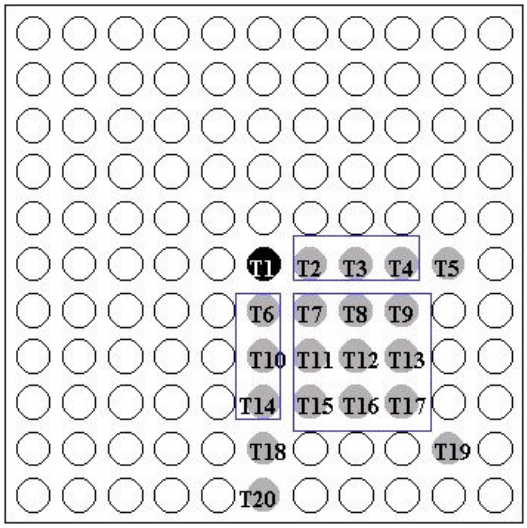

Fig. 57. Tube grouping for in-bundle mass estimate.

$$m_{ret} = M(T1) + 2M_{F1} + 2M_{F2} + 4M_{square} + 72 < m > \qquad (19)$$

where M_{F1} and M_{F2} denotes the sum of the masses of tubes T2, T3, T4 and T6, T10, T14, respectively, as shown in Fig. 57; M_{square} means the mass collected in the 3x3 tube square shown in the figure; and, finally, m is the mean mass of outer tubes (in this case T5, T18, T19 and T20), being 72 the number of outer tubes in the bundle.

Estimation of the mass leaving the bundle (m_{out}) was done from the extrapolation of the mass concentration measurements performed by membrane filters at the exit of the

bundle during the tests. More details of the CAAT experimental measurement method qualification can be found in Appendix III.

3.4. Calibration campaign

Previous to CAAT experiments, a calibration campaign was carried out to find out possible correlations among OPC, APS and ELPI measurements (Velasco et al, 2007). Since the three on-line devices rely on different physical measurement principles to estimate particle size (light scattering, time of flight, charge counting, respectively), and they are usually calibrated against latex particles, it is of an outstanding importance to asses their differences in the size estimation of "non-ideal" aerosol particles. Actually, when these instruments are used to measure aerosol particles of different nature, or physical properties than latex, the aerodynamic obstacles and/or flow shear stresses that the particles may suffer inside the device until reaching the measuring volume can make them, in case of powder agglomerated particles, to re-agglomerate and/or fragmentize. All these process may modify the original sampled aerosol and mislead in the estimation of the particle size distribution. As a result, different devices measuring the same aerosol sample provide both quantitative and qualitative different particle size distributions. These differences results in an uncertainty of the real aerosol particle size distribution that is being sampled. The pre-CAAT calibration campaign permitted to estimate these differences and to quantify the uncertainty in the characterization of aerosols expected during the CAAT experiments.

During the calibration campaign four different instruments (OPC, ELPI, APS and Mark III mass cascade impactor) were used in different configurations (in parallel and in series with the aerosol source and/or with different dilution stages) to measure monodisperse DEHS particles and/or polydisperse TiO_2 (Deg) agglomerates.

DEHS tests permitted the comparison of APS-ELPI, APS-OPC and ELPI–OPC. DEHS is a reference aerosol generated from an evaporation-condensation generator (Monodisperse Aerosol Generator TSI 3475), generally used for calibration purposes. Table XV shows the experimental test matrix used in these experiments.

Table XV. Test matrix for monodispersed aerosol calibration campaign.

Test Serie	Particle Size (µm)					Number Concentration (#/cm^3)	
	1.2	1.6	1.8	2	3.3	$1.3 \cdot 10^6$	$0.39 \cdot 10^6$
1	X					X	
2		X				X	
3			X			X	
4				X		X	
5					X	X	
6		X					X
7			X				X

Fig. 58.OPC-ELPI configuration with diluters for a DEHS test.

This comparison showed systematic differences found in the estimation of mean, median, mode and GSD of the aerosol size distribution for this type of spherical monodisperse particles. From DESH campaign, several observations were made:

- APS provided higher values of mean, median and GSD than ELPI systematically (25% of difference for mean and median and 40% difference for GSD). Mode estimation was similar. These differences are considered acceptable taking into account the order of magnitude in uncertainties of the available aerosol measurement devices assessed in the uncertainty analysis section.

- APS-OPC comparison showed that when the aerosol inlet pressure changed, the particle size distribution measured by APS changed considerably whereas it remained nearly invariable for OPC. This result indicated the need of a dilutor stage before APS to reduce inlet pressure during CAAT tests.

TiO_2 polydispersed tests permitted the comparison of APS-ELPI-Mark III cascade impactor for the thermal-hydrodynamic conditions of CAAT experiments using Deg agglomerates generated from the FBG. Table XVI shows the experimental test matrix used. Inlet mass flow rate was varied from 75 to 250 kg/h. The experiments were performed in the PECA-CAAT main line at the inlet isokinetic samples. The devices configuration and dilution stages were the ones used afterwards in the CAAT experiments. The main results of the campaign can be summarized as follows:

Table XVI. Test matrix for polydispersed aerosol calibration campaign.

Test Serie	Inlet Pressure (bar abs)			Gas mass flow rate (kg/h)		
	1.2	1.6	2.2	75	150	250
8	X			X		
9	X			X		
10			X			X
11			X			X
12		X			X	
13		X			X	
14			X			X
15		X		X		

- Systematic differences were found between APS and ELPI in the estimation of aerodynamic mean, median and mode. APS showed higher values than ELPI for these parameters. APS-ELPI GSD estimations did not show any systematic difference. In this case, values are in the same range within a band of dispersion.

- Mark III mass cascade impactor showed systematic higher values than ELPI (mass weights) in the estimation of aerodynamic mass mean, median and mode (2.5µm of shift for mean, 2.5µm of shift for median and 0.7µm of shift for mode). GSD estimations did not show any systematic difference.

- The shape of the particle size distribution obtained for APS and ELPI showed different tendencies for bins of aerodynamic diameter lower that 0.9µm

whereas it showed similar tendencies for bins of aerodynamic diameters higher than this value.

The systematic differences found between the instruments can be partially explained by the measurement range of each device. This range differs both in width and bin size. For example, APS measures from 0.5µm to 20µm whereas ELPI measures from 0.03µm to 9.9µm. Thus, the estimation of mean, median, mode and GSD of a theoretical particle size distribution with APS and ELPI will be different. Another source of error comes from the fact that APS measures aerodynamic count diameter whereas ELPI distinguish particles based on inertia in its impactor. Thus, it is actually distributing particles by an aerodynamic mass diameter criterion even though its output is provided in aerodynamic count diameter. The conversion from the former to the latter is performed by a calibration curve that relates charge with counts based on spherical latex particles.

The differences in the measurements found in the pre-CAAT calibration campaign were considered and quantified for the device uncertainty estimation. This estimation was done by comparing the particle size distributions in the region of intersection of the measurement range of the instruments. The distributions have been normalized by the total number of counts (or mass) in the area studied and each bin, by the diameter logarithm,

$$\mathrm{dLog}(\mathrm{Dp}) = \log_{10}\left(\frac{\mathrm{Dp}_{i+1}}{\mathrm{Dp}_i}\right) \tag{20}$$

where i is the computed stage or just normalizing the bin by the bin width dD_p. Fig. 59 shows the particle size distribution measured simultaneously for a TiO_2 (Deg) aerosol under CAAT experimental conditions for APS and ELPI. Comparisons have been based on the fraction of particle counted in each bin per unit of diameter logarithm. Both, qualitative and quantitative differences can be observed. Important uncertainties affect the description of the aerosols size distributions for particle aerodynamic diameters smaller than 0.9µm, whereas both devices estimate a similar distribution for particle aerodynamic diameters bigger 0.9µm.

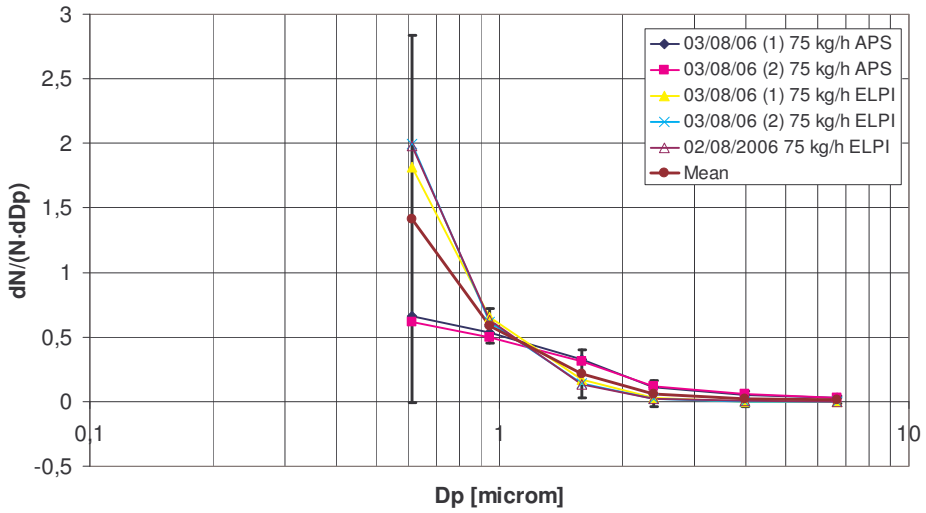

Fig. 59. Estimated uncertainty associated to TiO_2 aerosol size distribution from APS and ELPI measurements.

3.5. Uncertainty analysis

Uncertainty in the measurement of retention efficiency was quantified by error propagation calculus from the measured quantities, following ISO guidelines (ISO, 1995):

$$\eta = \frac{m_{ret}}{m_{in}} 100 = \frac{m_{ret}}{m_{ret} + m_{out}} 100 \quad \Rightarrow \quad \delta\eta = \sqrt{\left(\frac{\partial \eta}{\partial m_{ret}} \delta m_{ret}\right)^2 + \left(\frac{\partial \eta}{\partial m_{out}} \delta m_{out}\right)^2} \qquad (21)$$

with

$$\frac{\partial \eta}{\partial m_{ret}} = \frac{m_{out}}{(m_{ret} + m_{out})^2} 100 \text{ and } \frac{\partial \eta}{\partial m_{out}} = \frac{m_{ret}}{(m_{ret} + m_{out})^2} 100 \qquad (22)$$

where the uncertainty of each term in the retention efficiency formula has to be derived following the measurement chain used:

m_{ret} is extrapolated from measured from the collection of tubes mass using U-ring and wet paper techniques. After a systematic study to asses the uncertainty in the gravimetric measurements, δm_{ret} was estimated to be 10% of the measured mass m_{ret} with a minimum value of 1 gram.

m_{out} is estimated from membrane filters measurements at the oulet of the bundle, through the formula:

$$m_{out} = \frac{\overline{C}\left(g/m^3\right)\cdot\overline{\Phi}\left(kg/h\right)\cdot\Delta t\left(min\right)}{60\left(min/h\right)\cdot\rho\left(kg/m^3\right)} \tag{23}$$

were the symbol $\overline{\ }$ represents the average of the magnitude during the experiment. The corresponding uncertainty results:

$$\delta m_{out} = \sqrt{\left(\frac{\partial m_{out}}{\partial\overline{\Phi}}\delta\overline{\Phi}\right)^2 + \left(\frac{\partial m_{out}}{\partial(\Delta t)}\delta(\Delta t)\right)^2 + \left(\frac{\partial m_{out}}{\partial\rho}\delta\rho\right)^2 + \left(\frac{\partial m_{out}}{\partial\overline{C}}\delta\overline{C}\right)^2} \tag{24}$$

Thus, the calculus of δm_{out} requires the estimation of four uncertainties which can be assessed by the by the standard deviation in time of the variable and the resolution of the measurement device:

$$\delta\overline{\Phi} = \sqrt{(\sigma_\Phi)^2 + \delta\Phi^2} \approx \sigma_\Phi \tag{25}$$

$$\delta(\Delta t)=1s \tag{26}$$

$$\delta\rho(p,T) = \sqrt{\left(\frac{\partial\rho}{\partial p}\delta p\right)^2 + \left(\frac{\partial\rho}{\partial T}\delta T\right)^2} = \sqrt{\left(\frac{1}{R_g T}\delta p\right)^2 + \left(-\frac{p}{R_g T^2}\delta T\right)^2} \tag{27}$$

$$\delta\overline{C} = \sqrt{(\sigma_C)^2 + \delta C^2} \tag{28}$$

were the estimation of the uncertainty in the measurement of concentration through a membrane filter δC requires the analysis of the measurement change used in a filter:

$$C\left(g/m^3\right) = \frac{\Delta m(g)}{\frac{G_s\left(Nl/min\right)}{10^3\left(l/m^3\right)}\frac{1.29\left(kg/Nm^3\right)}{\rho\left(kg/m^3\right)}\cdot\frac{\Delta t(s)}{60(s/min)}} \tag{29}$$

and the associated uncertainty is:

$$\delta C = \sqrt{\left(\frac{\partial C}{\partial(\Delta m)}\delta(\Delta m)\right)^2 + \left(\frac{\partial C}{\partial(\Delta t)}\delta(\Delta t)\right)^2 + \left(\frac{\partial C}{\partial G_s}\delta G_s\right)^2 + \left(\frac{\partial C}{\partial\rho}\delta\rho\right)^2} \tag{30}$$

where $\delta(\Delta m)$ was estimated following the same criteria that δm_{ret}, and

$$\delta G_s = \sqrt{(\sigma_{G_s})^2 + \delta G_s^{\,2}} \approx \sigma_{G_s} \tag{31}$$

Finally, table XVII summarizes the order of magnitude of the relative uncertainty obtained from the different measurement techniques used in the CAAT.

Table XVII. Uncertainty estimation for different measurements techniques

Measurement technique	UNCERTAINTY ORDER OF MAGNITUDE $\frac{\delta(f)}{f}$	COMENTS
Membrane Filters	~10^{-1}-10^{-2}	Integral. Uncertainty with the balance. Important to repeat the weight several times
Cascade Impactors	~10^{-1}	Integral. Uncertainty with the balance. Repeat the weight several times. Lost of mass in the manipulation of the stages
OPC, APS, ELPI size distributions	d_{ae}>0.9μm ⇒ ~10^{0}-10^{-1}	Pre-CAATs differences of 50%
	d_{ae}<0.9μm ⇒ ~10^{0}	Pre-CAATs differences of 50-100%
OPC, APS, ELPI concentration	~10^{1}	Pre-CAATs differences of 50-1500%
d_{ae}, GSD Impactors	~10^{0}	Pre-CAATs differences of 100-200%
OPC, APS, ELPI mean count	~10^{0}	Pre-CAATs differences of 300%
OPC, APS, ELPI median count	~10^{0}	Pre-CAATs differences of 400%
OPC, APS, ELPI mode count	~10^{0}	Pre-CAATs differences of 100%
OPC, APS, ELPI GSD count	~10^{0}	Pre-CAATs differences of 50%
Mass Balance	~10^{1}-10^{2}	High loss of mass in the bundle dismount, base, support plate and lines.

3.6. Results and discussion

3.6.1. General observations

Table XVIII summarizes the major results of the experiments in terms experiments in terms of mass retention, in-bundle retention efficiency and decontamination factor. A detailed description of the experiments execution and measurements output can be found in Appendix IV.

Table XVIII. Experimental results and boundary conditions.

Test Number	1	2	3	4	5	6	7	8	9	10	11	12	13
Particle nature	TiO_2 (Deg)	TiO_2 (Deg)	TiO_2 (Nph)	TiO_2 (Nph)	TiO_2 (Nph)	SiO_2	SiO_2	SiO_2	SiO_2	SiO_2	SiO_2	TiO_2 (Deg)	SiO_2
Φ (kg/h)	93.4	225.0	99.7	169.0	125.0	105.8	148.4	183.7	133.96	167.1	237.0	145.0	81.4
$\delta\Phi/\Phi$ (%)[6]	19	2	17	37	13	3	2	16	3	7	19	2	4
Δp_{breach} (bar)	0.2	1.4	0.1	1.2	0.2	0.6	0.2	0.5	0.1	0.5	0.8	0.5	<0.1
Inlet d_{ae} (μm)	2.5	2.5	1.5	2.8	2.6	2	2.1	1.3	1.6	2.0	1.7	3.2	1.3
Inlet GSD	2.5	2.4	2.3	2.5	2.4	2.1	2.4	1.5	2.1	2.2	2.3	2.6	2.2
m_{ret} (g)	5.30	1.29	17.46	10.26	9.22	2.39	0.86	28.27	69.72	30.11	8.93	2.82	32.45
δm_{ret} (g)	1	1	1.75	1.03	1	1	1	2.83	76.98	3.01	1	1	3.25
m_{out} (g)	13.98	8.23	92.68	64.98	49.15	1.62	0.94	5.34	4.32	2.29	2.10	17.34	7.50
δm_{out} (g)	4.49	5.32	49.87	37.64	23.53	1.21	1.40	2.64	2.79	1.34	1.17	8.01	4.38
η (%)	27.48	13.53	15.85	13.64	15.79	59.47	48.03	84.11	94.16	92.94	80.93	14.00	81.24
$\delta\eta$ (%)	7.42	11.82	7.30	6.92	6.53	20.66	47.14	6.75	3.59	3.91	8.75	7.01	9.05
$\delta\eta/\eta$ (%)	27	87	46	50	41	34	98	8	4	4	11	50	11
DF	1.38	1.16	1.19	1.16	1.19	2.47	1.92	6.29	17.14	14.16	5.24	1.16	5.33

[6] δx represents the uncertainty associated to a variable x and estimated following the procedure of ISO Norm (1995).

As noted, a mass fraction lower than 30% was retained in the tube bundle for TiO_2 agglomerates, whereas it was notably higher (around 85%) for SiO_2 particles. This difference indicates that particle nature influences retention. CAAT-06 and CAAT-07 experiments reached one order of magnitude less aerosol concentration during the tests, so that the resulting uncertainty was too high for them to be considered. Hence, they were disregarded in the overall experiments discussion.

All in all, retention was nonuniform all over the tube bundle. The deposition of particles was observed to be uneven both radially and axially. The deposits surface density of aerosol mass decreased with radial distance from the breach. On the closest tubes thick and dense deposits were built-up, whereas deposits looked more spread farther away from the closest tubes. From the fourth tube row on, deposits surface density became very small.

Particle nature was observed to affect not just the overall retention, but also the deposition pattern. To illustrate this statement, the bundle can be split in two regions: the neighbor tubes and the rest of the bundle. Fig. 60 shows three pictures of the aerosol deposit distribution over the tubes surrounding the broken one for TiO_2 (Nph), TiO_2 (Deg) and SiO_2 tests. In the case of TiO_2 tests, hill-shaped deposits were built-up (in some cases they underwent sloughing when they reached a critical size). TiO_2(Nph) hill-shaped deposits resisted on tubes longer than TiO_2(Deg) ones, which fell-off easily and left a clean area on the tube surface. At the center of this region, it can be found a “spot” of noticeable surface density but negligible thickness. Very often, the hill-shaped deposits were found on the base of the tubes at the end of the experiments. By illuminating the bundle during the experiments using a laser extinction method, TiO_2(Deg) deposits were observed to get resuspended from the tube base after falling, whereas TiO_2(Nph) remained on the base. This indicates that TiO_2(Nph) particles are stickier and harder to remove from surfaces than the TiO_2(Deg) ones and that the deposits of the Deggusa powder are lighter and/or more loosely packed than the Nanophase ones. In addition, TiO_2 deposits patterns showed small, clean slot-type regions at both sides of the deposit peak close to the hill-shaped deposits.

In the case of SiO_2 tests, deposits were found to be significantly different from TiO_2 ones. The clean area was considerably extended and the aerosol deposits appeared further away from the breach. No hill-shaped deposits were found on the tubes in SiO_2 tests. Instead, there were found “spots” of noticeable surface density but negligible thickness, similar to the ones found in the TiO_2(Deg) tests but much shorter. Since eventually some tiny deposits appear also at the base of the tubes, this might indicate that SiO_2 deposits are heavier than the TiO_2(Deg) ones.

Fig. 60. Deposits found after TiO_2 (Nph), TiO_2 (Deg) and SiO_2 experiments.

Regarding the region further than the first neighbor tubes, Fig. 61 presents the deposited mass on tubes for two different tests (1/4 of the bundle is shown). Deposition profiles were notably different, TiO_2 (Nph) (a) resulted in a deposition

pattern with a sharp decrease where the neighbor tubes to the broken one have an important contribution to the total mass (2F deposit was found at the base), while SiO_2 ones (b) showed a milder decrease of the tube deposition with the distance to the break. Regardless deposition profiles, on-tube surface retention amounted to more than 80% of the total mass depleted; most of the remaining 20% was located on the lower plate and it was eventually observed to come from total or partial detachments of tube deposits (sloughing).

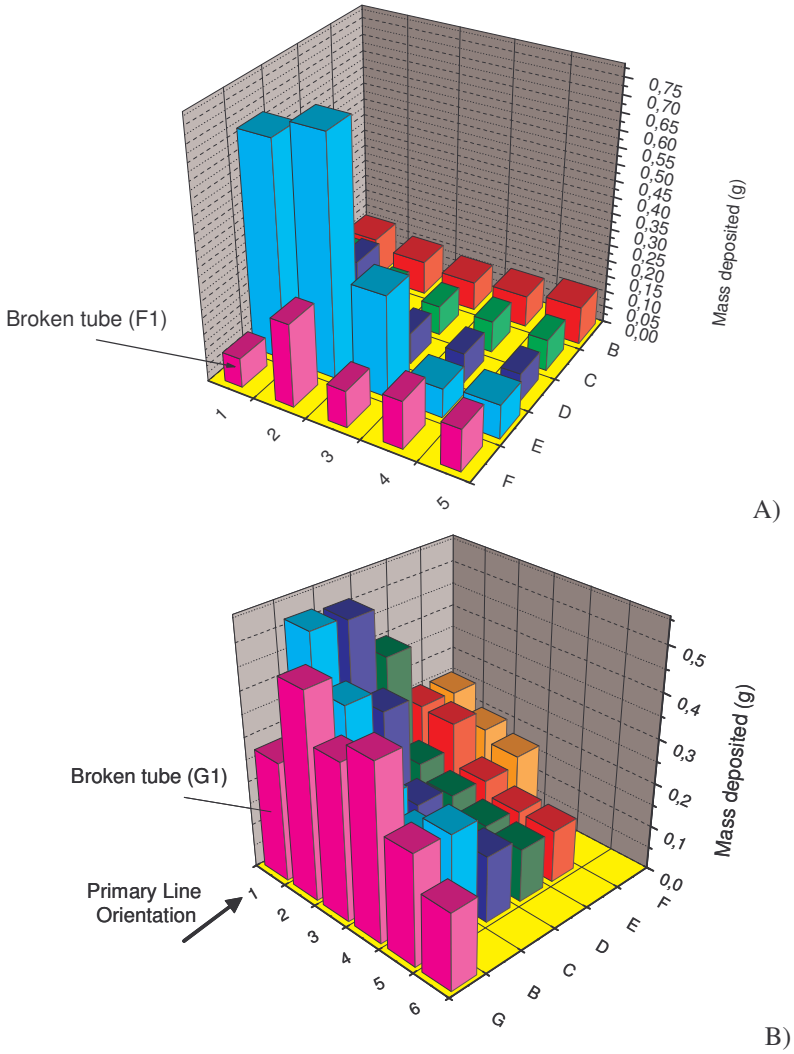

Fig. 61. Mass deposition profiles on the tubes near the broken one for different aerosol type tests.(a) TiO_2 (Nph).(b) SiO_2.

The aerodynamic investigation of the scenario under study (Velasco et al. 2008, Velasco et al. 2007, Herranz et al. 2005, López del Prá et al. 2007) permitted to get insights into the distribution of the aerosol deposits found. The gas exiting the breach approached the adjacent tubes at high velocity and it lost much of its momentum in the perpendicular direction to the tube axis. The Coanda effect enhances the adhesion of the gas to tube surface when the jet impinges on the neighbor tubes to the broken one, so that the vertical component of the gas trajectory is reinforced. The combined action of both processes would have resulted in the final jet trajectory observed through the tubes deposits (Fig. 24) as well as in the axial extension of the deposits in the wake of the tubes over the jet center trajectory line.

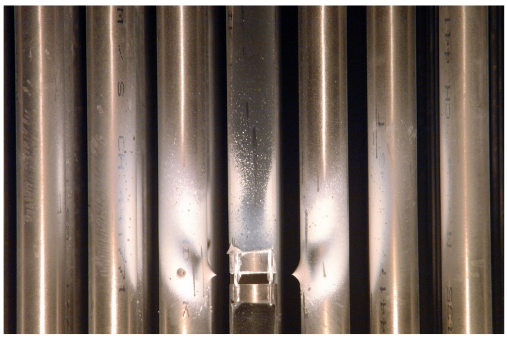

Fig. 24. Deposition pattern close to the breach for a TiO_2 experiment.

Fig. 62. Tube deposits detail for a TiO_2 experiment.

The jet generated from the breach impinges on the neighbour tubes at high velocity and it smashes particles against the tubes generating the hill-shaped deposits and/or the "spots" of noticeable surface density and negligible thickness. These "spots" would be related to compressed aerosol deposits that remained on tube at the center of the jet impinging region (i.e. in the stagnation zone) where the jet pressure on the tube surface is maximum. Around the stagnation zone, it appears a wall-jet region where the flow diverges, re-accelerates and spreads around the tube surface. This region is covered by deposits of relatively high surface density indicating that the wall-jet region is very effective in depleting aerosol particles.

Fig. 62, shows the deposit found in a tube facing the breach. In the upper part of the figure, it can be noticed a region where the wall-jet detaches from the surface and deposits disappear. This region is characterized by an increment of the surface roughness of the deposits that might be related to the transition of the wall-jet to turbulent regime and the subsequent increase of turbulence intensity and friction velocity in the area found in CFD simulations (Herranz et al., 2005).

In addition, Velasco et al. (2008) pointed that a gas vortex developed in the gap between the broken tube and the adjacent ones (Fig. 24). These results support the above interpretation on aerosol deposition. The deposits found on the broken tube over the breach would have been mainly driven by the eddy and/or recirculation region effect.

The clean slot-type regions at both sides of the hill-shaped deposits (Fig. 24) are located right where the jet touches the wall surface tangentially and the shear stress over the surface is maximum. Namely, the jet has a sweep effect on that region of the tube surface.

In the case of SiO_2 tests, the clean areas are considerably extended and cover practically the whole jet impinging region indicating that, at the flow conditions investigated, SiO_2 particles do not remain on the surface after impacting. Aerosol deposits appear downstream the jet impingement, in the wall-jet region where the flow surrounds the tube at lower velocity and disappears in the separation line where flow stream detaches and the tube wake incepts.

3.6.2. Influence of matrix variables

The experimental data obtained during the CAAT campaign were discussed in terms of mass retention efficiency of the bundle. This efficiency was studied and analyzed as a function of three primary variables: particle nature (agglomerates vs solid spheres), inlet gas mass flow rate (Φ) and inlet aerodynamic median diameter (inlet d_{ae}). Occasionally, data from other programs carried out under similar conditions have been considered to show a more complete picture of the scenario under analysis.

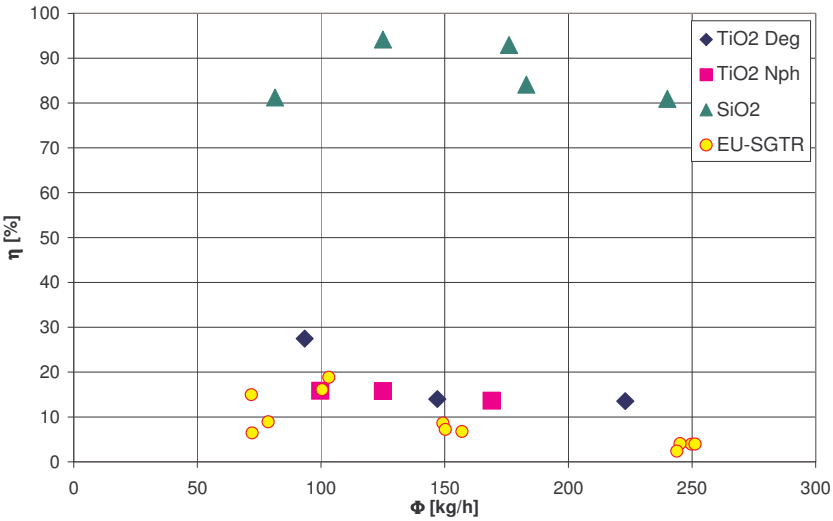

Fig. 63. Mass retention efficiency as a function of the inlet gas mass flow rate for CAAT and EU-SGTR experiments.

Fig. 63 shows the bundle retention efficiency versus inlet gas mass flow rate for the CAAT experiments. For comparison purposes, data from Herranz et al. (2006), which were based on TiO_2 (Nph) agglomerates, were also included (denoted as EU-SGTR). The figure shows that efficiency was strongly dependent on particle nature: SiO_2 particles were efficiently removed from the gas flow (retention efficiency ≥ 80%), whereas TiO_2 particles underwent substantially less net deposition (retention efficiency < 30%). In absolute terms, efficiency variation (η_{max}-η_{min}) was similar for both types of particles (around 15% in retention efficiency units). However, in relative terms the variation was different. SiO_2 variation represented hardly 16% of the mean efficiency value whereas TiO_2 variation represented around 50% of the mean efficiency value. In other words, TiO_2 particles were more sensitive to gas mass flow rate than SiO_2.

In order to focus the analysis just on the gas mass flow rate effect, a "non-dimensional" efficiency has been defined for each particle type as:

$$\bar{\eta} = \frac{\eta - \eta_{ref}}{\Delta\eta_{max}} \tag{32}$$

where η_{ref} is a reference efficiency taken to be the asymptotic value of efficiency when flow rate tends to very high values for each type of particles, and $\Delta\eta_{max}$ is the maximum efficiency difference (i.e., η_{max}-η_{ref}).

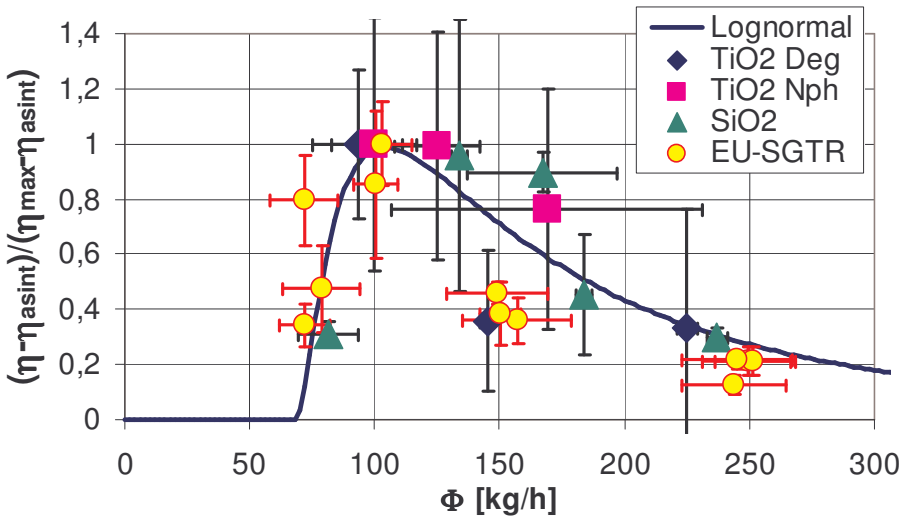

Fig. 64. Nondimensional mass retention efficiency as a function of the inlet gas mass flow rate for CAAT and EU-EU-SGTR experiments.

Fig. 64 shows that $\bar{\eta}$ behavior is similar regardless particle type: it increases up to a maximum value with the inlet gas mass flow rate (roughly located at 100 kg/h) and, then, it decreases monotonously. This evolution can be well correlated by a log-normal function,

$$\bar{\eta} = \frac{a_4}{\sqrt{2\pi}\cdot(\Phi - a_1)a_2}\exp\left(-\frac{\left(\mathrm{Ln}\left(\frac{\Phi - a_1}{a_3}\right)\right)^2}{2(a_2)^2}\right) \tag{33}$$

where the parameters a_1, a_2, a_3 are know as the location, scale and the shape parameters, respectively, and a_4 is a multiplicative factor. Note that Φ is in kg/h units. The values proposed for this fitting are: a_1=67.27, a_2=1, a_3=100 and a_4=150 with an average relative cuadratic error of 8%. Thus, the retention efficiency sensitivity to gas mass flow rate follows a lognormal behaviour. As a result, the TiO_2 and SiO_2 retention efficiency evolutions with the inlet gas mass flow rate can be described by Eqs. 34 and 35, respectively (Fig. 65):

$$\eta(\%) = \frac{3000}{\sqrt{2\pi}\cdot(\Phi - 67.27)}\exp\left(-\frac{\left(\mathrm{Ln}\left(\frac{\Phi - 67.27}{100}\right)\right)^2}{2}\right) \tag{34}$$

$$\eta(\%) = \frac{3000}{\sqrt{2\pi}\cdot(\Phi - 67.27)}\exp\left(-\frac{\left(\mathrm{Ln}\left(\frac{\Phi - 67.27}{100}\right)\right)^2}{2}\right) + 77 \tag{35}$$

where Φ is in kg/h units. The averaged relative cuadratic errors of the equations are 39% and 16%, respectively.

Underlying the above discussion on $\bar{\eta}$, Eqs. 34 and 35 are curves of the same family. The lognormal behavior of retention efficiency with inlet gas mass flow rate is consistent with the reported decreasing trend by Herranz et al. (2006) as $\eta \propto \Phi^{-2}$ for Φ>100 kg/h for TiO_2 particles (Eq. 1, Fig. 65):

$$\eta(\%) = \frac{\zeta}{\Phi^2} \quad with \quad \zeta = (1.81 \pm 0.7) \cdot 10^5 \left[\frac{kg}{h}\right]^2 \tag{1}$$

As observed, addition of PSI (2008) data obtained in similar ranges of particles size and higher gas mass flow rates in Fig. 65 supports the discussions above. It is worth to remark that PSI experiments used the same manufacturer than the one used in CAAT and EU-SGTR experiments for both TiO_2 and SiO_2 particles.

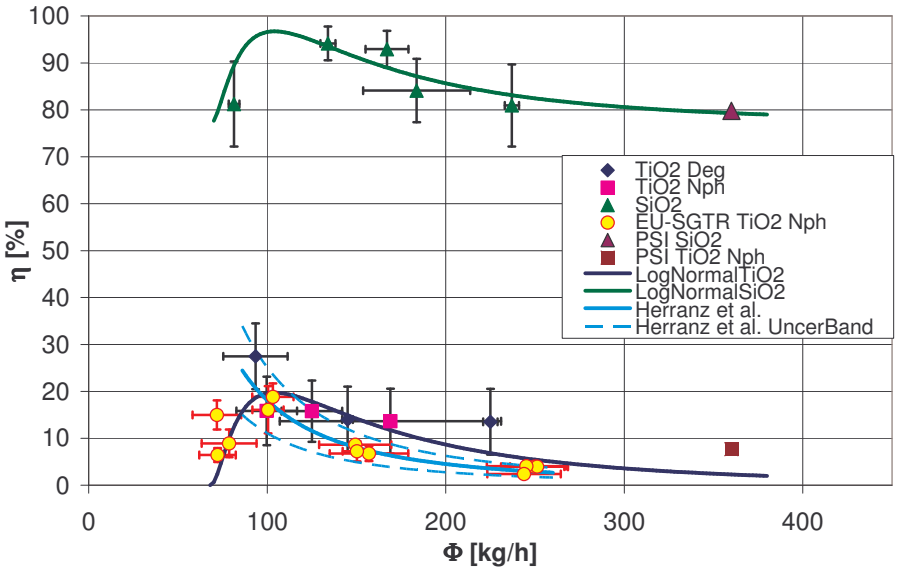

Fig. 65. Mass retention efficiency and uncertainty associated vs inlet gas mass flow rate. Analytical trends.

In short, particle nature and inlet gas mass flow rate affect the aerosol retention efficiency in the bundle. Nonetheless, whereas particle nature (i.e., agglomerates vs solid spheres) practically determines the quantitative range of retention efficiency, the gas mass flow rate does not play such a key role. Then, retention efficiency of both particle types could be approximately described by an equation of the type,

$$\eta(\%) = \frac{a_4}{\sqrt{2\pi}\cdot(\Phi - a_1)a_2} \exp\left(-\frac{\left(\mathrm{Ln}\left(\frac{\Phi - a_1}{a_3}\right)\right)^2}{2(a_2)^2}\right) + \psi \tag{36}$$

where a_i values are those of Eqs (34) and (35), and the ψ parameter sets the "baseline value" of retention efficiency and encapsulates most of particle nature influence. In other words, ψ will be presumably a function of particle properties like density, shape, size, charge, elasticity and/or fracture toughness. According to Eq. 36, the relative importance of the two terms on the right side depends on the type of particles: ψ largely dominates for SiO_2 particles, whereas both are significant contributors for TiO_2 agglomerates.

Fig. 66 shows the bundle retention efficiency versus the inlet d_{ae} for the CAAT and EU-SGTR data presented in Fig. 63. The vertical bars represent the experimental uncertainty in the retention efficiency of each experiment. The horizontal bars represent the GSD value of the inlet aerosol distribution measured in each experiment. Three main groups of data can be noticed in the figure. The first one consists of the CAAT experiments performed with polidispersed TiO_2 agglomerates whose inlet d_{ae} ranged from 1.5 to 3.5 µm. The second one is formed by the EU-SGTR experiments which were performed with polidispersed TiO_2 (Nph) agglomerates with inlet d_{ae} between 5 and 7.5 µm. The third group is formed by the CAAT experiments performed with monodispersed SiO_2 solid spheres of 1µm nominal diameter (d_{ae} around 1.4 µm). The dispersion found in the inlet d_{ae} for SiO_2 tests fell within the uncertainty associated to the measurement of inlet aerodynamic particle size. TiO_2 and SiO_2 data groups from CAAT experiments had similar inlet d_{ae} range whereas EU-SGTR data group had a different inlet d_{ae} range, with a bigger particle size. The d_{ae} range similarity between the TiO_2 and SiO_2 groups, again highlights that the source of such a difference in the retention efficiency is other than particle size: particle nature.

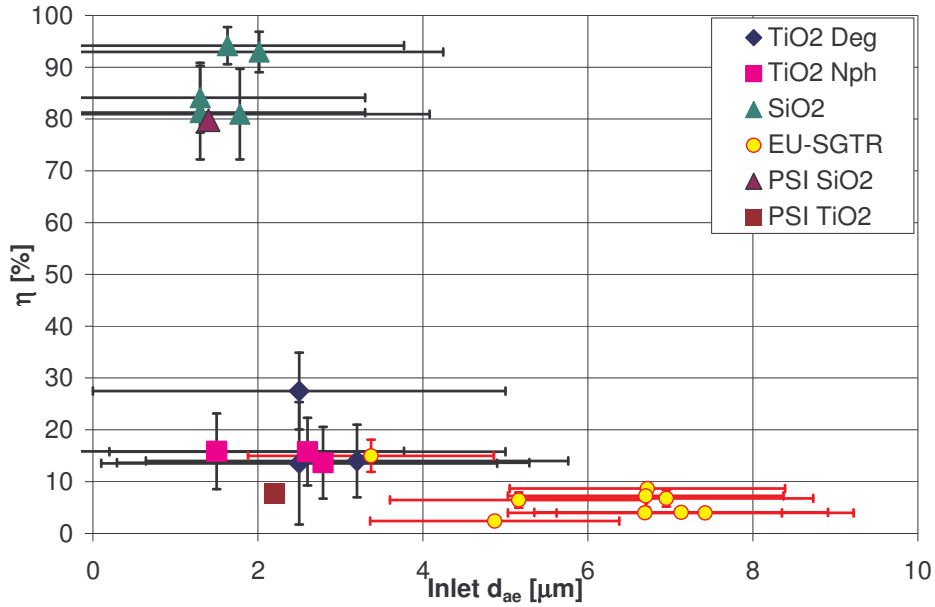

Fig. 66. Mass retention efficiency as a function inlet d_{ae} for CAAT and EU-SGTR data.

By comparing the TiO_2 data in the two size groups (i.e., 1.5-3.5 and 5-7.5), it may be noted that the bigger the agglomerate, the lower the retention. This could be related to the fact that large agglomerates are more loosely packed. This tendency cannot be applied to SiO_2 particles since data are reduced to a narrow size interval that falls within uncertainty in the particle size measurement. It is worth to note that PSI (2008) data under similar inlet d_{ae} conditions appear in the same region as CAAT ones, underlying their consistency.

In short, particle nature has a prime importance for in-bundle retention. Gas mass flow rate and particle aerodynamic size also affect retention efficiency, but their influence can not be considered as important as the particle nature one. The relative effect of gas mass flow rate and particle aerodynamic size on retention efficiency results to be of similar importance.

3.6.3. Phenomena involved

The CAAT experiments are of an integral nature. Measurements provide information on the net effect of a set of phenomena that are active in the scenario, but they do not allow quantitatively assessing the impact of each individual phenomenon. Nonetheless, from the integral data recorded some specifics can be discussed.

3.6.3.1. Global discussion

Herranz et al. (2007) indicated that according to their estimates inertial impaction and turbulent deposition should be the most effective retention mechanisms in the SGTR scenarios under study.

Both phenomena depend on variables such as particle diameter, tube diameter and gas velocity. Such dependencies may be expressed in terms of nondimensional numbers like Stk, Sc and Re_D. By taking Stk as a reference, two deposition regimes could be defined in the scenario: one dominated by turbulent deposition ($Stk \leq 0.1$) and another one governed by inertial impaction ($Stk > 0.1$). Such a classification agrees with Fuchs (1964) that claimed that there is a critical Stk below which no deposition by inertial impaction occurs.

In light of the results, inertial impaction would be responsible for the hill-shaped deposit on the adjacent tubes to the broken one (big particles striking the surface just in front of the breach) since the gas exiting the breach approached the adjacent tubes at high velocity. Turbulent deposition could also have removed effectively particles from the gas by turbulent diffusion and/or eddy deposition in the regions of high turbulent intensity, particularly on the tubes surface downstream the jet impingement, in the tube wakes and in the recirculating regions over the breach.

As previously discussed, in case of TiO_2 agglomerates, retention efficiency was found to decrease when inlet d_{ae} increased. This tendency is opposite to what it is expected

from inertial impaction and/or turbulent deposition processes that increase their collection efficiency with d_{ae}, with particle velocity and, in general terms, with Stk (Herranz et al. 2007). This suggests that other phenomena inhibiting net deposition like particle fragmentation, resuspension, tube vibration, erosion and/or bouncing must be present in the scenario.

3.6.3.2. Fragmentation

Fragmentation was not observed in SiO_2 particles, so that the next discussion is strictly focused in TiO_2 agglomerates. Again, this difference highlights the importance of particle nature on retention efficiency.

Fragmentation of agglomerates across the tube bank can be mainly driven by the high shear stresses in the flow and/or by particle-surface collision. These processes would make agglomerates to break up into particles of smaller size (Fuchs 1964), which would be harder to be trapped on surfaces. As big agglomerates would be more likely fragmented than small ones, their retention efficiency would consequently be lower. Namely, size of particles approaching tube surface would have been likely smaller than the measured one in the case of aggregates; this effect should have been more noticeable for large agglomerates.

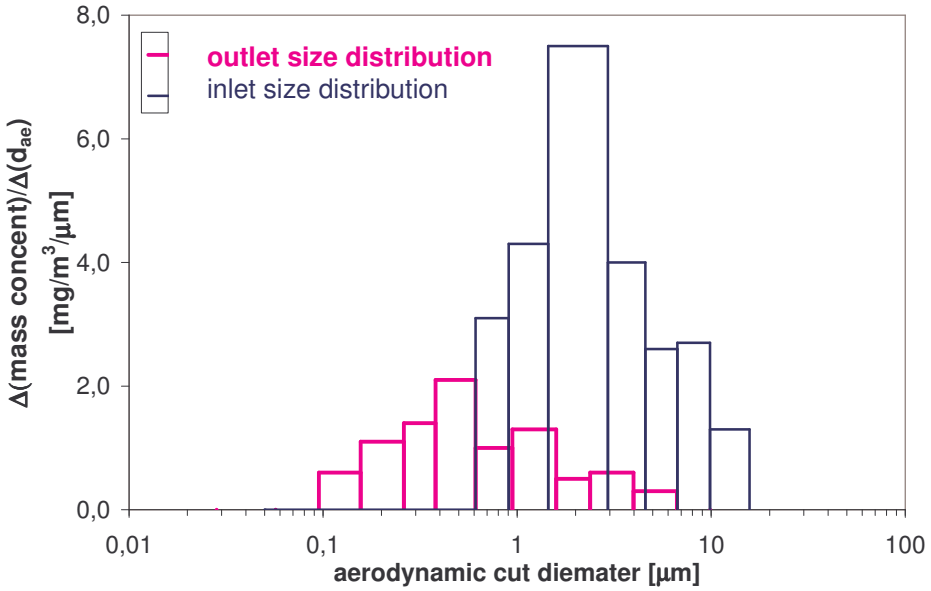

Fig. 67. Inlet / outlet aerosol size distribution for CAAT-02.

As the jet moves across the tube bundle, aerosol size distribution shifts towards small sizes. In most of TiO_2 experiments outlet size distributions showed a higher mass fraction at the smallest size bins, which highlights the splitting of bigger particles (Fig.

67). This observation was already noted by Herranz et al. (2006) in the EU-SGTR tests.

In the surroundings of the breach, pressure gradients, shear stress and particle kinetic energy reach maximum values. As a consequence flow-particle and particle-tube interactions are strong and agglomerate fragmentation is enhanced in this region. Fig. 68 shows the d_{ae} inlet/outlet ratio for CAAT and EU-SGTR experiments as a function of the jet pressure gradient at the breach:

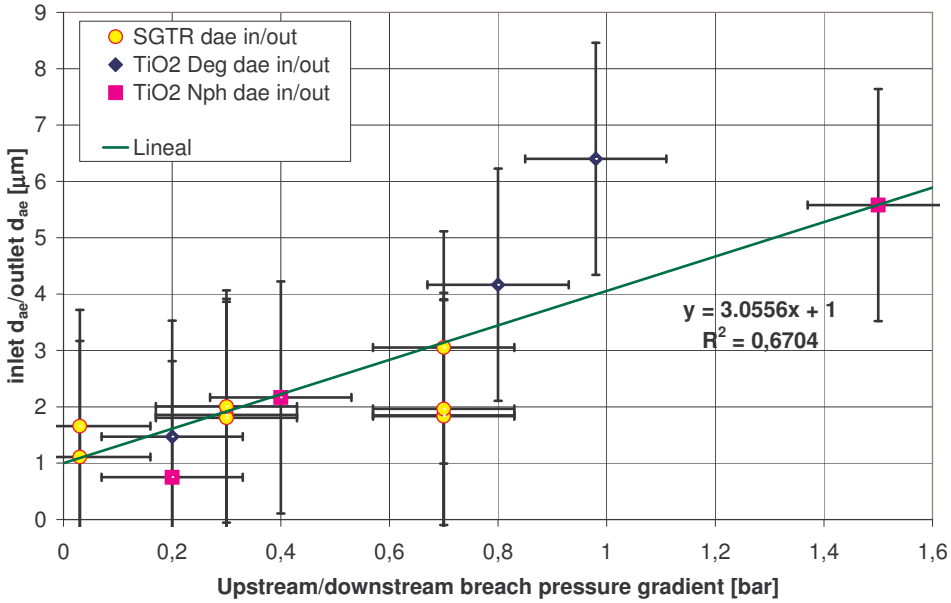

Fig. 68. Inlet/outlet d_{ae} vs pressure gradient at the breach for TiO_2 agglomerates from CAAT and EU-SGTR experiments.

$$\frac{\text{inlet } d_{ae}}{\text{outlet } d_{ae}} = \lambda \Delta p + 1 \quad \text{with} \quad \lambda = 3.0556 \ \left[\text{bar}^{-1}\right] \qquad R^2=0.67 \qquad (37)$$

Even though the low R^2 value indicates that other mechanisms than pressure jump must likely affect particle fragmentation, the data suggest a rough correlation between the fragmentation of the particles and the flow expansion at the breach (Eq. 37). Note that, as pressure gradient and inlet gas mass flow rate follow a linear relationship (Table V), the figure also illustrates a correlation between fragmentation and particle kinetic energy. These observations are consistent with those made by Brandt et al. (1987) and by Froeschke et al. (2003).

3.6.3.3. Resuspension

Resuspension of deposited particles in the tube bundle is a highly likely phenomenon under velocities and turbulent intensities that existed during the tests. The high Ma numbers reached during CAAT experiments (0.2-0.8) resulted in high on-tube wall shear stress fields and turbulence levels that, according to Blackwelder and Haritonidis (1983), were capable of promoting local instabilities (i.e. turbulent burst or sweeping eddies) in the viscous sublayer of the boundary layers developed over tube surfaces. Both phenomena enhance drag and lift forces acting on the deposited particles that may eventually detach particles from the substrate underneath. As a consequence, an increase of gas mass flow rates would yield a reduction of bundle retention efficiency.

As said above, given the integral nature of the CAAT experiments, no specific measurement of resuspension could be conducted. Measurements recorded provide information on the net deposition (i.e., the dynamic equilibrium between aerosol mechanisms depositing particles from the jet and removing particles from the surface). Nevertheless, the decreasing evolution of η with Φ increase ($\Phi \geq 100$kg/h seems to point that there must be a deposition inhibiting mechanism responsible for this that affected both SiO_2 and TiO_2 particles.

In order to assess the feasibility that resuspension was a working phenomenon in the CAAT experiments, a theoretical criterion for resuspension onset has been developed and tailored to the CAAT scenarios based on the force balance model (IRSN, 2006). Resuspension onset may be defined by the condition:

$$F_{aero} \geq F_{adh} \tag{38}$$

That is, as the aerodynamic forces pulling-off particles from the surface exceed the adhesive ones that keep them attached to the surface, resuspension starts. Removal forces acting on particles are the drag (F_D) and lift (F_L) forces induced by the flow. Adhesive forces include cohesion (F_C), electrostatic (F_E) and friction (F_f) forces. Equations for all these individual contributions have been proposed by several authors and are listed in Table XIX.

Table XIX. Forces contributing to the resuspension mechanism

Force type	Force name	Formula	Reference
Aerodynamic	Drag	$F_D = \frac{\pi d_{ae}^{\ 2}}{4}\tau_o$	Fromentin (1987)
	Lift	$F_L = A\nu^2\rho\left(\frac{d_{ae}u^*}{\nu}\right)^B$	Hall (1988)
Adhesive	Cohesion	$F_c = d_p\gamma_p H_c = d_{ae}H_c$	Brockmann (1985)
	Electrostatic	$F_E \propto \frac{\pi}{4}\varepsilon\frac{d_p}{l_q^{\ 2}} \propto \frac{\pi}{4}\varepsilon\frac{d_{ae}}{l_q^{\ 2}}$	Fauske & Ass (1984)
	Friction	$F_f=f\cdot(F_C+F_E)$	IRSN (2006)

Then, inclusion of the Table XIX expressions in Eq. 38 would yield,

$$\frac{\pi}{4}d_{ae}^{\ 2}\tau_o + A\nu^2\rho\left(\frac{d_{ae}\tau_o^{\ 1/2}}{\nu\rho^{1/2}}\right)^B - \left(d_{ae}H_c + \frac{\pi}{4}\varepsilon\frac{d_{ae}}{l_q^{\ 2}}\kappa\right)(1+f) \qquad (39)$$

where A and B were determined by Hall (1988) to be 4.21±0.23 and 2.31±0.02, respectively. By using the mean wall shear stress estimated through 3D CFD simulations of the CAAT tests carried out by Lopez del Prá et al. (2008) (Table XX), the normalized evolution of the lift aerodynamic force for CAAT and SGTR data have been derived (Fig. 69) and fitted by a linear law of $d_{ae}^{\ 2}\cdot\tau_0$:

Table XX. Mean wall shear stress values predicted for CAHT-CAAT experiments.

Inlet gas mass flow rate [kg/h]	Mean wall shear stress [Pa]	
	Guillotine breach	Fish-mouth breach
75	0.042	0.07
150	0.164	-
250	0.38	0.44

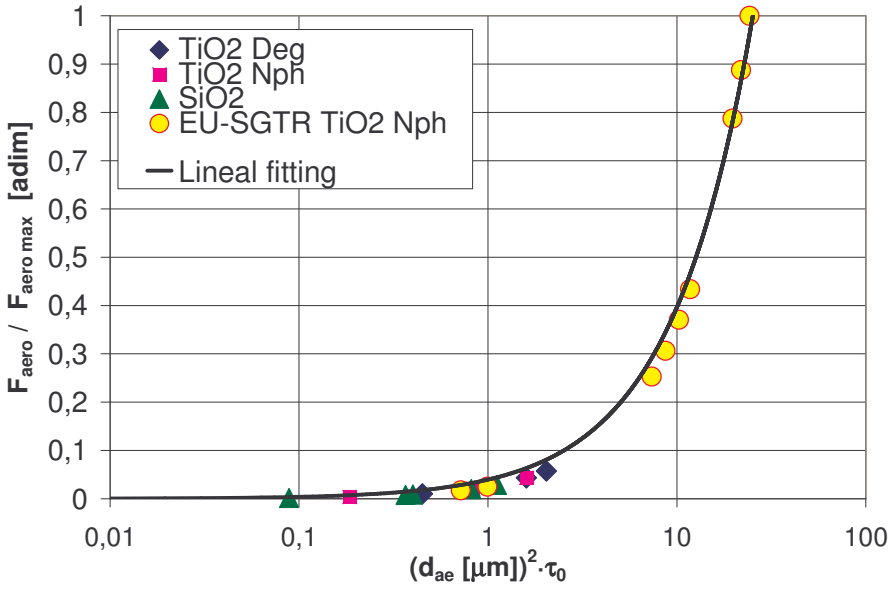

Fig. 69. Aerodynamic force predicted by force balance model for CAAT data.

$$\frac{F_{aero}}{F_{aero\ max}} = 0.0396 \cdot \left(d_{ae}\,(\mu m)\right)^2 \cdot \tau_0\,(Pa) \qquad R^2=0.99 \qquad (40)$$

This expression looks consistent with those in the table if B is approximated to ~2 and allows reaching a quite simple equation defining approximately the resuspension onset criterion for CAAT experiments:

$$\beta_1 \cdot \left(d_{ae}{}^2 \tau_0\right) - d_{ae}\beta_2 > 0 \;\Rightarrow \beta_1 \cdot \left(d_{ae} \cdot \tau_0\right) - \beta_2 > 0 \qquad (41)$$

Eq. 41 carries some key information. According to it, the product ($d_{ae}\cdot\tau_0$) could be understood as an indicator of resuspension intensity, since it can be seen as the result of

$$E_{res} = \int_L \tau_o \cdot d\ell \qquad (42)$$

so to say, ($d_{ae}\cdot\tau_0$) would represent the energy supplied per unit surface area by the flow to the deposited particle (note that L in the equation would be a characteristic length of the particle). Non-dimensional efficiency ($\bar{\eta}$) of experiments where resuspension is

likely to have played a role (i.e. data with inlet gas mass flow rate over $\bar{\eta}_{max}$ in Fig. 64) has been plotted vs this parameter (Fig. 70). As shown, the normalized efficiency can be correlated with $(d_{ae}\cdot\tau_0)$ following a gaussian law:

$$\bar{\eta} = \alpha_1 \exp\left(-\frac{(d_{ae}\cdot\tau_0)^2}{\alpha_2^{\,2}}\right) + \alpha_3 \qquad (43)$$

where the values proposed for the parameters are: α_1=0.80±0.08, α_2=0.611±0.300 [µm·Pa] and α_3=0.20±0.08. The average relative cuadratic error of the correlation is 24% and the uncertainty band for the correlation (which is based on the uncertainty of the experimental parameters α_i) accounts for a confidence interval of 85%. Therefore, this confirms that $(d_{ae}\cdot\tau_0)$ can be taken as an indicator of the resuspension process and supports that deposits in all those CAAT experiments with Φ≥100 kg/h underwent resuspension. In addition, the gaussian shape shown in the figure dictates that as $(d_{ae}\cdot\tau_0)$ increases $\bar{\eta}$ decreases to finally reach an asymptotic value. These results indicate that once a certain magnitude of $(d_{ae}\cdot\tau_0)$ has been reached, no matter how far it keeps growing, resuspension practically holds the same intensity.

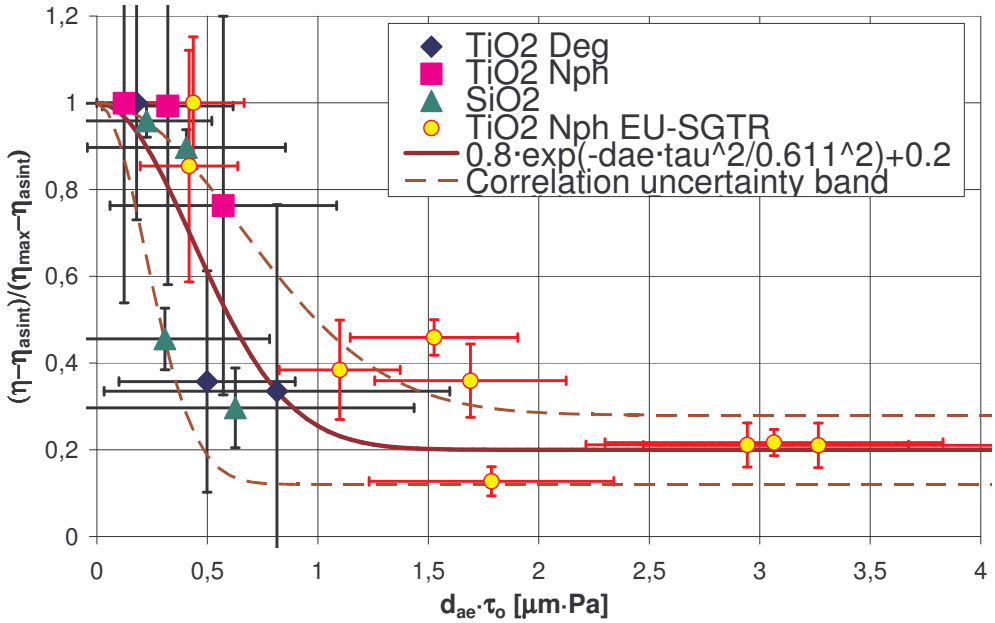

Fig. 70. $\bar{\eta}$ vs $(d_{ae}\cdot\tau_0)$.

Finally, it has to be remarked that influence of particle nature on resuspension is encapsulated in the reference value (η_{ref}) used in the definition of $\overline{\eta}$. Such an effect would be implicit in some of the variables involved in the resuspension forces, like the particle-surface interaction parameter (H_c) or the electrostatic properties of the particles materials.

3.6.3.4. Bouncing

In the CAAT experiments, there appeared "clean regions" on the tubes facing the breach (Fig. 60). Two potential mechanisms could be responsible for those "clean regions": bouncing and/or erosion. At any given location over tube surface just a fraction of the interacting particles would get stuck on the tube. The condition those particles have to comply with may be expressed:

$$v_{crit} < v_{normal} < v_{rebound} \tag{44}$$

Otherwise, particles either do not impact on the surface ($v_{normal}<v_{crit}$) or rebound ($v_{normal}>v_{rebound}$). As noted, the above criterion refers to the normal velocity component, so that for a given particle velocity, the tube zone on which particles do not stick depends on particle trajectory or, more specifically, on the particle angle of incidence (i.e., the angle between the trajectory vector and the tangent to the tube surface). That is, under the same kinetic conditions, angles near 90º entail higher bouncing probability than smaller ones. These observations agree with the ones indicated by Rosner et al. (1995), Konstandopoulos et al. (2006) for particle impaction on curved surfaces.

Erosion consists of a momentum exchange between a colliding particle and on-surface deposits. As a matter of fact, it could be seen as a specific type of bouncing in which the colliding particle bounces and transfers enough momentum (i.e., energy) to deposit as to detach a fraction of it (i.e., some resuspension occurs). Thus, contrary to general bouncing conditions, for a given velocity the smaller the particle angle of incidence, the higher the probability of causing an "effective" collision.

According to the aerodynamic characterization of the scenario carried out by Velasco et al. (2008) (i.e., high velocity and turbulence fields), both bouncing and erosion might have taken place in the break stage bundle. Even though the CAAT observation of "clean regions" on the facing tubes had a generic nature, the region extension depended on particle nature. Whereas in the TiO_2 tests, those zones were restricted to small side spots on facing tube surfaces, the SiO_2 tests showed much broader "clean regions" (Fig. 24). Therefore, particle nature also affected the deposition pattern through "inhibiting" deposition mechanisms, like bouncing and/or erosion.

The fact of existing hill-shaped deposits in front of the breach in the TiO_2 experiments might indicate that the probability of bouncing for TiO_2 agglomerates is low. In

addition, the lateral location of “clean regions” just where the jet trajectory is practically tangential (i.e., maximum friction velocity), might be understood as a result of erosion (since at such spot erosion is maximum). The lack of hill-shaped deposits in SiO_2 tests seems to indicate a highly intense bouncing in this case. Nonetheless, erosion could not be fully ruled out as a working mechanism over tube sides.

Additionally, one can discuss other aspects also influenced by particle nature. Deformation capability and toughness are two particle properties particularly relevant for the differences observed. Deformation capability would affect the elastic/inelastic nature of collisions. Agglomerates can be characterized by a quasi-plastic behavior because of which inelastic collisions would happen more likely than for solid spheres (SiO_2), which show a quasi elastic behavior. On the other hand, this would also mean that TiO_2 deposits would undergo more compaction than SiO_2 ones. Both aspects would be consistent with the different “clean region” extensions observed.

Nonetheless, even though evidences seem to point out that erosion played a major role in TiO_2 tests and rebound did in SiO_2 tests, one should not try to be too conclusive based on indirect evidences. None mechanism, either erosion or bouncing, can be entirely ruled out from any scenario. This statement is further emphasized by the fact that particle properties like agglomerate toughness (i.e., an energy measure of primary-to-primary particle interaction in agglomerates) would presumably play a significant role in the scenario (as discussed above) and it would affect both bouncing and erosion

3.6.3.5. Tube vibration

In addition to these phenomena, there might be other mechanical effects, like tube vibration, that would also influence the net deposition in the bundle. Given the slenderness of the tube bundle, jet impingement on tubes did presumably result in flow-induced vibrations or flapping (Khushnood et al., 2004). Those vibrations would have prevented particles from being effectively retained by enhancing resuspension to some extent. Even though, quantitative conclusions cannot be firmly drawn from the data available, this mechanism should not be ruled out as a significant phenomenon playing a role in the scenario.

3.7. Experimental correlations

Different approaches have been intended to correlate the bundle retention efficiency with characteristic nondimensional numbers.

3.7.1. Phenomena approach

Based on previous insights and discussions concerning major phenomena present in the scenario, the bundle retention efficiency could be written in the form:

$$\eta(\%) = \frac{3534420}{\sqrt{2\pi}\cdot(\mathrm{Re}_D - 79254)} \exp\left(-\frac{\left(\mathrm{Ln}\left(\frac{\mathrm{Re}_D - 79254}{117814} \right) \right)^2}{2} \right) + \psi \qquad (45)$$

As discussed earlier, ψ takes into account the particle nature effect and for TiO_2 agglomerates it can be correlated as a function of particle aerodynamic diameter as:

$$\psi = a_5 - a_6 \left(\frac{\mathrm{Stk}}{\mathrm{Ma}} \right)^{1/2} \qquad (46)$$

The values proposed based on the available data are a_5=22.78%, a_6=10.434%. In these expressions Stk would account for the particle size effect and Re_D and Ma would encapsulate the flow field influence. These equations would be applicable in the following ranges of the non-dimensional numbers: Re_D=(0.8-3.0)·10^5, Stk=(0.03-5.30), Ma=(0.2-1.5) and Stk/Ma=(0.14-3.52). The average relative error of the correlation is 67%.

An analysis of Eq. 45 provides some insights regarding phenomena acting in the scenario. TiO_2 agglomerates retention is low and the $(Stk/Ma)^{1/2}$ term is negligible with respect to Re_D term. This is consistent with previous discussions, in which aspects like their loose packing or potential to fragmentation indirectly point that the inlet size of TiO_2 agglomerates seems not to be a key variable for their behavior. As for deposition mechanisms, their low density and small size resulting from fragmentation would enhance turbulent mechanisms over inertial ones. SiO_2 particles, however, do not share some of the above features of TiO_2 agglomerates and, as a consequence, the ψ term becomes more relevant.

The structure of Eq. 45 suggests that turbulence mechanisms and inertial mechanisms behave independently as particle depletion process. Nonetheless, an attempt to consider their dependency has been considered by adopting an equation of the type

$$\eta = \sqrt{\eta_i^{\,2} + \eta_j^{\,2} - \eta_i \eta_j} \qquad (47)$$

and using the Eq. 45 and 46. The resulting correlation

$$\eta(\%)=\left(\left(\frac{3534420}{\sqrt{2\pi}\cdot(\mathrm{Re_D}-79254)}\exp\left(-\frac{\left(\mathrm{Ln}\left(\frac{\mathrm{Re_D}-79254}{117814}\right)\right)^2}{2}\right)\right)^2+\left(22.78-10.434\left(\frac{\mathrm{Stk}}{\mathrm{Ma}}\right)^{1/2}\right)^2-\left(\frac{3534420}{\sqrt{2\pi}\cdot(\mathrm{Re_D}-79254)}\exp\left(-\frac{\left(\mathrm{Ln}\left(\frac{\mathrm{Re_D}-79254}{117814}\right)\right)^2}{2}\right)\right)\left(22.78-10.434\left(\frac{\mathrm{Stk}}{\mathrm{Ma}}\right)^{1/2}\right)\right)^{0.5} \quad (48)$$

has an average error of around 26% (nearly 60% lower than Eq. 45 one). In Fig. 71, the experimental efficiencies available are presented as a function of the predictions from Eq. 48. The figure shows that most of experimental data falls inside of the 50% variation band, which should be considered good enough if measurement uncertainty of the experiments is taken into account.

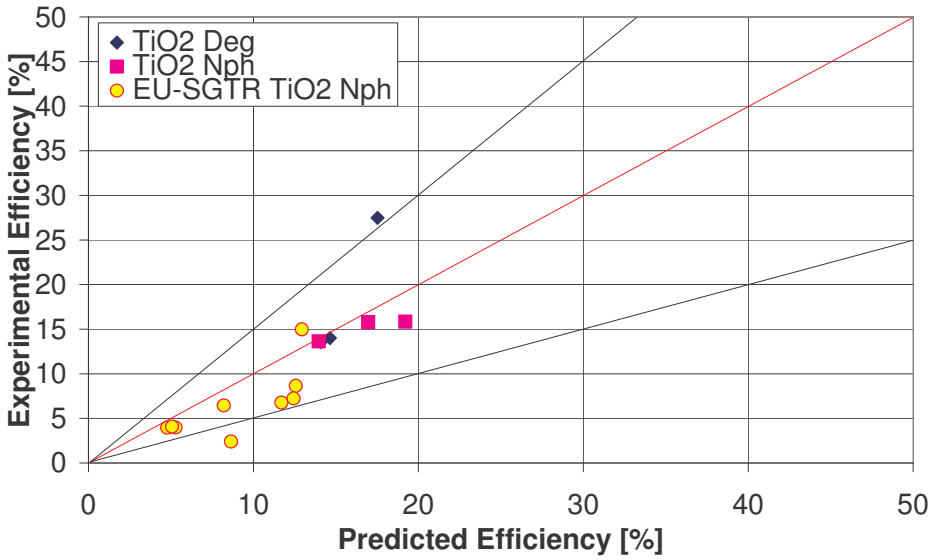

Fig. 71. Equation 48 predictions vs experimental data.

As previously discussed, CAAT data presented a similar retention efficiency tendency with inlet gas mass flow rate but different mean retention efficiency level for particles of different nature (TiO_2 agglomerates vs SiO_2 solid spheres). Eqs. 34 and 35 followed the same structure showing that the difference of the two types of particles studied can be described through a particle nature parameter ψ. This different tendency has been discussed to be related to phenomena that are particle nature dependent like fragmentation, resuspension, and/or bouncing.

3.7.2. Statistical approach

Apart from the previous approach, a correlation of retention efficiency has been sought just based on non-dimensional numbers considered in the open literature for similar scenarios. The best fit attained has been:

$$\eta(\%) = 5.28287 + \frac{\mathrm{Log}(\mathrm{Re}_D)}{0.204281 + 114187\mathrm{Stk}_{effMa}^{\ 7.97043}} \tag{49}$$

with

$$\mathrm{Stk}_{effMa} = \mathrm{Stk}\cdot\mathrm{Corr}(\mathrm{Re}_p)\cdot\mathrm{Corr}(\mathrm{Ma}) =$$

$$= \mathrm{Stk}\cdot\left(3\frac{0.158^{0.5}\,\mathrm{Re}_p^{1/3} - \mathrm{a\,tan}\left(0.158^{0.5}\,\mathrm{Re}_p^{1/3}\right)}{0.158^{1.5}\,\mathrm{Re}_p}\right)\cdot\left(\frac{1-\frac{5}{12}\mathrm{Ma}^2}{\left(1+\frac{\gamma-1}{2}\mathrm{Ma}^2\right)^{0.67}}\right) \tag{50}$$

Stk_{effMa} is a measure of the ratio between inertial and viscosity forces, once the drag force out of the Stokes law regime and the correction for the compressibility effects using the Mach non-dimensional number are considered (Israel & Rosner, 1983). In Fig. 72 it can be observed how Eq. 49 behaves with respect to data. The average error of the correlation with respect to the experimental data is 57%. These equations would be applicable in the following ranges of the non-dimensional numbers: Re_D=(0.8-3.0)·10^5, Stk=(0.03-5.30), Ma=(0.2-1.5) and Re_p=(2-463).

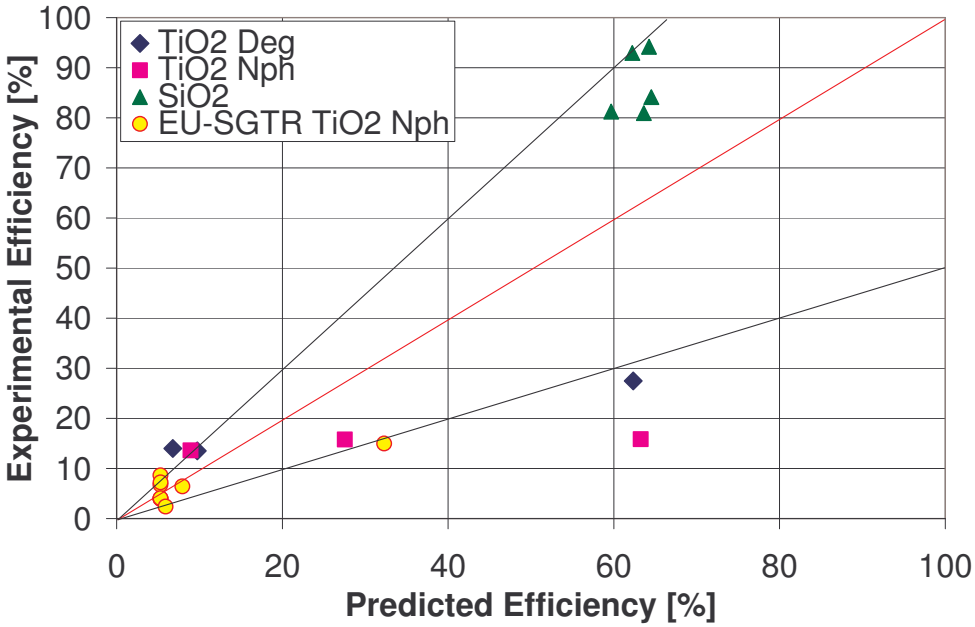

Fig. 72. Equation 49 predictions vs experimental data.

Chapter 4

Conclusions and Future Work

4.1. Conclusions

This thesis seeks to get insights into the source term retention efficiency of the break stage of a dry SG in a PWRs under hypothetical severe accident SGTR sequences. In order to do so, experimental research has been devoted to characterize gas aerodynamics across the tube bundle and the nature of the aerosol particles influence in the mass retention efficiency. Aerodynamics of the particle-laden gas jet expanding across the secondary side of the SG determines to a large extent radioactive retention in the break stage since it defines the regions were depletion mechanisms are enhanced. Whereas, the nature of the particles is a key open issue due to the existing uncertainty in the properties of the source term particles present in the scenario. As a result of this research program, an experimental database on aerodynamics and aerosol retention in the break stage of a dry SG under SGTR conditions have been built up and is available to validate CFD codes and aerosol retention models.

This chapter is structured in four sections. It is firstly presented the lessons learned from the experimental investigations performed. Secondly, the main scientific results and specific conclusions of the research are detailed in two sections according to the overall thesis approach, one relating the aerodynamics investigation and another devoted to the aerosol investigation. Finally, orientations for future research programs are pointed out.

4.1.1. Experimental conclusions: lessons learnt form experiments

The experience gained during the experimental campaigns performed on present research has shown several outputs and/or lessons learned that will be detailed in this section in order to assist future experimentations.

- The **mock-up** of the break stage of the secondary side of the SG was designed limiting the size of transverse section of a break stage (not the axial size) due to space limitations. The criteria followed to decide the number of tube rows that would be representative of the scenario under study was based on CFD simulations of the sequence that determined the jet penetration in terms of tube rows. Comparison of the experimental results with PSI data obtained in a facility that doubled the number of tube rows, shows that the criteria adopted was correct and that scale factors does not affect overall retention of the break stage.

- As discussed in the CAHT section, PIV technique suffered from **seeding** drawbacks when applied in the present scenario. Due to the interest on analyzing the aerodynamic behaviour of the aerosol used in the CAAT experiments, the CAHT campaign was performed using TiO_2 powder as seeding particles. Particles inertia due to the agglomeration in the generation process (FBG), generated a systematic error in the measurement of the velocity field at high velocities. This systematic error was limited to the space in front of the breach, where flow velocities are maxima and seeding

particles are forced to change in direction at the breach and accelerate in the jet expansion until reaching the velocity of the gas. In addition, this area is the more challenging one from the seeding concentration point of view. The configuration of the problem studied that force the flow to turn nearly 90º, also promotes the non-uniformity of the seeding just in front of the breach, forming areas of very high concentration (smoke) as well as region with nearly no density of particles, enhancing the previous problem. After trying different seeding powders ((Deg) and (Nph)) and the use of a Venturi cone to try to reduce seeding size by agglomerates break-up, it was decided to overcome the drawback by using a complementary measurement technique (Pitot tube) to fulfill the aerodynamic measurements. This limitation have been reported by different authors in compressible flows and have been overcome by different techniques, the most efficient one is the use of a cyclone before the mixture of the seeding flow with the main one.

- The aerosol experimental campaign (CAAT) have highlight the importance of using **instrumentation** based on different physical measurement principles to measure the aerodynamic particle size distribution of an aerosol under the studied conditions. The use of integral gravimetric instruments (like cascade impactors and membrane filters) permits to obtain very valuable mass based measurements like the aerodynamic mass median diameter. However, they do not permit to characterize properly time evolution of these properties. The use of online particle size instrumentation (like OPC, APS, ELPI which are based on particle count measurements) permits to complement the previous data to obtain time evolution data as well as to characterize additional aerosol particles properties like charge.

- Estimation of the **measurement uncertainty** in the experiments raise as a especially important issue in case of aerosol technology. Commercially available online particle size instrumentation is usually aimed to chemical and pharmacologic laboratories where working conditions are stable and standard. The application of this instrumentation to our scenario where there exits over pressure and relatively high aerosol concentrations requires the use of diluters that might influence aerosol size distributions. On the other hand, this instrumentation is calibrated against ideal particles (latex) whose behaviour is different from the agglomerate particles one. Thus, a calibration campaign is always required to properly assess measurements uncertainty. A cross comparison of the outputs measured for the same sample with different instruments is also very useful. In our experiments, it was used instruments based on different measurements principles (light scattering, time of flight, inertia+charging) to obtain a better approach to the actual aerosol distribution.

4.1.2. Aerodynamic investigation: CAHT conclusions

A thorough characterization of the gas flow coming out from a broken tube under SGTR conditions was carried out with 2D-PIV. A scaled-down mock-up with representative dimensions of a real SG and an ad-hoc wind tunnel were built. By optimizing the experimental configuration and optical access, PIV provided aerodynamic data relevant for radioactive particle retention in a challenging nuclear safety scenario. These data were supplemented with Pitot tube measurements to overcome PIV shortcomings. Two type of breaches were investigated, guillotine and fish-mouth. The main results observed in the guillotine breach configuration may be summarized as follows:

- The jet flows within the tube bundle following a generic quasi-parabolic trajectory evolving from an oblique cross flow configuration to an axial one.

- Mean flow field near the breach is substantially affected by the entrainment of initially stagnant gas into the jet. This effect is fostered by the presence of tubes and their tight packing. As a result, gas recirculation is set up over and under the breach (the upper “loop” being more intense than the lower one).

- Jet penetration and axial gas entrainment are considerably enhanced when increasing inlet gas mass flow rate.

- Turbulence intensity level close to the breach increases linearly with the inlet gas mass flow rate. Typical values in the range investigated round 120-160% in the 1st gap.

- Comparison of free and “in-bundle” jets showed that the tubes acts as turbulence enhancers increasing mean turbulence in the 1st gap between 20 and 60%.

The main insights gained into the fish-mouth breach configuration may be summarized as follows:

- As in the guillotine case, the jet evolves within the tube bundle from an oblique cross flow configuration to an axial one.

- A fish-mouth type breach generates a conical jet expansion across the bundle whereas a guillotine breach generates an axis-symmetric tulip-like jet expansion The different momentum exchange surface area between jet and surrounding gas, results in milder velocity decays for the fish-mouth jet.

- Fish-mouth type breaches generate an elliptic jet with “quasi top-hat” velocity profile with slightly higher magnitudes of velocities in the lower part of the breach.

- The breach type affects drastically the jet evolution and results to be a key factor in the flow field behavior in the surroundings of the breach. Comparison of “fish-mouth” and “guillotine” jets showed different vertical velocity profiles (top-hat vs Gaussian) and different in-jet flow entrainment for the same inlet conditions.

- Jet similarities between breaches are reduced to z/H<1 of the breach symmetry plane. In this domain, velocity profiles become self-similar when they are turned into non-dimensional ones with respect to the breach height.

- Both types of breaches show similar level of local turbulence intensity in the first gap.

The presence of tubes affects drastically the jet behavior by two principal effects: a distortion of the jet shape and an increase of the maximum jet velocity and turbulence near the breach. The jet tends to flow over tube surfaces. As a result, jet penetration is attenuated, whereas upwards motion is fostered. Given the high level of turbulence measured in the presence of tubes, this jet bending means that particles would deposit on these first neighbor surfaces by turbulent mechanisms. In addition, the high velocities reached in the initial cross-flow orientation of the jet, make particles accumulate on neighbor surfaces facing the breach. There are evidences that an increase of gas mass flow rates could enhance particle deposition by turbulent and inertial mechanisms.

4.1.3. Aerosol investigation: CAAT conclusions

A bench-scale experimental program has been carried out to investigate the retention capability of the break stage of a dry SG when the particle laden jet expands through it. The influence of particle nature in the bundle retention has been studied using the inlet gas mass flow rate as parameter. Two different types of polydispersed TiO_2 agglomerates as well as monodispersed SiO_2 solid spheres were used as aerosols. By characterizing aerosol mass size distribution entering and leaving the bundle and the on-tube retained mass, the mass retention efficiency of the bundle was obtained for each type of aerosol.

This research has demonstrated that even in the worst credible conditions of SGTR sequences (i.e. dry secondary side, high gas flow rates and weakly bonded aggregates), aerosols are retained in the nearby of a tube breach. Retention is mainly caused by inertial impaction and turbulent deposition. Nevertheless, the potential decontamination in the secondary side of the break stage gets reduced due to the action of other phenomena which inhibit deposition, like fragmentation, resuspension, tube vibration bouncing and/or erosion. Additionally, the results highlighted other significant specifics:

- Particle nature substantially affects aerosol retention in the tube bundle. Mass retention was found to be low for TiO_2 agglomerates (less than 30%) whereas it was much higher for SiO_2 solid spheres (around 85%).

- Radial and axial deposits distribution in the bundle was shown to be different depending on the type of aerosol. Mass surface-density distribution in the closest tubes to the break showed different pattern even for the same compound used (TiO_2) obtained from different manufacturers.

- The retention efficiency sensitivity to gas mass flow rate follows a lognormal behaviour. The maximum retention is attained near 100 kg/h. This evolution with flow rate resulted to be similar for both type of compounds.

- The influence of particle nature on the retention efficiency evolution with mass flow rate can be accomplished by an "offset" or "particle nature parameter" (ψ):

$$\eta(\%) = \frac{a_4}{\sqrt{2\pi}\cdot(\Phi - a_1)a_2}\exp\left(-\frac{\left(\mathrm{Ln}\left(\frac{\Phi - a_1}{a_3}\right)\right)^2}{2(a_2)^2}\right) + \psi \qquad (36)$$

  The relative importance of the two terms on the right side depends on the type of particles: ψ largely dominates for SiO_2 particles, whereas both are significant contributors for TiO_2 agglomerates.

- Particle size also influences retention efficiency: the bigger the TiO_2 agglomerates the lower retention efficiency (no data were available for SiO_2).

- Among these variables, particle nature was noted to have a prime importance in retention, whereas gas mass flow rate and particle aerodynamic size, although also affect retention efficiency, did not play such a key role. The relative effect of gas mass flow rate and particle aerodynamic size results to be of similar importance for TiO_2 agglomerates.

Discussion of the data available showed that big TiO_2 agglomerates (inlet d_{ae}~7μm) results in lower retention than small TiO_2 agglomerates (inlet d_{ae}~2μm). This can be explained by the fact that the formers are more likely to fragment into small secondary agglomerates due to the high shear stresses in the flow and/or by particle-tube collisions what would consequently make them harder to be trapped.

In light of the results, a theoretical criterion for resuspension onset has been developed and tailored to the CAAT scenarios. Based on it, the product ($d_{ae}\cdot\tau_0$) is proposed as an indicator of the intensity of the resuspension mechanism in the bundle. Results show that as ($d_{ae}\cdot\tau_0$) increases, retention efficiency decreases to finally reach an asymptotic value indicating that no matter how far it keeps growing, resuspension practically holds the same intensity.

In the CAAT experiments, there appeared "clean regions" on the tubes facing the breach as a result of bouncing and/or erosion mechanisms. The region extension of this regions depended on particle nature. Whereas in the TiO_2 tests, those zones were restricted to small side spots on facing tube surfaces, the SiO_2 tests showed much broader "clean regions"

In addition to these mechanisms, tube vibrations induced by the flow would influence net deposition in the bundle by preventing particles from being retained and/or induce resuspension. Even though, quantitative conclusions cannot be firmly drawn from the data available, this mechanism should not be ruled out as a major quantitative contributor to the inhibition of retention in the tube bundle.

Finally, regarding aerosol retention during actual SGTR melt-down sequences, the results presented and discussed have important implications. In light of them, some decontamination in the secondary side of a steam generator should be credited, even in the absence of water over the breach. However, the significance of retention within the break stage of the steam generator depends strongly on particle nature. This investigation has shown that agglomerates with low packing density experience a substantially lower retention than more dense particles and are more prone to deposition inhibiting phenomena like fragmentation. Factors other than particle nature, like gas mass flow rate and particle diameter, also influence aerosol depletion, but their impact is much more limited than the particle nature one. Further than the retention magnitude, in-bundle deposition in the break stage results in a shift of aerosol size distribution towards smaller diameters. This is of an enormous significance for further retention in other bundle stages or even in the steam generator upper structures.

4.2. Future work

The present research has highlight different open task that should be addressed in future research lines.

A thorough understanding of the aerosol phenomena within the break stage requires to keep on getting insights into gas aerodynamics. Experimental efforts should focus on turbulence characterization of the gas aerodynamics in the scenario. This information is essential to validate turbulent deposition models that rely on Sc number correlations. Thus, experimental measurements should move towards high sampling-frequency techniques like 3D Laser Doppler Velocimetry (LDV) and/or 3D hot wire anemometry (HWA). These techniques would increase spatial resolution of data

obtained, would complement PIV measurements and permit to fulfill the available aerodynamic database. From that information, eddy diffusivity, ε, in the scenario might be characterized. This way, mass retention efficiency data of the bundle could be used to tune turbulence deposition models.

Regarding aerosol nature influence, present results have highlighted the influence of particle nature on retention efficiency. These results should be confirmed by further experimentation using other types of particles like liquid droplets and/or sintered particles. This information is essential to develop and/or validate aerosol retention models. The use of soluble aerosols (as CsI or CsOH) is relatively challenging from the experimental point of view, nonetheless, its trial would lead to meaningful insights into aerosol nature effect on retention. These data would help to properly assess the "particle nature dependent parameters" defined in the correlation proposed what is essential to develop and/or validate aerosol retention models.

As discussed in this work, these parameters might be well correlated with the particle nature depented variables involved in the resuspension mechanism such as particle-surface interaction (H_c) and the electrostatic properties of the particles materials. This should be confirmed through specifally designed new experiments. The confirmation should be made following a methodology of relative comparison of the results (sticky vs non-sticky surface, time evolution of the depostint layer height,…) since actual resuspension is a multilayer phenomenon and thus surface properties get easily modified since particles potentially resuspendable are not in direct contact with the substrate but with other layers of deposited particles. Actually, this is one of the mains limitations in the modelling of resuspension, that should be faced in future investigations.

During the experiments, evidences of tube vibrations due to flapping were found. These vibrations would enhance particle resuspension or rebound in the scenario. Its actual influence on the mass retention efficiency might be assessed by characterizing the vibration modes using piezoelectric sensors (PCBs) and/or strain gauges.

Finally, the presence of steam and/or water in the scenario should not be forgotten, since it might lead to wet surfaces in bundle where aerosol might be depleted by different mechanisms. It this sense, it might be interesting to investigate the scenario where the tube break is close to the water level. Even if breach is over it, the jet-pool interaction would behave as a droplet source, and an additional aerosol would appear in the atmosphere. Its interaction with the jet particles might act as an additional sink for the source term aerosol.

Nomenclature

a_1, a_2, a_3, a_4	fitting parameters for Equation 33
a_5, a_6	fitting parameters for Equation 46
A, B	Experimental constants proposed by Hall (1988) for aerodynamic lift force of a deposited particle.
AMMD	aerodynamic mass median diameter
acfm	actual cubic feet per minute
APS	aerodynamic particle sizer.
ARTIST	aerosol retention in steam generator.
atan	arc tan
b	spreading defined as the value of θ where $U=0.5U_{max}$.
C	aerosol mass concentration
CAAT	Ciemat Artist Aerosol Tests.
CAHT	Ciemat Artist hydrodynamics tests
C_c	Cunningham slip correction factor.
CFD	Computational Fluid Dynamics.
Corr(Ma)	correction factor for Stk due to Ma effects.
Corr(Re_p)	correction factor for Stk due to Re_p effects.
C_s	aerosol mass concentration of the sample.
D	tube diameter.
d	particle diameter.
d( )	differential of ( )
$(d_{ae})_{50\%}$	aerodynamic cut median diameter of the tube breach.
d($diam_{ae}$)	aerodynamic cut diameter differential.
d(mass conc)	mass concentration differential.
d_{ae}	aerodynamic median diameter.
$D_{ae, cut}$	aerodynamic cut diameter of an impactor stage.
$D_{ae, g}$	aerodynamic geometric diameter of an impactor stage.
DF	decontamination factor $(1-\eta)^{-1}$.
D_p	nominal particle diameter of an instrument bin.
d_p	particle diameter
ELPI	electrical low pressure impactor.
E_{res}	energy supplied by the flow per unit of surface to the deposited particle.
f	generic function
f	particle-surface friction factor
FBG	fluidized bed generator.
F_c	particle-surface cohesive force.
FD	facing diagonal.
F_D	deposited particle drag force.
F_E	particle-surface electrostatic force.

F_f	Particle-surface friction force.
FI	filter.
F_L	deposited particle lift force.
$FM_{aerosol}$	aerosol mass flow rate (g/h).
FM_s	sampling flow rate.
FT	facing tube.
FV_s	volumetric flow rate sampled (l/min).
FV_{sys}	main line flow rate (m^3/h).
G	Flow rate sampled by a filter (Nm^3/s).
GSD, Geom. Std. Dev.	geometric standard deviation.
H	breach height.
$H_c=F_c/d_{ae}$	proportionality constant between cohesion forces and particle aerodynamic diameter.
IMP PRIM	cascade impactor primary side.
IMP SEC	cascade impactor secondary side.
L1F1	secondary side sampling line 1 filter 1.
L1F2	secondary side sampling line 1 filter 2.
L2F1	secondary side sampling line 2 filter 1.
L2F2	secondary side sampling line 2 filter 2.
l_q^2	distance of separation of a particle charge from an opposite charge in a gas having a dielectric constant ε.
M	in appendix IV, aerosol mass concentration through the impactor stage (mg/m^3)
m_1	mass of the sample after the measurement.
$Ma=v/(\gamma \cdot R_g \cdot T)^{0.5}$	Mach number
m_{cum}	in appendix IV, cumulative percentage of total mass per impactor stage.
m_{filt}	mass collected by a filter.
m_{in}	aerosol particle mass at the inlet of the bundle.
m_o	mass of the sample before the measurement.
m_{out}	aerosol particle mass measured at the outlet of the bundle.
m_p	in appendix IV, percentage of total mass per impactor stage.
m_{ret}	aerosol particle mass retained at the tube bundle.
M_{Ti}	mass collected from the tube “Ti”
m_{total}	total mass collected.
MW_s	molecular weight of the sampled gas.
N	number of particles counted by an instrument in a bin.
n. a.	not available.
OPC	optical particle counter.
P	pressure sensor.
p	pitch, i.e. minimum distance between two neighbor tubes.

	gas pressure.
P1I1	primary side sampling line 1 filter 1.
P1I2	primary side sampling line 1 filter 2.
P2I1	primary side sampling line 2 filter 1.
P2I2	primary side sampling line 2 filter 2.
P_b	pressure at the bundle.
PDF	probability density function.
PECA	platform for experimental characterization of aerosols..
P_{in}	pressure upstream the breach.
PLC	programmable logic controller.
Press	dynamic pressure measured by the pressure transducer in the Pitot measurements.
P_s	static pressure.
PSA	probabilistic safety assessments.
P_t	total pressure.
PWR	pressurized water nuclear reactor.
Q	mass flow rate sensor..
r, R	radial distance to the axis of the broken tube.
RANS	Reynolds averaged Navier Stokes equations
$Re_D. = 4\tilde{\cdot}\mu\pi D)$	tube Reynolds number.
$Re_H. = U_o \cdot H/\nu$	impinging jets Reynolds number.
$Re_p = U_o \cdot d_p/\nu$	particle Reynolds number.
R_g	air gas constant ($Pa \cdot m^3/(kg \cdot K)$).
RMS	root mean square.
$Sc = \mu_{gas}/(\rho_{gas} \cdot \varepsilon_t)$	Turbulent Schmidt number.
SEM	scanning electron microscopy.
SG	steam generator.
SGTR	steam generator tube rupture.
SNR	signal to noise ratio.
SR	spreading rate.
$Stk = C_c \frac{\rho_{particle} \cdot (d_{particle})^2 \cdot Vtheo}{18 \cdot \mu_{gas} \cdot D}$	Stokes Number
Stk_{effMa}	effective Stokes number corrected for Ma effects. Equation 50.
T	temperature of the flow.
t_s	sampling time.
t_{start}	time at the start of the sampling.
TU	turbulence intensity based on the local velocity modulus at each point: $100 \cdot (u_{RMS}^2 + v_{RMS}^2)^{0.5}/(U^2+V^2)^{0.5}$.
u*	friction velocity
U, V	radial and axial velocity components
u', v'	velocity fluctuations from the mean value for u and v.

v	velocity.
v_{crit}	critical velocity
v_{normal}	normal component of the particle impaction velocity against a surface.
$v_{rebound}$	rebound velocity
v_s	volumetric flow sampled (l).
$Vtheo=4\Phi/(\rho\pi D^2)$	theoretical velocity.
xo	radial distance at the point where the profile cross the jet trajectory.
X_{steam}	steam fraction introduced in the gas.
$y_+=y\cdot(\rho\cdot\tau_o)^{0.5}/\mu$	normalized wall distance.
z	axial distance to the breach center.

Greek

$\chi_{VRMS}=\sum_i^n\left((v_{RMS})_i-\overline{v_{RMS}}\right)^4\Big/\left(\sum_i^n\left((v_{RMS})_i-\overline{v_{RMS}}\right)^2\right)^2$	flatness factor of V_{RMS}.
ζ	proportionality constant for Equation 1.
θ	coordinate normal to the jet axis
Φ	gas mass flow rate at the inlet of the bundle.
η	mass retention efficiency at the tube bundle.
η_{act}	dynamic viscosity of the sampled gas in actual flow conditions.
η_{ref}	reference mass retention efficiency at the bundle.
	in appendix IV, dynamic viscosity of the sampled gas in reference conditions.
μ	dynamic viscosity.
ρ	gas density.
ρ_s	density of the sampled gas.
ρ_p	particle density.
$\delta\#$	estimated uncertainty associated with variable #.
$\Lambda=(r-D/2)/p$	dimensionless spacing.
Δt	pulse lapse in CAHT, sampling lapse time in CAAT
Δx	spatial displacement.
$\Delta x'$	pixel displacement.
$\Delta\eta$	mass retention efficiency interval.
Δp_{breach}	pressure jump at the tube breach.
Δp	gas pressure difference.
$\Delta m=m_1-m_o$	mass collected by the sample during the measurement.
τ_o	wall shear stress
δ_o	thickness of the jet at the nozzle for jets Choi &

	Wood
ε_{laser_mis}	velocity uncertainty due to the laser misalignment.
ε_{turb}	velocity uncertainty due to the turbulence nature of the flow.
ε_t	eddy diffusivity.
ε	medium dielectric constant.
ν	kinematic viscosity of the gas.
γ	ratio of specific heats of the gas.
γ_p	particle shape factor.
α	jet to free stream velocity ratio for Choi & Wood.
α_1, α_2, α_3	fitting parameters for Equation 43.
β_1, β_2	fitting parameters for Equation 41.
$\kappa=F_E/(\pi\varepsilon d_{ae}/(4l_q^2))$	proportionality constant in the electrostatic forces relationship with particle diameter.
λ	fitting parameter for Equation 37.

Subscripts

filt	filter
gas	gas.
L	Characteristic length of the particle
max	maximum
min	minimum
normalized	normalized.
p	particle.
s	Sampling.
stage	impactor stage
T	tube.

Symbols

$\overline{\quad}$	
$\langle\ \rangle$,	average

References

Abramovich G.N.,1963. *The theory of turbulent jets, MIT Press*, Massachusetts.

Allison C.M. et al, 1995, *SCDAP/RELAP5/MOD3.1 Code Manual*, NUREG/CR-6150.

Arreghini F., Jacquemain D., Garnier Y., 2000. *Summary of Fission Product Behavior and Structure Material Behavior in FPT1*, presented at 4th Technical Seminar on the PHEBUS-FP Programme, March 20-22, Marseille, France.

Arts, Boerrigter, Buchlin, Carbonaro, Degrez, Denos, Fletcher, Olivari, Riethmuller, Braembussche, 2001. *Measurement techniques in fluid dynamics*, 2nd edition, von Karman Institute for Fluid Dynamics.

Auvinen, A., Jokiniemi, J.K., Lähde, A., Routamo, T., Lundström, P., Tuomisto, H., Dienstbier, J., Güntay, S., Suckow, D., Dehbi, A., Slootman, M., Herranz, L.E.., Peyres, V., Polo, J., 2005. *Steam generator tube rupture (SGTR) scenarios*. Nucl. Eng. Des. Vol.235, pp. 457-472.

Aylor, D.E., Ferrandino, F.J., 1985. *Rebound of pollen and spores during deposition on cylinders by inertial impaction*. Atmospheric Environment, Vol.19 (5), pp.803-806.

Balabani S., Yianneskis M., 1996. *An experimental study of the mean flow and turbulence structure of cross-flow over tube bundles*, Proc. IMechE C, J. Mech. Eng. Sci. Vol.210, pp.317–331.

Bakker P., Slootman M., Dienstbier J., Güntay S., Herranz L., Jokiniemi J., Routamo T., 2001. *Accident Management Aspects of EU-SGTR Project,* NEA/CSNI/R(2001)20 Proc of the Workshop on Implementation of Severe Accident Management Measures., Villigen, Switzerland.

Barata J.M.M., Durao D.F.G., Heitor M.V., McGuirk J.J., 1992. *The turbulence characteristics of a single impinging jet through a crossflow*. Exp Thermal Fluid Sci, Vol.5, pp.487-498.

Blackwelder, R. F., Haritonidis J. H., 1983. *Scaling of the bursting frequency in turbulent boundary layers*. J. Fluid Mechanics, Vol.132, pp.87-103.

Brandt O., Rajathurai A.M., Roth P., 1987. *First observations on break-up of particle agglomerates in shock waves*. Experiments in Fluids, Vol.5, pp.86-94.

Brockmann, J.E., 1985. *Range of possible dynamic and collision shape factors*. Report SAND84-0410, Vol. 2, App. F.

Choi Y., Wood I.R., 1966. *Momentum diffusion from a two-dimensional jet*. Report no 90, Water Research Laboratory. University of New South Wales, Australia.

Cornaro C., Fleischer A.S., Goldstein R.J., 1999. *Flow visualization of a round jet impinging on cylindrical surfaces*. Exp. Thermal Fluid Sci. Vol.6, pp.66-78

Da Silva, H.C., Kenton, M.A., 2007. *Level 2 analysis to estimate LERF risk from a thermally induced rupture of a steam generator tube defect*. Nucl. Eng. Des. Doi:10.1016/j.nucengdes.2007.09.007.

Degussa Inc., 2005. *Aeroxide P25 product specifications data sheet*. Frankfurt, Germany.

Dehbi A., Güntay S., Suckow D., 2001. *Test Matrix for the ARTIST Consortium Experiments*, Draft, TM-42-01-01, Paul Scherrer Institut.

Douglas, P.L., Ilias, S., 1988. *On the deposition of aerosol particles on cylinders in turbulent cross flow*. J. Aerosol Sci. Vol.19 (4), pp.451–462.

Fauske & Associates, Inc., 1984. *Resuspension of deposited aerosols following primary system or containment failure*. IDCOR Technical Report 11.6.

Fouras A., Soria J., 1998. *Accuracy of out-of-plane vorticity measurements derived from in-plane velocity field data*. Exp in Fluids Vol.25, pp.409-430.

Froeschke, S., Kohler, S., Weber, A.P., Kasper, G., 2003. *Impact fragmentation of nanoparticle agglomerates*, J. Aerosol Sci. Vol.34, pp.275-287.

Fromentin, A., 1987. *Dry resuspension: state of the art*. Draft Report, Paul Scherrer Institut, Würenlingen, Switzerland.

Fuchs N.A., 1964. *Mechanics of Aerosols*, Pergamon, New York.

Fung J.C.H., Vassilicos JC, 2003. *Inertial particle segregation by turbulence*, Physical Review E 68:046309-1-7.

Girshovich T.A., 1966. *Theoretical and experimental study of a plane turbulent jet in a cross-flow*. Fluid Dyn Vol.9, pp.84-86

Güntay S., Dehbi A., Suckow D., Birchley J., 2002. *ARTIST: an international project investigating aerosol retention in a ruptured steam generator*. Proc of Int congress on advanced nuclear power plants ICAPP'02, June 9-13, Hollywood, Florida.

Güntay S., Suckow D., Dehbi A., Kapulla R., 2004. *ARTIST: introduction and first results*. Nucl Eng Des Vol.231, pp.109-120.

Güntay. S, 2007. *How efficient are PWR steam generators as the last barrier during an accident?*, Information Meeting of Artist project for CSN, November 19, Madrid, Spain.

Hall, D., 1988. *Measurements of the mean force on a particle near a boundary in turbulent flow*. Journal of Fluid Mechanics, Vol.187, pp.451-466.

Herranz L., Del Prá C.L., Velasco F.J.S., Muñoz-Cobo J.L., Escrivá A, 2005. *Insights into aerosol depletion from a high velocity flow across a tube bank: a key scenario for nuclear safety*. Proc of 6th World conf on experimental heat transfer, fluid mechanics and thermodynamics. April 17-21, Miyagi, Japan.

Herranz L.E., Del Prá C.L., Dehbi A., 2007. *Major Challenges to modeling aerosol retention near a tube breach during steam generator tube rupture sequences*. Nucl Tech Vol.158, pp.83-93.

Herranz L.E., Velasco, F.J.S., Del Prá, C.L., 2006. *Aerosol retention near the tube breach during steam generator tube rupture sequences*. Nucl Technol Vol.154, pp.85-94.

Heskestad G., 1966. *Hot-wire measurements in a radial turbulent jet*, Trans. ASME J. Appl. Mech., pp.417-424.

Hinds W.C., 1982. *Aerosol technology*, Jonh Wiley & Sons, New York.

Hooper J.D., 1980. Nucl Eng Des Vol.60, pp.365.

Hussain F., Husain H.S., 1989. *Elliptic jets. Part 1. Characteristics of unexcited and excited jets*. J. Fluid Mech Vol.208, pp.257-320.

Hwang, S.S., Namgung, C., Jung, M.K., Kim, H.P., Kim, J.K., 2008. *Rupture pressure of wear degraded Alloy 600 steam generator tubings*. J. Nucl. Mat. 373 71–74.

Ingham D.B., Hildyard M.L., Heggs P.J., 1989. The particle collection efficiency of a cascade of cylinders. Canadian J. Chem. Eng. Vol.67, pp.545-553.

IRSN, 2006. *Astec VI.3 Sophaeros module: theoretical manual rev.1*. Note technique Semic-2006-379.

ISO NORM, 1995. *Guide to expression of uncertainty in measurement. Corrected and Reprinted.* ISBN 92-67-10188-9. International Organization for Standardization, Geneva, Switzerland.

Israel R., Rosner D.E., 1983. *Use of a generalizad Stokes number to determine the aerodynamic capture efficiency of non-stokesian articles from a compressible gas flow*. Aerosol Sci. Tech., Vol.2, pp.45.

Khushnood S., Khan Z.M., Malik M.A., Koreshi Z.U., Khan M.A., 2004. *A review of heat exchanger tube bundle vibrations in two-phase cross-flow*. Nucl Eng Des Vol.230, pp.233-251.

Konstandopoulos A. G. Labowsky M., Rosner D.E., 1993. *Inertial deposition of particles from potential flow past cylinder arrays*. J. Aerosol Sci., Vol.24 (4), pp.471-483.

Konstandopoulos A.G., 2006. *Particle sticking/rebound criteria at oblique impact*. J. Aerosol Sci., Vol.37, pp.292-305.

Lee J., Lee S.J., 2000. *The effect of nozzle aspect ratio on stagnation region heat transfer characteristics of elliptic impinging jet*. Int J Heat Mass Transfer Vol.43, pp.555-575.

Lee S.J., Baek S.J., 1994. *The effect of aspect ratio on the near-field turbulent structure of elliptic jets*. Flow Meas Instrum Vol.5 (3), pp.170-180.

López del Prá C., Sánchez-Velasco F.J., Herranz L.E., 2007. *CFD Modeling of a gas jet in the nearby of a broken tube in a shell-and-tube heat exchanger: application to a risk-dominant scenario in nuclear power plants*. Proc. 5th Int Conf on Heat Transfer, Fluid Mechanics and Thermodynamics, July, Sun City South Africa.

López del Prá C., Velasco F.J.S., Herranz L.E., 2008. *Aerodynamics of a gas entering the secondary side of a vertical shell-and-tube heat exchanger: Numerical analysis of anticipated severe accident SGTR conditions*. Accepted for publication in Engineering Applications of Computational Fluid Mechanics.

Lourenço, 1982. PhD Thesis, Von Karman Institute, Belgium.

McLaughlin C., McComber P., Gakwaya A., 1986. Numerical calculation of particle collection by a row of cylinders in a viscous fluid. Canadian J. Chem. Eng. Vol.64, pp.205-210.

Meyer K.E., *Experimental and numerical investigation of turbulent flow and heat transfer in staggered tube bundles*, Ph.D. Thesis, Technical University of Denmark, 1994.

Moens J.B., 1995. *Development of a new D-PIV technique to investigate the flow behind a bluff body*, Project Report 1995-01, von Karman Institute for Fluid Dynamics.

Nagase Inc., 2006. *Seahostar product specifications data sheet*. Japan.

Nanophase Inc., 2002. *NANOTEK product specifications data sheet*. Romeoville, IL, USA.

New T.H., Lim T.T., Lou S.C., 2004. *Flow field study of an elliptic jet in crossflow using DPIV technique*. Exp Fluids Vol.36, pp.604-619.

New T.H., Lim T.T., Luo S.C., 2003. *Elliptic jets in crossflow*. J Fluid Mech Vol.494, pp.119-140.

Pau K.T., 1983. *The rebound of particles from natural surfaces*. J. Colloid Interface Sci., Vol.93(2), pp.442.

Paul S.S., Tachie M.F., Ormiston S.J., 2007. *Experimental study of turbulent cross-flow in a staggered tube bundle using particle image velocimetry*. Int J Heat Fluid Flor Vol. 28, pp. 441-453.

PSI, 2008. *Summary report on ARTIST Phase II tests for retention in the break stage*. Artist 72-08. TM-42-08-04. Paul Scherrer Institut. Switzerland.

Quarini, J.1999. CFD model of the PSI steam generator. Report submitted to Paul Scherrer Institut.

Quinn W.R., 1989. *On the mixing in an elliptic turbulent free jet*. Phys Fluids B1 pp.1716-1722

Raffel M., Willert C.E., Kompenhans J., 1998. *Particle Image Velocimetry – A Practical Guide*, Springer.

Rajaratman N., 1976. *Turbulent Jets*. Amsterdam: Elsevier Scientific Publishing Company.

Ranz W.E., Wong J.B., 1952. *Impaction of dust and smoke particles on surface body and body collectors*, Ind. & Eng. Chem., Vol.44 (6), pp.1371.

Rosner et al., 1995. *Local size distributions of particles deposited by inertial impaction on a cylindrical target in dust-laden streams*. J. Aerosol Sci. Vol. 26. No. 8, pp. 1257-1279.

Rowe D.S., Johnson B.M., Knudsen J.G., 1974. Int. J. Heat Mass Transfer. Vol.17, pp.407.

Sánchez-Velasco F.J., López del Prá C.L., Herranz L.E., 2006. *Aerodynamics of a radial jet from a tube breach in a shell and tube heat exchanger*. Proc of 13th Int Symp of Applications of Laser Techniques to Fluid Mechanics. June 26-29, Lisbon, Portugal.

Scarano F., Riethmuller M.L., 2000. *Advances in iterative multigrid PIV image processing*. Exp Fluids Vol.29, pp.S51-S60.

Schlichting H., Gersten K., 2000. *Boundary Layer Theory*. Chap. 12.2.3. Ed Springer.

Schuh H., Persson B., 1964. *Heat transfer on circular cylinders exposed to free-jet flow*. Int J Heat Mass Transfer Vol.7, pp.1257-1271.

Schwarz W.H., 1963. *The radial free jet*, Chem. Eng. Sci. Vol.18, pp.779-786.

Seale W.J., 1982. *Measurements and predictions of fully developed turbulent flow in a simulated rod bundle*. J Fluid Mech Vol.123, pp.99-423.

Sears W.R., 1948. *The boundary layer of yawed cylinders*. J Aeronaut Sci Vol.15, pp.49-52.

Shayesteh M.V., Shabaka I.M.N.A., Bradshaw P., 1985. *Turbulent structure of a three-dimensional impinging jet in a crossflow*. AIAA Paper 85-0044, AIAA 23rd Aerospace Science Meeting, 14-17 Jan, Reno, Nevada.

Sherif S.A., Pletcher R.H., 1989. *Measurements of the flow and turbulence characteristics of round jets in crossflow*. J Fluids Eng. Vol.111, pp.165-171.

Simoin O., Barcouda M., 1988. *Measurement and prediction of turbulent flow entering a staggered tube bundle*, Proceedings of 4th International Symposium on Applications of Laser Anemometry to Fluid Mech., Lisbon, Portugal.

Sparrow E.M., Lovell B.J., 1980. *Heat transfer characteristics of an obliquely impinging circular jet*. J. Heat Transfer Vol.102, pp.202-209.

Tsiang R.C., Wang C.S., Tien C., 1982. Dynamics of particle deposition on model fibre filters. Chem. Eng. Sci. Vol.37, pp.1661-1673.

TSI Corporate, 1997. *PIV hardware operation's manual*. P/N 1990831, St Paul, Minnesota, USA.

TSI Insight 3G, 2004. *User's Guide.* P/N 1980511. St Paul, Minnesota, USA.

US NRC, 1990. *Severe accident risks: an assessment of five U.S. nuclear power plants*, Vol.2. Sandia National Laboratory Report NUREG-1150.

US NRC, 1996, *Steam generator tube failures*, NUREG/CR-6365.

Velasco F.J.S., López del Prá C.L., Herranz L.E., 2008. *Experimental study of aerosol renoval from a gas jet moving through a tube bank.* European Aerosol Conference 2008, August 24-29, Thessalonica, Greece.

Velasco F.J.S., López del Prá C.L., Herranz L.E., 2007. *Uncertainty on experimental aerosol characterization: calibration tests supporting aerosol studies under severe accident SGTR conditions*. European Aerosol Conference 2007, September 9-14, Salzburg, Austria.

Wang, H.C., John, W., 1998. *Dynamic adhesion of particles impacting a cylinder*. (pp. 211-224) In: *Particles on surfaces*. K.L. Mittal (Ed.), New York: Plenum.

Wessel R.A., Righi J., 1988. *Generalized correlations for inertial impaction of particles on a circular cylinder*. Aerosol Sci. & Tech. Vol.9(1), pp.29-60.

Wild J.M., 1949. *The boundary layer of yawed infinite wings*. L Aeronaut Sci Vol.16, pp.41-45.

Witze P.O., Dwyer H.A., 1976. *The turbulent radial jet*. J Fluid Mech Vol.75, pp.401-417.

Wong, J.B., Johnstone, H.F., 1953. Engineering Experimental Station, University of Illinois, Tech. Rep. No. 11.

Zhu C., Lin C.-H., Cheung C.-S., 2000. *Inertial impaction-dominated fibrous filtration with rectangular or cilindrical fibers*. Powder Technol., Vol.112, pp.149.

Appendixes

Appendix I: CAHT facility detail plans

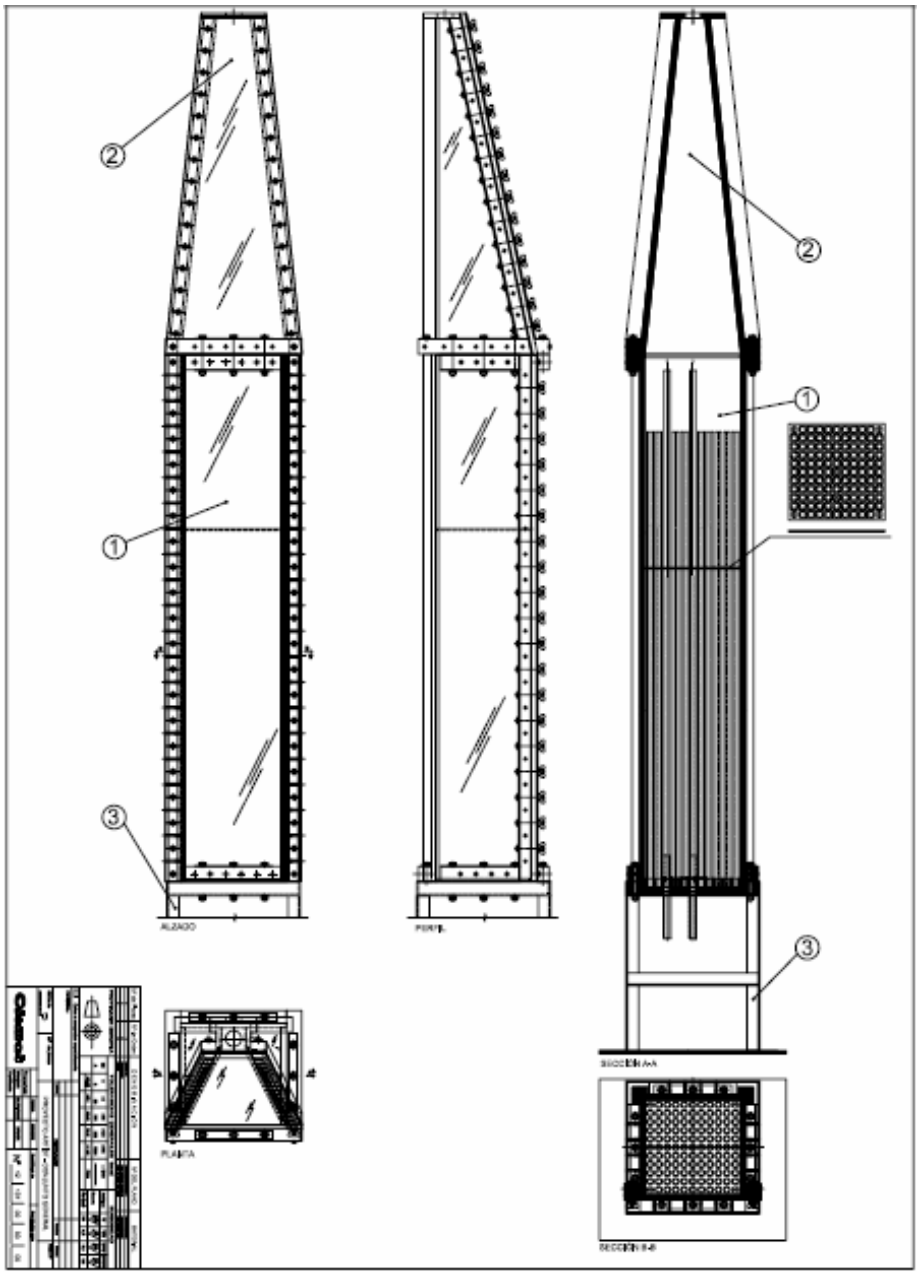

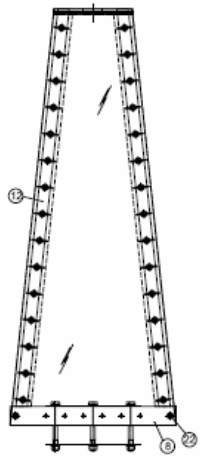

ALZADO

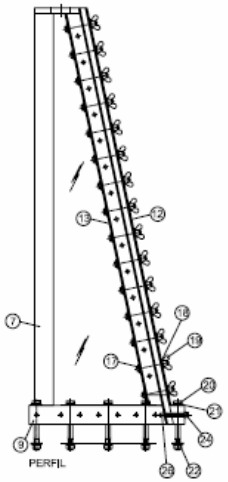

PERFIL

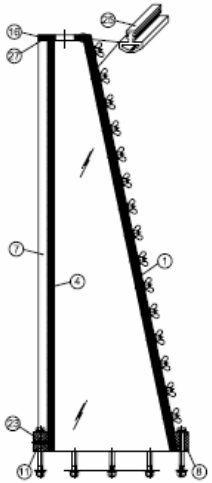

SECCIÓN A-A

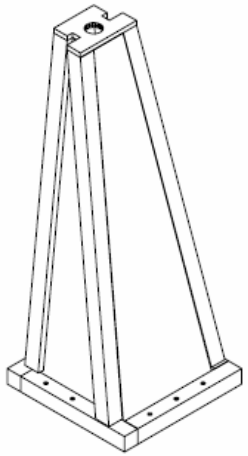

PERSPECTIVA

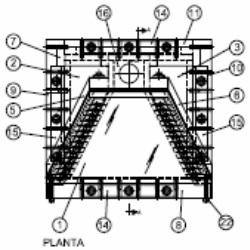

PLANTA

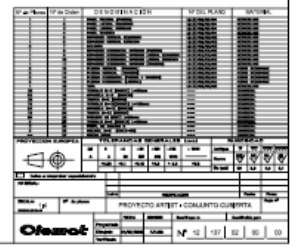

Ofesrot

PROYECTO ARTEST + CONJUNTO CUBIERTA

Nº 12 | 137 | 02 | 00 | 03

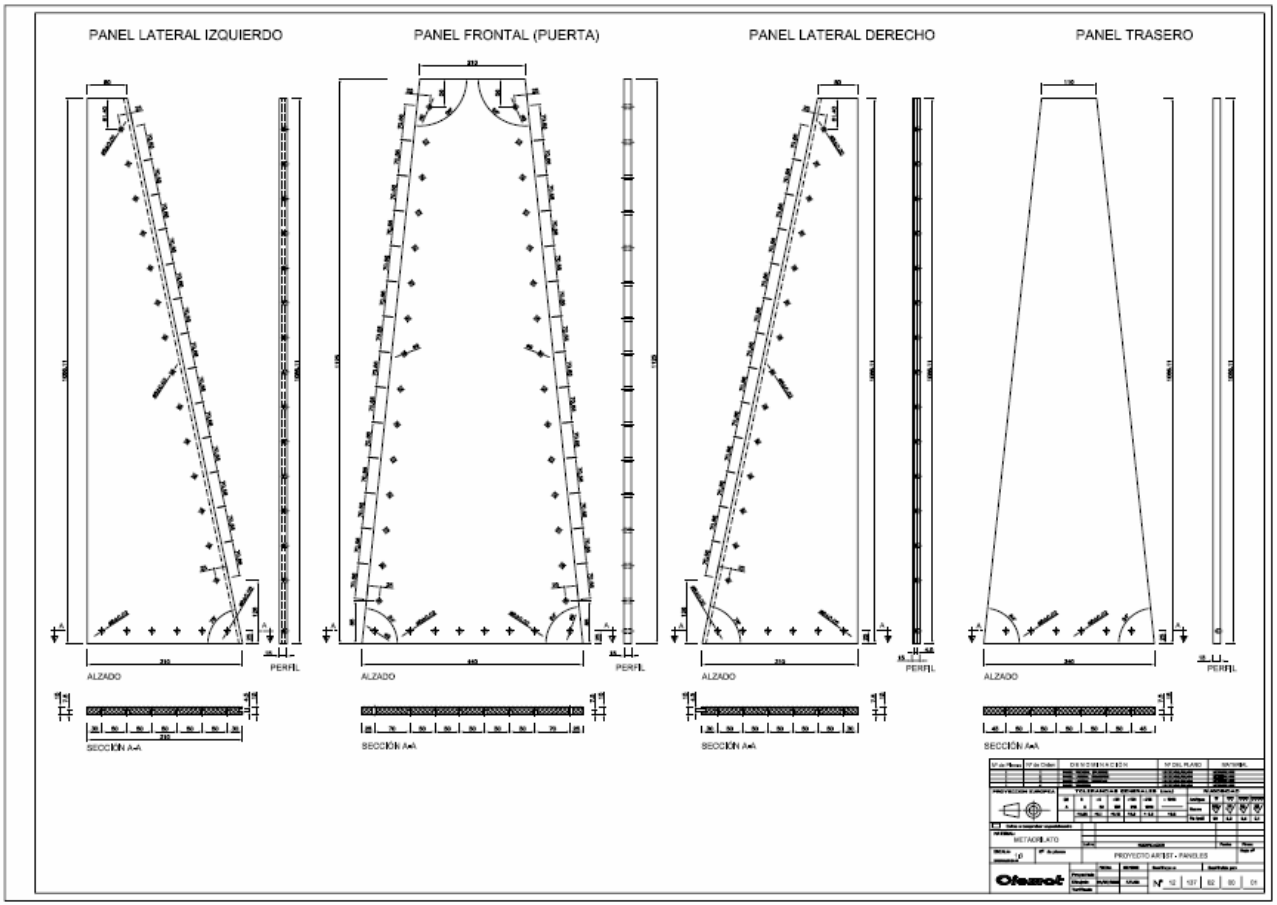
PANEL LATERAL IZQUIERDO
PANEL FRONTAL (PUERTA)
PANEL LATERAL DERECHO
PANEL TRASERO
ALZADO
PERFIL
SECCIÓN A-A
METACRILATO
PROYECTO ARTIST - PANELES
Ofesrot

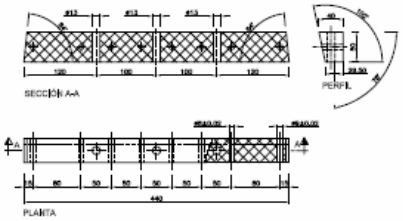

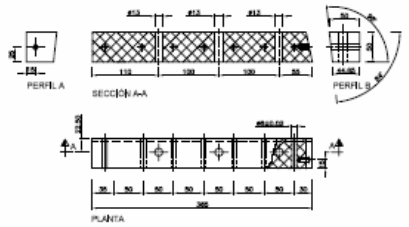

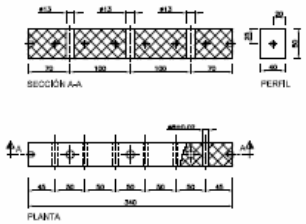

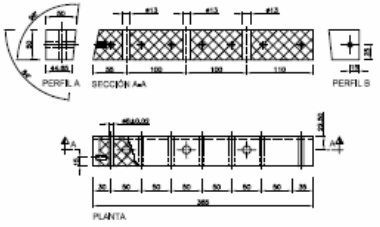

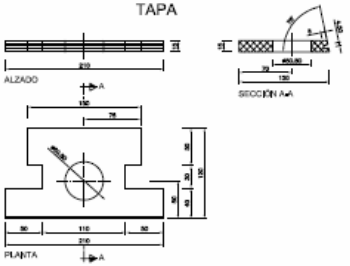

REFUERZO HORIZONTAL
INFERIOR FRONTAL (PUERTA)
SECCIÓN A-A
PERFIL
PLANTA
440
REFUERZO HORIZONTAL
INFERIOR LATERAL IZQ.
PERFIL A
SECCIÓN A-A
PERFIL B
PLANTA
365
REFUERZO HORIZONTAL
INFERIOR TRASERO
SECCIÓN A-A
PERFIL
PLANTA
340
REFUERZO HORIZONTAL
INFERIOR LATERAL DCHO.
PERFIL A
SECCIÓN A-A
PERFIL B
PLANTA
365
TAPA
ALZADO
210
SECCIÓN A-A
PLANTA
150
110
210
Nº de Piezas
Nº de Orden
DENOMINACIÓN
Nº DEL PLANO
MATERIAL
PROYECCIÓN EUROPEA
TOLERANCIAS GENERALES
METACRILATO
PROYECTO ARTIST / REFUERZOS HORIZONTALES Y TAPA
Nº 12 137 02 00 02

REFUERZO VERTICAL DERECHO

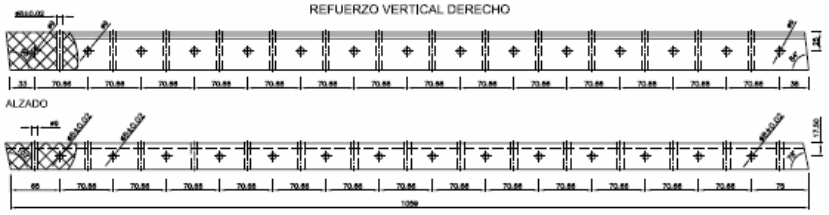

REFUERZO VERTICAL IZQUIERDO

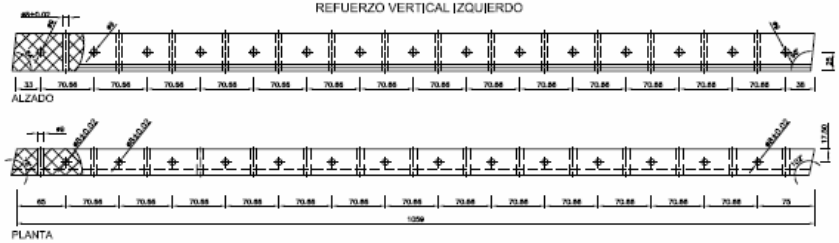

MOLDURA

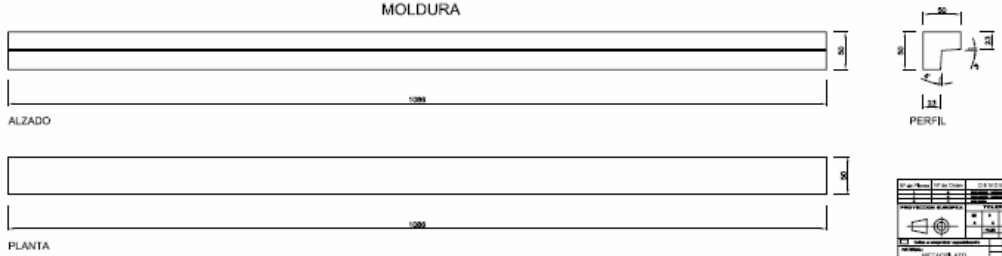

METACRILATO

Ofesmat

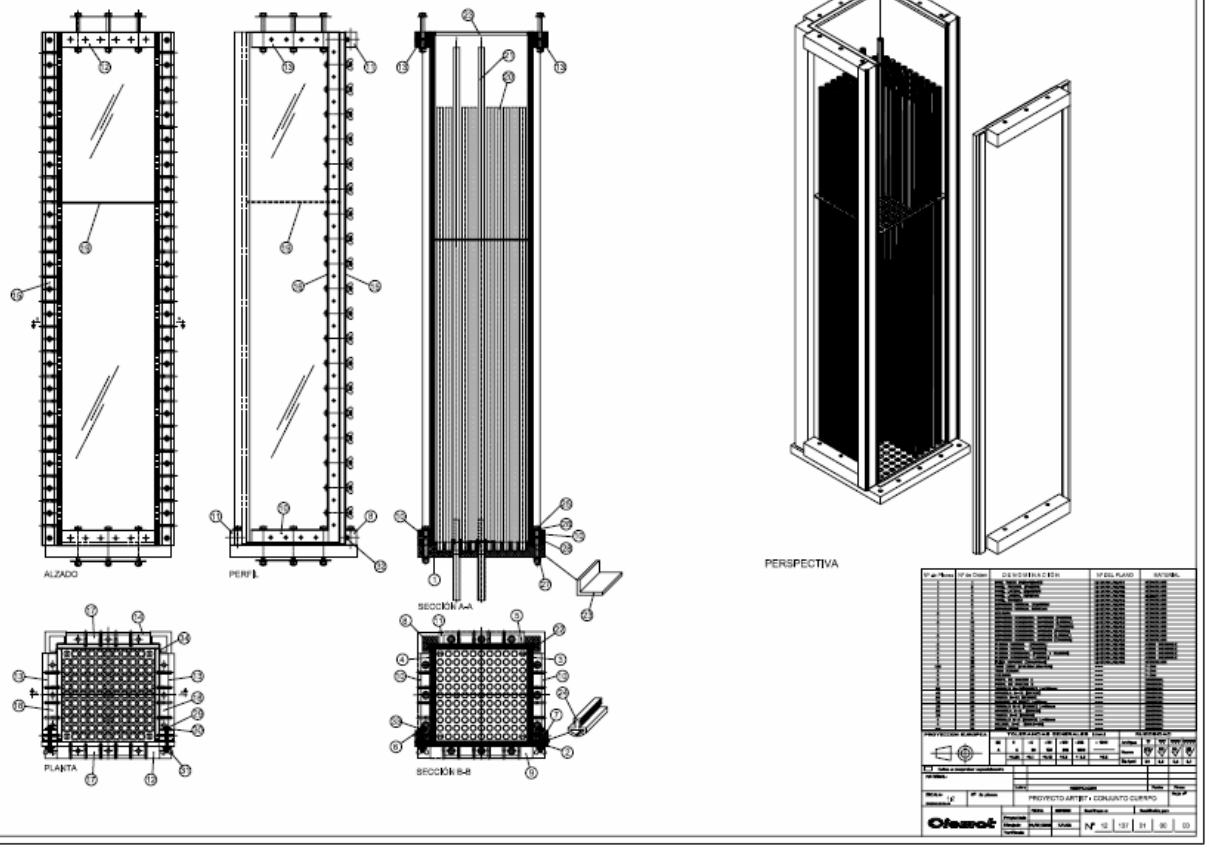
ALZADO
PERFIL
SECCIÓN A-A
PERSPECTIVA
PLANTA
SECCIÓN B-B

BASE TUBOS (420x420x50)

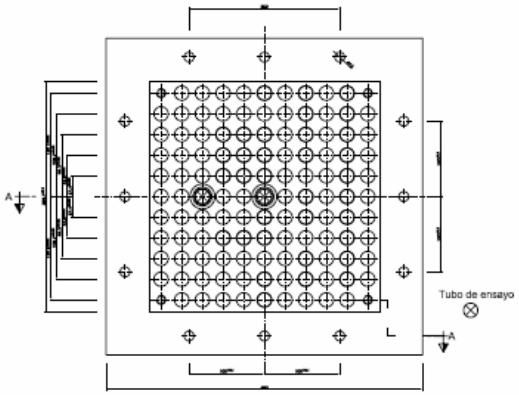

PLANTA

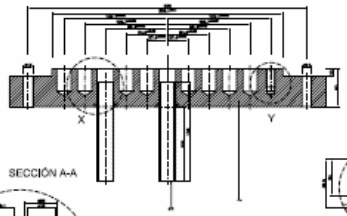

SECCIÓN A-A

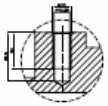

DETALLE Y esc.2:1

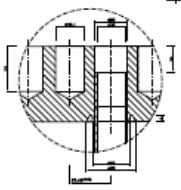

DETALLE X esc.2:1

PLACA SOPORTE (310x310x5)

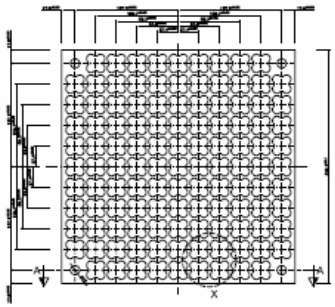

PLANTA

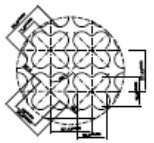

DETALLE X esc.2:1

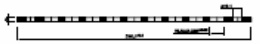

SECCIÓN A-A

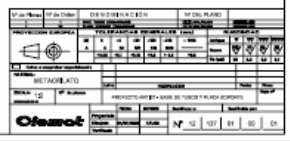

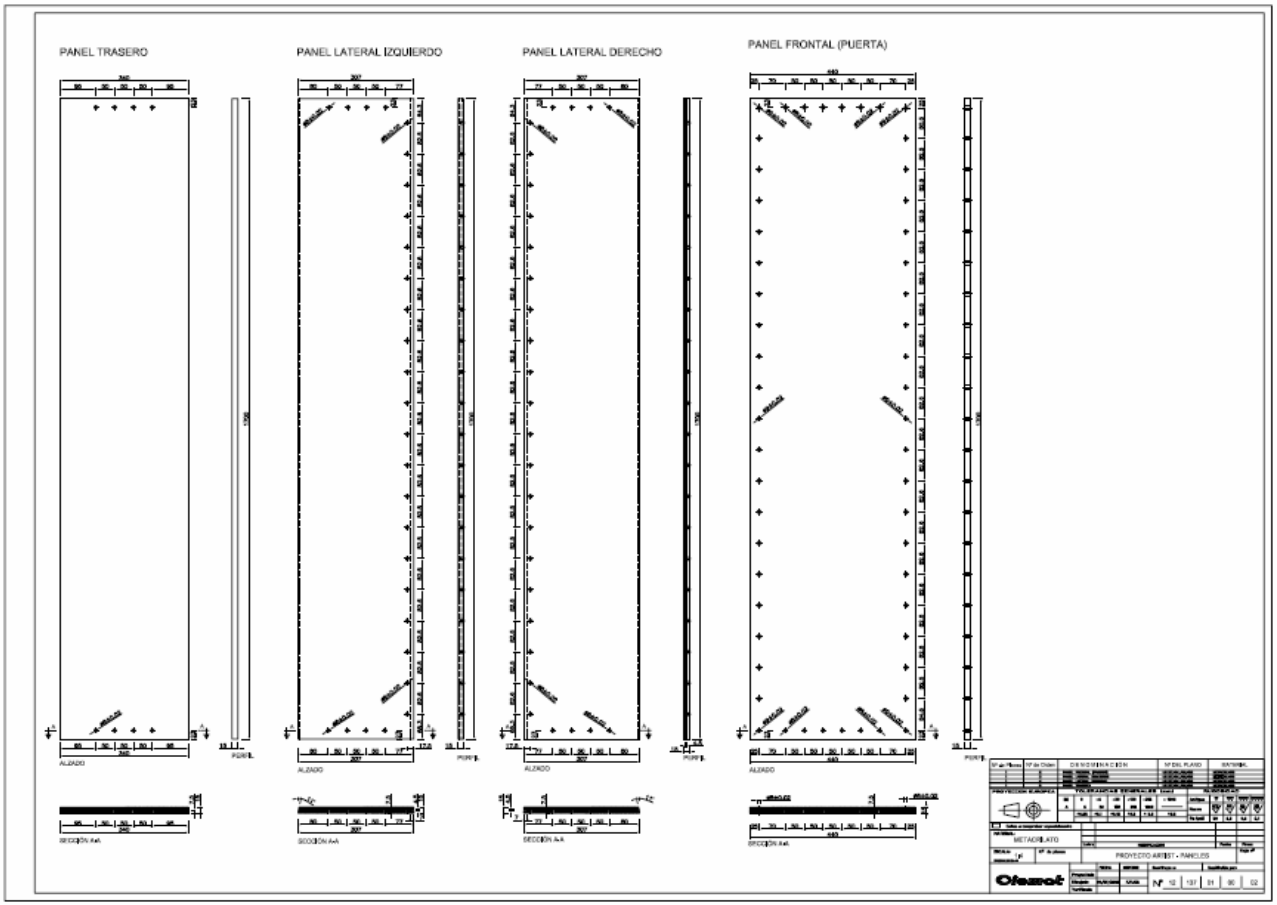
PANEL TRASERO
PANEL LATERAL IZQUIERDO
PANEL LATERAL DERECHO
PANEL FRONTAL (PUERTA)
ALZADO
PERFIL
SECCIÓN A-A
METACRILATO
PROYECTO ARTIST - PANELES
Ofesrot

REFUERZO HORIZONTAL
SUPERIOR TRASERO

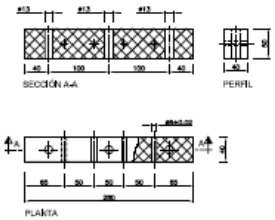

REFUERZO HORIZONTAL
SUPERIOR LATERAL IZQ.

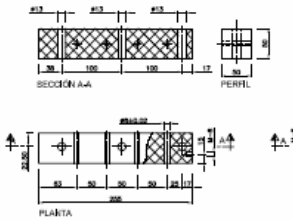

REFUERZO HORIZONTAL
SUPERIOR LATERAL DCHO.

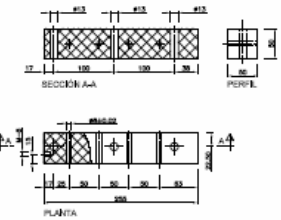

REFUERZO HORIZONTAL
SUPERIOR FRONTAL (PUERTA)

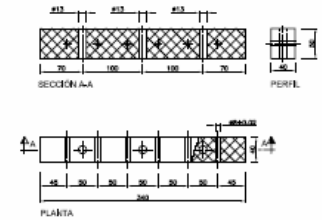

REFUERZO HORIZONTAL
INFERIOR TRASERO

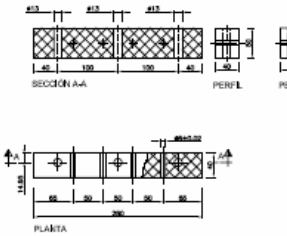

REFUERZO HORIZONTAL
INFERIOR LATERAL IZQ.

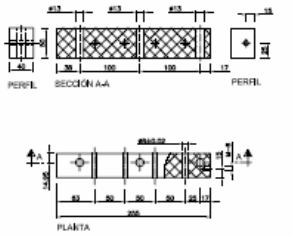

REFUERZO HORIZONTAL
INFERIOR LATERAL DCHO.

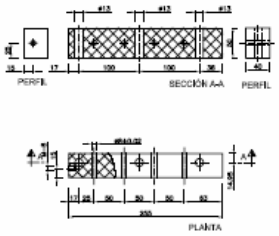

REFUERZO HORIZONTAL
INFERIOR FRONTAL (PUERTA)

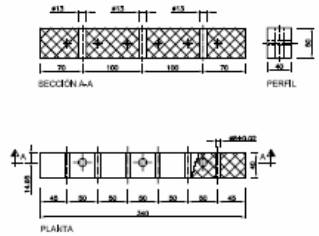

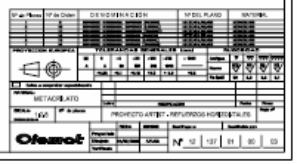

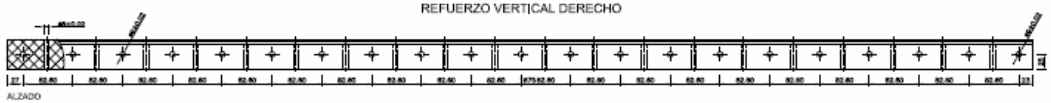

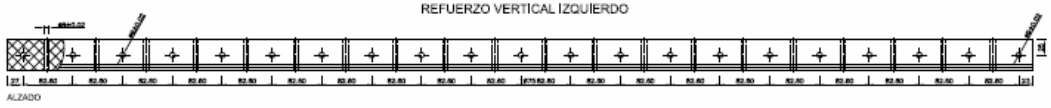

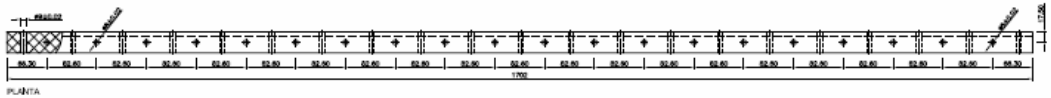

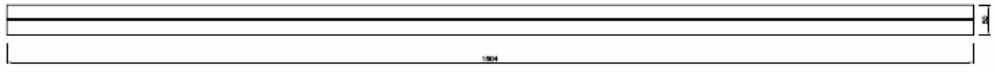

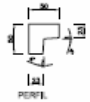

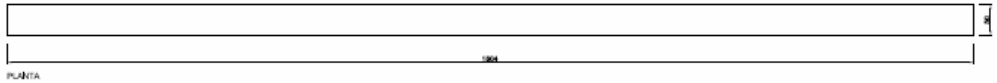

REFUERZO VERTICAL DERECHO
27
82.60
875
23
35
4.5
50
ALZADO
PERFIL
66.30
1702
17.50
PLANTA
REFUERZO VERTICAL IZQUIERDO
ALZADO
PERFIL
PLANTA
MOLDURA
50
1904
33
ALZADO
PERFIL
PLANTA
Nº de Piezas
Nº de Orden
DENOMINACIÓN
Nº DEL PLANO
MATERIAL
PROYECCIÓN EUROPEA
TOLERANCIAS GENERALES
METACRILATO
1/10
PROYECTO MEDEI - REFUERZOS VERTICALES Y MOLDURA
Ofemat
Nº 10 137 01 00 04

Appendix II: Description of main variables of PIV post-processing script

- `x, y_mesh`: Horizontal and vertical spatial vectors expressed in milimiters. The coordinate origin is set in the left down side of the PIV image. The sufix `_mesh` indicates that the variable has been re-arranged to coincide with the spatial position of the corresponding pixel so that the variable field reproduce spatially the initial image.
- `u_mesh, v_mesh, vel_mod`: Matrixes of x*y_mesh size. They contain the x and y mean velocity components fields and the velocity modulus fields obtained from the averaged of data from the `*.vec` files.
- `SNR_mesh`: Matrixes of x*y_mesh size with the signal to noise ratio field obtained from the corss-correlation of the images. The SNR is the ratio first to second maximum values in the correlation.
- `Count, count_mesh` : Matrixes of x*y_mesh size with field of number of valid velocity data obtained after the filtering. These variables are used to compute the statistical moment fields.
- `u_std_good_mesh, v_std_good_mesh, velmag_std_good_mesh` : Matrixes of x*y_mesh size with the standard deviation field of `_mesh, v_mesh y vel_mod.`
- `Ma, Re` : Matrixes of x*y_mesh size with the Mach y Reynolds field computed from:
```
ro=ro_fix;
aair=sqrt(gamma*Rair*Tair); %m/s
Re=ro*D*0.001*vel_mod/mu;
Ma=vel_mod/aair;
```
- `Time_res` : Matrixes of x*y_mesh size with the residence time of the particle in the measured zone (i.e. window) and computed from:
`Time_res(i,j)=sqrt(deltax*deltay)/vel_mod(i,j);`
where `deltax, deltay` is the spatial resolution of the processing defined by the distance between two neighbour windows expressed in milimiters which is the distance between two neighbour vectors.
- `div, w`: Matrixes of x*y_mesh size with the velocity divergence and vorticity fields computed from central differences in cylindrical coordinates (being `x` the radial coordinate and `y` the axial one) for guillotine experiments and in cartesian coordinates in the fish-mouth experiments:
```
div(i,j)=(x(i)*u_mesh(i,j)-x(i-1)*u_mesh(i-
1,j))/(deltax*x(i)) + (v_mesh(i,j)-v_mesh(i,j-
1))/(deltay);
w(i,j)=(u_mesh(i,j)-u_mesh(i,j-1))/(deltay)-
(v_mesh(i,j)-v_mesh(i-1,j))/(deltax);
```

- `u_prim2, v_prim2, u_prim_div_v_prim` : Matrixes of x*y_mesh size with Re stresses $\overline{u'^2}, \overline{v'^2}$ fields. They are statistically defined as the velocity variance fields. `u_prim_div_v_prim` is the ratio: $\frac{\overline{u'^2}}{\overline{v'^2}}$.
- `ReSt_good_mesh` : Matrixes of x*y_mesh size with the $\overline{-u' \cdot v'}$ Reynold stress field. It is statistically defined as the negative covariance of the u and v velocity components.
- `ReStress_NonDim_func_prim` Matrixes of x*y_mesh size with the dimensionless Reynolds stress $\frac{\overline{-u' \cdot v'}}{\sqrt{\overline{u'^2} \cdot \overline{v'^2}}}$ field. Statistically defined as the covariance divided by the standard deviation of the velocity components.
- `angle` : Matrixes of x*y_mesh size with the velocity vector angle field obtainde from:

```
angle(i,j)=180/pi*atan(v_mesh(i,j)/u_mesh(i,j))-
ang_corr;
if (v_mesh(i,j)<0 & u_mesh(i,j)< 0) |
(v_mesh(i,j)>0 & u_mesh(i,j)< 0)
angle(i,j)=angle(i,j)+180;
end
if v_mesh(i,j)<0 & u_mesh(i,j)> 0
angle(i,j)=angle(i,j)+360;
end
```

- `dU, dV, dvel_mod, dU_rel, dV_rel, dvel_mod_rel, dangle, dangle_rel` : Matrixes of x*y_mesh size with the uncertainties associated to `u_mesh, v_mesh, vel_mod` and their relative values obtained from:

```
dU(i,j)=abs(t*((un_deltaXprima*calibx./deltaTx(i,j)
).^2+(un_calibx*u_mesh_pix(i,j)./deltaTx(i,j)).^2+(
un_deltaT*calibx*u_mesh_pix(i,j)./(deltaTx(i,j).^2)
).^2).^0.5);
dV(i,j)=abs(t*((un_deltaXprima*caliby./deltaTy(i,j)
).^2+(un_caliby*v_mesh_pix(i,j)./deltaTy(i,j)).^2+(
un_deltaT*caliby*v_mesh_pix(i,j)./(deltaTy(i,j).^2)
).^2).^0.5);
dU_rel(i,j)=100*abs(dU(i,j)/u_mesh(i,j));
dV_rel(i,j)=100*abs(dV(i,j)/v_mesh(i,j));
dvel_mod(i,j)=abs(((dU(i,j).*u_mesh(i,j)./vel_mod(i
,j)).^2+(dV(i,j).*v_mesh(i,j)./vel_mod(i,j)).^2).^0
.5);
dvel_mod_rel(i,j)=100*abs(dvel_mod(i,j)/vel_mod(i,j
));
dangle(i,j)=un_ang_corr +
180/pi*(((v_mesh(i,j)/((u_mesh(i,j))^2+(v_mesh(i,j)
```

```
)^2))*dU(i,j))^2+(1/(u_mesh(i,j)*(1+(v_mesh(i,j)/u_
mesh(i,j))^2))*dV(i,j))^2)^0.5;
dangle_rel=100*dangle./angle;
```

being:

```
deltaTx(i,j)=abs(u_mesh_pix(i,j)*calibx./u_mesh(i,j
));
deltaTy(i,j)=abs(v_mesh_pix(i,j)*caliby./v_mesh(i,j
));
```

where `u_mesh_pix`, `v_mesh_pix`, are the mean velocity fields expresed in (pixels / s) units.

- `TUu_good`, `TUv_good`, `TUvelmag_good`, `TUu_mesh`, `TUv_mesh`, `TUvelmag_mesh` : Matrixes of x*y_mesh size with the turbulent intensity values associated to `u_mesh`, `v_mesh`, `vel_mod`, defined as:

```
TUu_good(i,j)=100*abs(u_std_good_mesh
(i,j)/u_mesh(i,j));
TUv_good (i,j)=100*abs(v_std_good_mesh
(i,j)/v_mesh(i,j));
TUvelmag_good (i,j)=abs(((velmag_std_good_mesh
(i,j)/vel_mod(i,j));
```

`TUu_mesh`, `TUv_mesh`, `TUvelmag_mesh`, represent the same variables re-arranged to coincide with the spatial position of the corresponding pixel so that the variable field reproduce spatially the initial image.

- `velmag_skew_good_mesh`, `velmag_flat_good_mesh` Matrixes of x*y_mesh size with the skewness and flatness velocity fields associated to the variable `vel_mod` and normalized with the standard deviation. They are computed from:

$$\text{velmag\_skew\_good\_mesh}(i,j)=\frac{\sum_{k}^{\text{count}}\left(\text{velmag}(i,j,k)-\text{vel\_mod}(i,j)\right)^3}{\text{count\_mesh}(i,j)\left(\text{velmag\_std\_good\_mesh}(i,j)\right)^3}$$

$$\text{velmag\_flat\_good\_mesh}(i,j)=\frac{\sum_{k}^{\text{count}}\left(\text{velmag}(i,j,k)-\text{vel\_mod}(i,j)\right)^4}{\text{count\_mesh}(i,j)\left(\text{velmag\_std\_good\_mesh}(i,j)\right)^{43}}$$

where `velmag(i,j,k)` is the instantaneous velocity field associated to the k-esim `*.vec` file.

Appendix III: CAAT experimental measurements qualification

MASS BALANCE DISCUSSION

Mass balance of the experiments was performed by comparing the mass incoming the bundle (m_{in}) obtained from mass concentration measurements at the inlet of the bundle with the mass retained on the tubes (m_{ret}) and the mass going out from the bundle (m_{out}) obtained from mass concentration measurements at the outlet of the bundle. Fig.III.1 shows $m_{in}/(m_{ret}+ m_{out})$ as a function of the inlet mass flow rate of each tests with aerosol particle nature as parameter. The uncertainty in the estimation of $m_{in}/(m_{ret}+ m_{out})$ have been also represented as error bars. Results shows, that mass balance agrees (i.e. in=ret+out) within the uncertainty band of the mass measurements in all cases except for the SiO_2 low concentration tests.

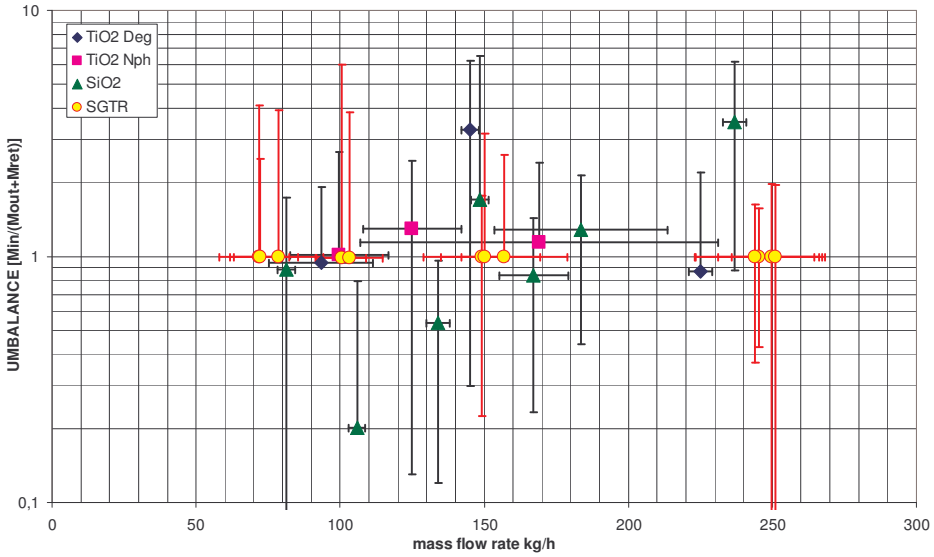

Fig.III.1. Mass balance versus inlet gas mass flow rate.

SENSITIVITY ANALYSIS OF M_{RET} CALCULUS METHOD

The potential error of the methodology used in the calculus of m_{ret} from the extrapolation of tube mass collection was assessed by varying the number of tubes collected used in the extrapolation. Fig.III.2 shows the variation of the resulting efficiency versus the CAAT test number with the number of tubes collected as parameter. Legend shows the tubes removed from the collection named following Fig. 54 nomenclature. Results show that SiO_2 tests have much less sensibility to the

number of tubes collected when estimating efficiency than TiO_2 tests. TiO_2 tests show variations of up to 35% when the number of tubes is halved.

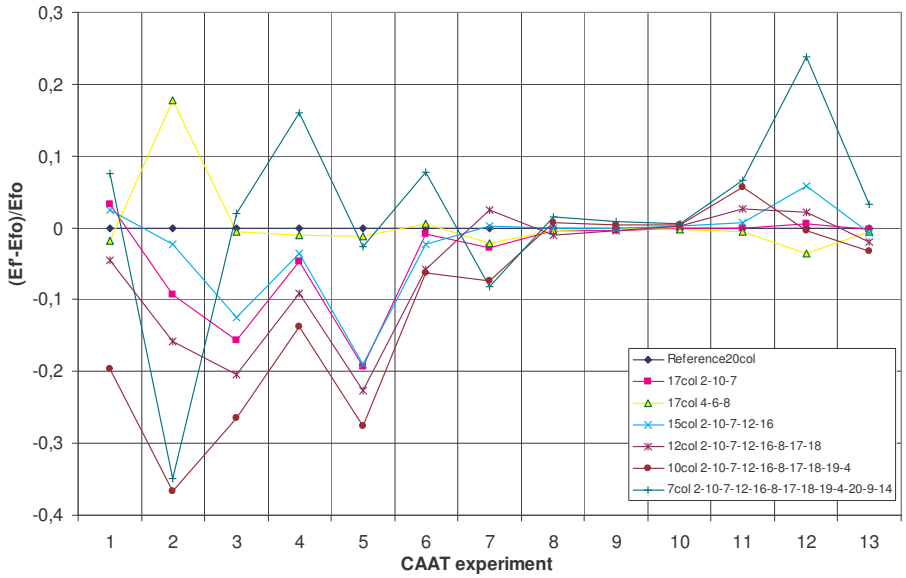

Fig.III.2. Sensitivity analysis of the m_{ret} calculus method.

Appendix IV: CAAT experiments execution and measurements

INTRODUCTION

This appendix tries to illustrate and summarize the execution, measurements and results of the CAAT experiments. To do so, it has been divided in three main sections according to the particle nature of the aerosol used in the experiments. Each section follows the same structure: test execution, thermal-hydraulic results, aerosol results which include integral behaviour, on-line size distributions and deposition pattern.

A. TiO_2 DEGUSA EXPERIMENTS: CAAT-01, CAAT-02, CAAT-12

Three tests were executed using Degussa TiO_2 aerosol. These tests were conducted successfully on March 1, 2007, March 15, 2007 and November 7, 2007 respectively. The design inlet gas mass flow rates used in these tests were 100 kg/h, 250kg/h and 150kg/h. Fig.IV.1 shows the configuration of the CAAT-PECA facility used during these tests.

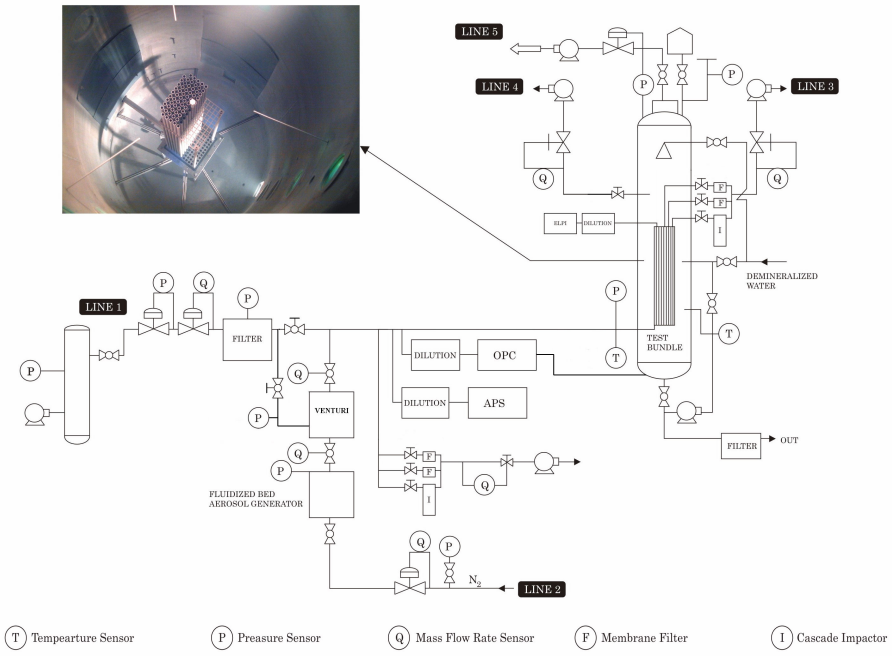

Fig.IV.1. Scheme of the PECA facility for CAATs TiO_2 experiments.

A.1 SUMMARY OF TESTS EXECUTION

In order to show the procedure followed during the tests, Table.IV.1 shows the test sequence of CAAT-02 which is similar to the rest. Fig.IV.2 shows the main thermal-hydraulic variables evolution as a function of time with the test procedure explanation chart and Fig.IV.3 shows the aerosol device measurement schedule for CAAT-02.

Day Time, h	Main Action
08:10	ELPI warm up
09:00	OPC lamp warm up
10:35	Compressor start up and flow increase up to desired conditions
11:08	Stabilized flow conditions reached
11:08	Dilution air started. DAS, APS, ELPI, OPC measurements started
11:09	Aerosol generation started
11:11	Primary side membrane filter P1F1 secondary side membrane filter L1F1 measurement started
11:15	Primary side membrane filter P1F1 secondary side membrane filter L1F1 measurement end
11:15	Primary side Impactador MARK secondary side impactor ANDER measurement started
11:17	Primary side Impactador MARK measurement end
11:22	Primary side Impactador MARK measurement restarted
11:24	Primary side Impactador MARK measurement end
11:24	Secondary side Impactor ANDER measurement end
11:26	Primary side membrane filter P2F1 secondary side membrane filter L2F1 measurement started
11:29	Primary side membrane filter P2F1 secondary side membrane filter L2F1 measurement end
11:31	Primary side membrane filter P1F2 secondary side membrane filter L1F2 measurement started
11:35	Primary side membrane filter P1F2 secondary side membrane filter L1F2 measurement end
11:37	Primary side membrane filter P2F2 secondary side membrane filter L2F2 measurement started
11:41	Primary side membrane filter P2F2 and secondary side membrane filter L2F2 measurement end
11:42	Shutdown of aerosol generation and facility
11:45	End of test

Table.IV.1. Test sequence for CAAT-02.

The tests begin with compressor start up, the stabilization of the inlet gas mass flow rate and the Venturi bypass flow rate. Once these variables are stabilized, the aerosol generation is started. Membrane filters and impactor measurements are sequentially performed for time durations which provide reasonable aerosol sampled masses. Inlet aerosol size distribution is characterized by APS every 20 seconds whereas outlet aerosol size distribution is characterized on-line by ELPI every second. An additional characterization of the inlet aerosol size distribution is performed every 4 minutes by measuring during 60 seconds with the OPC. After the end of the gravimetric sampling the aerosol injection is finished and the compressor is shutdown. The aerosol injection during the test last for 36 minutes in the case of CAAT-02, 46 minutes for CAAT-01 and 42 minutes in the case of CAAT-12. An additional resuspension phase was introduced at the end of CAAT-12 (10min keeping the thermal-hydraulic conditions after the stop of aerosol injection) to asses the influence of this mechanism in this kind of particles.

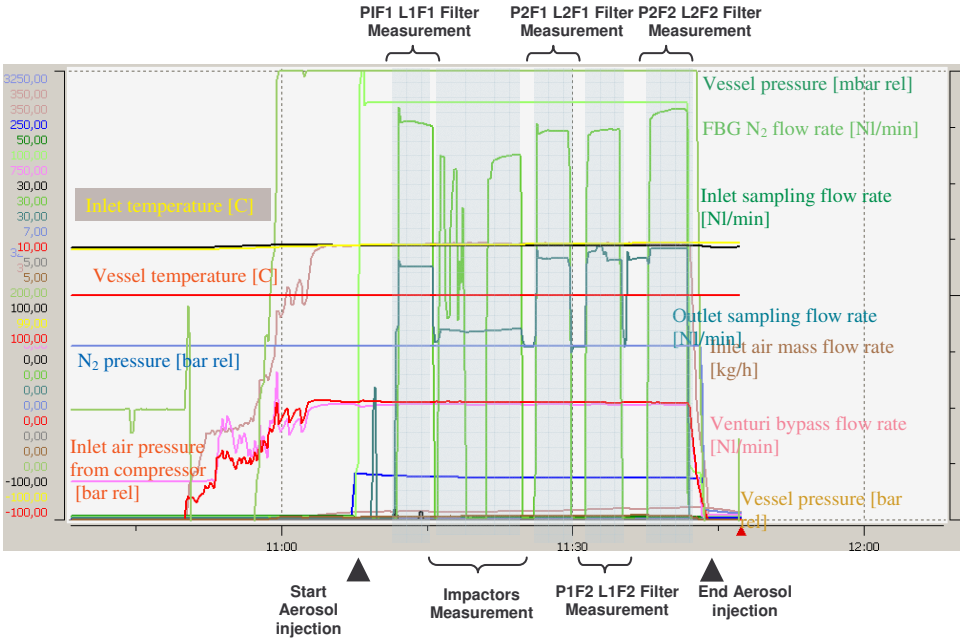

Fig.IV.2. Test evolution of the thermal-hydraulics variables scanned by the data adquisition system (DAS) for CAAT-02.

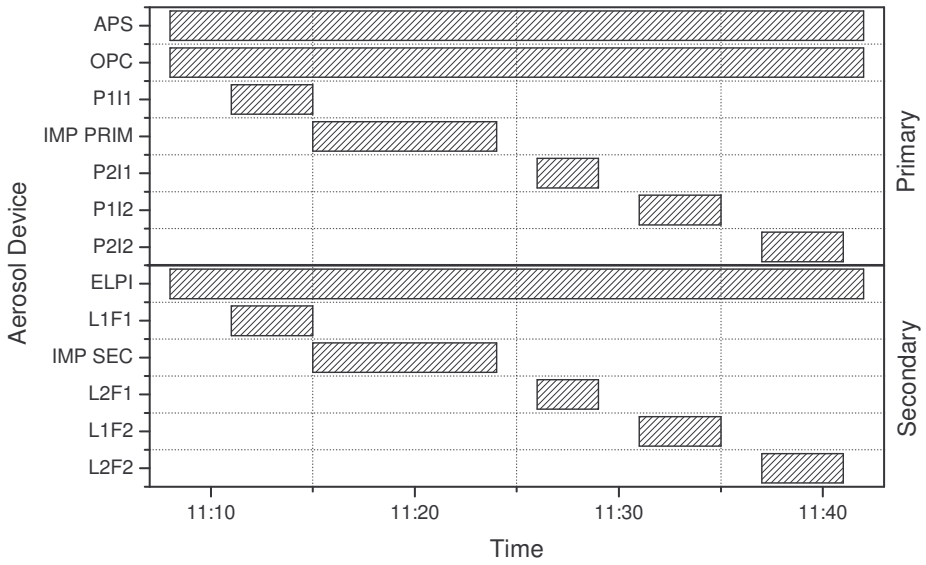

Fig.IV.3. Aerosol measurement schedule for CAAT-02.

A.2 THERMAL-HYDRAULIC RESULTS

The mean values of the most important thermal hydraulic parameters are shown in Table.IV.2 and 3 for the primary and secondary side.

Variable	Units	Mean Value CAAT01	Mean Value CAAT02	Mean Value CAAT12	Resolution	Set point CAAT01	Set point CAAT02	Set point CAAT12
Compressor air mass flow rate	Kg/h	86.20	215.00	160.00	±0.01	92	240	141
Compressor air manometric pressure	Bar rel	1.40	2.60	2.40	±0.01	-	-	-
Venturi bypass flow rate	Nl/min	294.0	192.3	86.8	±0.1	500	500	500
FBG N_2 flow rate	Nl/min	92.8	92.9	287.0	±0.1	100	100	100
FBG N_2 manometric pressure	Bar rel	2.3	2.7	2.7	±0.1	2.3	2.7	2.7
Synthetic air flow rate	Nl/min	-	23.3	25.8	±0.1	-	100	100

Total mass flow rate through the breach	Kg/h	93.4	223.0	183.0	±0.1	100	250	150
Flow temperature	ºC	22.0	22.1	26.5	±0.1	-	-	-
Manometric Pressure at primary side	Bar	0.2	1.6	0.7	±0.1	0.3	1.2	0.6
Manometric Pressure at the FBG vessel	Bar	0	1	1.2	±0.2	-	-	-
Sampling flow rate	Nl/min	22.0	26.5	32.3	±0.1	-	-	-

Table.IV.2. Mean values in CAAT-01, CAAT-02, CAAT-12 for primary side.

Variable	**Units**	**Mean Value CAAT01**	**Mean Value CAAT02**	**Mean Value CAAT12**	**Resolution**	**Set point**
Flow temperature	ºC	19.0	22.5	25.6	±0.1	-
Blower duty	%	0	37	10	±1	0
PECA Vessel manometric pressure	mbar	58	200	200	±1	50
Dilution air flow rate	Nl/min	-	-	-	±0.1	-
Dilution air manometric pressure	Bar	2	0.2	0.4	±0.2	-
Laboratory barometric pressure	mmHg	-	-	693	±1	-
Laboratory ambient temperature	ºC	19.0	21.0	25.0	±0.1	-
Sampling flow rate	Nl/min	18.0	18.1	26.1	±0.1	-

Table.IV.3. Mean values in CAAT-01, CAAT-02, CAAT-12 for secondary side.

A.3 AEROSOL RESULTS

The aerosol used in this test is Aeroxide TiO_2 P25 from Degussa Inc. (Degussa, 2005). It has a primary particle diameter of 21nm based on BET SSA (Specific Surface Area)

measurements. SEM analysis shows that particle morphology is close to spherical. More details on the aerosol characteristics are given in Table.IV.4.

TiO_2 aerosol characteristics	Units	Value
Average primary particle diameter	Nm	0.021
Specific surface area	m^2/g	~50
Bulk density	g/cm^3	0.13

Table.IV.4. Aerosol characteristics.

A.3.1 INTEGRAL BEHAVIOUR

Once the gravimetric measurements are performed and the experiment is finished, samples are weight and the post-processing is performed. Detailed information on collected aerosol masses on membrane filters and impactors is shown in Table.IV.5, 6 and 7.

Tag Name	ID	Note	m_0	m_f	Δm	t_s	t_{Start}	FM_s	p_s	T_s	MW_s	X_{steam}	FV_{sys}	η_{act}	FV_s	V_s	C_s	$FM_{aerosol}$	$<FM_{aerosol}>$
			mg	mg	mg	s	s	nl/min	bar(a)	°C	kg/kmol	%	m^3/h	Pa s	l/min	l	g/m^3	g/h	g/h
P1-I1	FI		140,200	186,900	46,700	240	11:00	20,60	1,120	22,0	28,970	0,000	63,5	1,8229E-05	20,10	80,40	0,58084	36,860	16,39
P2-I1	FI		145,600	149,900	4,300	240	11:20	20,60	1,120	22,0	28,970	0,000	59,7	1,8229E-05	20,10	80,40	0,05348	3,191	
P3-I1	FI		142,900	162,500	19,600	240	11:25	20,60	1,120	22,0	28,970	0,000	59,7	1,8229E-05	20,10	80,40	0,24378	14,545	
P1-I2	FI		140,100	155,700	15,600	240	11:32	20,60	1,120	22,0	28,970	0,000	56,5	1,8229E-05	20,10	80,40	0,19403	10,962	
M-III	IMP		-	-	20,600	311	11:10	20,60	1,120	22,0	28,970	0,0	64,1	1,8229E-05	20,10	104,19	0,19772	12,666	
S1-I1	FI		145,700	175,600	29,900	240	11:00	17,70	0,981	19,3	28,970	0,000	71,8	1,8100E-05	19,54	78,15	0,38260	27,466	18,85
S2-I1	FI		140,700	159,200	18,500	240	11:20	17,70	0,973	19,3	28,970	0,000	68,1	1,8100E-05	19,70	78,81	0,23475	15,980	
S1-I2	FI		145,500	173,100	27,600	240	11:25	17,70	0,974	19,3	28,970	0,000	68,0	1,8100E-05	19,67	78,69	0,35076	23,838	
S2-I2	FI		145,600	155,500	9,900	240	11:32	17,70	0,973	19,3	28,970	0,000	64,4	1,8100E-05	19,69	78,75	0,12571	8,096	
ELPI	IMP		-	-	4,100	2460	10:59	10,00	0,975	19,3	28,970	0,000	71,7	1,8100E-05	11,10	455,16	0,00901	0,646	
AI	IMP		-	-	1,700	311	11:10	16,80	0,991	19,3	28,970	0,0	71,7	1,8100E-05	18,36	95,15	0,01787	1,282	

t_s measurement lapse FV_{sys} flow rate at the main line

Table.IV.5. Filters and Impactors information for CAAT-01.

Tag Name	ID	Note	m_0	m_f	Δm	t_s	t_{Start}	FM_s	p_s	T_s	MW_s	X_{steam}	FV_{sys}	η_{act}	FV_s	V_s	C_s	$FM_{aerosol}$	$<FM_{aerosol}>$
			mg	mg	mg	s	s	nl/min	bar(a)	°C	kg/kmol	%	m^3/h	Pa s	l/min	l	g/m^3	g/h	g/h
P2-I1	FI		128,100	150,500	22,400	230	11:00	16,90	1,120	22,0	28,970	0,000	80,3	1,8229E-05	16,49	63,21	0,35437	28,460	6,93
P3-I1	FI		127,700	134,600	6,900	200	11:20	17,40	1,120	22,0	28,970	0,000	75,4	1,8229E-05	16,98	56,59	0,12192	9,193	
P2-I2	FI		127,500	127,500	0,000	234	11:25	18,10	1,120	22,0	28,970	0,000	75,4	1,8229E-05	17,66	68,88	0,00000	0,000	
P3-I2	FI		126,700	129,900	3,200	202	11:32	17,60	1,120	22,0	28,970	0,000	71,3	1,8229E-05	17,17	57,82	0,05535	3,946	
M-III	IMP		-	-	26,700	311	11:10	20,60	1,120	22,0	28,970	0,0	81,1	1,8229E-05	20,10	104,19	0,25627	20,773	
S1-I1	FI		127,100	133,400	6,300	200	11:24	18,34	0,981	19,3	28,970	0,000	22,6	1,8100E-05	20,24	67,48	0,09336	2,106	1,33
S2-I1	FI		126,200	137,200	11,000	230	11:09	15,46	0,973	19,3	28,970	0,000	14,3	1,8100E-05	17,21	65,97	0,16675	2,392	
S1-I2	FI		126,200	128,100	1,900	202	11:29	19,32	0,974	19,3	28,970	0,000	15,3	1,8100E-05	21,47	72,29	0,02628	0,402	
S2-I2	FI		125,800	128,100	2,300	234	11:35	17,89	0,973	19,3	28,970	0,000	13,9	1,8100E-05	19,90	77,61	0,02964	0,411	
ELPI	IMP		-	-	5,500	2460	10:59	10,00	0,975	19,3	28,970	0,000	22,3	1,8100E-05	11,10	455,16	0,01208	0,269	
AI	IMP		-	-	14,400	311	11:10	16,80	0,991	19,3	28,970	0,0	22,3	1,8100E-05	18,36	95,15	0,15134	3,368	

t_s measurement lapse FV_{sys} flow rate at the main line

Table.IV.6. Filters and Impactors information for CAAT-02.

Tag Name	ID	Note	m_0	m_1	Δm	t_s	t_{Start}	FM_s	p_s	T_s	MW_s	X_{steam}	FV_{sys}	η_{act}	FV_s	V_s	C_s	$FM_{aerosol}$	$<FM_{aerosol}>$
			mg	mg	mg	s	s	nl/min	bar(a)	°C	kg/kmol	%	m^3/h	Pa s	l/min	l	g/m^3	g/h	g/h
P2-I1	FI		125,700	183,000	57,300	287	11:25	25,78	1,823	20,0	28,970	0,000	67,2	1,8133E-05	15,35	73,43	0,78031	52,415	76,16
P1-I1	FI		125,800	245,500	119,700	223	11:47	29,84	1,923	20,0	28,970	0,000	63,7	1,8133E-05	16,85	62,61	1,91189	121,863	
P2-I2	FI		126,800	210,700	83,800	223	11:52	29,85	1,923	20,0	28,970	0,000	62,7	1,8133E-05	16,85	62,63	1,33803	83,843	
P1-I2	FI		126,200	198,800	72,600	414	11:58	25,68	1,923	20,0	28,970	0,000	64,1	1,8133E-05	14,50	100,02	0,72588	46,506	
M-III	IMP		-	-	78,100	590	12:31	28,87	1,923	26,8	28,970	0,0	64,6	1,8457E-05	16,68	163,98	0,47628	30,750	
S1-I1	FI		127,700	166,300	38,600	287	11:25	50,94	1,123	20,0	28,970	0,000	109,1	1,8133E-05	49,25	235,58	0,16385	17,870	19,96
S2-I1	FI		126,700	158,200	31,500	223	11:47	51,94	1,123	20,0	28,970	0,000	109,2	1,8133E-05	50,22	186,64	0,16878	18,424	
S1-I2	FI		126,300	169,700	43,400	239	11:52	49,09	1,123	20,0	28,970	0,000	107,3	1,8133E-05	47,46	189,05	0,22957	24,636	
S2-I2	FI		125,800	180,500	54,700	414	11:58	47,57	1,123	20,0	28,970	0,000	109,7	1,8133E-05	45,99	317,31	0,17238	18,915	
ELPI	IMP		-	-	22,200	2280	12:24	10,00	1,123	20,0	28,970	0,000	110,1	1,8133E-05	9,67	367,39	0,06043	6,655	
AI	IMP		-	-	3,836	1052	12:31	44,19	1,123	25,6	28,970	0,0	110,1	1,8400E-05	43,54	763,40	0,00503	0,554	

t_s measurement lapse FV_{sys} flow rate at the main line

Table.IV.7. Filters and Impactors information for CAAT-12.

Information relative to the impactors discrete aerosol size distribution at the primary and secondary side of the break stage is also post-processed and presented in summary tables. As an example, Table.IV.8 and 9 present the results obtained for CAAT-01.

Tag Name:	Inlet Mark III
Identification:	CAAT-01

Notes: Correct measurement at the inlet. Weighed just the filters

Integrale Data of Measurement:

Meas-Fluid:			Air		
t_s	311	s	FV_{sys}	64,1	m3/h
t_{Start}	11:10	s	FV_s	20,10	l/min
P_s	1,12	bar(a)	V_s	104,19	l
T_s	22,00	°C	C_s	197,72	mg/m3
MW_s	28,97	kg/kmol	$FM_{aerosol}$	12,67	g/h
X_{steam}	0,000	%	η_{ref}	1,820E-05	Pa-s
m_{total}	20,600	mg	η_{act}	1,823E-05	Pa-s
			AMMD	3,0	µm
			GSD	2,9	

Device Parameter:

Modell	Andersen Mark III	
S/N:		
Supplier:	Andersen Sampler Inc.	
Calibration:		
Reference Flow Rate:	14,2	l/min
Reference Temperature:	21,1	°C
Reference Pressure:	1,0133	bar_a
Reference Fluid:	Air	

Stage		D_{ae} ref	D_{ae} cut	D_{ae} g	m_0	m_1	Δm	m_p	m_{cum}	M	$dM/d\log(D_p)$
		µm	µm	µm	mg	mg	mg	%	%	mg/m^3	mg/m^3
M-0	0	--	--	--	143,800	145,800	2,000	9,7087	90,29	19,197	0
M-1	1	13,400	11,272	--	151,400	152,000	0,600	2,9126	87,38	5,759	0
M-2	2	8,400	7,066	8,924	143,200	144,200	1,000	4,8544	82,52	9,598	47,323
M-3	3	5,700	4,795	5,821	150,900	153,800	2,900	14,078	68,45	27,835	165,287
M-4	4	3,900	3,281	3,966	139,500	142,600	3,100	15,049	53,40	29,755	180,539
M-5	5	2,500	2,103	2,627	153,000	156,600	3,600	17,476	35,92	34,554	178,920
M-6	6	1,230	1,035	1,475	142,900	147,600	4,700	22,816	13,11	45,112	146,451
M-7	7	0,770	0,648	0,819	152,600	154,700	2,100	10,194	2,91	20,156	99,090
M-8	8	0,520	0,437	0,532	141,400	141,800	0,400	1,9417	0,97	3,839	22,520
M-F	Backup	0,050	0,050	0,050	203,800	204,000	0,200	0,9709	0,00	1,920	2,038
Sum							20,600	100,00			

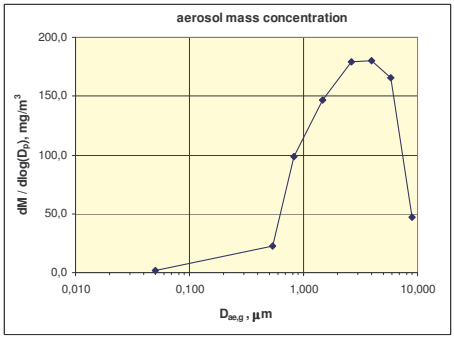

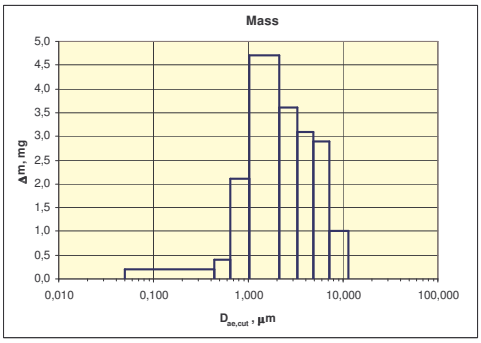

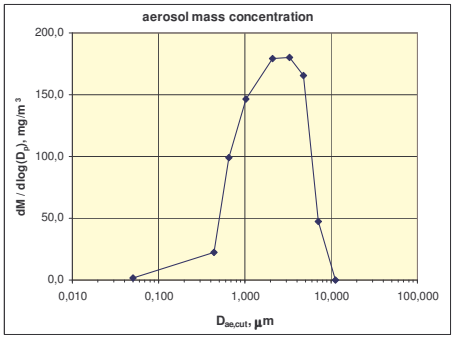

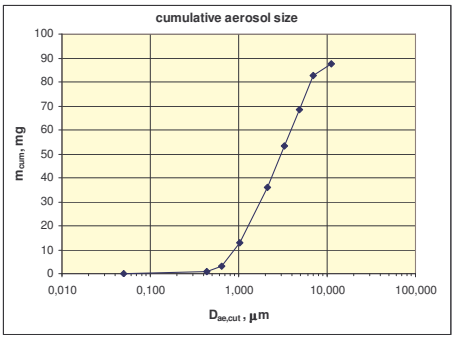

Table.IV.8. Primary side impactor information for CAAT-01.

Tag Name:	Outlet ELPI
Identification:	ELPI

Notes: Measure during the hole experiement. Diluted up to 11:27 no dilut after

Integrale Data of Measurement:

Meas-Fluid:			Air		
t_s	2460	s	FV_{sys}	71,74	m^3/h
t_{Start}	10:59	s	FV_s	10,00	l/min
P_s	0,975	bar(a)	V_s	455,16	l
T_s	19,3	°C	C_s	9,01	mg/m^3
MW_s	28,97	kg/kmol	$FM_{aerosol}$	0,646	g/h
X_{steam}	0	%	η_{ref}	1,820E-05	Pa-s
m_{total}	4,100	mg	η_{act}	1,810E-05	Pa-s
			AMMD	1,7	µm
			GSD	3,2	

Device Parameter:

Modell	ELPI	
S/N:	2363	
Supplier:	Dekati	
Calibration:	12.12.2005, Timo Alanen	
Reference Flow Rate:	9,98	l/min
Reference Temperature:	21,6	°C
Reference Pressure:	1,0	bar_a
Exhaust Pressure:	100,0	mbar
Diameter critcal Orifice:		mm
Reference Fluid:	Air	

Stage		$D_{ae,ref}$	d_{nozzle}	$D_{ae,cut}$	$D_{ae,g}$	m_0	m_1	Δm	m_p	m_{cum}	M	$dM/d\log(D_p)$	p_{Stage}
		µm	mm	µm	µm	mg	mg	mg	%	%	mg/m^3	mg/m^3	bar_a
EL-13	0	9,88		9,88	--	38064,200	38064,400	0,200	4,878	95,12	0,439	#VALOR!	1,01320
EL-12	1	6,660		6,660	8,112	38727,900	38728,200	0,300	7,317	87,80	0,659	3,848	1,01300
EL-11	2	3,980		3,980	5,148	38255,000	38255,300	0,300	7,317	80,49	0,659	2,948	1,01240
EL-10	3	2,380		2,380	3,078	39000,600	39001,000	0,400	9,756	70,73	0,879	3,935	1,01170
EL-9	4	1,590		1,590	1,945	38633,100	38634,000	0,900	21,951	48,78	1,977	11,287	1,00990
EL-8	5	0,945		0,945	1,226	38740,300	38741,400	1,100	26,829	21,95	2,417	10,695	1,00480
EL-7	6	0,611		0,611	0,760	38570,700	38571,400	0,700	17,073	4,88	1,538	8,120	0,99590
EL-6	7	0,380		0,380	0,482	38230,300	38230,500	0,200	4,878	0,00	0,439	2,130	0,97110
EL-5	8	0,261		0,261	0,315	37647,600	37647,600	0,000	0,000	0,00	0,000	0,000	0,89460
EL-4	9	0,156		0,156	0,202	38724,400	38724,400	0,000	0,000	0,00	0,000	0,000	0,69010
EL-3	10	0,095		0,095	0,122	38134,200	38134,200	0,000	0,000	0,00	0,000	0,000	0,39550
EL-2	11	0,057		0,057	0,074	38607,500	38607,500	0,000	0,000	0,00	0,000	0,000	0,22490
EL-1	12	0,028		0,028	0,040	38563,500	38563,500	0,000	0,000	0,00	0,000	0,000	0,10000
Sum						.		4,100	100,00				

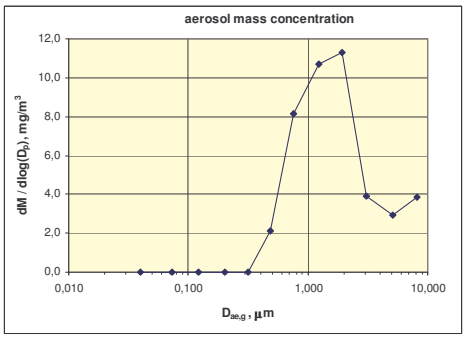

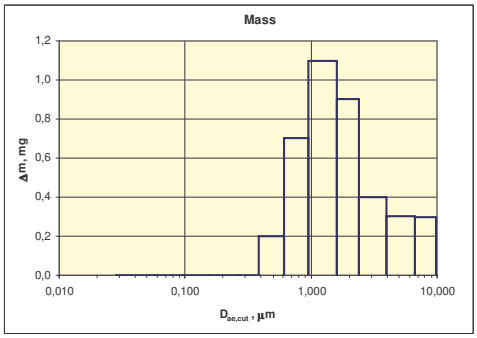

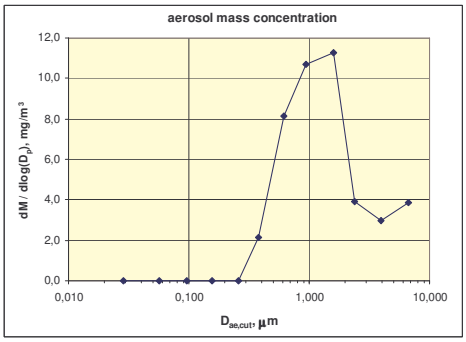

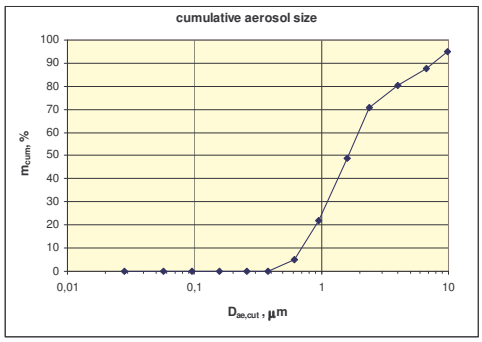

Table.IV.9. Secondary side ELPI impactor information for CAAT-01.

A.3.2. ONLINE AEROSOL SIZE DISTRIBUTION AT THE PRIMARY AND SECONDARY SIDE

On-line measurement device used during the experiments permit to obtain the evolution of the count size distribution of the aerosol with time during the experiments, as well as the main statistics properties like median diameter, mean diameter and GSD of the distribution. As an example, Fig.IV.4 shows APS the count mean diameter, count median diameter and GSD evolution with time during CAAT-02 for the primary side (upstream the breach).

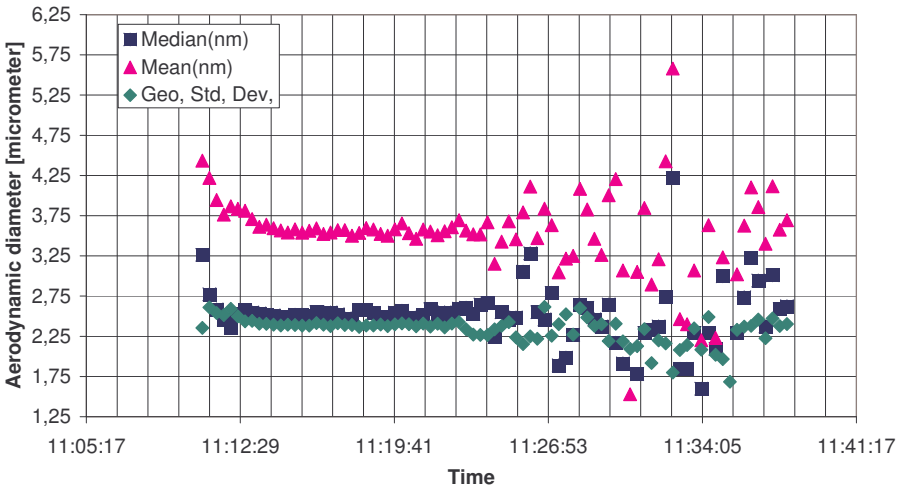

Fig.IV.4. APS primary side count mean, median diameter and GSD for CAAT-02.

Fig.IV.5 shows OPC count size distribution evolution with time during CAAT-02 at the primary side. Fig.IV.6 shows OPC the count mean diameter, count median diameter and GSD evolution with time during CAAT-02. Distributions show lognormal distributions with GSD around 1.75.

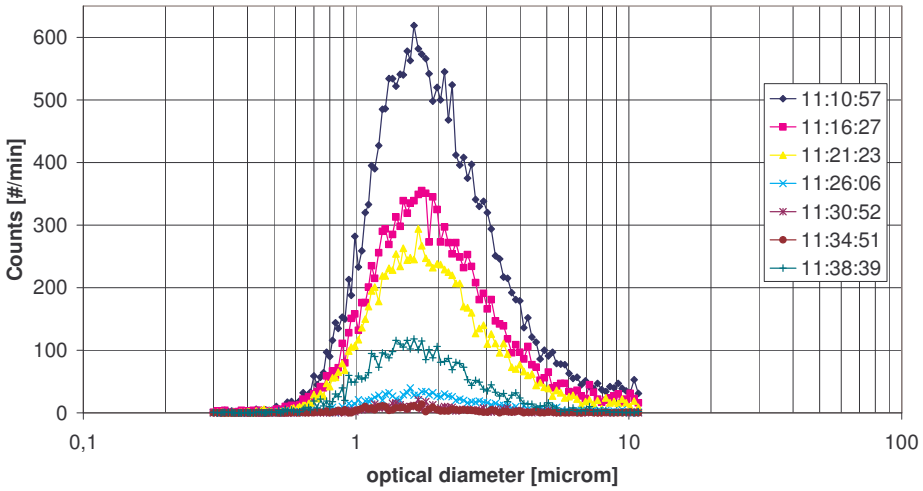

Fig.IV.5. OPC primary side count size distribution for CAAT-02.

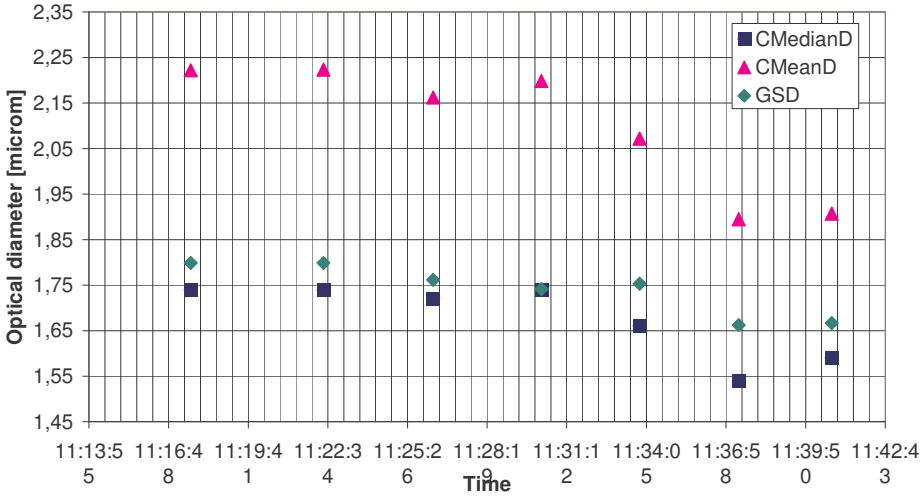

Fig.IV.6. OPC primary side count mean, median diameter and GSD for CAAT-02.

As an example of the type of distribution at the secondary side, Fig.IV.7 and Fig.IV.8 shows ELPI particle count size distribution as well as the count mean diameter, count median diameter and GSD evolution with time during CAAT-02 at the secondary side (downstream the breach). As shown, secondary side data obtained at the exit of the bundle presents much more steady values that the one found at the primary side.

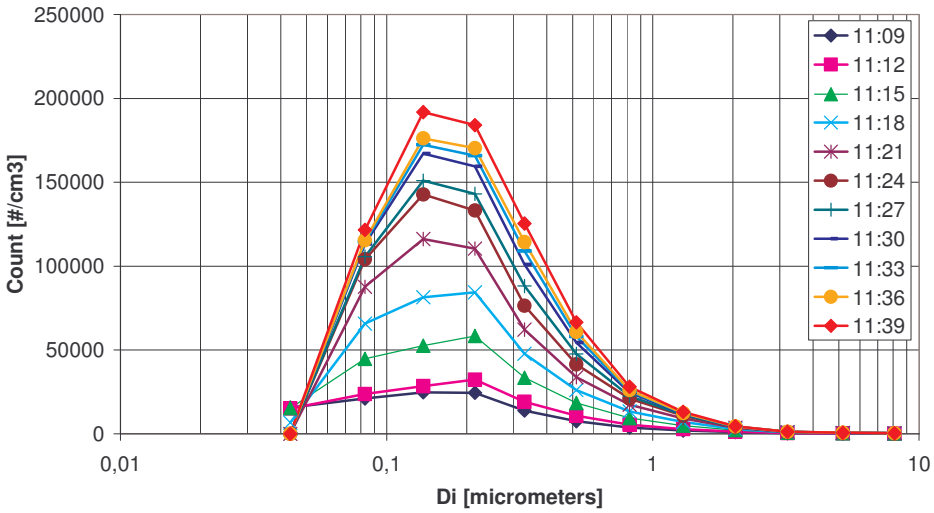

Fig.IV.7. ELPI secondary side count size distribution for CAAT-02.

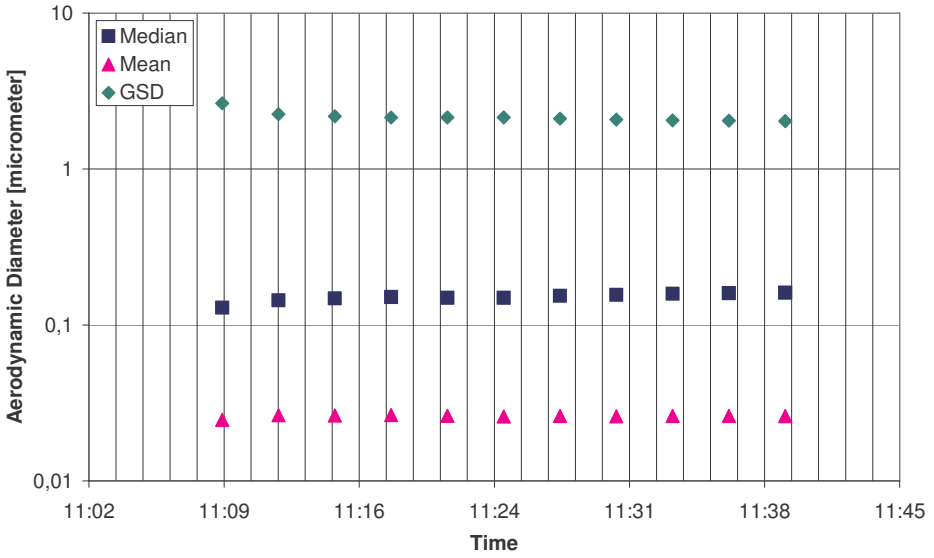

Fig.IV.8. ELPI secondary side count mean, median diameter and GSD for CAAT-02.

A.3.3. AEROSOL DEPOSITION PATTERN AND RETENTION EFFICIENCY ESTIMATION

Fig.IV.9, 10 and 11 show the on-tube deposition pattern found for CAAT-01, CAAT-02 and CAAT-12 by using U-ring and wet-paper techniques. Comapared to Nanophase TiO_2 experiments, mass deposits were found to be relatively small.

Several asymmetries can be noticed in the pattern. This might indicate an influence of the primary line orientation in the aerosol deposits.

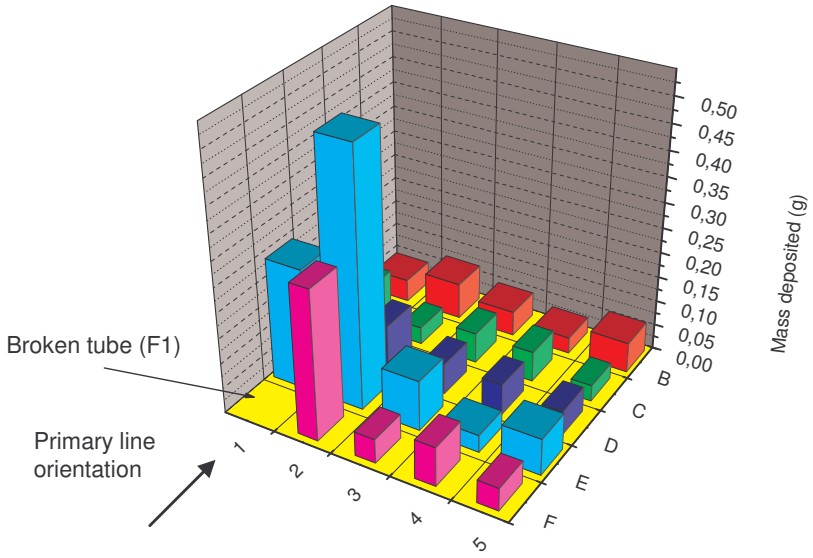

Fig.IV.9. On tube mass deposition pattern for CAAT-01.

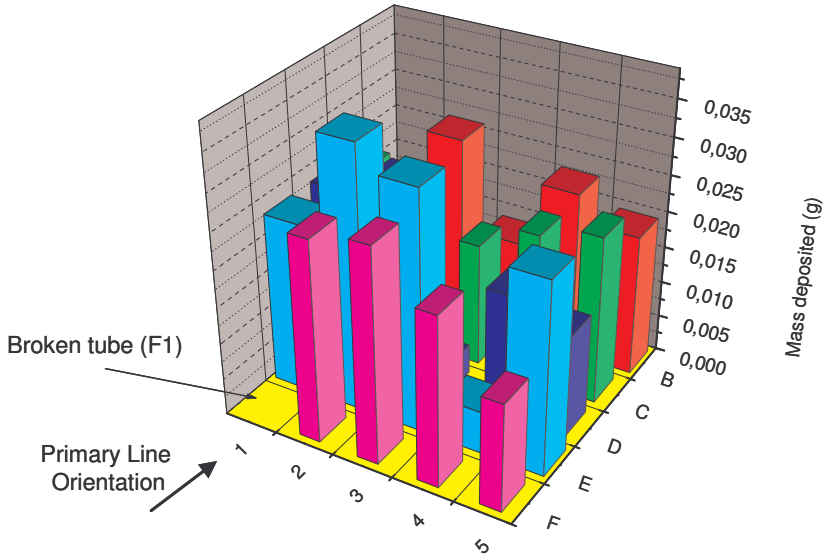

Fig.IV.10. On tube mass deposition pattern for CAAT-02.

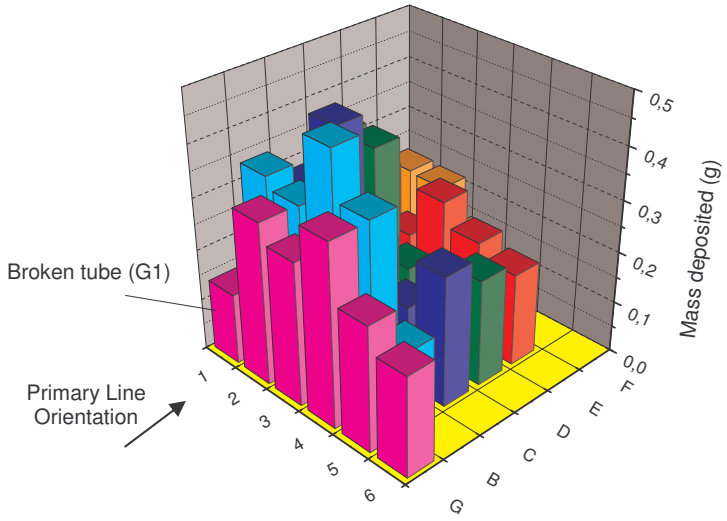

Fig.IV.11. On tube mass deposition pattern for CAAT-12.

Finally, Fig. 12 shows de DF as a function of the particle size using primary and secondary side low pressure impactor measurement (Dek/ELPI):

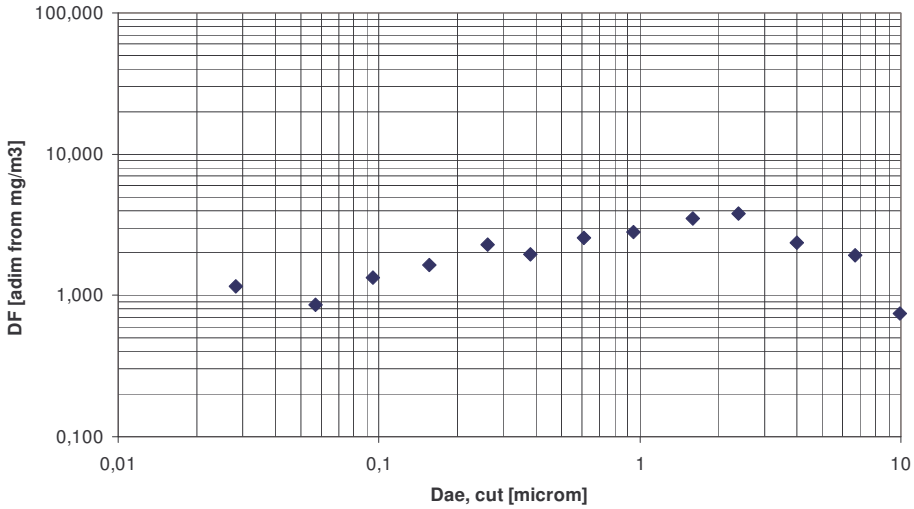

Fig.IV.12. DF as a function of aerodynamci cut diameter for CAAT-12.

Table.IV.10 shows the retention efficiency based on the following formula:

$$\eta(\%) = \frac{M_{BUNDLE}}{M_{OUT} + M_{BUNDLE}} \cdot 100$$

Experiment	Design inlet gas mass flow rate [kg/h]	Mean Value [%]	Estimated Uncertainty [%]
CAAT-01	100	27.48	7.42
CAAT-02	250	13.53	11.82
CAAT-12	150	14.00	7.01

Table.IV.10. Retention efficiency estimations for TiO_2 Degussa tests.

B. TiO_2 NANOPHASE EXPERIMENTS: CAAT-03, CAAT-04, CAAT-05

Three tests were executed using Nanophase TiO_2 aerosol. These tests were conducted successfully on March 29, 2007, April 20, 2007 and May 10, 2007 respectively. The design inlet gas mass flow rates used in these tests were 100 kg/h, 200kg/h and 150kg/h.

B.1 TEST EXECUTIONS

The configuration of the CAAT-PECA facility used as well as the test execution and aerosol measurement procedure followed during these tests are similar to the one used for the Degusa TiO_2 experiments. Thus, it will be not repeated here the description.

B.2 THERMAL-HYDRAULIC RESULTS

The mean values of the most important thermal hydraulic parameters are shown in Table.IV.11 and 12 for the primary and secondary side.

Variable	Units	Mean Value CAAT03	Mean Value CAAT04	Mean Value CAAT05	Resolution	Set point CAAT03	Set point CAAT04	Set point CAAT05
Compressor air mass flow rate	Kg/h	92.42	159	117	±0.01	93	193	143
Compressor air manometric pressure	Bar	1.34	2.30	1.70	±0.01	-	-	-
Venturi bypass flow rate	Nl/min	128.3	132.6	113	±0.1	500	500	500
FBG N_2 flow rate	Nl/min	92.7	92.5	92.4	±0.1	100	100	100
FBG N_2 manometric pressure	Bar	2.7	2.7	2.7	±0.1	2.7	2.7	2.7
Synthetic air flow rate	Nl/min	-	23.3	-	±0.1	-	100	-
Total mass flow rate through the breach	Kg/h	99.7	169.0	125.0	±0.1	100	200	150
Flow temperature	ºC	19.9	22.9	21.0	±0.1	-	-	-
Manometric Pressure at	Bar	0.2	1.4	0.4	±0.1	0.3	1	0.6

primary side								
Manometric Pressure at the FBG vessel	Bar	0.1	1.0	0.6	±0.2	-	-	-
Sampling flow rate	Nl/min	15	23.7	26.4	±0.1	-	-	-

Table.IV.11. Mean values in CAAT-03, CAAT-04, CAAT-05 for primary side.

Variable	**Units**	**Mean Value CAAT03**	**Mean Value CAAT04**	**Mean Value CAAT05**	**Resolution**	**Set point**
Flow temperature	ºC	22.4	21.4	22.1	±0.1	-
Blower duty	%	20	45	3	±1	-
PECA Vessel manometric pressure	mbar rel	130	370	200	±1	50
Dilution air flow rate	Nl/min	101.5	15.5	15.1	±0.1	100
Dilution air manometric pressure	Bar rel	2.4	1.6	1.6	±0.2	2
Laborator Barometric pressure	mmHg	692	693	692	±1	-
Laboratory ambient temperature	ºC	21.0	25.0	21.0	±0.1	-
Sampling flow rate	Nl/min	21.2	28.6	24.7	±0.1	-

Table.IV.12. Mean values in CAAT-03, CAAT-04, CAAT-05 for secondary side.

B.3 AEROSOL RESULTS

The aerosol used in these tests is NanoTek TiO_2 from Nanophase Inc. (Nanophase, 2002). The aerosol is originally produced by the evaporation condensation technique using plasma torques. It has a primary particle diameter of 40nm based on SSA (Specific Surface Area) measurements, and the particle morphology is close to spherical. More details on the aerosol characteristics are given in Table.IV.13.

TiO_2 aerosol characteristics	**Units**	**Value**
Average primary particle diameter	Nm	21.8
Specific surface area	m^2/g	20.3

Bulk density	g/cm^3	0.2

Table.IV.13. Aerosol characteristics.

B.3.1. INTEGRAL BEHAVIOUR

Detailed information on collected aerosol masses on membrane filters and impactors is shown in Table.IV.14 through 16.

Tag Name	ID	Note	m_0	m_f	Δm	t_s	t_{Start}	FM_s	p_s	T_s	MW_s	X_{steam}	FV_{sys}	η_{act}	FV_s	V_s	C_s	$FM_{aerosol}$	$<FM_{aerosol}>$
			mg	mg	mg	s	s	nl/min	bar(a)	°C	kg/kmol	%	m^3/h	Pa s	l/min	l	g/m^3	g/h	g/h
P1-I1	FI		127,700	283,700	156,000	310	11:20	20,81	1,123	19,7	28,970	0,000	74,5	1,8119E-05	20,10	103,84	1,50225	111,875	106,52
P2-I1	FI		128,600	253,400	124,800	289	11:43	21,76	1,123	20,0	28,970	0,000	73,9	1,8133E-05	21,04	101,33	1,23159	90,988	
P1-I2	FI		128,500	265,600	137,100	245	11:50	22,35	1,123	20,0	28,970	0,000	75,4	1,8133E-05	21,61	88,23	1,55382	117,124	
P2-I2	FI		129,500	271,500	142,000	303	11:56	21,18	1,123	20,0	28,970	0,000	77,3	1,8133E-05	20,48	103,41	1,37318	106,080	
M-III	IMP		-	-	76,400	283	11:27	21,62	1,123	19,8	28,970	0,0	74,0	1,8124E-05	20,89	98,52	0,77545	57,367	
S1-I1	FI		127,200	293,600	166,400	309	11:20	16,09	0,973	21,3	28,970	0,000	86,4	1,8195E-05	18,02	92,80	1,79310	154,839	125,67
S2-I1	FI		128,400	283,700	155,300	290	11:43	18,92	1,120	22,6	28,970	0,000	74,7	1,8257E-05	18,50	89,41	1,73697	129,772	
S1-I2	FI		128,400	226,600	98,200	247	11:50	20,47	1,120	22,7	28,970	0,000	76,3	1,8262E-05	20,02	82,42	1,19149	90,855	
S2-I2	FI		128,200	305,900	177,700	310	11:56	21,60	1,120	23,1	28,970	0,000	78,3	1,8281E-05	21,15	109,30	1,62584	127,229	
ELPI	IMP		-	-	-5,300	4053	10:55	10,00	1,083	22,4	28,970	0,000	79,6	1,8249E-05	10,10	682,37	-0,00777	-0,619	
AI	IMP		-	-	25,200	889	11:27	12,35	1,052	22,4	28,970	0,0	79,6	1,8248E-05	12,85	190,34	0,13239	10,545	

t_s measurement lapse FV_{sys} flow rate at the main line

Table.IV.14. Filters and Impactors information for CAAT-03.

Tag Name	ID	Note	m_0	m_f	Δm	t_s	t_{Start}	FM_s	p_s	T_s	MW_s	X_{steam}	FV_{sys}	η_{act}	FV_s	V_s	C_s	$FM_{aerosol}$	$<FM_{aerosol}>$
			mg	mg	mg	s	s	nl/min	bar(a)	°C	kg/kmol	%	m^3/h	Pa s	l/min	l	g/m^3	g/h	g/h
P2-I1	FI		127,100	225,600	98,500	298	11:20	21,15	1,724	22,6	28,970	0,000	107,8	1,8257E-05	13,43	66,70	1,47666	159,217	109,45
P1-I1	FI		127,900	186,800	58,900	276	11:43	22,79	2,924	22,6	28,970	0,000	57,7	1,8257E-05	8,53	39,26	1,50024	86,590	
P2-I2	FI		125,700	196,200	70,500	244	11:50	22,43	2,924	23,0	28,970	0,000	52,4	1,8276E-05	8,41	34,21	2,06087	107,936	
P1-I2	FI		125,200	191,200	66,000	298	11:56	22,08	2,924	22,8	28,970	0,000	52,3	1,8267E-05	8,27	41,09	1,60611	84,062	
M-III	IMP		-	-	19,100	276	11:27	21,88	1,724	23,1	28,970	0,0	108,5	1,8281E-05	13,92	64,05	0,29822	32,354	
S1-I1	FI		127,500	172,800	45,300	298	11:20	16,78	1,124	21,3	28,970	0,000	164,7	1,8195E-05	16,28	80,86	0,56024	92,247	79,93
S2-I1	FI		128,400	181,600	53,200	276	11:43	19,48	0,878	21,4	28,970	0,000	191,4	1,8200E-05	24,19	111,30	0,47801	91,510	
S1-I2	FI		126,500	171,500	45,000	244	11:50	20,96	1,424	21,4	28,970	0,000	107,0	1,8200E-05	16,05	65,26	0,68950	73,753	
S2-I2	FI		127,600	176,100	48,500	298	11:56	21,92	1,424	21,4	28,970	0,000	107,0	1,8200E-05	16,79	83,39	0,58161	62,212	
ELPI	IMP		-	-	52,100	2760	11:09	10,00	1,424	21,4	28,970	0,000	142,6	1,8200E-05	7,66	352,29	0,14789	21,091	
AI	IMP		-	-	12,200	967	11:25	12,27	1,304	21,4	28,970	0,0	142,6	1,8200E-05	10,26	165,36	0,07378	10,522	

t_s measurement lapse FV_{sys} flow rate at the main line

Table.IV.15. Filters and Impactors information for CAAT-04.

Tag Name	ID	Note	m_0	m_f	Δm	t_s	t_{Start}	FM_s	p_s	T_s	MW_s	X_{steam}	FV_{sys}	η_{act}	FV_s	V_s	C_s	$FM_{aerosol}$	$<FM_{aerosol}>$
			mg	mg	mg	s	s	nl/min	bar(a)	°C	kg/kmol	%	m^3/h	Pa s	l/min	l	g/m^3	g/h	g/h
P1-I1	FI		126,900	240,200	113,300	240	11:20	24,30	1,123	19,7	28,970	0,000	74,5	1,8119E-05	23,47	93,88	1,20688	89,878	115,03
P2-I1	FI		128,000	295,600	167,600	240	11:43	22,30	1,123	20,0	28,970	0,000	73,9	1,8133E-05	21,56	86,24	1,94341	143,577	
P1-I2	FI		128,000	293,100	165,100	240	11:50	26,40	1,123	20,0	28,970	0,000	75,4	1,8133E-05	25,52	102,10	1,61711	121,894	
P2-I2	FI		126,800	263,700	136,900	240	11:56	26,10	1,123	20,0	28,970	0,000	77,3	1,8133E-05	25,23	100,94	1,35631	104,777	
M-III	IMP		-	-	155,600	283	11:27	21,62	1,123	19,8	28,970	0,0	74,0	1,8124E-05	20,89	98,52	1,57932	116,836	
S1-I1	FI		128,800	212,900	84,100	240	11:20	24,30	0,973	21,3	28,970	0,000	86,4	1,8195E-05	27,21	108,86	0,77258	66,714	76,75
S2-I1	FI		127,500	230,800	103,300	240	11:43	24,60	1,120	22,6	28,970	0,000	74,7	1,8257E-05	24,05	96,21	1,07373	80,220	
S1-I2	FI		127,700	221,600	93,900	240	11:50	29,30	1,120	22,7	28,970	0,000	76,3	1,8262E-05	28,66	114,63	0,81918	62,465	
S2-I2	FI		127,200	250,400	123,200	245	11:56	24,70	1,120	23,1	28,970	0,000	78,3	1,8281E-05	24,19	98,78	1,24725	97,603	
ELPI	IMP		-	-	1,300	4053	10:55	10,00	1,083	22,4	28,970	0,000	79,6	1,8249E-05	10,10	682,37	0,00191	0,152	
AI	IMP		-	-	18,813	889	11:27	12,35	1,052	22,4	28,970	0,0	79,6	1,8248E-05	12,85	190,34	0,09884	7,872	

t_s measurement lapse FV_{sys} flow rate at the main line
Table.IV.16. Filters and Impactors information for CAAT-05.

Information relative to the impactors discrete aerosol size distribution at the primary and secondary side of the break stage is shown in Table.IV.17 and 18 for CAAT-04.

Tag Name:	Inlet Mark III
Identification:	CAAT-04

Notes: Weighted filters, metal support & cross plate

Integrale Data of Measurement:

Meas-Fluid:				Air	
t_s	276	s	FV_{sys}	108,5	m3/h
t_{Start}	11:27	s	FV_s	13,92	l/min
P_s	1,72	bar(a)	V_s	64,05	l
T_s	23,10	°C	C_s	1355,25	mg/m3
MW_s	28,97	kg/kmol	$FM_{aerosol}$	147,03	g/h
X_{steam}	0,000	%	η_{ref}	1,820E-05	Pa-s
m_{total}	86,800	mg	η_{act}	1,828E-05	Pa-s
			AMMD	1,6	µm
			GSD	4,8	

Device Parameter:

Model	Andersen Mark III	
S/N:		
Supplier:	Andersen Sampler Inc.	
Calibration:		
Reference Flow Rate:	14,2	l/min
Reference Temperature:	21,1	°C
Reference Pressure:	1,0133	bar_a
Reference Fluid:	Air	

Stage		D_{ae} ref	D_{ae} cut	D_{ae} g	m_0	m_1	Δm	m_p	m_{cum}	M	$dM/dlog(D_p)$
		µm	µm	µm	mg	mg	mg	%	%	mg/m^3	mg/m^3
M-0	0	--	--	--	32104,400	32119,000	14,600	20,222	120,22	227,957	0
M-1	1	13,400	13,563	--	21322,200	21332,000	9,800	13,573	100,00	153,012	0
M-2	2	8,400	8,502	10,738	21925,400	21932,600	7,200	9,9723	86,43	112,417	554,255
M-3	3	5,700	5,769	7,004	22741,400	22746,300	4,900	6,7867	76,45	76,506	454,299
M-4	4	3,900	3,947	4,772	22865,400	22873,000	7,600	10,526	69,67	118,662	719,994
M-5	5	2,500	2,530	3,160	12521,000	12532,300	11,300	15,651	59,14	176,432	913,567
M-6	6	1,230	1,245	1,775	12575,400	12590,500	15,100	20,914	43,49	235,763	765,379
M-7	7	0,770	0,779	0,985	12651,300	12662,100	10,800	14,958	22,58	168,625	828,975
M-8	8	0,520	0,526	0,640	21905,500	21911,000	5,500	7,6177	7,62	85,874	503,697
M-F	Backup	0,050	0,050	0,050	19765,000	19027,200	0,000	0	0,00	0,000	0,000
Sum							72,200	100,00			

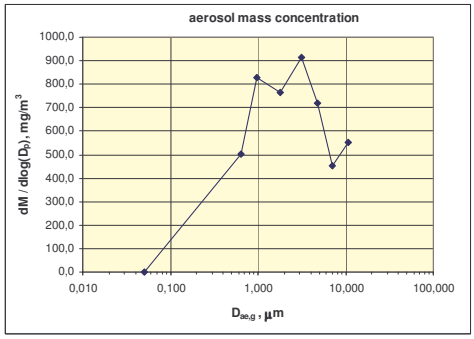

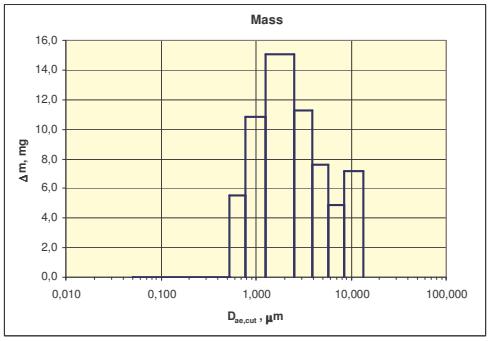

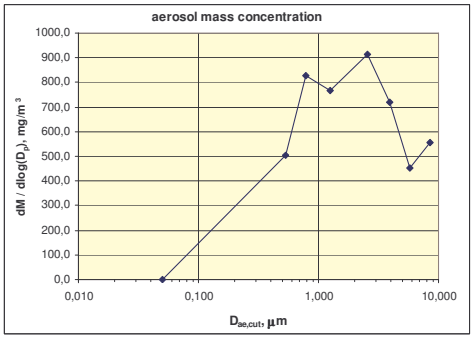

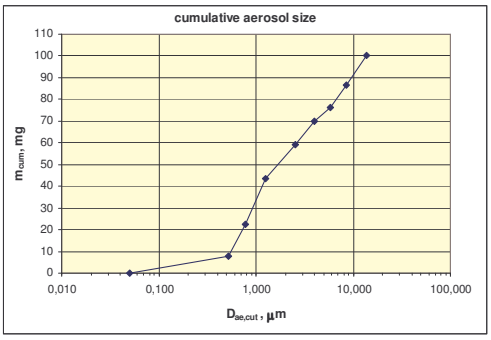

Table.IV.17. Primary side impactor information for CAAT-04.

Tag Name:	Outlet ELPI
Identification:	ELPI

Notes: Mimimum and maximum weights.

Integrale Data of Measurement:

Meas-Fluid:			Air		
t_s	2760	s	FV_{sys}	142,61	m^3/h
t_{Start}	11:09	s	FV_s	10,00	l/min
P_s	1,424	bar(a)	V_s	352,29	l
T_s	21,4	°C	C_s	147,89	mg/m^3
MW_s	28,97	kg/kmol	$FM_{aerosol}$	21,091	g/h
X_{steam}	0	%	η_{ref}	1,820E-05	Pa-s
m_{total}	52,100	mg	η_{act}	1,820E-05	Pa-s
			AMMD	0,5	µm
			GSD	5,3	

Device Parameter:

Modell	ELPI	
S/N:	2363	
Supplier:	Dekati	
Calibration:	12.12.2005, Timo Alanen	
Reference Flow Rate:	9,98	l/min
Reference Temperature:	21,6	°C
Reference Pressure:	1,0	bar_a
Exhaust Pressure:	100,0	mbar
Diameter critcal Orifice:		mm
Reference Fluid:	Air	

Stage		$D_{ae,e}$	d_{nozzle}	$D_{ae,cut}$	$D_{ae,g}$	m_0	m_1	Δm	m_p	m_{sum}	M	$dM/dlog(D_p)$	p_{Stage}
		µm	mm	µm	µm	mg	mg	mg	%	%	mg/m^3	mg/m^3	bar_a
EL-13	0	9,88		9,88	--	38147,100	38150,800	3,700	7,645	107,64	10,503	#VALOR!	1,01320
EL-12	1	6,660		6,660	8,112	38798,000	38801,900	3,900	8,058	100,00	11,070	64,632	1,01300
EL-11	2	3,980		3,980	5,148	38297,000	38300,600	3,600	7,438	91,94	10,219	45,703	1,01240
EL-10	3	2,380		2,380	3,078	38948,800	38952,800	4,000	8,264	84,50	11,354	50,846	1,01170
EL-9	4	1,590		1,590	1,945	38629,800	38634,700	4,900	10,124	76,24	13,909	79,397	1,00990
EL-8	5	0,945		0,945	1,226	38739,000	38744,300	5,300	10,950	66,12	15,044	66,578	1,00480
EL-7	6	0,611		0,611	0,760	38485,800	38490,300	4,500	9,298	55,17	12,773	67,445	0,99590
EL-6	7	0,380		0,380	0,482	38220,900	38225,100	4,200	8,678	45,87	11,922	57,801	0,97110
EL-5	8	0,261		0,261	0,315	37704,100	37708,000	3,900	8,058	37,19	11,070	67,856	0,89460
EL-4	9	0,156		0,156	0,202	38656,800	38660,200	3,400	7,025	29,13	9,651	43,178	0,69010
EL-3	10	0,095		0,095	0,122	38110,200	38113,800	3,600	7,438	22,11	10,219	47,541	0,39550
EL-2	11	0,057		0,057	0,074	38618,400	38621,900	3,500	7,231	14,67	9,935	44,690	0,22490
EL-1	12	0,028		0,028	0,040	38530,500	38534,100	3,600	7,438	7,44	10,219	33,604	0,10000
Sum								48,400	100,00				

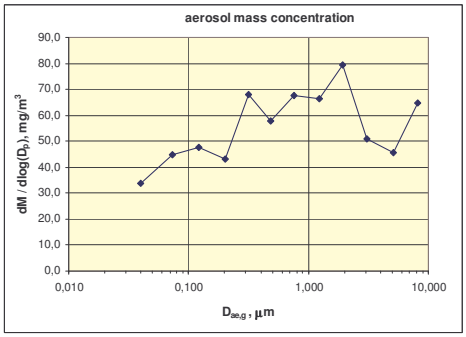

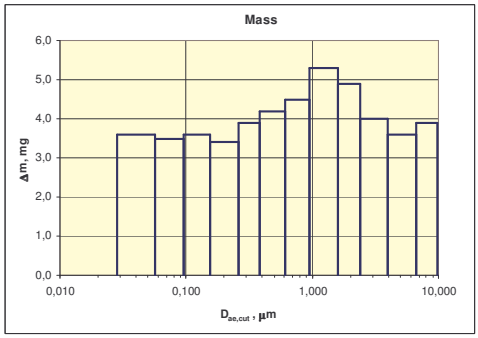

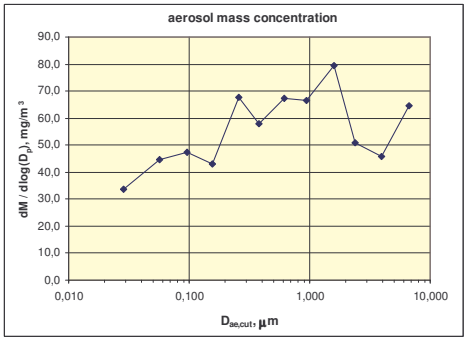

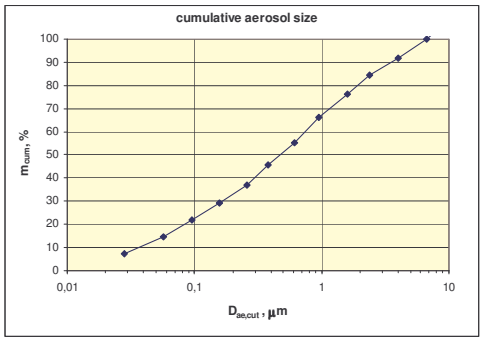

Table.IV.18. Secondary side ELPI impactor information for CAAT-04.

B.3.2 ONLINE AEROSOL SIZE DISTRIBUTION AT THE PRIMARY AND SECONDARY SIDE

As an example, Fig.IV.13 shows the APS count size distribution evolution with time for CAAT-05 of the aerosol distribution at the primary side. Fig.IV.14 shows APS the count mean diameter, count median diameter and GSD evolution with time during CAAT-05.

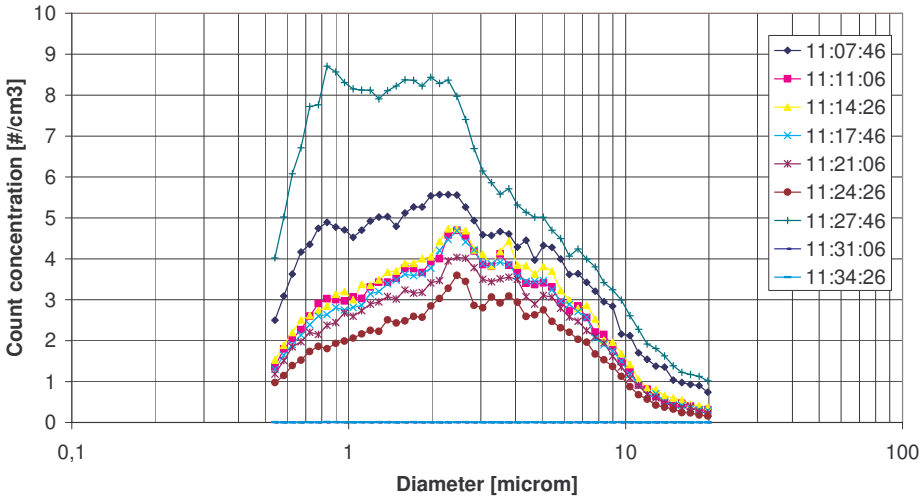

Fig.IV.13. APS primary side count size distribution for CAAT-05.

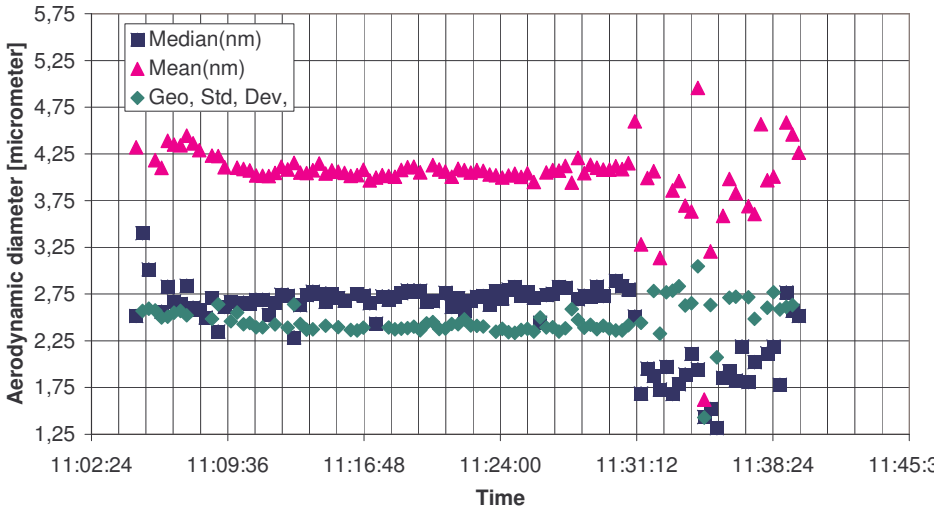

Fig.IV.14. APS primary side count mean, median diameter and GSD for CAAT-05.

Fig.IV.15 shows the OPC count size distribution evolution with time. Fig.IV.16 shows OPC the count mean diameter, count median diameter and GSD evolution with time during CAAT-05.

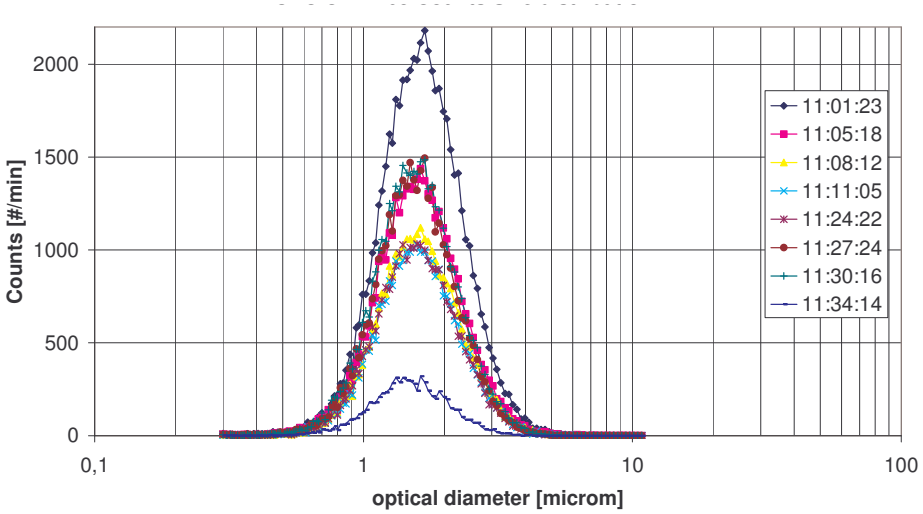

Fig.IV.15. OPC primary side count size distribution for CAAT-05.

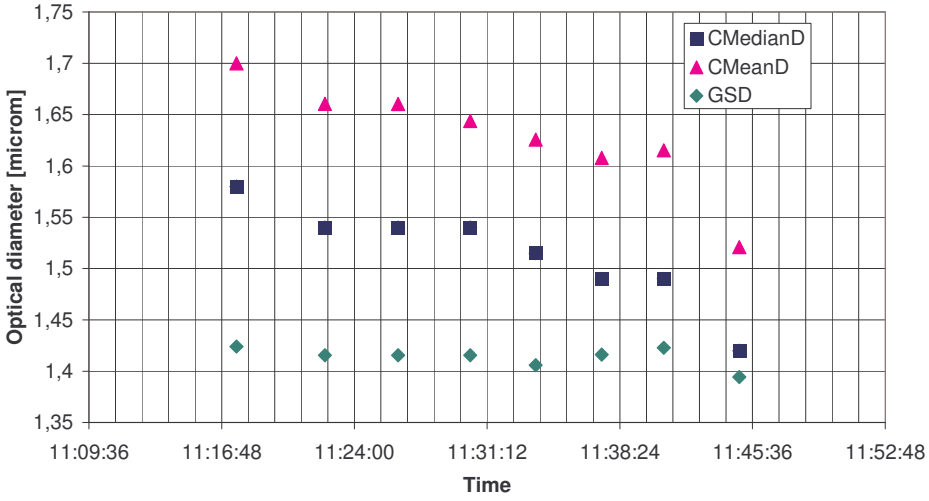

Fig.IV.16. OPC primary side count mean, median diameter and GSD for CAAT-05.

Fig.IV.17 shows the averaged particle count size distribution for CAAT-05 measured by ELPI at the secondary side. Fig.IV.18 shows ELPI the count mean diameter, count median diameter and GSD evolution with time during CAAT-05. Distributions show that median diameter and GSD have steady values around 0.1 and 1.9 respectively.

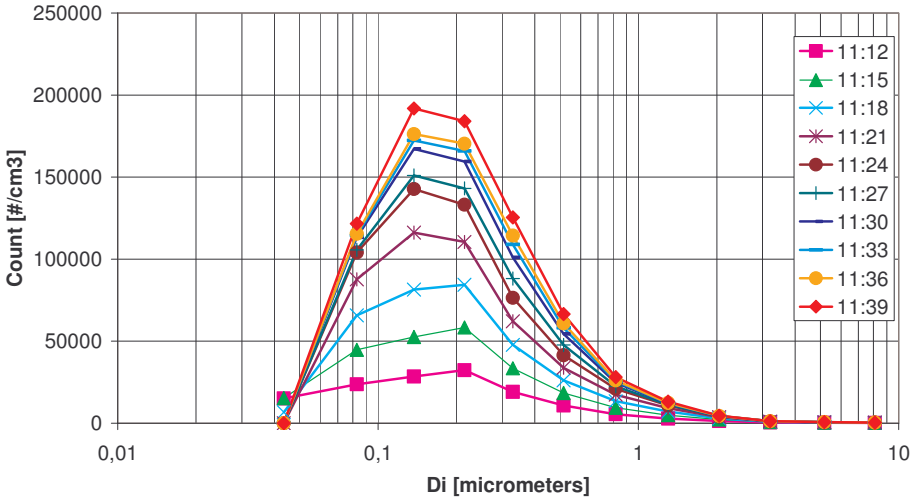

Fig.IV.17. ELPI secondary side count size distribution for CAAT-05.

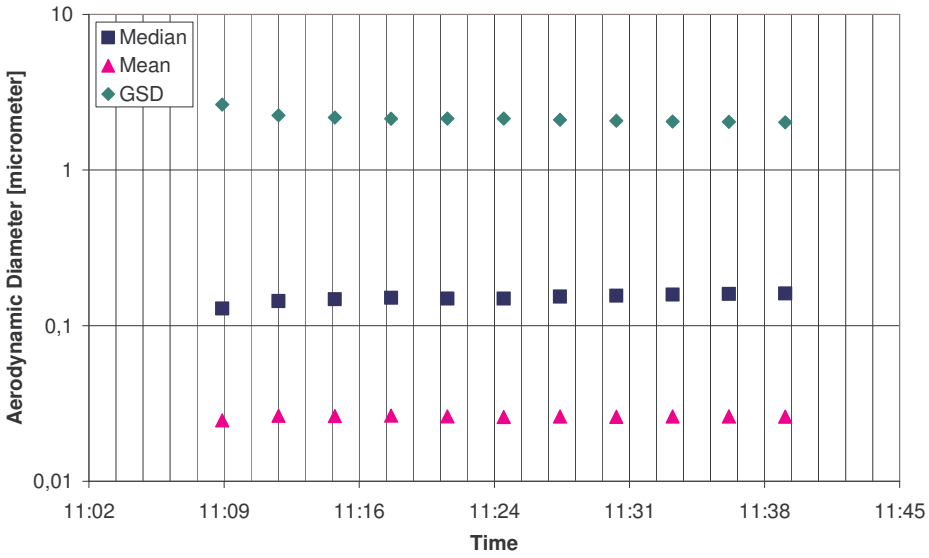

Fig.IV.18. ELPI secondary side count mean, median diameter and GSD for CAAT-05.

B.3.3. AEROSOL DEPOSITION PATTERN AND RETENTION EFFICIENCY ESTIMATION

Qualitative observations during the washing dismounting and cleaning process of the remark the quantitative and qualitative difference in the deposition pattern found between TiO_2 Degussa tests and TiO_2 Nanophase tests. Fig.IV.19 through 21 show the

on-tube deposition pattern found for CAAT-03, CAAT-04 and CAAT-05 tests. Mass deposits were found to be much higher in the first row of neighbor tubes. Several asymmetries can be noticed in the pattern, as in E1 and F2 tubes for CAAT-03. The fall of some deposits during the dismounting process considerably contribute to it.

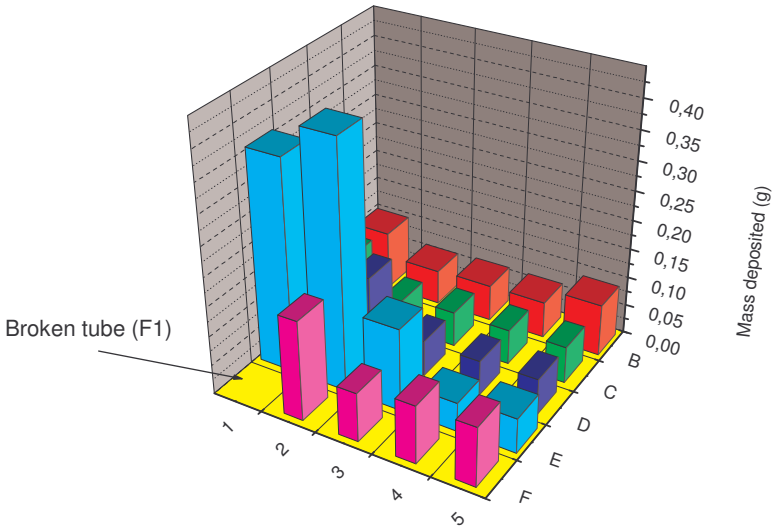

Fig.IV.19. On tube mass deposition pattern for CAAT-03.

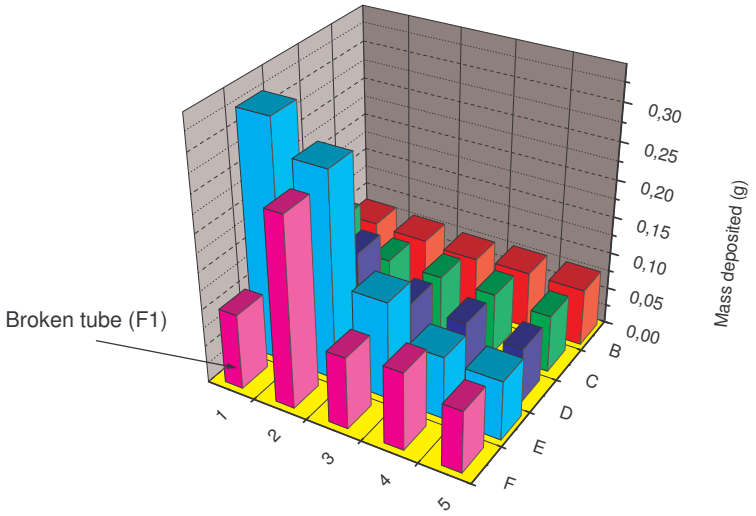

Fig.IV.20. On tube mass deposition pattern for CAAT-04.

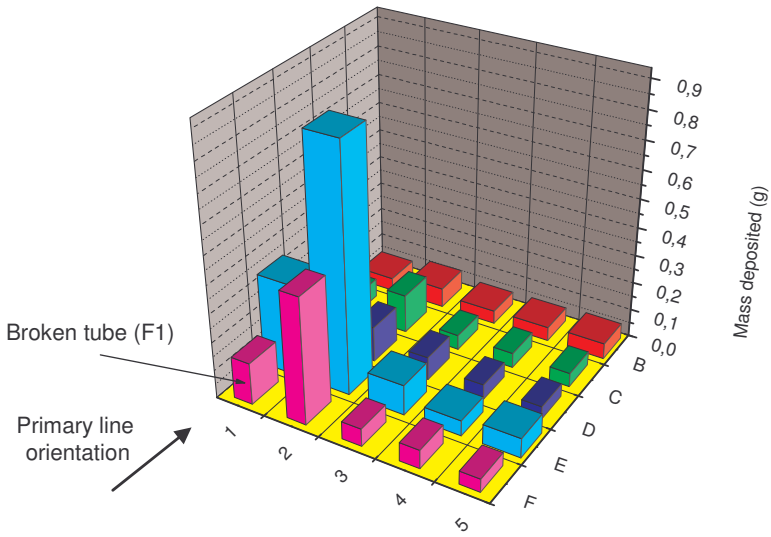

Fig.IV.21. On tube mass deposition pattern for CAAT-05.

Table.IV.19 shows the retention efficiency results:

Experiment	**Design inlet gas mass flow rate [kg/h]**	**Mean Value [%]**	**Estimated Uncertainty [%]**
CAAT-03	100	15.85	7.30
CAAT-04	250	13.64	6.92
CAAT-05	150	15.79	6.53

Table.IV.19. Retention efficiency estimations for TiO_2 Nanophase tests.

C. SiO_2 EXPERIMENTS: CAAT-06, CAAT-07, CAAT-08, CAAT-09, CAAT-10, CAAT-11 and CAAAT-13

Six tests were executed using Nagase SiO_2 aerosol. These tests were conducted on June 21, 2007, July 11, 2007, August 26, 2007, September 24, 2007, October 4, 2007, October 24, 2007 and January 17, 2008 respectively. The design inlet gas mass flow rates used in these tests were 100 kg/h, 150kg/h, 200 kg/h, 100kg/h, 150 kg/h and 75kg/h, respectively. CAAT-06 and CAAT-07 tests were designed and executed with low inlet aerosol concentration compared to the rest of SiO_2 and TiO_2 CAAT tests. CAAT-08, CAAT-09, CAAT-10, CAAT-11 and CAAT-13 were designed and executed with an inlet aerosol concentration similar to the TiO_2 CAAT experiments. Fig.IV.22 shows the configuration of the CAAT-PECA facility used during these tests. As shown, the main difference with respect to TiO_2 experiments is the introduction of a cascade impactor downstream the OPC as well as the removal of the Venturi cone.

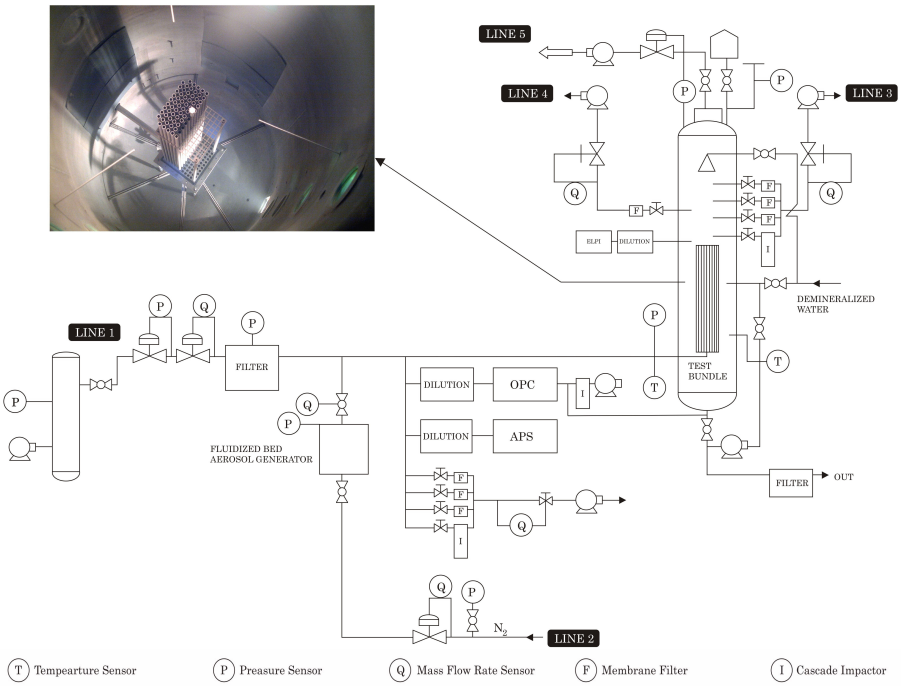

Fig.IV.22. Scheme of the PECA facility for CAATs SiO_2 experiments.

C.1. SUMMARY OF TEST EXECUTION

Test execution procedure for SiO_2 experiments is similar to the one used in TiO_2 experiments, except for the introduction of a resuspension phase after the end of the

aerosol injection. The main actions of the test are summarized in Table.IV.20 for CAAT-09 which is similar to the rest of tests. Fig.IV.23 shows the main thermal-hydraulic variables evolution as a function of time with the test procedure explanation chart and Fig.IV.24 shows the aerosol device measurement schedule for CAAT-09.

Day Time, h	**Main Action**
08:10	ELPI warm up
9:00	OPC lamp warm up
11:20	Compressor start up and flow increase up to desired conditions
11:35	Reach of stabilized flow conditions
11:36	Dilution air started. DAS, APS, ELPI, OPC measurements started
11:36	Aerosol generation started
11:36	Primary side OPC DEK Impactor started
11:37	Primary side membrane filter P1F1 secondary side membrane filter L1F1 measurement started
11:43	Primary side membrane filter P1F1 secondary side membrane filter L1F1 measurement end
11:43	Primary side Impactador MARK secondary side impactor ANDER measurement started
11:55	Primary side Impactador MARK measurement end
12:01	Secondary side Impactor ANDER measurement end
12:01	Primary side membrane filter P2F1 secondary side membrane filter L2F1 measurement started
12:06	Primary side membrane filter P2F1 secondary side membrane filter L2F1 measurement end
12:09	Primary side membrane filter P1F2 secondary side membrane filter L1F2 measurement started
12:14	Primary side membrane filter P1F2 secondary side membrane filter L1F2 measurement end
12:15	Primary side membrane filter P2F2 secondary side membrane filter L2F2 measurement started
12:20	Primary side membrane filter P2F2 and secondary side membrane filter L2F2 measurement end
12:20	Aerosol generation end
12:20	Resuspension test started
12:21	Primary side Dekati Impactor end
12:30	Resuspension test end
12:30	Shutdown of air compressor and facility
12:31	End of test

Table.IV.20. Test sequence for CAAT-09.

The test began with compressor start up, the stabilization of the inlet gas mass flow rate. No Venturi by-pass flow was used in this test. The aerosol generation was started at 11:36. Membrane filters and impactor measurements are sequentially performed for time durations which provide reasonable aerosol sampled masses. Inlet aerosol size distribution was characterized by APS whereas outlet aerosol size distribution was characterized on-line by ELPI. An additional characterization of the inlet aerosol size distribution was performed every 4 minutes by measuring during 60 seconds with the OPC. A Dekati low pressure impactor was used after the OPC to characterize inlet aerosol mass size distribution. This impactor was sampling during the whole test. At 12:20 the aerosol injection was finished and the resuspension test was started. At 12:30 the resuspension test was finished and the compressor and the rest of the facility was shutdown. The aerosol injection during the test lasted for 54 minutes. The resuspension test lasted for 10 minutes.

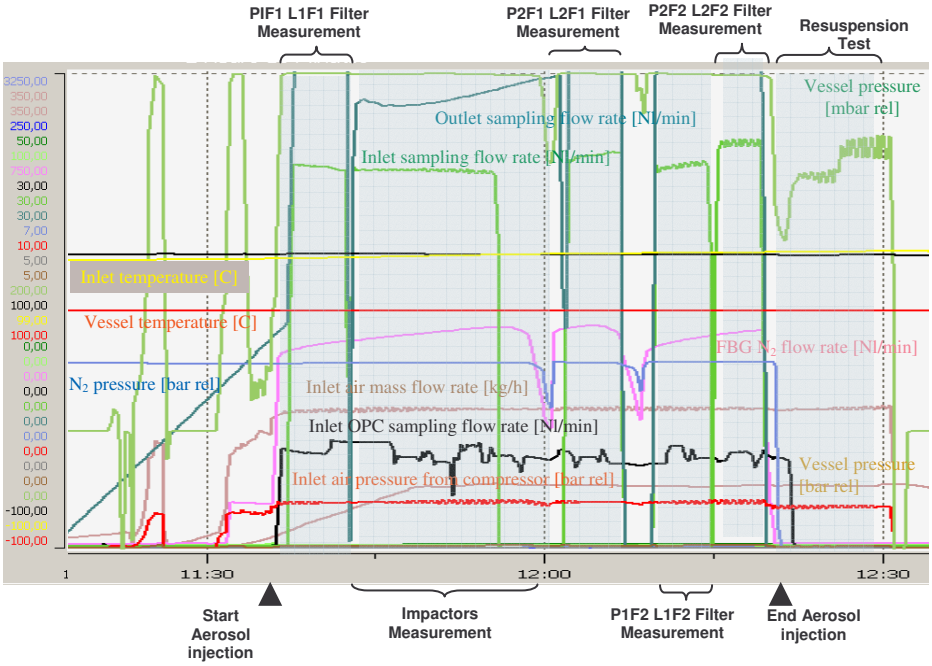

Fig.IV.23. Thermal-hydraulics variables of the test.

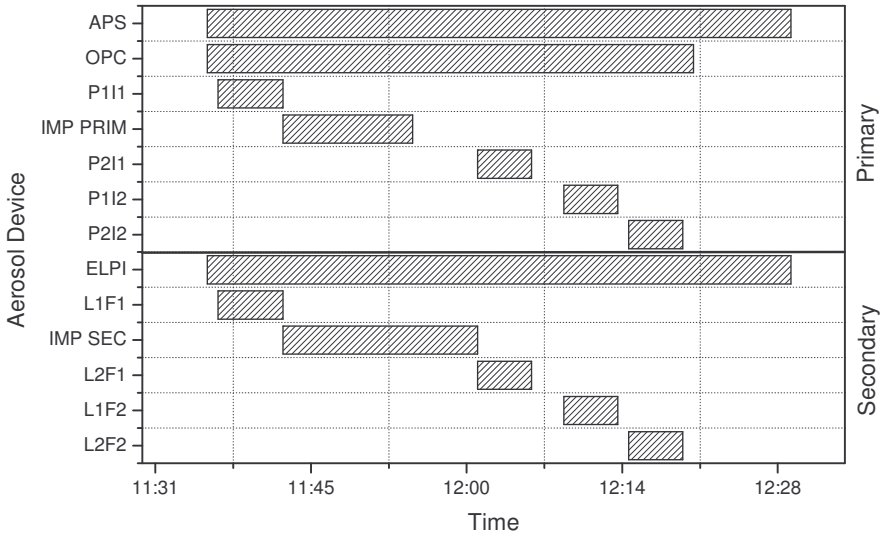

Fig.IV.24. Aerosol measurement schedule.

C.2 THERMAL-HYDRAULIC RESULTS

The mean values of the most important thermal hydraulic parameters are shown in Table.IV.21 through 24 for the primary and secondary side.

Variable	Units	Mean Value CAAT-06	Mean Value CAAT-07	Resolution	Set point CAAT-06	Set point CAAT-07
Compressor air mass flow rate	Kg/h	98.90	141.10	±0.01	93	143
Compressor air manometric pressure	Bar	1.36	1.20	±0.01	-	-
Venturi bypass flow rate	Nl/min	108.0	65.3	±0.1	100	100
FBG N_2 flow rate	Nl/min	92.6	93.0	±0.1	100	100
FBG N_2 manometric pressure	Bar	2.7	2.7	±0.1	2.7	2.7
Total mass flow rate through the breach	Kg/h	105.9	148.4	±0.1	100	150

Flow temperature	ºC	21.2	26.8	±0.1	-	-
Manometric Pressure at primary side	Bar	0.8	0.4	±0.1	0.3	0.6
Manometric Pressure at the FBG vessel	Bar	0.1	0.2	±0.2	-	-
Sampling flow rate	Nl/min	28.9	29.7	±0.1	-	-

Table.IV.21. Mean values in CAAT-06, CAAT-07 for primary side.

Variable	**Units**	**Mean Value CAAT-08**	**Mean Value CAAT-09**	**Mean Value CAAT-10**	**Resolution**	**Set point CAAT-08**	**Set point CAAT-09**	**Set point CAAT-10**
Compressor air mass flow rate	Kg/h	160.00	102.37	144.50	±0.01	175	80	125
Compressor air manometric pressure	Bar	2.40	0.98	1.71	±0.01	-	-	-
Venturi bypass flow rate	Nl/min	-	-	-	±0.1	-	-	-
FBG N_2 flow rate	Nl/min	287.0	334.6	331.0	±0.1	350	350	350
FBG N_2 manometric pressure	Bar	2.7	2.7	2.7	±0.1	2.7	2.7	2.7
Total mass flow rate through the breach	Kg/h	183	134.0	167.1	±0.1	200	100	150
Flow temperature	ºC	26.5	22.9	19.9	±0.1	-	-	-
Manometric Pressure at primary side	Bar	0.65	0.3	0.7	±0.1	1	0.3	0.6
Manometric Pressure at the FBG vessel	Bar	1.2	1.0	1.2	±0.2	-	-	-
Sampling	Nl/min	32.3	33.2	37.8	±0.1	-	-	-

flow rate								

Table.IV.22. Mean values in CAAT-08, CAAT-09, CAAT-10 for primary side.

Variable	Units	Mean Value CAAT-11	Mean Value CAAT-13	Resolution	Set point CAAT-11	Set point CAAT-13
Compressor air mass flow rate	Kg/h	214.71	56.05	±0.01	225	50
Compressor air manometric pressure	Bar	2.16	0.53	±0.01	-	-
Venturi bypass flow rate	Nl/min	-	-	±0.1	-	-
FBG N_2 flow rate	Nl/min	324.0	341.1	±0.1	350	350
FBG N_2 manometric pressure	Bar	2.7	2.7	±0.1	2.7	2.7
Total mass flow rate through the breach	Kg/h	237.0	81.4	±0.1	250	75
Flow temperature	ºC	17.4	27.5	±0.1	-	-
Manometric Pressure at primary side	Bar	1.0	0.2	±0.1	1.2	0.2
Manometric Pressure at the FBG vessel	Bar	1.4	0.8	±0.2	-	-
Sampling flow rate	Nl/min	42.4	47.5	±0.1	-	-

Table.IV.23. Mean values in CAAT-11, CAAT-13 for primary side.

Variable	Units	Mean Value CAAT-06	Mean Value CAAT-07	Mean Value CAAT-08	Mean Value CAAT-09	Mean Value CAAT-10	Mean Value CAAT-11	Mean Value CAAT-13	Resolution
Flow temperature	ºC	24.4	25.2	25.6	23.7	20.8	19.5	22.4	±0.1
Blower duty	%	0	85	10	18	54	29	5	±1
PECA Vessel manometric pressure	mbar rel	161	200	200	200	200	200	200	±1

Dilution air flow rate	Nl/min	0	0	0	0	0	0	0	±0.1
Dilution air manometric pressure	Bar rel	0	0	0	0	0	0	0	±0.2
Laboratory Barometric pressure	mmHg	693	694	693	692	692	692	693	±1
Laboratory ambient temperature	ºC	21.0	25.2	25.0	22.0	20.0	19.0	23.0	±0.1
Sampling flow rate	Nl/min	23.4	25.2	26.1	24.4	29.2	30.9	21.6	±0.1

Table.IV.24. Mean values in CAAT-06, CAAT-07, CAAT-08, CAAT-09, CAAT-10, CAAT-11, CAAT-13 for secondary side.

C.3. AEROSOL RESULTS

The aerosol used in these tests is Seahostar SiO_2 from Nagase (Nagase, 2006). The aerosol generation process is patented and not specified. It has a primary particle diameter of 1.02 µm, and the particle morphology is spherical. More details on the aerosol characteristics are given in Table.IV.25.

SiO_2 aerosol characteristics	**Units**	**Value**
Average primary particle diameter	nm	1020
True density proposed by Nagase	g/cm^3	~2

Table.IV.25. Aerosol characteristics.

C.3.1. INTEGRAL BEHAVIOUR

Detailed information on collected aerosol masses on membrane filters and impactors fos SiO_2 tests is shown in Table.IV.26 through 32.

Tag Name	ID	Note	m_0	m_f	Δm	t_s	t_{Start}	FM_s	p_s	T_s	MW_s	X_{steam}	FV_{sys}	η_{act}	FV_s	V_s	C_s	$FM_{aerosol}$	$<FM_{aerosol}>$
			mg	mg	mg	s	s	nl/min	bar(a)	°C	kg/kmol	%	m^3/h	Pa s	l/min	l	g/m^3	g/h	g/h
P2-I1	FI		126,900	130,600	3,700	298	11:20	21,82	1,124	21,2	28,970	0,000	78,0	1,8191E-05	21,16	105,10	0,03520	2,744	1,34
P1-I1	FI		126,100	127,400	1,300	276	11:43	22,79	1,124	21,8	28,970	0,000	77,3	1,8219E-05	22,14	101,86	0,01276	0,987	
P2-I2	FI		126,700	128,100	1,400	244	11:50	22,43	1,124	21,9	28,970	0,000	80,0	1,8224E-05	21,80	88,66	0,01579	1,263	
P1-I2	FI		125,900	126,400	0,500	298	11:56	22,08	1,124	22,0	28,970	0,000	78,7	1,8229E-05	21,47	106,62	0,00469	0,369	
M-III	IMP		-	-	3,300	276	11:27	21,88	1,124	21,3	28,970	0,0	81,5	1,8195E-05	21,23	97,64	0,03380	2,755	
S1-I1	FI		125,300	133,300	8,000	298	11:20	16,78	1,083	24,4	28,970	0,000	81,8	1,8343E-05	17,07	84,79	0,09435	7,715	3,48
S2-I1	FI		126,700	132,200	5,500	276	11:43	19,48	1,098	24,4	28,970	0,000	79,9	1,8343E-05	19,55	89,92	0,06116	4,885	
S1-I2	FI		126,500	127,400	0,900	244	11:50	20,96	1,098	24,4	28,970	0,000	82,6	1,8343E-05	21,03	85,51	0,01052	0,869	
S2-I2	FI		138,300	138,900	0,600	298	11:56	22,13	1,090	24,0	28,970	0,000	81,7	1,8324E-05	22,34	110,97	0,00541	0,442	
ELPI	IMP		-	-	7,000	2160	11:52	10,00	1,092	24,4	28,970	0,000	84,8	1,8343E-05	10,09	363,15	0,01928	1,634	
AI	IMP		-	-	1,348	967	11:25	12,27	1,092	24,4	28,970	0,0	84,8	1,8343E-05	12,38	199,45	0,00676	0,573	

t_s measurement lapse FV_{sys} flow rate at the main line

Table.IV.26. Filters and Impactors information for CAAT-06.

Tag Name	ID	Note	m_0	m_1	Δm	t_s	t_{Start}	FM_s	p_s	T_s	MW_s	X_{steam}	FV_{sys}	η_{act}	FV_s	V_s	C_s	$FM_{aerosol}$	$<FM_{aerosol}>$
			mg	mg	mg	s	s	nl/min	bar(a)	°C	kg/kmol	%	m^3/h	Pa s	l/min	l	g/m^3	g/h	g/h
P2-I1	FI		126,700	135,900	9,200	243	12:36	24,17	1,325	26,7	28,970	0,000	89,4	1,8452E-05	20,25	82,00	0,11220	10,034	4,73
P1-I1	FI		125,900	127,600	1,700	243	12:42	24,07	1,325	26,8	28,970	0,000	97,2	1,8457E-05	20,17	81,69	0,02081	2,024	
P2-I2	FI		125,700	128,300	2,600	231	12:46	25,87	1,325	26,9	28,970	0,000	99,9	1,8462E-05	21,69	83,49	0,03114	3,110	
P1-I2	FI		126,800	133,700	6,900	523	12:52	24,98	1,325	26,9	28,970	0,000	99,0	1,8462E-05	20,94	182,52	0,03780	3,742	
M-III	IMP		-	-	1,800	414	12:31	23,60	1,325	26,8	28,970	0,0	98,6	1,8457E-05	19,78	136,45	0,01319	1,301	
S1-I1	FI		126,400	129,300	2,900	243	12:36	28,27	1,125	25,2	28,970	0,000	104,8	1,8381E-05	27,75	112,39	0,02580	2,704	1,43
S2-I1	FI		126,700	128,700	2,000	231	12:42	31,62	1,125	25,6	28,970	0,000	114,1	1,8400E-05	31,08	119,66	0,01671	1,906	
S1-I2	FI		127,400	127,900	0,500	231	12:46	30,78	1,125	26,0	28,970	0,000	117,3	1,8419E-05	30,30	116,64	0,00429	0,503	
S2-I2	FI		125,800	127,200	1,400	523	12:52	30,27	1,125	26,3	28,970	0,000	116,4	1,8433E-05	29,82	259,96	0,00539	0,627	
ELPI	IMP		-	-	6,900	2280	12:24	10,00	1,125	25,8	28,970	0,000	115,7	1,8408E-05	9,84	373,74	0,01846	2,135	
AI	IMP		-	-	0,277	645	12:31	23,87	1,125	25,6	28,970	0,0	115,7	1,8400E-05	23,46	252,23	0,00110	0,127	

t_s measurement lapse FV_{sys} flow rate at the main line

Table.IV.27. Filters and Impactors information for CAAT-07.

Tag Name	ID	Note	m_0	m_1	Δm	t_s	t_{Start}	FM_s	p_s	T_s	MW_s	X_{steam}	FV_{sys}	η_{act}	FV_s	V_s	C_s	$FM_{aerosol}$	$<FM_{aerosol}>$
			mg	mg	mg	s	s	nl/min	bar(a)	°C	kg/kmol	%	m^3/h	Pa s	l/min	l	g/m^3	g/h	g/h
P1-I1	FI		126,000	248,000	122,000	310	11:20	20,81	1,123	19,7	28,970	0,000	74,5	1,8119E-05	20,10	103,84	1,17484	87,492	48,79
P2-I1	FI		127,700	275,400	147,700	289	11:43	21,76	1,123	20,0	28,970	0,000	73,9	1,8133E-05	21,04	101,33	1,45757	107,684	
M-III	IMP		-	-	25,600	283	11:27	21,62	1,123	19,8	28,970	0,0	74,0	1,8124E-05	20,89	98,52	0,25984	19,222	
Dek	IMP		-	-	94,800	3180	11:26	28,25	1,123	20,0	28,970	0,0	74,0	1,8133E-05	27,31	1447,57	0,06549	4,848	
S1-I1	FI		126,500	144,500	18,000	309	11:20	21,50	0,973	21,3	28,970	0,000	86,4	1,8195E-05	24,08	124,00	0,14516	12,535	5,71
S2-I1	FI		127,300	147,000	19,700	290	11:43	30,20	1,120	22,6	28,970	0,000	74,7	1,8257E-05	29,53	142,71	0,13804	10,313	
ELPI	IMP		-	-	16,400	4053	10:55	10,00	1,083	22,4	28,970	0,000	79,6	1,8249E-05	10,10	682,37	0,02403	1,914	
AI	IMP		-	-	0,510	889	11:27	12,35	1,052	22,4	28,970	0,0	79,6	1,8248E-05	12,85	190,34	0,00268	0,213	

t_s measurement lapse FV_{sys} flow rate at the main line

Table.IV.28. Filters and Impactors information for CAAT-08.

Tag Name	ID	Note	m_0	m_1	Δm	t_s	t_{Start}	FM_s	p_s	T_s	MW_s	X_{steam}	FV_{sys}	η_{act}	FV_s	V_s	C_s	$FM_{aerosol}$	$<FM_{aerosol}>$
			mg	mg	mg	s	s	nl/min	bar(a)	°C	kg/kmol	%	m^3/h	Pa s	l/min	l	g/m^3	g/h	g/h
P2-I1	FI		128,400	226,700	98,300	272	11:39	25,52	1,223	24,0	28,970	0,000	88,8	1,8324E-05	22,96	104,10	0,94424	83,855	43,24
P1-I1	FI		127,200	170,600	43,400	271	12:04	26,40	1,223	24,0	28,970	0,000	89,4	1,8324E-05	23,76	107,30	0,40448	36,161	
P2-I2	FI		127,400	177,400	50,000	303	12:11	24,00	1,223	24,0	28,970	0,000	91,3	1,8324E-05	21,60	109,06	0,45946	41,871	
P1-I2	FI		128,200	140,200	12,000	271	12:15	24,52	1,223	24,0	28,970	0,000	91,8	1,8324E-05	22,06	99,65	0,12043	11,057	
M-III	IMP		-	-	255,200	766	12:31	24,36	1,323	26,8	28,970	0,0	98,8	1,8457E-05	20,46	261,16	0,97718	96,544	
S1-I1	FI		126,700	143,300	16,600	287	11:39	36,17	1,123	24,0	28,970	0,000	96,7	1,8324E-05	35,45	169,55	0,09790	9,469	4,80
S2-I1	FI		127,200	136,000	8,800	271	12:04	38,78	1,123	24,0	28,970	0,000	97,4	1,8324E-05	38,00	171,65	0,05127	4,991	
S1-I2	FI		126,300	130,100	3,800	303	12:11	36,96	1,123	24,0	28,970	0,000	99,5	1,8324E-05	36,22	182,93	0,02077	2,066	
S2-I2	FI		126,500	129,600	3,100	271	12:15	37,23	1,123	24,0	28,970	0,000	100,0	1,8324E-05	36,49	164,81	0,01881	1,881	
ELPI	IMP		-	-	33,500	2280	12:24	10,00	1,123	24,0	28,970	0,000	115,9	1,8324E-05	9,80	372,40	0,08996	10,429	
AI	IMP		-	-	9,707	1101	12:31	29,10	1,123	25,6	28,970	0,0	115,9	1,8400E-05	28,67	526,13	0,01845	2,139	

t_s measurement lapse FV_{sys} flow rate at the main line

Table.IV.29. Filters and Impactors information for CAAT-09.

Tag Name	ID	Note	m_0	m_1	Δm	t_s	t_{Start}	FM_s	p_s	T_s	MW_s	X_{steam}	FV_{sys}	η_{act}	FV_s	V_s	C_s	$FM_{aerosol}$	$<FM_{aerosol}>$
			mg	mg	mg	s	s	nl/min	bar(a)	°C	kg/kmol	%	m^3/h	Pa s	l/min	l	g/m^3	g/h	g/h
P2-I1	FI		127,500	207,800	80,300	298	11:03	30,53	1,623	20,0	28,970	0,000	94,0	1,8133E-05	20,42	101,43	0,79171	74,397	34,61
P1-I1	FI		125,600	152,000	26,400	266	11:29	30,34	1,523	20,0	28,970	0,000	90,2	1,8133E-05	21,63	95,89	0,27533	24,835	
P2-I2	FI		127,100	148,000	20,900	224	11:34	32,18	1,623	21,0	28,970	0,000	85,6	1,8181E-05	21,60	80,64	0,25918	22,179	
P1-I2	FI		127,100	138,300	11,200	170	11:39	31,42	1,623	21,0	28,970	0,000	90,9	1,8181E-05	21,09	59,75	0,18745	17,031	
M-III	IMP		-	-	########	584	12:31	29,85	1,323	26,8	28,970	0,0	98,8	1,8457E-05	25,06	243,95	-44,90096	-4436,185	
S1-I1	FI		127,400	132,500	5,100	298	11:03	40,79	1,123	20,0	28,970	0,000	135,8	1,8133E-05	39,44	195,89	0,02604	3,536	2,83
S2-I1	FI		127,800	129,700	1,900	255	11:29	45,53	1,123	20,0	28,970	0,000	122,3	1,8133E-05	44,02	187,08	0,01016	1,243	
S1-I2	FI		126,500	131,700	5,200	224	11:34	44,54	1,123	21,0	28,970	0,000	123,7	1,8181E-05	43,20	161,30	0,03224	3,988	
S2-I2	FI		127,700	130,200	2,500	170	11:39	46,72	1,123	21,0	28,970	0,000	131,3	1,8181E-05	45,32	128,42	0,01947	2,557	
ELPI	IMP		-	-	20,100	2280	12:24	10,00	1,123	20,5	28,970	0,000	115,9	1,8157E-05	9,68	368,02	0,05462	6,332	
AI	IMP		-	-	1,035	1212	12:31	32,85	1,123	25,6	28,970	0,0	115,9	1,8400E-05	32,37	653,79	0,00158	0,184	

t_s *measurement lapse* FV_{sys} *flow rate at the main line*

Table.IV.30. Filters and Impactors information for CAAT-10.

Tag Name	ID	Note	m_0	m_1	Δm	t_s	t_{Start}	FM_s	p_s	T_s	MW_s	X_{steam}	FV_{sys}	η_{act}	FV_s	V_s	C_s	$FM_{aerosol}$	$<FM_{aerosol}>$
			mg	mg	mg	s	s	nl/min	bar(a)	°C	kg/kmol	%	m^3/h	Pa s	l/min	l	g/m^3	g/h	g/h
P2-I1	FI		127,800	189,300	61,500	468	11:15	32,80	1,823	19,0	28,970	0,000	110,8	1,8085E-05	19,47	151,83	0,40506	44,894	35,36
P1-I1	FI		126,500	172,800	46,300	468	11:35	32,47	1,923	19,0	28,970	0,000	105,0	1,8085E-05	18,27	142,49	0,32494	34,104	
P2-I2	FI		127,700	178,400	50,700	489	11:56	33,34	1,923	19,0	28,970	0,000	104,2	1,8085E-05	18,76	152,87	0,33166	34,547	
P1-I2	FI		127,200	151,200	24,000	298	11:59	32,12	1,923	19,0	28,970	0,000	104,4	1,8085E-05	18,07	89,75	0,26741	27,905	
M-III	IMP		-	-	38,800	595	12:31	32,80	1,323	26,8	28,970	0,0	156,6	1,8457E-05	27,54	273,11	0,14207	22,253	
S1-I1	FI		127,100	130,500	3,400	468	11:15	47,44	1,123	17,6	28,970	0,000	179,1	1,8018E-05	45,49	354,80	0,00958	1,716	2,05
S2-I1	FI		126,600	131,500	4,900	468	11:35	50,54	1,123	17,6	28,970	0,000	178,9	1,8018E-05	48,47	378,03	0,01296	2,319	
S1-I2	FI		126,800	131,600	4,800	500	11:56	48,30	1,123	17,6	28,970	0,000	177,5	1,8018E-05	46,31	385,96	0,01244	2,208	
S2-I2	FI		127,000	129,600	2,600	298	11:59	49,32	1,123	17,6	28,970	0,000	177,9	1,8018E-05	47,29	234,89	0,01107	1,969	
ELPI	IMP		-	-	4,300	2280	12:24	10,00	1,123	17,6	28,970	0,000	183,8	1,8018E-05	9,59	364,38	0,01180	2,169	
AI	IMP		-	-	0,134	1148	12:31	38,65	1,123	25,6	28,970	0,0	183,8	1,8400E-05	38,08	728,62	0,00018	0,034	

t_s *measurement lapse* FV_{sys} *flow rate at the main line*

Table.IV.31. Filters and Impactors information for CAAT-11.

Tag Name	ID	Note	m_0	m_1	Δm	t_s	t_{Start}	FM_s	p_s	T_s	MW_s	X_{steam}	FV_{sys}	η_{act}	FV_s	V_s	C_s	$FM_{aerosol}$	$<FM_{aerosol}>$
			mg	mg	mg	s	s	nl/min	bar(a)	°C	kg/kmol	%	m^3/h	Pa s	l/min	l	g/m^3	g/h	g/h
P1-I1	FI		130,900	162,700	31,800	298	11:39	21,60	1,124	22,8	28,970	0,000	62,4	1,8267E-05	21,06	104,59	0,30405	18,965	61,94
P2-I1	FI		127,100	260,200	133,100	287	12:04	23,12	1,124	22,4	28,970	0,000	64,1	1,8248E-05	22,51	107,67	1,23620	79,200	
P2-I2	FI		128,700	331,700	203,000	287	12:11	22,85	1,124	22,3	28,970	0,000	63,5	1,8243E-05	22,24	106,38	1,90834	121,261	
P1-I2	FI		128,700	179,500	50,800	297	12:15	23,36	1,124	22,2	28,970	0,000	62,8	1,8238E-05	22,73	112,50	0,45155	28,343	
M-III	IMP		-	-	122,300	595	12:31	21,84	1,124	22,6	28,970	0,0	62,7	1,8257E-05	21,28	211,00	0,57962	36,361	
S1-I1	FI		128,100	196,300	68,200	298	11:39	51,93	1,124	23,0	28,970	0,000	62,4	1,8276E-05	50,66	251,61	0,27105	16,918	9,84
S2-I1	FI		126,600	137,100	10,500	287	12:04	53,30	1,124	23,0	28,970	0,000	64,2	1,8276E-05	52,00	248,72	0,04222	2,710	
S1-I2	FI		127,400	177,300	49,900	287	12:11	52,23	1,124	23,0	28,970	0,000	63,7	1,8276E-05	50,95	243,73	0,20474	13,040	
S2-I2	FI		127,200	153,200	26,000	297	12:15	50,57	1,124	23,0	28,970	0,000	62,9	1,8276E-05	49,33	244,20	0,10647	6,701	
ELPI	IMP		-	-	19,900	2280	12:24	10,00	1,124	23,0	28,970	0,000	63,4	1,8276E-05	9,76	370,71	0,05368	3,402	
AI	IMP		-	-	3,735	882	12:31	45,07	1,124	25,6	28,970	0,0	63,4	1,8400E-05	44,35	652,01	0,00573	0,363	

t_s *measurement lapse* FV_{sys} *flow rate at the main line*

Table.IV.32. Filters and Impactors information for CAAT-13.

Information relative to the impactors discrete aerosol size distribution at the primary and secondary side of the break stage is shown in Tables.IV:33 through 35.

Tag Name:	Inlet Mark III
Identification:	CAAT-10

Notes: Correct measurement at the inlet. Weighed just the filters

Integrale Data of Measurement:

Meas-Fluid:			Air		
t_s	584	s	FV_{sys}	98,8	m3/h
t_{Start}	12:31	s	FV_s	25,06	l/min
P_s	1,32	bar(a)	V_s	243,95	l
T_s	26,80	°C	C_s	110,68	mg/m3
MW_s	28,97	kg/kmol	$FM_{aerosol}$	10,93	g/h
X_{steam}	0,000	%	η_{ref}	1,820E-05	Pa-s
m_{total}	27,000	mg	η_{act}	1,846E-05	Pa-s
			AMMD	1,3	µm
			GSD	6,1	

Device Parameter:

Modell	Andersen Mark III	
S/N:		
Supplier:	Andersen Sampler Inc.	
Calibration:		
Reference Flow Rate:	14,2	l/min
Reference Temperature:	21,1	°C
Reference Pressure:	1,0133	bar_a
Reference Fluid:	Air	

Stage		D_{ae} ref µm	D_{ae} cut µm	D_{ae} g µm	m_0 mg	m_1 mg	Δm mg	m_p %	m_{cum} %	M mg/m^3	dM/dlog(D_p) mg/m^3
M-0	0	--	--	--	139,900	145,900	6,000	28,571	128,57	24,595	0
M-1	1	13,400	10,157	--	149,600	153,600	4,000	19,048	100,00	16,397	0
M-2	2	8,400	6,367	8,042	141,400	142,400	1,000	4,7619	80,95	4,099	20,210
M-3	3	5,700	4,321	5,245	151,500	153,000	1,500	7,1429	76,19	6,149	36,512
M-4	4	3,900	2,956	3,574	143,900	145,800	1,900	9,0476	69,05	7,788	47,257
M-5	5	2,500	1,895	2,367	151,500	154,900	3,400	16,19	60,00	13,937	72,167
M-6	6	1,230	0,932	1,329	143,900	151,200	7,300	34,762	43,81	29,924	97,144
M-7	7	0,770	0,584	0,738	152,200	152,700	0,500	2,381	9,05	2,050	10,076
M-8	8	0,520	0,394	0,480	143,800	144,100	0,300	1,4286	6,67	1,230	7,213
M-F	Backup	0,050	0,050	0,050	204,000	205,100	1,100	5,2381	5,24	4,509	5,029
Sum							21,000	100,00			

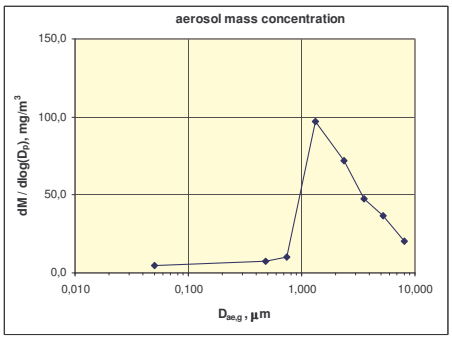

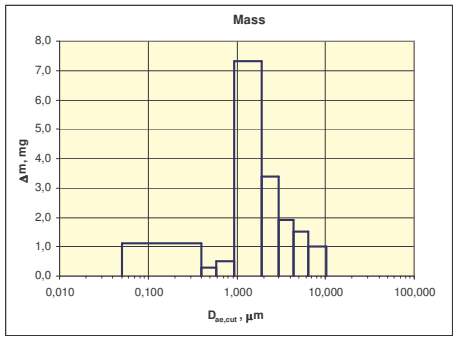

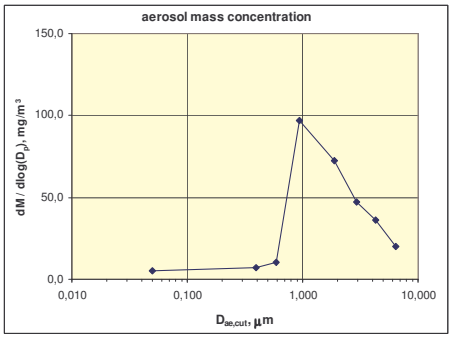

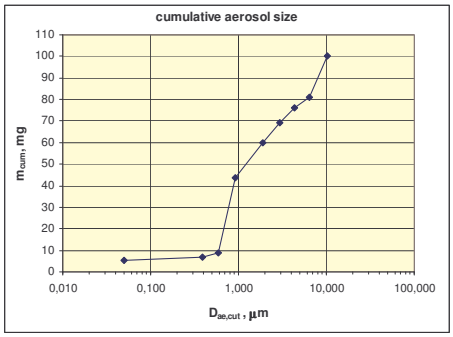

Table.IV.33. Primary side Mark impactor information for CAAT-10.

Tag Name:	Inlet OPC Imp
Identification:	Dek

Notes:

Using last premeasurement and first postmeasurement sample

Integrale Data of Measurement:

Meas-Fluid:			Air		
t_s	2280	s	FV_{sys}	115,94	m^3/h
t_{Start}	12:24	s	FV_s	10,00	l/min
P_s	1,123	bar(a)	V_s	388,02	l
T_s	20,5	°C	C_s	117,93	mg/m^3
MW_s	28,97	kg/kmol	$FM_{aerosol}$	13,672	g/h
X_{steam}	0	%	η_{ref}	1,820E-05	Pa-s
m_{total}	43,400	mg	η_{act}	1,816E-05	Pa-s
			AMMD	1,4	µm
			GSD	2,1	

Device Parameter:

Modell	LPI	
S/N:	2363	
Supplier:	Dekati	
Calibration:	12.12.2005, Timo Alanen	
Reference Flow Rate:	9,98	l/min
Reference Temperature:	21,6	°C
Reference Pressure:	1,0	bar_a
Exhaust Pressure:	100,0	mbar
Diameter critcal Orifice:		mm
Reference Fluid:	Air	

Stage		$D_{ae,ref}$ µm	$D_{ae,cut}$ µm	$D_{ae,g}$ µm	m_0 mg	m_t mg	Δm mg	m_p %	m_{cum} %	M mg/m^3	$M/dlog(D$ mg/m^3	p_{Stage} bar_a
EL-13	0	9,88	9,88	--	38501,200	38505,500	4,300	10,997	111,00	11,684	######	1,01320
EL-12	1	6,660	6,660	8,112	38568,200	38572,100	3,900	9,974	100,00	10,597	61,870	1,01300
EL-11	2	3,980	3,980	5,148	38022,200	38025,700	3,500	8,951	90,03	9,510	42,535	1,01240
EL-10	3	2,380	2,380	3,078	38777,000	38785,900	8,900	22,762	81,07	24,184	108,298	1,01170
EL-9	4	1,590	1,590	1,945	38938,600	38948,500	9,900	25,320	58,31	26,901	153,562	1,00990
EL-8	5	0,945	0,945	1,226	38687,800	38693,400	5,600	14,322	32,99	15,217	67,341	1,00480
EL-7	6	0,611	0,611	0,760	38738,400	38739,800	1,400	3,581	18,67	3,804	20,086	0,99590
EL-6	7	0,380	0,380	0,482	38807,300	38808,300	1,000	2,558	15,09	2,717	13,174	0,97110
EL-5	8	0,261	0,261	0,315	38163,600	38164,700	1,100	2,813	12,53	2,989	18,321	0,89460
EL-4	9	0,156	0,156	0,202	38559,200	38560,200	1,000	2,558	9,72	2,717	12,157	0,69010
EL-3	10	0,095	0,095	0,122	38548,700	38549,500	0,800	2,046	7,16	2,174	10,113	0,39550
EL-2	11	0,057	0,057	0,074	39072,000	39073,200	1,200	3,069	5,12	3,261	14,668	0,22490
EL-1	12	0,028	0,028	0,040	38455,000	38455,800	0,800	2,046	2,05	2,174	7,149	0,10000
Sum							39,100	100,00				

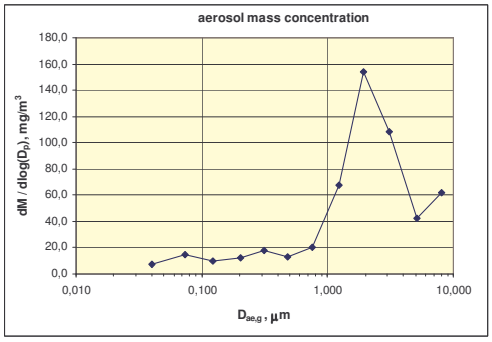

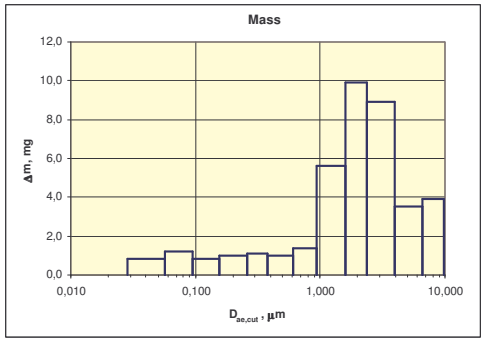

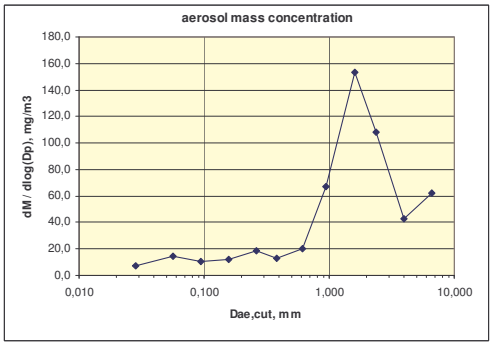

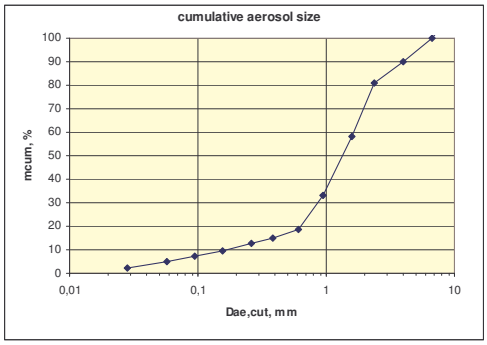

Table.IV.34. Primary side OPC Dekati impactor information for CAAT-10.

Tag Name:	Outlet Andersen
Identification:	CAAT-10

Notes:

Weight increased in 0,014

Integrale Data of Measurement:

Meas-Fluid:			Air		
t_s	1212	s	FV_{sys}	115,9	*m3/h*
t_{Start}	12:31	s	FV_s	32,37	*l/min*
P_s	1,12	*bar(a)*	V_s	653,79	*l*
T_s	25,60	*°C*	C_s	4,81	*mg/m3*
MW_s	29,0	*kg/kmol*	$FM_{aerosol}$	0,56	*g/h*
X_{steam}	0,000	%	η_{ref}	1,820E-05	*Pa-s*
m_{total}	3,146	*mg*	η_{act}	1,840E-05	*Pa-s*
			AMMD	1,0	*µm*
			GSD	1,2	

Device Parameter:

Modell	Sierra Andersen	
S/N:		
Supplier:	Andersen Sampler Inc.	
Calibration:		
Reference Flow Rate:	9,911	l/min
Reference Temperature:	25,0	°C
Reference Pressure:	1,0133	bar_a
Reference Fluid:	Air	

Stage		$D_{p,50}$ ref	$D_{p,50}$ cut	$D_{ae,g}$	m_0	m_1	Δm	m_p	m_{cum}	M	$dM/dlog(D_p)$
		µm	µm	µm	mg	mg	mg	%	%	mg/m^3	mg/m^3
	--	--	--	--	--	--	--	--	--	--	--
AI-1	1	15,000	8,346	--	83,655	83,684	0,029	0,9218	100,00	0,044	0
AI-2	2	9,200	5,119	6,536	83,383	83,389	0,006	0,1907	99,08	0,009	0,043
AI-3	3	3,700	2,059	3,246	84,361	84,385	0,024	0,7629	98,89	0,037	0,093
AI-4	4	2,200	1,224	1,587	82,101	84,110	2,009	63,859	98,12	3,073	13,610
AI-5	5	1,400	0,779	0,976	83,867	83,890	0,023	0,7311	34,27	0,035	0,179
AI-6	6	0,760	0,423	0,574	84,317	84,631	0,314	9,9809	33,53	0,480	1,810
AI-7	7	0,420	0,234	0,314	85,155	85,478	0,323	10,267	23,55	0,494	1,918
AI-8	8	0,250	0,139	0,180	83,701	83,819	0,118	3,7508	13,29	0,180	0,801
AI-9	9	0,1005	0,056	0,088	84,681	84,741	0,060	1,9072	9,54	0,092	0,232
AI-10	10	0,0192	0,011	0,024	85,070	85,194	0,124	3,9415	7,63	0,190	0,264
Backup	Backup	0,013	0,013	0,013	127,345	127,461	0,116	3,6872	3,69	0,177	0,172
Sum	REF				84,65	84,661	3,146	100,00			

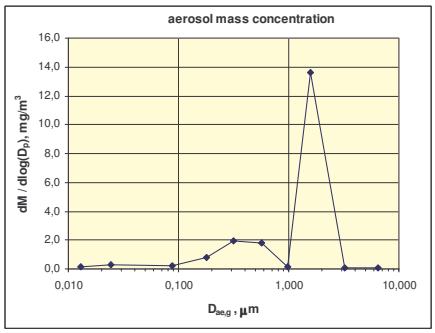

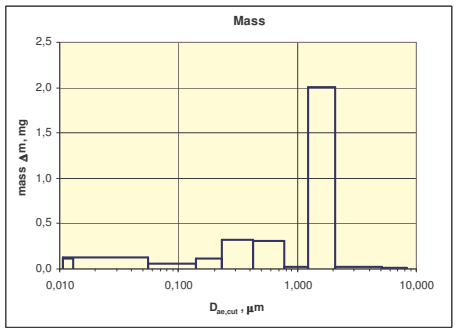

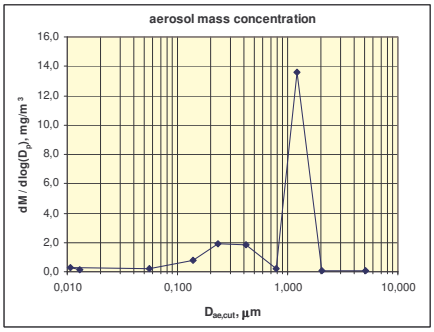

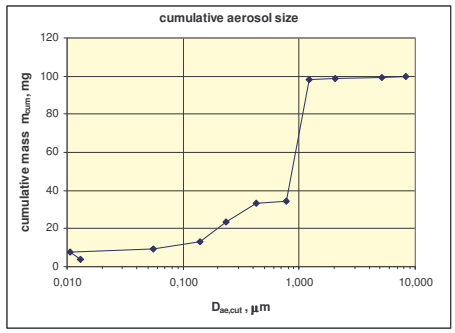

Table.IV.35. Secondary side Andersen impactor information for CAAT-10.

C.3.2. ONLINE AEROSOL SIZE DISTRIBUTION AT THE PRIMARY AND SECONDARY SIDE

As an example, Fig.IV.25 and 26 shows APS the count mean diameter, count median diameter and GSD evolution with time during CAAT-13 for primary side.

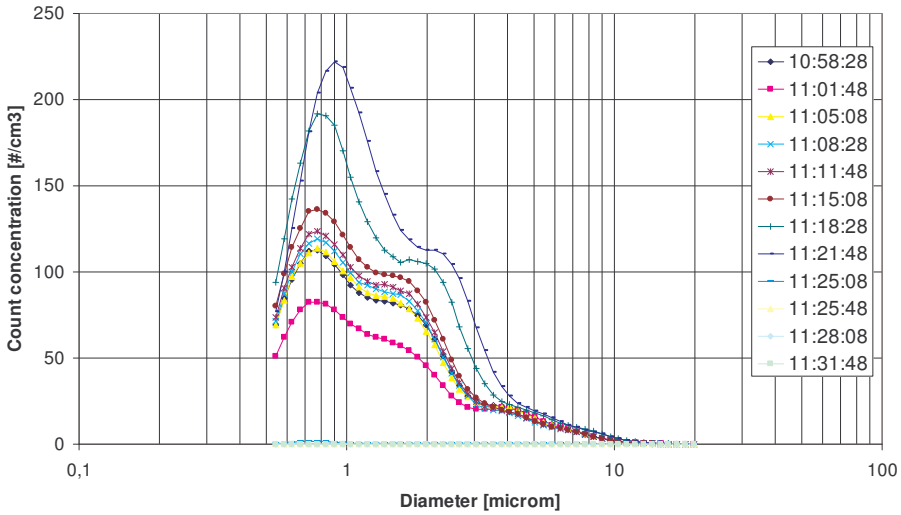

Fig.IV.25. APS primary side count size distribution for CAAT-13.

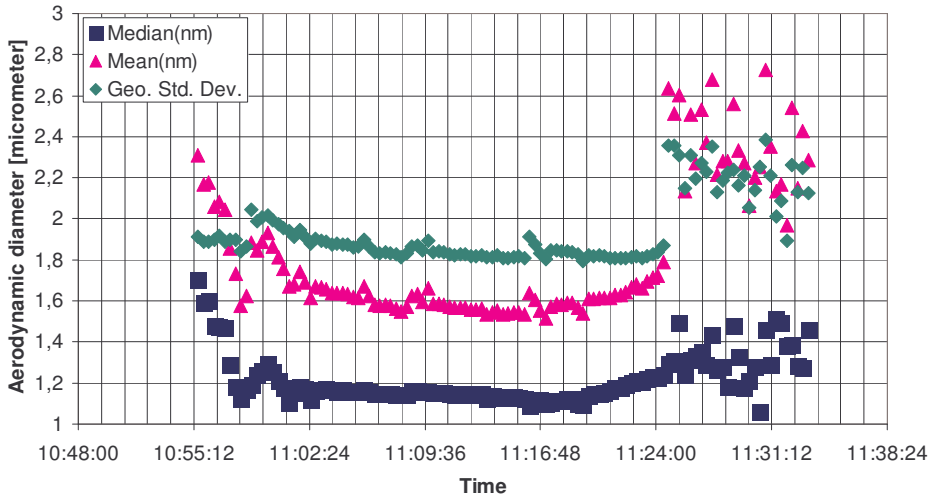

Fig.IV.26. APS primary side count mean, median diameter and GSD for CAAT-13.

Fig.IV.27 shows the OPC count size distribution evolution with time. Fig.IV.28 shows OPC the count mean diameter, count median diameter and GSD evolution with time during CAAT-13.

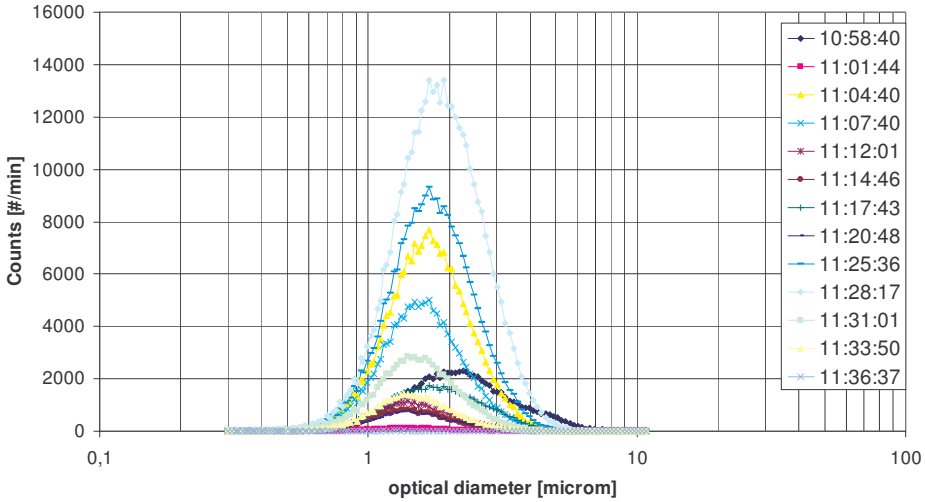

Fig.IV.27. OPC primary side count size distribution for CAAT-13.

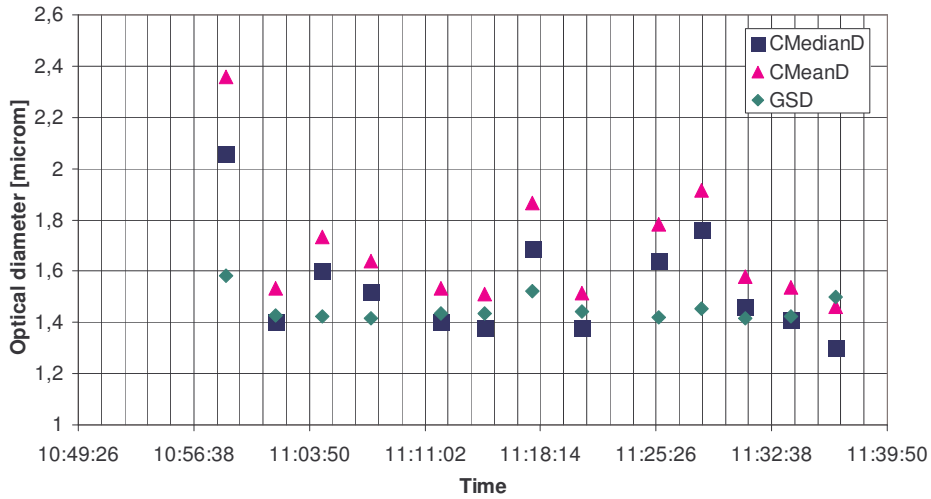

Fig.IV.28. OPC primary side count mean, median diameter and GSD for CAAT-13.

Fig.IV.29 shows the averaged particle count size distribution for CAAT-13 measured by ELPI at the secondary side. Fig.IV.30 shows ELPI the count mean diameter, count median diameter and GSD evolution with time during CAAT-13. Time evolution of

properties show that median diameter and GSD does not vary with time keeping a steady value.

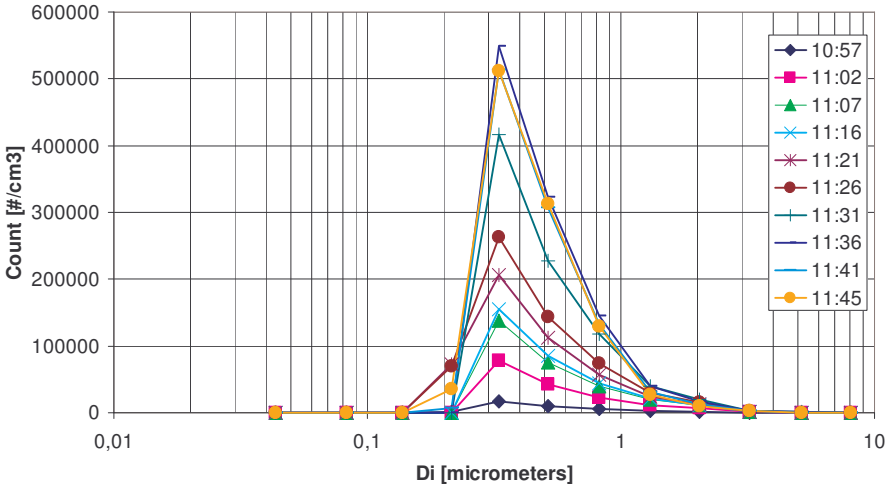

Fig.IV.29. ELPI secondary side count size distribution for CAAT-13.

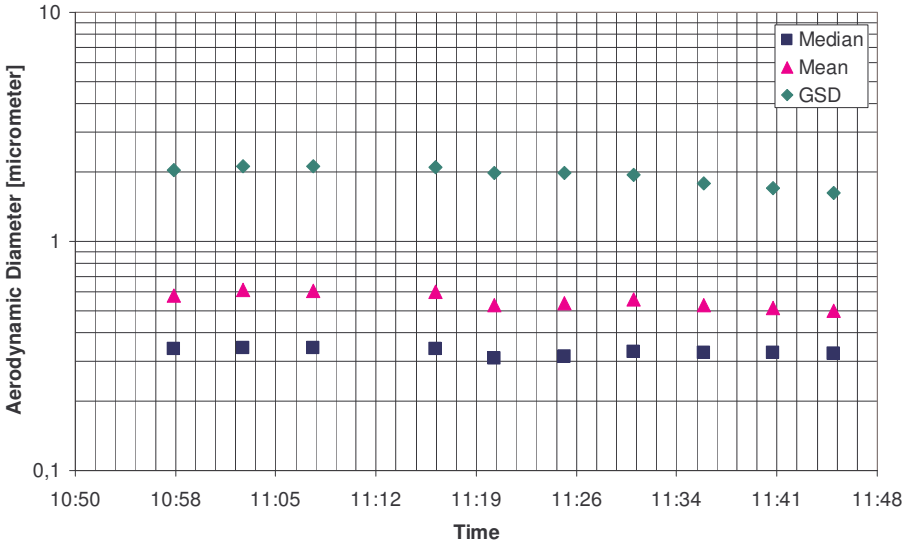

Fig.IV.30. ELPI secondary side count mean, median diameter and GSD for CAAT-13.

C.3.3. AEROSOL DEPOSITION PATTERN AND RETENTION EFFICIENCY ESTIMATION

Qualitative and quantitative observations of the deposition found during SiO_2 CAAT tests remarks the difference in the deposition pattern found between TiO_2 Degussa

tests and TiO_2 Nanophase tests and SiO_2 tests. Fig.IV.31 to 37 show the on-tube deposition pattern found for CAAT-06, CAAT-07, CAAT-08, CAAT-09, CAAT-10, CAAT-11 and CAAT-13.

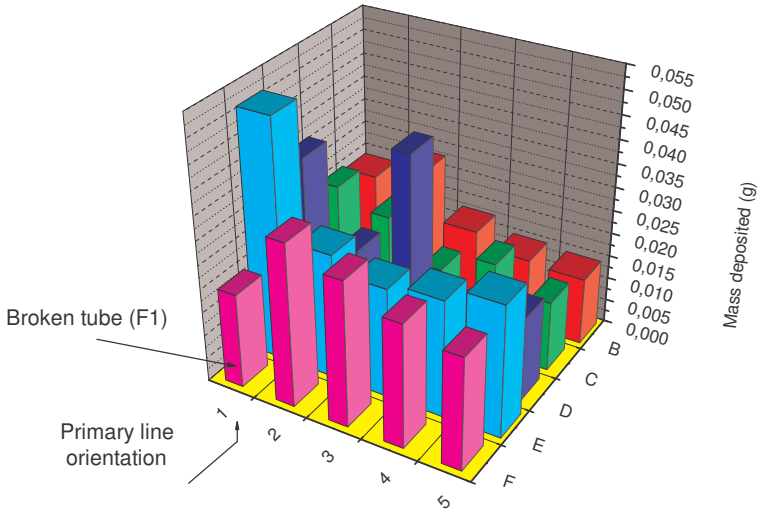

Fig.IV.31. On tube mass deposition pattern for CAAT-06.

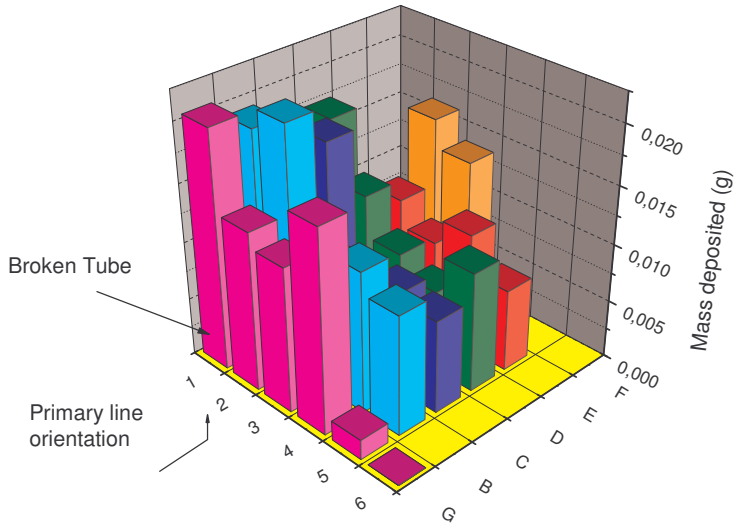

Fig.IV.32. On tube mass deposition pattern for CAAT-07.

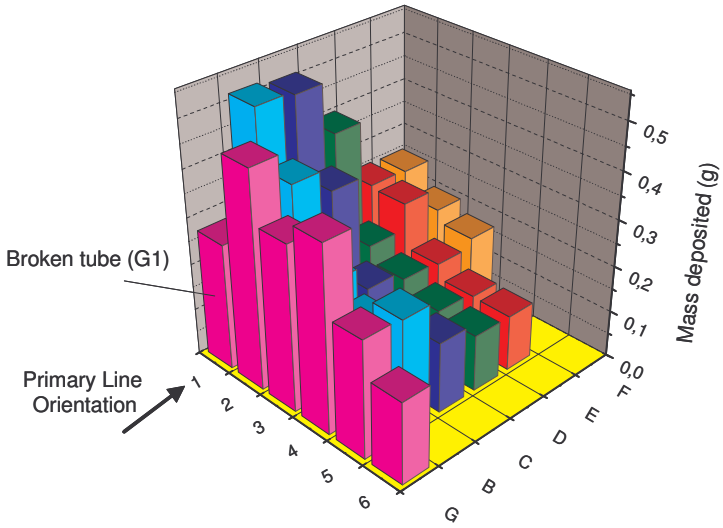

Fig.IV.33. On tube mass deposition pattern for CAAT-08.

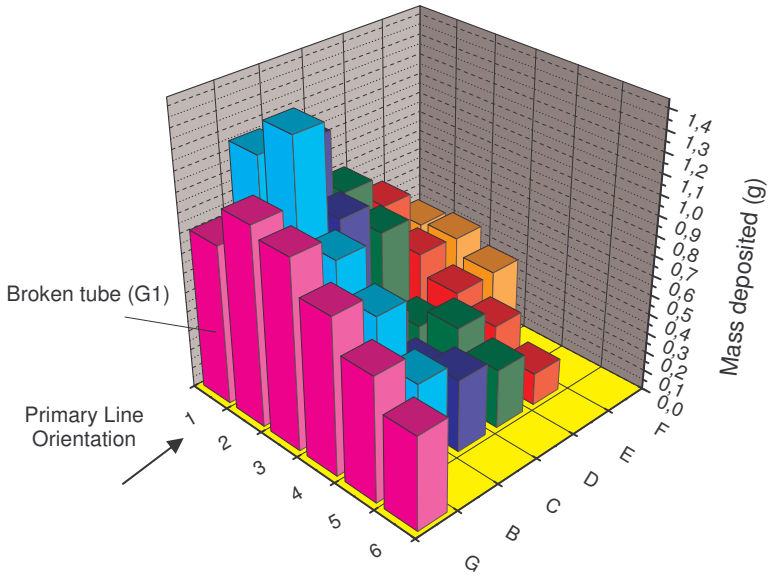

Fig.IV.34. On tube mass deposition pattern for CAAT-09.

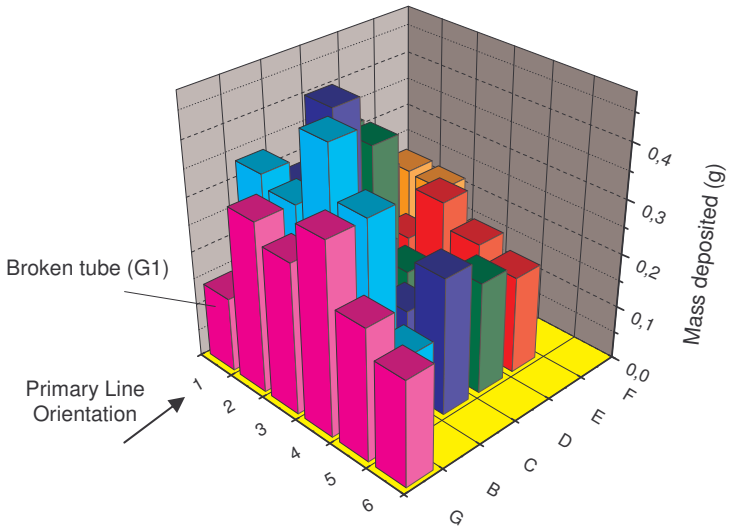

Fig.IV.35. On tube mass deposition pattern for CAAT-10.

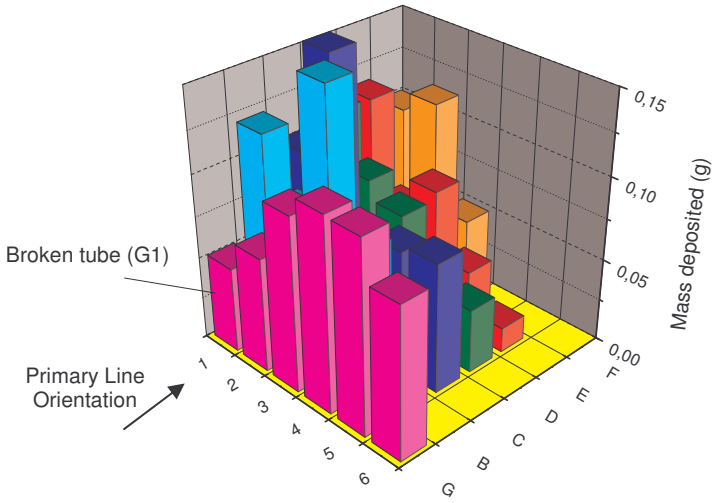

Fig.IV.36. On tube mass deposition pattern for CAAT-11.

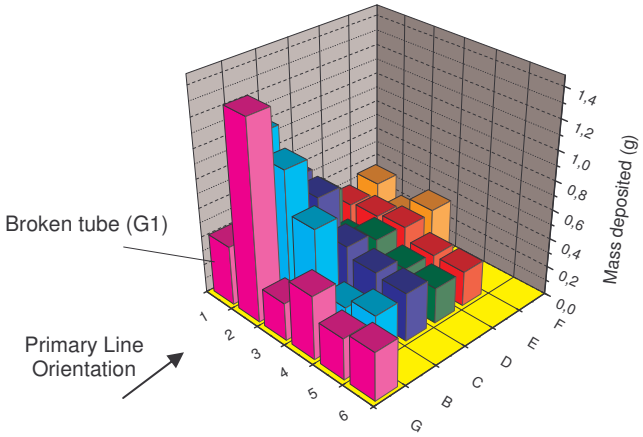

Fig.IV.37. On tube mass deposition pattern for CAAT-13.

Fig.IV.38 shows de DF as a function of the particle size using primary and secondary side low pressure impactor measurement (Dek/ELPI) for CAAT-09:

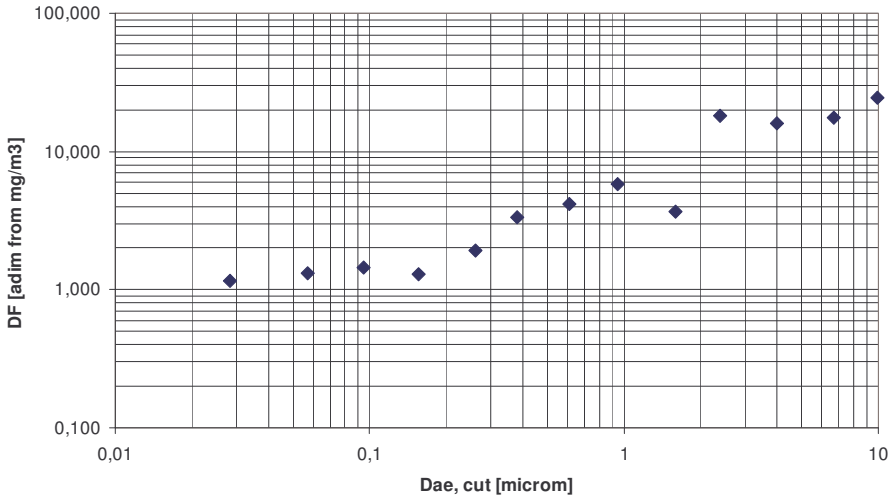

Fig.IV.38. DF as a function of aerodynamci cut diameter for CAAT-09.

Finally, Table.IV.36 shows the retention efficiency results:

Experiment	Design inlet gas mass flow rate [kg/h]	Mean Value [%]	Estimated Uncertainty [%]
CAAT-06	100	59.47	20.66
CAAT-07	150	48.03	47.14
CAAT-08	200	84.11	6.75
CAAT-09	100	94.16	3.59
CAAT-10	150	92.94	3.91
CAAT-11	250	80.93	8.75
CAAT-13	75	81.24	9.05

Table.IV.36. Retention efficiency estimations for SiO_2 tests.